



HAL
open science

Aspects of multiband systems : Quantum geometry, flat bands, and multifold fermions

Ansgar Graf

► **To cite this version:**

Ansgar Graf. Aspects of multiband systems : Quantum geometry, flat bands, and multifold fermions. Condensed Matter [cond-mat]. Université Paris-Saclay, 2022. English. NNT : 2022UPASP153 . tel-04047054

HAL Id: tel-04047054

<https://theses.hal.science/tel-04047054v1>

Submitted on 27 Mar 2023

HAL is a multi-disciplinary open access archive for the deposit and dissemination of scientific research documents, whether they are published or not. The documents may come from teaching and research institutions in France or abroad, or from public or private research centers.

L'archive ouverte pluridisciplinaire **HAL**, est destinée au dépôt et à la diffusion de documents scientifiques de niveau recherche, publiés ou non, émanant des établissements d'enseignement et de recherche français ou étrangers, des laboratoires publics ou privés.

Aspects of multiband systems:
Quantum geometry, flat bands, and
multifold fermions

*Aspects des systèmes multibandes:
Géométrie quantique, bandes plates et fermions multiples*

Thèse de doctorat de l'université Paris-Saclay

École doctorale n° 564 : Physique en Île-de-France (PIF)
Spécialité de doctorat : Physique
Graduate School : Physique
Référent : Faculté des sciences d'Orsay

Thèse préparée dans l'unité de recherche
Laboratoire de Physique des Solides (Université Paris-Saclay, CNRS)
sous la direction de **Mark Oliver GOERBIG**, directeur de recherche
sous la co-direction de **Frédéric PIÉCHON**, chargé de recherche

Thèse soutenue à Paris-Saclay, le 06 décembre 2022, par

Ansgar GRAF

Composition du jury

Membres du jury avec voix délibérative

Cristina BENA Directrice de Recherche Université Paris-Saclay, CEA, CNRS Institut de Physique Théorique	Présidente
Adolfo GRUSHIN Chargé de Recherche Université Grenoble Alpes, CNRS Institut Néel	Rapporteur
Titus NEUPERT Professeur Universität Zürich	Rapporteur
David CARPENTIER Directeur de Recherche École normale supérieure de Lyon, CNRS Laboratoire de Physique	Examineur

Titre : Aspects des systèmes multibandes : Géométrie quantique, bandes plates et fermions multiples

Mots clés : Bandes d'énergie ; Structure électronique ; Semi-métaux ; Topologie ;

Résumé : La théorie des bandes des solides est une pierre angulaire de la physique de la matière condensée depuis près d'un siècle. Au cours des dernières décennies, elle a été étendue pour inclure systématiquement les effets provenant des propriétés géométriques et topologiques des fonctions d'onde électroniques. Cette approche a été appliquée avec succès pour expliquer une pléthore de phénomènes observés dans une variété de matériaux cristallins, ainsi que dans des réseaux périodiques artificiels. Alors qu'une description effective impliquant seulement deux bandes ($N = 2$) autour de l'énergie de Fermi est souvent employée dans des modèles simples, ces dernières années, de nombreux systèmes physiques qui nécessitent intrinsèquement une description multibande ($N > 2$) ont été mis en évidence. Il s'agit notamment des systèmes 2D et quasi-2D à bande plate ainsi que des semi-métaux topologiques 3D. Inspiré par ces développements, le présent travail étudie théoriquement plusieurs aspects fondamentaux des systèmes multibandes. Premièrement, une nouvelle approche des observables dans les systèmes multibandes est développée. Elle est basée sur les projecteurs propres et les vecteurs de Bloch correspondants, et peut aider à surmonter les problèmes provenant de la dépendance de jauge et des singularités in-

contrôlées des états propres d'énergie. Deuxièmement, en exploitant le concept d'un état localisé compact – une fonction d'onde avec une amplitude strictement nulle en dehors d'une petite région du réseau –, une méthode simple et intuitive pour construire un nombre arbitraire de modèles de liaisons fortes à bande plate est présentée. La méthode permet également de concevoir la présence de croisements de bandes multiples à l'énergie de la bande plate d'une manière contrôlée. De plus, elle peut être considérée comme un schéma de classification des bandes plates basé sur la relation entre le hamiltonien de Bloch et l'état localisé compact. Troisièmement, une nouvelle classe de semi-métaux 3D avec des croisements de bandes d'énergie linéaires multiples est proposée. Cette classe présente des excitations à basse énergie fondamentalement différentes des fermions chiraux multiples des semi-métaux topologiques connus : chaque point de croisement agit comme un dipôle de Berry au lieu d'un monopôle de Berry, avec des signatures claires dans les niveaux de Landau et le transport semiclassique. Cette phase semi-métallique est également étroitement liée au concept récemment proposé d'un isolant de Hopf multibande topologique, ouvrant plusieurs perspectives intéressantes.

Title : Aspects of multiband systems : Quantum geometry, flat bands, and multifold fermions

Keywords : Energy bands ; Electronic structure ; Semimetals ; Topology ;

Abstract : The band theory of solids has been a cornerstone of condensed matter physics for almost a century. In recent decades it has been extended to systematically include effects originating from geometric and topological properties of electronic wave functions. This has been successfully applied to explain a plethora of phenomena observed in a variety of crystalline materials, as well as in artificial periodic lattices. While an effective description involving only two bands ($N = 2$) around the Fermi energy is often employed in simple models, in recent years many physical systems that intrinsically necessitate a multiband description ($N > 2$) have come into focus. These include, notably, 2D and quasi-2D flat-band systems as well as 3D topological semimetals. Inspired by such developments, the present work theoretically investigates several fundamental aspects of multiband systems. First, a new approach to observables in multiband systems is developed. It is based on eigenprojectors and the corresponding Bloch vectors, and helps to overcome issues originating from the gauge dependency and uncontrolled singularities

of energy eigenstates. Second, exploiting the concept of a compact localized state – a wave function with strictly zero amplitude outside a small region of the lattice –, a simple and intuitive method to construct arbitrarily many flat-band tight-binding models is presented. The method also allows to design the presence of multifold band crossings at the flat-band energy in a controlled way. Moreover, it can be viewed as a flat-band classification scheme based on the relation between the Bloch Hamiltonian and the compact localized state. Third, a new class of 3D semimetals with multifold linear energy band crossings is proposed. This class features low-energy excitations fundamentally different from the chiral multifold fermions of known topological semimetals : each crossing point acts as a Berry dipole instead of a Berry monopole, with clear signatures in Landau levels and semiclassical transport. As discussed in detail, this semimetallic phase is also closely related to the recently proposed concept of a topological multiband Hopf insulator, opening several interesting perspectives.

Contents

Preface	i
Outline of the thesis	v
1 Quantum geometry and topology in solid-state physics	1
1.1 Basic band theory	1
1.2 Introduction to quantum geometry	2
1.2.1 General setup	2
1.2.2 Main objects of quantum geometry	3
1.2.3 Origin of quantum geometry	5
1.3 Topology in band theory	7
1.3.1 Zoo of topological matter	7
1.3.2 Topology versus quantum geometry	8
1.4 Example: From graphene to Chern insulators	10
1.4.1 Dirac semimetal: Graphene	11
1.4.2 Semenoff insulator	13
1.4.3 Chern insulator: Haldane's model	13
1.5 Influence of geometry and topology on physics	14
1.5.1 Topological edge states	15
1.5.2 Physical consequences of topological edge states	18
1.5.3 Quantum geometry in orbital magnetism	20
1.5.4 Quantum geometry in the superfluid weight	22
1.5.5 Quantum geometry in magnetotransport	23
2 From two-band to multiband systems	27
2.1 Physical motivation (I) – Flat bands	27
2.1.1 Flat bands in simple lattice models	28
2.1.2 Flat bands in experiments	30
2.2 Physical motivation (II) – multifold band crossings	31
2.2.1 Multifold crossings in simple models	31
2.2.2 Multifold crossings in experiments	34
2.3 Mathematical motivation (I) – Hamiltonian and $\mathfrak{su}(N)$ algebra	35
2.3.1 Two-band systems	36
2.3.2 Multiband systems	36
2.4 Mathematical motivation (II) – Internal parameters and Bloch spheres	39
2.4.1 Two-band systems	39
2.4.2 Multiband systems	43

3	Bloch vector approach to observables	47
3.1	Introduction	47
3.2	Motivation: Eigenstates versus eigenprojectors and Bloch vectors . . .	48
3.3	Writing observables in terms of Bloch vectors	49
3.3.1	First examples	49
3.3.2	Berry curvature, quantum metric and orbital magnetization . .	50
3.3.3	General observables	53
3.4	Eigenprojectors and Bloch vectors from the Hamiltonian	54
3.4.1	Eigenprojectors as a function of the Hamiltonian matrix . . .	54
3.4.2	Bloch vectors as a function of the Hamiltonian vector	56
3.4.3	Observables in terms of the Hamiltonian	57
3.5	Example: Pseudospin- s fermions	58
3.6	Conclusions	60
4	Designing flat-band models with multifold band crossings	61
4.1	Introduction	61
4.2	Basics of flat-band physics	62
4.2.1	Compact localized states and associated Bloch states	62
4.2.2	Link between compact localized states and flat bands	64
4.2.3	Wannier states versus compact localized states	67
4.3	Building flat-band models from compact localized states	68
4.4	Flat-band models with quadratic band touching	70
4.4.1	Two-band models	70
4.4.2	Three-band models	73
4.4.3	N -band models	76
4.5	Flat-band models with linear band crossing	78
4.5.1	Three-band models	79
4.5.2	N -band models	88
4.6	Further remarks on the flat-band design method	90
4.6.1	Scarcity of linear flat-band models	90
4.6.2	Interpolating between linear and quadratic band touching . . .	91
4.6.3	Flat-band models beyond the linear or quadratic class	92
4.7	Perspectives of flat-band systems	92
4.7.1	Quantum geometry of flat-band models	93
4.7.2	Designing magnetic flat-band models	95
4.7.3	Designing models with more than one flat band	97
4.8	Conclusions	98
5	Multifold fermions beyond Berry monopoles	101
5.1	Introduction	101
5.2	Motivation: Exploring the matrix space of linear Hamiltonians	103
5.3	Continuum models for multifold Hopf semimetals	104
5.3.1	Models and symmetries	104
5.3.2	Physical properties (I) – Landau levels	106
5.3.3	Physical properties (II) – Anomalous Hall effect	110
5.3.4	Physical properties (III) – Magnetoconductivity	112

5.4	Tight-binding models for multifold Hopf semimetals	114
5.4.1	Valley-Hopf semimetals	114
5.4.2	Topological Hopf semimetals	117
5.4.3	Physical properties from a lattice perspective	118
5.5	Multiband Hopf semimetals and Hopf insulators	119
5.5.1	Two-band and multiband Hopf insulators	119
5.5.2	Lattice models for multiband Hopf insulators	122
5.5.3	Hopf semimetals as topological phase transitions	125
5.5.4	Berry dipoles from merging of monopoles	127
5.6	Perspectives of Hopf semimetals and insulators	129
5.6.1	Linear band crossings with Berry multipole structure	129
5.6.2	Hopf-Haldane analogy	130
5.6.3	Dimensional reduction and tensor monopoles	133
5.7	Conclusions	134
Conclusions		137
Appendix I		141
I.A	Recap on tight-binding theory and Bloch basis	141
I.B	Quantum geometry in early band theory formalisms	142
I.C	Magnetotransport in multiband systems to linear order in \mathbf{B}	143
Appendix II		146
II.A	Gell-Mann and spin matrices	146
II.B	The generalized Bloch sphere	148
Appendix III		151
III.A	General recipe to find a Bloch vector expression	151
III.B	$SU(N)$ Jacobi identities	152
III.C	Alternative QGT formula in terms of Bloch vectors	153
III.D	Derivation of Eq. (3.26)	154
III.E	Closed-form solutions for energy eigenvalues	156
III.F	Eigenstates from eigenprojectors	157
III.G	Derivation of Eq. (3.32)	157
III.H	Berry curvature for N -band systems	159
Appendix IV		161
IV.A	Relation between CLSs and real-space tight-binding models	161
IV.B	Two-band Hamiltonian with a flat band	162
IV.C	Band touching scenarios for the quadratic three-band Hamiltonian	163
IV.D	Examples for three-dimensional flat-band models	163
Appendix V		165
V.A	Continuum model construction via pseudomolecule	165
V.B	Landau levels of multifold Hopf semimetals	167
V.C	Landau levels of pseudospin- s fermions	171
V.D	Onsager quantization with intraband and interband coupling	174

V.E Semiclassical transport theory for MHS models	178
V.F Continuum limit of multiband Hopf insulators	180
Synthèse en français	183
Bibliography	191

Acknowledgements

First and foremost, I would like to express my gratitude to my PhD advisor, Frédéric Piéchon, who helped me enormously with his omnipresence, endless patience, and bright mind. He has been a perfect example of a true researcher, and I have learned a lot from his creative, critical and passionate way of working. I will always remember the time after the lockdown 2020, when we were basically the only two people present at the lab for weeks.

My sincere thanks also goes to my two original PhD advisors, Mark Goerbig and Marc Gabay. Although we did not find a common path scientifically, both have been very helpful in getting my thesis started. I further thank Philippe Mendels and Marcello Civelli for bringing me to the LPS, Andrej Mesaros for his brilliance in answering any question about topology, as well as the jury members Adolfo Grushin, Titus Neupert, Cristina Bena and David Carpentier for making the effort of reviewing my manuscript and coming to Orsay. A big thanks also to the administrative staff, especially Marie-France Mariotto, Christophe Nicolosi and Véronique Thieulart, for countless answered questions.

The preparation of the thesis would have been quite boring without the many good friends at the lab. Cheers to Mateo for being a superb office mate, as well as to Baptiste, Étienne, Marina and Jean-Baptiste for the great time we had especially this last year. Cheers also to Helen, Léo, Alice and Xavier, who are amazing people even though they are experimentalists. I also wish good luck to Lise and Florian across the hallway, and thank the previous PhD students Pierre and Xin as well as our short-term postdocs Jonathan and Dinya for bringing life to the theory group.

Of course, many friends outside of the laboratory have helped me enormously to persevere. I have to mention especially Ganesh and Marta, Viktor, Selen, Marine and Christian.

Finally, my friends and family back in Germany have been a calm anchor throughout. Thank you to Leonie for always being there, to my brothers and father for visiting and helping me move, and especially to my grandparents Gerhard and Regine for their endless care packages, confidence and support. I dedicate this thesis to you.

Preface

Crystalline solids played a major role in the scientific and industrial revolutions of the 19th century. Substantial knowledge about their properties was accumulated by physicists, chemists and engineers, mainly concerning macroscopically observable properties such as electrical and thermal conductance, flexibility, melting temperature, et cetera. Despite being invaluable for technological applications, much of this knowledge was of a rather empirical nature, and many fundamental questions about the microscopic structure of crystals remained unanswered. To mention a well-known example, the observed electrical conductance and heat capacity of metals could not be explained satisfactorily using phenomenological models based on classical physics such as that of Drude (1900).

Establishing more reliable explanations for the behavior of solids only became possible after the emergence of the theory of quantum mechanics in the early 20th century. Two notions following from the quantum theory proved of particular importance: First, the realization that electrons can be viewed as waves, and therefore that the wave equation found by Schrödinger (1926) should be solved for electrons moving in the presence of the periodic potential landscape created by the atoms in a crystal. Second, the fact that electrons exhibit Fermi-Dirac statistics (Fermi 1926; Dirac 1926) and carry a spin degree of freedom (Pauli 1925). After decisive contributions by the likes of Sommerfeld (1928), Bloch (1929), Brillouin (1930) and others, who implemented these fundamental ideas quantitatively, a very mature sub-field of physics quickly arose; it has come to be known as *solid-state physics* (Ashcroft and Mermin 1976).

At first glance, describing the physics of solids quantitatively is a very complicated many-body problem. However, history has taught us that

“it is [...] possible to view much of solid-state physics in terms of certain elementary excitations which interact only weakly with one another”
(Pines 1963).

Such elementary excitations serve to effectively decompose the inner workings of a solid into several parts. They can be associated to the motion of nuclei vibrating around their equilibrium positions (phonons); to the motion of non-interacting conduction electrons forming a Fermi gas (single-particle excitations); to the motion of interacting electrons forming a Fermi liquid (quasi-particle excitations); to the collective motion of spins (magnons), and many more. Depending on the physical circumstances of interest, describing a solid theoretically then boils down to focusing on a certain elementary excitation.

This thesis mainly follows the standard approach that approximates a solid as being a Fermi gas in the presence of a periodic lattice potential. Within this framework, one is interested in single-particle excitations that are described by the well-known *band theory of solids* (Singleton 2001). Exploiting the lattice periodicity, this theory formulates the problem in Fourier (or reciprocal) space, and encodes the properties of

the single-particle excitations in the so-called Bloch Hamiltonian $H(\mathbf{k})$. The parameter \mathbf{k} is known as the wave vector (or crystal momentum). From $H(\mathbf{k})$, one obtains the energy band structure $\epsilon_\alpha(\mathbf{k})$, where α is the band index. At zero temperature, the bands are filled up to the Fermi energy E_F by electrons, defining a Fermi surface as the subspace of reciprocal space that satisfies $\epsilon_\alpha(\mathbf{k}) = E_F$.

During the second half of the 20th century, the band theory of solids was successfully used to construct the band structures (and Fermi surfaces) of insulators, semiconductors and metals, an essential achievement that provided the basis for the modern electronics industry. However, beyond the band structure, there exists important information encoded in the quantum mechanical eigenstates $|\psi_\alpha(\mathbf{k})\rangle$ of the Bloch Hamiltonian. This gives rise to *interband effects* on observable properties of crystals, as was quite explicitly pointed out in certain works¹ from the 1940s to the 1970s. However, those theories were perhaps not formulated in a sufficiently general and accessible way, such that the universal nature of interband effects, which are also known as *quantum geometrical*, *band geometrical*, or simply *geometrical* effects, was not adequately appreciated. Most importantly, it remained unknown that they can give rise to *topological physics* under the right circumstances.

Today, it is well known that the standard band theory of solids has to be augmented by geometrical and topological concepts. This extended band theory is known as *topological band theory* (Hasan and Kane 2010; Qi and Zhang 2011; Bansil et al. 2016; Cayssol and Fuchs 2021). Materials described by topological band theory are currently a major focus of solid-state research laboratories all over the globe. This is because they host a variety of unconventional phenomena when it comes to conducting electricity, responding to magnetic fields, pressure, light beams, et cetera, which holds promise for future technological applications.

Perhaps the most crucial breakthrough responsible for the ultimate success of modern topological band theory consisted in the exfoliation of single graphene layers by Novoselov et al. (2004) [see also the review article by Castro Neto et al. (2009)]. Especially after Kane and Mele (2005) predicted the existence of a quantum spin Hall effect in graphene, a veritable “gold rush” on condensed matter systems with non-trivial geometry and topology began. As a consequence, many topological materials were discovered in the following decade, among which the most important ones are three-dimensional (3D) topological insulators (Hasan and Moore 2011) and 3D topological semimetals (Armitage et al. 2018).

This development benefitted greatly from the fact that numerous scientific contributions that had previously implicitly or explicitly addressed quantum geometric and topological effects, as well as their physical consequences, could now be understood from a new perspective and treated in a unified way. Here are some prominent examples for this:

- 1.) It was realized that the quantum Hall effect (Klitzing et al. 1980), whose quantized conductance plateaus were explained by topological arguments early on (Thouless et al. 1982; Avron et al. 1983), is only one particular example out of a whole family of topological quantum matter. Indeed, the quantum Hall

¹See Appendix I.B for more details and references.

effect is now viewed as a 2D topological insulator in class A of the tenfold way symmetry classification (Ryu et al. 2010).

- 2.) Berry’s geometrical phase (Simon 1983; Berry 1984), acquired by a quantum system upon traversing a closed loop in parameter space, has found countless applications in various branches of physics. Its extremely universal character and the ensuing physical consequences are now fully appreciated (Wilczek and Shapere 1989; Resta 2000; Xiao et al. 2010).
- 3.) Haldane’s proposal for a quantum Hall effect without net magnetic field (Haldane 1988), at the time considered to be purely a toy model, is now viewed as the first genuine topological insulator (based on standard non-magnetic Bloch states, in contrast to the quantum Hall effect) and is called Chern insulator (or quantum anomalous Hall effect).
- 4.) Dirac (1928) and Weyl (1929) fermions, historically introduced in a high-energy context and later proposed to exist in condensed matter (Nielsen and Ninomiya 1983; Volovik 1987; Fang et al. 2003), are now known to be crucial for understanding the exotic physics of topological semimetals (Armitage et al. 2018).
- 5.) Parameter-dependent quantum systems – and thus solids with a Bloch Hamiltonian $H(\mathbf{k})$ – are equipped with a rich geometric structure, encoded not only by Berry’s phase, but also by the quantum metric (Provost and Vallee 1980), reminiscent of the metric structure used to describe the geometry of spacetime in general relativity. This quantum metric is now known to play a fundamental role in the response of crystals to external perturbations.

From a theoretical physicist’s point of view, it has to be noted that a big portion of progress made in topological band theory may be ascribed to effective models:

“Looking back at how this new field of topological quantum matter has developed since the initial discoveries in about 1980, I am struck by how important the use of stripped-down toy models has been in discovering new physics” (Haldane 2017).

In particular, the kind of effective models we have in mind are those based on the tight-binding approximation (Simon 2013) or on low-energy continuum theories. Both tight-binding and continuum Hamiltonians are frequently used to model single-particle excitations in a small energy window around the Fermi energy, which qualitatively captures much of the essential low-energy physics. Also in this thesis, we will extensively employ such effective models.

In the simplest case, tight-binding or continuum models used in topological band theory are *two-band models*, because one is often predominantly interested in the physics of the conduction and valence band edges (in the case of insulators) or of the two bands crossing near the Fermi energy (in the case of semimetals). Such two-band models have simple and well-known properties. Famous examples include the models that have been developed for graphene (Wallace 1947), Weyl semimetals (Nielsen and Ninomiya 1983), Chern insulators (Haldane 1988), or Hopf insulators (Moore et al.

2008). However, in recent years, an increasing number of systems that necessitate going beyond a two-band description have come into focus. Here we mention some important examples:

- 1.) Many lattices with flat energy bands are described by models involving more than two bands (Leykam et al. 2018). These systems are of interest because electrons in the flat band have quenched kinetic energy and are susceptible to Coulomb interaction effects, providing an interesting avenue to strongly correlated quantum phases. Experimentally accessible systems exhibiting flat-band physics were recently found, such as twisted bilayer materials (Cheng et al. 2019; Andrei and MacDonald 2020; Mogera and Kulkarni 2020) and Kagome metals (Lin et al. 2018; Kang et al. 2020; Liu et al. 2020).
- 2.) Topological semimetals with multiple energy bands that simultaneously cross at certain points in the first Brillouin zone have been discovered (Bradlyn et al. 2016; Lv et al. 2021). Such multifold crossing points, which generalize Weyl semimetals and cannot be captured by two-band models, give rise to unique transport and optical properties.
- 3.) Three-level and more generally multilevel quantum systems (dubbed qutrits and qudits, respectively) are emerging as alternative platforms to build quantum computers, presenting several advantages over qubit-based approaches, see for example Wang et al. (2020) or Blok et al. (2021).

Motivated by these developments, this thesis is devoted to delving into the physics of *multiband systems*, that is, systems that involve $N > 2$ energy bands. In particular, we will focus on three aspects that were already mentioned above: the quantum geometry of multiband systems, flat-band physics in multiband systems, and the properties of multifold band crossings. Those are a priori distinct topics but they are also intricately linked: quantum geometry is strongly enhanced in the vicinity of multifold crossings, multifold crossings are often accompanied by flat bands, and flat bands have very peculiar quantum geometric properties. To describe multiband systems quantitatively, we typically employ tight-binding or continuum models described by $N \times N$ Bloch Hamiltonian matrices. The phenomenology contained in such Hamiltonians is much richer than in the two-band case, hence the existence of many physical phenomena that cannot exist in a two-band system is to be expected. The goal of this thesis is to study in depth a certain number of these phenomena. In order to do so, we will proceed as summarized in the following.

Outline of the thesis

Chapters 1 and 2 give an introduction to topics of relevance for this thesis that are essentially known in the literature, as well as a motivation for the work conducted in this thesis:

Chapter 1 – To begin with, we recall basic aspects of band theory, such as the Bloch Hamiltonian and the tight-binding approach (Section 1.1). We then introduce the guiding theme of this thesis, that is, the concept of quantum geometry, along with the main geometric objects of interest, namely quantum metric and Berry curvature (Section 1.2). Afterwards, we deal with the connection between quantum geometry and topology, and mention a number of topological invariants which will be of importance later on (Section 1.3). These concepts are illustrated by a discussion of 2D systems ranging from graphene to Chern insulators (Section 1.4). To close the chapter, we aim to illustrate that quantum geometry and topology are ubiquitous in the physical response of crystalline systems, and present a number of relevant examples ranging from topological edge states to the role of quantum geometry in transport (Section 1.5).

Chapter 2 – This chapter is devoted to motivating the study of multiband systems, that is, systems with more than two bands. We first give a physical motivation based on a selection of multiband systems that have been widely studied recently, namely flat-band lattices in 2D (Section 2.1) and multifold band crossings in 3D (Section 2.2). We discuss both types of systems at the level of simple models and underline their importance to experiments. This is followed by a more mathematical motivation. It is inspired by the rich mathematical structure of the $\mathfrak{su}(N)$ algebra underlying multiband Hamiltonians (Section 2.3), and by the corresponding complexity of the internal parameter space (Section 2.4).

After this preparation, we present original material that constitutes the core of this thesis. We arrange the material in three chapters, each of which focuses on a different aspect of multiband systems and each of which is based on a published article or preprint (see below). While there are many links between these three chapters, they can essentially be read independently from one another:

Chapter 3 – In this short chapter, we develop a rather general formalism that expresses observables in multiband systems in terms of *Bloch vectors*; these are a vectorial representation of the Hamiltonian's eigenprojectors. After a short introduction (Section 3.1) we argue that such Bloch vectors present several advantages over the conventional eigenstate-based approach to observables (Section 3.2). We then explain how to write any observable in a multiband system in terms of Bloch vectors, and illustrate these ideas via simple examples, notably the quantum geometric tensor and orbital magnetization (Section 3.3).

Next, we discuss how the eigenprojectors and Bloch vectors can be related in a unique way to the Hamiltonian, which allows (at least in principle) to compute any observable without the need for the construction of energy eigenstates (Section 3.4). In particular, we thus arrive at a multiband generalization of the well-known “skyrmion density” formula for the Berry curvature of a two-band system. To close the chapter, we apply the formalism to a pedagogical example (Section 3.5) and provide a brief summary (Section 3.6).

Chapter 4 – In this chapter we turn to the realm of flat bands. After an introduction providing an overview of related previous work (Section 4.1), we summarize some basics of flat-band physics, in particular the important notion of a *compact localized state* (Section 4.2). Based on the knowledge about such states, we proceed to develop a powerful method to construct flat-band tight-binding models (Section 4.3). This method provides (infinitely many) flat-band models on any periodic lattice, in any spatial dimension and with any number of bands. Moreover, as detailed in Sections 4.4 and 4.5, the method provides considerable control over the existence and character of multifold band crossings at the flat band energy, and can be viewed as a new flat-band classification scheme. After some additional remarks on peculiarities of the flat-band systems thus obtained (Section 4.6), and after highlighting some interesting perspectives such as the quantum geometry of the multifold crossings or the construction of magnetic flat bands (Section 4.7), the chapter concludes with a summary in Section 4.8.

Chapter 5 – This final chapter focuses on 3D (topological) semimetals with multifold band crossings. While widely known topological semimetals are based on momentum space singularities with Berry monopole structure, multiband crossings in 3D can also exhibit more exotic quantum geometric properties, as explained in Sections 5.1 and 5.2. To showcase this, we introduce a class of semimetals with the peculiar property that each crossing point carries a *Berry dipole*. We call these *multifold Hopf semimetals*, and study their physical properties both at the level of continuum (Section 5.3) and tight-binding Hamiltonians (Section 5.4). In particular, we unveil clear signatures of the Berry dipole in Landau levels, anomalous Hall effect and magnetoconductivity, which are similar to but also fundamentally different from what happens in Weyl semimetals. We then provide a link between multifold Hopf semimetals and a particular class of topological insulators known as Hopf insulators (Section 5.5). In the course of this, we also introduce the first known lattice models for multiband Hopf insulators. After mentioning some perspectives in Section 5.6 (such as close connections to Haldane’s model and 4D tensor monopoles), the chapter again closes with a brief summary (Section 5.7).

As mentioned above, each of these three chapters has emerged from a published article or preprint: Chapter 3 is based on Graf and Piéchon (2021a), but also goes beyond in that it adopts a more general point of view that includes quantities beyond the quantum geometric tensor. Chapter 4 is mostly based on Graf and Piéchon (2021b), but also goes beyond; in particular, it provides a more detailed introduction,

presents an improved method for constructing linear flat-band models, and offers several interesting perspectives including magnetic flat bands. Finally, Chapter 5 is essentially based on a recent preprint by Graf and Piéchon (2022), but again goes beyond in that it presents a more thorough discussion of multiband Hopf insulators and much more detailed perspectives.

To conclude the manuscript, a summary of the main results established in this thesis is given, along with an outlook regarding future perspectives. Finally, we note that two other scientific articles involving the author have appeared during the three years of preparing this thesis (Kozlovsky et al. 2020; Graf et al. 2020); they deal with topological insulator nanowires and are not relevant to the material presented here.

Chapter 1

Quantum geometry and topology in solid-state physics

This chapter first contains a brief summary of the standard band theory for non-interacting crystals, which forms the main framework for the entire thesis. This is followed by a detailed introduction to the notion of quantum geometry, which is fundamental to all further chapters. We then briefly introduce topological concepts in solid-state physics and their connection to quantum geometry. The chapter concludes with an extensive discussion of the influence of quantum geometry and topology on the physics of crystalline solids, illustrating the ubiquity of such effects.

1.1 | Basic band theory

Band theory describes a crystalline solid as a Fermi gas in the presence of a periodic electrostatic potential created by the lattice of atomic ions. The corresponding stationary Schrödinger equation (in an arbitrary representation) is given by

$$H|\Psi\rangle = \epsilon|\Psi\rangle, \quad (1.1)$$

where the Hamiltonian $H = \mathbf{p}^2/(2m) + V$ describes single-particle excitations and the lattice potential has the property $V(\mathbf{r} + \mathbf{R}_i) = V(\mathbf{r})$ for any Bravais vector \mathbf{R}_i . In other words, H commutes with the translation operator $\mathcal{T}_{\mathbf{R}_i}$. Assuming an (infinite) crystal with periodic boundary conditions, Bloch (1929) showed that the eigenfunctions of H can be written in the form

$$|\Psi_\alpha(\mathbf{k})\rangle = e^{i\mathbf{k}\cdot\mathbf{r}}|\psi_\alpha(\mathbf{k})\rangle, \quad (1.2)$$

where in coordinate representation the identity $\psi_{\alpha,\mathbf{k}}(\mathbf{r} + \mathbf{R}_i) = \psi_{\alpha,\mathbf{k}}(\mathbf{r})$ holds. In Bloch's theorem (1.2) two quantum numbers appear: α is a band index and \mathbf{k} is the crystal momentum lying in the first Brillouin zone. Inserting into Eq. (1.1), one can write the lattice Schrödinger equation as

$$H(\mathbf{k})|\psi_\alpha(\mathbf{k})\rangle = \epsilon_\alpha(\mathbf{k})|\psi_\alpha(\mathbf{k})\rangle, \quad (1.3)$$

where the Bloch Hamiltonian is defined as $H(\mathbf{k}) \equiv e^{-i\mathbf{k}\cdot\mathbf{r}} H e^{i\mathbf{k}\cdot\mathbf{r}}$.

Below, we will often adopt a tight-binding approximation and work in the Bloch basis, see Appendix I.A for a detailed recap on this. Then Eq. (1.3) simply becomes a linear algebra problem: $H(\mathbf{k})$ is an $N \times N$ Hermitian Bloch Hamiltonian matrix, whose size is determined by the number N of tight-binding orbitals $a = A, B, \dots$ per

unit cell. Its real eigenvalues $\epsilon_\alpha(\mathbf{k})$ (with $\alpha = 1, \dots, N$) form a band structure in the Brillouin zone, and its eigenstates

$$|\psi_\alpha(\mathbf{k})\rangle = (c_{\alpha,A}(\mathbf{k}), c_{\alpha,B}(\mathbf{k}), \dots)^T \quad (1.4)$$

are complex orthonormal vectors¹ in band space, $\langle \psi_\alpha(\mathbf{k}) | \psi_\beta(\mathbf{k}) \rangle = \delta_{\alpha\beta}$. Quite often, one is particularly interested in the continuum limit of Eq. (1.3) around some point \mathbf{k}_0 in the Brillouin zone, described by a corresponding local continuum Schrödinger equation

$$H(\mathbf{q}) |\psi_\alpha(\mathbf{q})\rangle = \epsilon_\alpha(\mathbf{q}) |\psi_\alpha(\mathbf{q})\rangle, \quad (1.5)$$

where $\mathbf{q} = \mathbf{k} - \mathbf{k}_0$. We will frequently use both the lattice (tight-binding) and continuum (low-energy) approach.

1.2 | Introduction to quantum geometry

In this section, we explain that quantum geometric effects are in general encountered for any parameter-dependent quantum system. Further, we introduce the main objects required to study quantum geometry in practice, in particular the quantum geometric tensor.

1.2.1 | General setup

Consider a generic parameter-dependent quantum system described by a Hamiltonian $H(\mathbf{x})$ and Schrödinger equation

$$H(\mathbf{x}) |\psi_\alpha(\mathbf{x})\rangle = \epsilon_\alpha(\mathbf{x}) |\psi_\alpha(\mathbf{x})\rangle, \quad (1.6)$$

with eigenvalues $\epsilon_\alpha(\mathbf{x})$ that form a band structure in parameter space, and corresponding eigenstates $|\psi_\alpha(\mathbf{x})\rangle$. While we usually have in mind the case of band theory considered above ($\mathbf{x} = \mathbf{k}$), it will prove convenient to keep \mathbf{x} general.

In many physical situations the parameters \mathbf{x} of the Hamiltonian are varied, $\mathbf{x} \rightarrow \mathbf{x} + \Delta\mathbf{x}$, for example when a crystal is subject to an external magnetic field, a bias voltage, a light pulse, an applied strain, and so on. Many features of the response of the system to such external perturbations can be rephrased in terms of information already encoded in the unperturbed Hamiltonian $H(\mathbf{x})$. An important part of such information is contained in the energy levels $\epsilon_\alpha(\mathbf{x})$ and band velocities $\mathbf{v}_\alpha(\mathbf{x}) = \nabla_{\mathbf{x}} \epsilon_\alpha(\mathbf{x})$. Another part, however, is encoded in the eigenstates $|\psi_\alpha(\mathbf{x})\rangle$ of the unperturbed system, and in particular their parametric derivatives $|\partial_j \psi_\alpha(\mathbf{x})\rangle$, where $\partial_j \equiv \partial/\partial x_j$. For example, physical quantities χ such as electrical conductivity tensors or magnetic susceptibilities of a crystal are in general functions $\chi = f(\epsilon_\alpha, \nabla \epsilon_\alpha, |\psi_\alpha\rangle, \nabla |\psi_\alpha\rangle)$ of all those four objects. While the role of the energy bands and band velocities in such quantities is for the most part well known, considerable attention has in recent decades shifted to the eigenstates $|\psi_\alpha(\mathbf{x})\rangle$. To put it

¹This is because of the normalization $\langle \Psi_\alpha(\mathbf{k}) | \Psi_\beta(\mathbf{k}) \rangle = \delta_{\alpha\beta}$. However, note that, since more generally $\langle \Psi_\alpha(\mathbf{k}) | \Psi_\beta(\mathbf{k}') \rangle = \delta_{\alpha\beta} \delta_{\mathbf{k}\mathbf{k}'}$, one has $\langle \psi_\alpha(\mathbf{k}) | \psi_\alpha(\mathbf{k}') \rangle \neq \delta_{\mathbf{k}\mathbf{k}'}$ according to Eq. (1.2), which is crucial for the existence of quantum geometry, as we will see in Eq. (1.15) below.

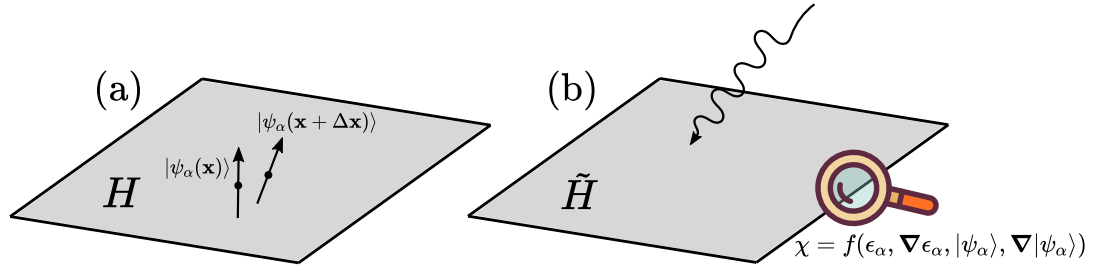


Fig. 1.1 – (a) The unperturbed system H has an intrinsic parameter dependence. (b) This dependence is unveiled or “explored” by the physical response of the system to a perturbation. The part of the physical response determined by the eigenstates and their parametric derivatives is the quantum geometric one.

simply, the subject of quantum geometry is to provide a quantitative theory of the information encoded in the geometry, that is, the \mathbf{x} -dependence, of the eigenstates, and to describe how this geometry is unveiled in the physical properties of the system of interest. A rough visual summary of these ideas is given in Fig. 1.1.

Historically, the first theories that contain quantum geometrical notions appeared in the work of experts on band theory in the 1940s-1970s. Such theories addressed interband effects in crystalline solids, and while the term “quantum geometry” was not used at the time, most aspects of quantum geometry were already known. An impressive summary of such approaches was given by Blount (1962b). In particular, he explicitly introduced the most fundamental quantum geometric quantities, now known as Berry connection and Berry curvature, 22 years before Berry’s seminal paper (Berry 1984). Nevertheless, Blount’s work did not receive a lot of attention, perhaps because it is rather formal and tailor-made for the specific language of band theory ($\mathbf{x} = \mathbf{k}$), instead of adopting a general point of view independent of the particular parameter space. Most importantly, at the time there was a lack of simple models to illustrate quantum geometric effects, and no link to topological concepts was established.

In contrast, the modern theory of quantum geometry, mainly established by Berry (1984), describes quantum geometry as a universal phenomenon applying to any parameter-dependent system $H(\mathbf{x})$, and provides direct links to topology. In particular, Berry’s theory was greatly popularized by the concurrent discovery of the quantum Hall effect (Klitzing et al. 1980). Indeed, there is a deep connection between the topological interpretation of the quantum Hall effect (Thouless et al. 1982) and Berry’s phase, as first pointed out by Simon (1983).

1.2.2 | Main objects of quantum geometry

Berry connection, curvature, and phase

The most important quantum geometric quantities known today are listed in the following. In accordance with the fundamental idea of quantum geometry formulated above, they are all computed from the eigenstates $|\psi_\alpha(\mathbf{x})\rangle$ and their parametric derivatives. The first quantity that should be mentioned is the *Berry connection* (Simon

1983; Berry 1984)

$$\mathcal{A}_{\alpha,j}(\mathbf{x}) \equiv -\text{Im} \langle \psi_{\alpha}(\mathbf{x}) | \partial_j \psi_{\alpha}(\mathbf{x}) \rangle = i \langle \psi_{\alpha}(\mathbf{x}) | \partial_j \psi_{\alpha}(\mathbf{x}) \rangle, \quad (1.7)$$

a gauge field that plays a role analogous to an electromagnetic vector potential. It can also conveniently be written in the vectorial form $\mathcal{A}_{\alpha} = (\mathcal{A}_{\alpha,1}, \mathcal{A}_{\alpha,2}, \dots)$. A second important object is the *Berry curvature*

$$\Omega_{\alpha,ij}(\mathbf{x}) = \partial_i \mathcal{A}_{\alpha,j}(\mathbf{x}) - \partial_j \mathcal{A}_{\alpha,i}(\mathbf{x}) = -2 \text{Im} \langle \partial_i \psi_{\alpha}(\mathbf{x}) | \partial_j \psi_{\alpha}(\mathbf{x}) \rangle, \quad (1.8)$$

which is the corresponding antisymmetric gauge-invariant tensor and plays a role analogous to a magnetic field. In a 3D parameter space, which will be the most important scenario during this thesis, it can be written in the form of a pseudovector as

$$\mathbf{\Omega}_{\alpha}(\mathbf{x}) = \nabla_{\mathbf{x}} \times \mathcal{A}_{\alpha}(\mathbf{x}) = (\Omega_{\alpha,23}(\mathbf{x}), \Omega_{\alpha,31}(\mathbf{x}), \Omega_{\alpha,12}(\mathbf{x})). \quad (1.9)$$

Finally, the *Berry phase*

$$\gamma_{\alpha} = \oint \mathcal{A}_{\alpha}(\mathbf{x}) \cdot d\mathbf{x} \quad (1.10)$$

is accumulated when the Hamiltonian traverses a closed loop in parameter space. While the Berry connection is gauge-dependent, the Berry phase of a closed loop is gauge-invariant (modulo 2π). It can be viewed as being analogous to a magnetic flux.

The importance of Berry connection, curvature and phase for contemporary quantum theory, and particularly for condensed matter physics, cannot be overstated. The perhaps most simple and pedagogical example illustrating their role is the Aharonov-Bohm effect, which can be viewed as a Berry phase effect (Berry 1984). Later in this chapter, we will mention in more detail some additional physical situations where the Berry quantities appear.

Quantum metric and quantum geometric tensor

Besides the Berry quantities, there are other important and closely related quantum geometric objects, most prominently the *quantum metric* (Provost and Vallee 1980)

$$g_{\alpha,ij}(\mathbf{x}) = \text{Re} \langle \partial_i \psi_{\alpha}(\mathbf{x}) | \partial_j \psi_{\alpha}(\mathbf{x}) \rangle - \mathcal{A}_{\alpha,i}(\mathbf{x}) \mathcal{A}_{\alpha,j}(\mathbf{x}). \quad (1.11)$$

It is a metric tensor of Riemannian kind, familiar from differential geometry and general relativity, and moreover it can be viewed as the symmetric counterpart of the Berry curvature. A convenient way to illustrate this consists in introducing the *quantum geometric tensor (QGT)* (Berry 1989; Resta 2011; Kolodrubetz et al. 2017):

$$T_{\alpha,ij}(\mathbf{x}) = \text{Re} T_{\alpha,ij}(\mathbf{x}) + i \text{Im} T_{\alpha,ij}(\mathbf{x}) = g_{\alpha,ij}(\mathbf{x}) - \frac{i}{2} \Omega_{\alpha,ij}(\mathbf{x}). \quad (1.12)$$

The QGT unifies quantum metric (real part) and Berry curvature (imaginary part) in a single complex gauge-invariant tensor field. An explicit expression for the QGT, summarizing Eqs. (1.8) and (1.11), is

$$T_{\alpha,ij}(\mathbf{x}) = \langle \partial_i \psi_{\alpha}(\mathbf{x}) | [1_N - P_{\alpha}(\mathbf{x})] | \partial_j \psi_{\alpha}(\mathbf{x}) \rangle, \quad (1.13)$$

where we have introduced the eigenprojector $P_\alpha(\mathbf{x}) = |\psi_\alpha(\mathbf{x})\rangle \langle \psi_\alpha(\mathbf{x})|$ for the band α . The influence of the quantum metric on physical effects is more subtle than that of Berry connection, curvature and phase, but it has started to attract growing attention in recent years, as we discuss in more detail later in this chapter.

1.2.3 | Origin of quantum geometry

Let us elucidate the origin of the main quantum geometric quantities listed above. Suppose again that we have a quantum system (1.6). Upon a variation of parameters, the Hamiltonian changes as

$$H(\mathbf{x} + \Delta\mathbf{x}) \approx H(\mathbf{x}) + \nabla_{\mathbf{x}}H \cdot \Delta\mathbf{x}. \quad (1.14)$$

It is now important to realize that the latter term is not diagonal in the eigenbasis of the unperturbed Hamiltonian, since in general $\langle \psi_\alpha | \nabla_{\mathbf{x}}H \cdot \Delta\mathbf{x} | \psi_\beta \rangle \neq 0$ for $\beta \neq \alpha$. In other words, when the parameters are varied, any state $|\psi_\alpha\rangle$ feels the presence of the other states $|\psi_\beta\rangle$ of the system via *interband coupling* mediated by the gradients of the Hamiltonian. Roughly speaking, this is how interband (geometric) effects come about when an external perturbation is applied to a crystal (compare also Fig. 1.1).

To make this idea more quantitative, it is instructive to study the evolution of a single eigenstate when the parameters are varied.² Namely, consider the overlap (Provost and Vallee 1980)

$$\langle \psi_\alpha(\mathbf{x}) | \psi_\alpha(\mathbf{x} + \Delta\mathbf{x}) \rangle = \mathcal{F}_\alpha e^{-i\Delta\varphi_\alpha}, \quad (1.15)$$

where $\mathcal{F}_\alpha = |\langle \psi_\alpha(\mathbf{x}) | \psi_\alpha(\mathbf{x} + \Delta\mathbf{x}) \rangle|$. Such an overlap is non-zero whenever the states do not form an orthonormal basis in \mathbf{x} -space, as is the case, for example, for the lattice-periodic part $|\psi_\alpha(\mathbf{k})\rangle$ of the Bloch states (1.2). Let us expand the overlap (1.15) in a Taylor series as

$$\begin{aligned} \langle \psi_\alpha(\mathbf{x}) | \psi_\alpha(\mathbf{x} + \Delta\mathbf{x}) \rangle &= 1 + \sum_i \langle \psi_\alpha(\mathbf{x}) | \partial_i \psi_\alpha(\mathbf{x}) \rangle \Delta x_i \\ &+ \frac{1}{2} \sum_{ij} \langle \psi_\alpha(\mathbf{x}) | \partial_{ij} \psi_\alpha(\mathbf{x}) \rangle \Delta x_i \Delta x_j + \mathcal{O}(|\Delta\mathbf{x}|^3). \end{aligned} \quad (1.16)$$

Separating into real and imaginary parts, one then has

$$\begin{aligned} \mathcal{F}_\alpha \cos \Delta\varphi_\alpha &= 1 - \frac{1}{2} \sum_{ij} \text{Re} \langle \partial_i \psi_\alpha(\mathbf{x}) | \partial_j \psi_\alpha(\mathbf{x}) \rangle \Delta x_i \Delta x_j, \\ \mathcal{F}_\alpha \sin \Delta\varphi_\alpha &= \sum_i \mathcal{A}_{\alpha,i}(\mathbf{x}) \Delta x_i - \frac{1}{2} \sum_{ij} \text{Im} \langle \psi_\alpha(\mathbf{x}) | \partial_{ij} \psi_\alpha(\mathbf{x}) \rangle \Delta x_i \Delta x_j \end{aligned} \quad (1.17)$$

²Such an ansatz assumes the eigenstates to be non-degenerate, and implicitly separates the intraband coupling $\langle \psi_\alpha(\mathbf{x}) | \psi_\alpha(\mathbf{x}') \rangle$ (slow dynamics) from the interband coupling $\langle \psi_\alpha(\mathbf{x}) | \psi_{\alpha'}(\mathbf{x}) \rangle$ (fast dynamics). More precisely, by projecting to a single eigenstate, one effectively integrates out the fast (interband) dynamics, but with a memory encoded in the quantum geometric structure (Berry 1989; Cayssol and Fuchs 2021). Accordingly, all quantum geometric quantities that we consider are associated to a single eigenstate labeled by α .

to quadratic order in $|\Delta\mathbf{x}|$, where we used $\text{Re}\langle\psi_\alpha|\partial_{ij}\psi_\alpha\rangle = -\text{Re}\langle\partial_i\psi_\alpha|\partial_j\psi_\alpha\rangle$, and where the Berry connection defined in Eq. (1.7) already pops up.

Consider now the limit of states infinitesimally close in parameter space, which will give rise to the Berry quantities and the quantum metric in a natural way. From Eq. (1.17) we can immediately write down the infinitesimal phase difference of the overlap as

$$d\varphi_\alpha = \sum_i \mathcal{A}_{\alpha,i}(\mathbf{x})dx_i + \mathcal{O}(|d\mathbf{x}|^2), \quad (1.18)$$

which is just the infinitesimal Berry phase according to Eq. (1.10). Moreover, the modulus \mathcal{F}_α allows to define the quantum metric via the relation (Provost and Vallee 1980; Berry 1989)

$$ds^2 = \sum_{ij} g_{\alpha,ij}(\mathbf{x})dx_idx_j \equiv 1 - |\langle\psi_\alpha(\mathbf{x})|\psi_\alpha(\mathbf{x} + d\mathbf{x})\rangle|^2. \quad (1.19)$$

This is known as the *Hilbert-Schmidt quantum distance*. Note that is reasonable that the line element ds^2 should vanish if the neighboring states $|\psi_\alpha(\mathbf{x})\rangle$ and $|\psi_\alpha(\mathbf{x} + d\mathbf{x})\rangle$ have an inner product of modulus one, while it should be maximal ($ds^2 = 1$) if the states are orthogonal. Computing \mathcal{F}_α^2 to second order in $|\Delta\mathbf{x}|$ from Eq. (1.17) and taking the continuum limit, one readily finds that the quantum metric defined by Eq. (1.19) takes the explicit form (1.11) in terms of eigenstates.

There is an alternative expression for the QGT, which explicitly emphasizes the interband nature of the phenomenon, and the fact that quantum geometry cannot exist in a single-band system. Namely, rewrite the QGT of Eq. (1.13) as $T_{\alpha,ij} = \sum_{\beta \neq \alpha} \langle\partial_i\psi_\alpha|P_\beta|\partial_j\psi_\alpha\rangle$ and use the identity

$$\langle\psi_\beta(\mathbf{x})|\partial_i H(\mathbf{x})|\psi_\alpha(\mathbf{x})\rangle = (\epsilon_\alpha(\mathbf{x}) - \epsilon_\beta(\mathbf{x}))\langle\psi_\beta(\mathbf{x})|\partial_i\psi_\alpha(\mathbf{x})\rangle, \quad (1.20)$$

which is valid for $\beta \neq \alpha$, as can be easily seen by differentiating the Schrödinger equation (1.6). Then one has

$$T_{\alpha,ij}(\mathbf{x}) = \sum_{\beta \neq \alpha} \frac{\langle\psi_\alpha(\mathbf{x})|\partial_i H(\mathbf{x})|\psi_\beta(\mathbf{x})\rangle \langle\psi_\beta(\mathbf{x})|\partial_j H(\mathbf{x})|\psi_\alpha(\mathbf{x})\rangle}{[\epsilon_\alpha(\mathbf{x}) - \epsilon_\beta(\mathbf{x})]^2}. \quad (1.21)$$

At a conceptual level, Eq. (1.21) clearly shows that the QGT of a given band α can be viewed as being due to virtual interband transitions between α and all other bands $\beta \neq \alpha$. At a practical level, it involves the parametric velocity operators $\partial_i H$ instead of derivatives of eigenstates, which is convenient for computation. Therefore, it is the most common formula used for computing the QGT.

Here we have presented the essence of quantum geometry from a modern and practical point of view. However, one should be aware that there is much early work that adopts somewhat different perspectives on quantum geometry. For example, as already mentioned, a very mature theory of interband effects was developed in the 1940s-1970s in the solid-state physics community. In Appendix I.B we present some key ideas of this theory, based on the review of Blount (1962b). A second perspective that we have mentioned views quantum geometry as arising from the variation of a given eigenstate in parameter space. A popular and rather visual way to formulate this consists in a parallel transport approach, see for example Berry (1989).

1.3 | Topology in band theory

Topology, as a branch of mathematics, historically arose from the classification of shapes of 3D objects such as spheres, tori, et cetera. Its general purpose is to describe properties of sets (topological spaces) that are unchanged when certain continuous deformations are applied. Topology crucially relies on *topological invariants*, that is, integer numbers that cannot change smoothly during any deformation, but only in jumps. The classic example is that of a donut and a coffee mug, which are topologically equivalent because they can be smoothly deformed into each other without changing the topological invariant $g = 1$ that counts the number of holes.

In condensed matter physics, topological notions are associated to the (electronic) ground state of the system. In particular, if one manages to create a ground state labeled by some topological invariant, one can expect it to be robust to certain local deformations, such as impurities and disorder, until, upon applying too strong a deformation or upon breaking an important symmetry, the topological invariant is changed abruptly. If observable properties of the system can be linked to the topological invariant, one can expect them to not change at all as long as the topological invariant remains unchanged. This kind of exceptional robustness afforded by topological protection cannot be reached by any other means, and one hopes to put it to use in future electronic devices, explaining the current burst of interest in topological matter.

The quantum Hall effect (Klitzing et al. 1980) constitutes a prime example for such physics, where the relevant topological number is the Thouless-Kohmoto-Nightingale-den Nijs invariant (Thouless et al. 1982; Avron et al. 1983), an example of a Chern number. The relevant observable linked to this number is the Hall conductivity. As a consequence of the topological protection, there is an extraordinary precision of the Hall conductivity quantization.

In the following, we first give a brief overview of the vast number of topological systems in condensed matter known today, and then provide a link to the main topic of interest in this thesis, namely quantum geometry. More details on physical consequences of topology will be given in Section 1.5 below.

1.3.1 | Zoo of topological matter

The quantum Hall effect is one of the earliest and most striking manifestations of topological quantum physics, but it requires rather extreme conditions, in particular a very strong external magnetic field. During the last two decades, however, it has become clear that topological effects in condensed matter are actually rather ubiquitous and do not necessarily require extreme conditions. A vast amount of topological phases has been identified.

First, and foremost, insulating phases. This class includes quantum Hall systems and their cousins, most notably 2D quantum spin Hall insulators (Maciejko et al. 2011) and quantum anomalous Hall insulators (Weng et al. 2015), as well as spin-orbit induced 3D topological insulators (Hasan and Moore 2011). All these systems are characterized by a *stable* topology and classified by the tenfold way scheme (Ryu et al. 2010). The tenfold way symmetry class they belong to predicts what perturbations

the topological phases are robust to. For example, the quantum Hall state belongs to symmetry class A, where all relevant symmetries (time-reversal, particle-hole and chiral symmetries) are broken, such that it is robust to both magnetic and non-magnetic disorder. In contrast, the quantum spin Hall and 3D topological insulators belong to symmetry class AII, which requires time-reversal symmetry, thus they are not robust to magnetic disorder. Indeed, the observed conductance plateaus in the quantum spin Hall effect (König et al. 2007) are less perfect than those of the quantum Hall effect.

Since the tenfold way classification is based only on non-spatial symmetries, it is not sufficient to describe all topological phases that are possible in crystalline insulators. In particular, the tenfold way can be extended to include spatial symmetries (Shiozaki and Sato 2014; Ando and Fu 2015), such as reflections, rotations and translations. Moreover, recently, subtle types of topology were found, which evade the tenfold way and its extensions altogether. Those include *fragile* topological (Po et al. 2018) and *delicate* topological (Nelson et al. 2021) insulators. Delicate topological insulators are of relevance to Chapter 5.

A second main class of topological phases consists of semimetals, most notably the widely studied Dirac and Weyl semimetals (Armitage et al. 2018) as well as unconventional multifold semimetals (Lv et al. 2021). The latter will play an important role in Chapter 5. For semimetals, the topological classification applies to the Fermi surface instead of the ground state. The classification can again be carried out considering only non-spatial symmetries (Matsuura et al. 2013), and can be enriched by adding spatial symmetries (Chiu et al. 2016).

While the topologically non-trivial insulators and semimetals mentioned above arise from single-particle physics, topological phases can also exist in the presence of interactions. The simplest case, namely topological superconductors treated at the mean-field level (Sato and Ando 2017), can be viewed as an effective single-particle problem and thus fits into the framework of the standard tenfold way. However genuinely interacting phases do not. For example, interactions may alter the symmetry classification or induce completely new topological phases, but this is a wide field in itself (Rachel 2018), which we will not delve into any further. Finally, beyond electronic systems, the same ideas can be applied to cold atoms (Cooper et al. 2019), light (Ozawa et al. 2019), metamaterials (Xin et al. 2020), and so on.

1.3.2 | Topology versus quantum geometry

While at first glance only concerned with global properties of a system, topology is actually closely linked to geometry. For example, the Euler characteristic $\mathcal{N}_{\text{Euler}}$ classifying the shape of a Riemannian manifold M can be linked to the Gaussian curvature of M and the geodesic curvature of its boundary ∂M through the theorem of Gauss-Bonnet (Carmo 2016). For a two-sphere \mathbb{S}^2 of radius R , it follows

$$\mathcal{N}_{\text{Euler}} = \frac{1}{2\pi} \int_{\mathbb{S}^2} dA \frac{1}{R^2} = 2, \quad (1.22)$$

and the same Euler characteristic is associated to any surface homeomorphic to a sphere.

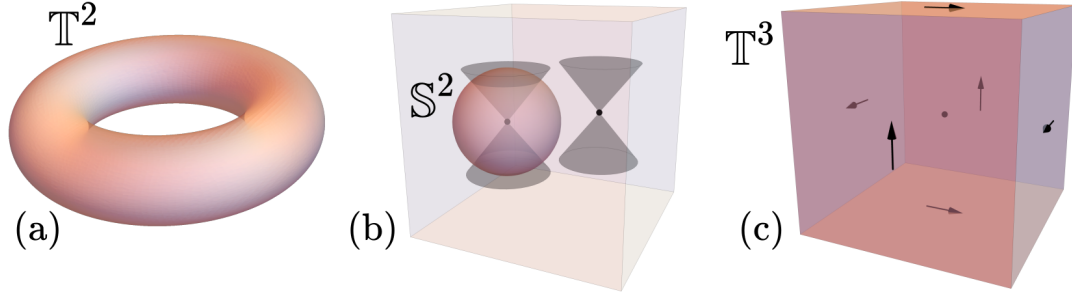


Fig. 1.2 – (a) Toroidal Brillouin zone for a 2D crystal. (b) In a topological semimetal (in particular a Weyl semimetal), the integration domain for the local Chern number is a 2D surface enclosing a given energy crossing point. (c) The Brillouin zone for a 3D crystal is a three-torus, which can be formed from a cube by connecting the faces that have matching arrows.

In a similar way, the topology of a quantum system is intricately linked to quantum geometry. Roughly speaking, while quantum geometry concerns local (\mathbf{x} -dependent) properties, recall the discussion of Section 1.2, topology describes global features of the parameter-dependent Hamiltonian $H(\mathbf{x})$. This link explicitly appears when computing topological invariants for most of the systems belonging to the zoo of topological phases outlined above. More precisely, while there is a huge number of different topological invariants specifying those phases, and while the precise way how to compute those invariants depends on the dimension and symmetries of the phase of interest, they are typically obtained by integrating \mathbf{k} -dependent quantum geometric densities over the Brillouin zone. Mathematically speaking, this is because the invariants classify the topological properties of the Bloch fiber bundle: the base space of this fiber bundle is the Brillouin zone (a torus \mathbb{T}^D for spatial dimension D) containing \mathbf{k} , and the fibers are complex vector spaces containing the eigenstates $|\psi_\alpha(\mathbf{k})\rangle$.

Out of the zoo of known topological numbers, we here present only a selection of three examples that will be of relevance later on (mostly in Chapter 5), namely the Chern number of a 2D insulator and of a 3D semimetal (a stable topological invariant), and the Hopf number of a 3D insulator (a delicate topological invariant).

The Chern number is the most famous topological number in solid-state physics, since it is the relevant invariant for the quantum Hall effect (Thouless et al. 1982; Avron et al. 1983). For a non-degenerate band α of an infinite 2D crystal, the corresponding Chern number is just the integral of the Berry curvature over the Brillouin zone [cf. Fig. 1.2(a)]:

$$\mathcal{N}_\alpha^{\text{Chern}} = \frac{1}{2\pi} \int_{\text{BZ}} d^2k \Omega_{\alpha,xy}(\mathbf{k}). \quad (1.23)$$

The total Chern number of the ground state is then obtained by summing over all occupied bands: $\mathcal{N}_{\text{Chern}} = \sum_{\alpha \in \text{occ}} \mathcal{N}_\alpha^{\text{Chern}}$. If this integer is non-zero, it implies that the Chern class of the corresponding Bloch bundle is non-trivial, meaning that the Bloch bundle is topologically inequivalent (“twisted”) to a trivial (“untwisted”) Bloch bundle.

To characterize 3D topological semimetals (Lv et al. 2021), one also frequently employs the concept of a Chern number. In accordance with the above discussion,

the topology of interest is not that of the ground state, but that of the Fermi surface. In such semimetals, there are usually several Fermi surface pockets such that the topology can be defined only locally for each pocket. In particular, in the standard case of a conical band crossing, see Fig. 1.2(b), and for a Fermi level close to the crossing, the Fermi surface is a sphere, and the Chern number measures the flux of Berry curvature (1.9) through that sphere:

$$C_\alpha = \frac{1}{2\pi} \int_{\mathbb{S}^2} d\mathbf{S}_\mathbf{q} \cdot \boldsymbol{\Omega}_\alpha(\mathbf{q}). \quad (1.24)$$

Here the momentum $\mathbf{q} = (q_x, q_y, q_z)$ is measured from the crossing point, around which a low-energy theory (1.5) can be constructed.

Finally, let us mention the Hopf number. As we will describe in more detail in Chapter 5, it was originally only defined for 3D two-band insulators (Moore et al. 2008), but was very recently generalized to 3D multiband systems (Lapierre et al. 2021). Being based on a multigap topological classification, the Hopf number cannot be associated to an individual band or an occupied subspace. In contrast, it is associated to the whole band structure. Nevertheless, the general expression can again be written as an integral of a geometric \mathbf{k} -space density over the Brillouin zone [cf. Fig. 1.2(c)],

$$\mathcal{N}_{\text{Hopf}} = \frac{1}{24\pi^2} \int_{\text{BZ}} d^3k \chi(\mathbf{k}), \quad \chi(\mathbf{k}) \equiv \epsilon_{ijk} \text{Tr}[u_i(\mathbf{k})u_j(\mathbf{k})u_k(\mathbf{k})]. \quad (1.25)$$

Here we have introduced the *Hopf density* $\chi(\mathbf{k})$, with $u_i(\mathbf{k}) \equiv U^\dagger(\mathbf{k})\partial_i U(\mathbf{k})$, and where $U(\mathbf{k})$ is an $N \times N$ unitary matrix diagonalizing the N -band Bloch Hamiltonian $H(\mathbf{k})$. Repeated lower indices imply summation (Einstein convention) and ϵ_{ijk} is the Levi-Civita antisymmetric tensor.

1.4 | Example: From graphene to Chern insulators

An instructive way to illustrate quantum geometry, topology, and their interplay in a bit more detail consists in studying simple toy models. In particular, here we will discuss a minimal tight-binding model for graphene first introduced by Wallace (1947), as well as some extensions of it: Semenoff's model for graphene with a sublattice imbalance (Semenoff 1984), and Haldane's model for a Chern (or quantum anomalous Hall) insulator (Haldane 1988). Note that these models are not only instructive but also experimentally realized: Semenoff insulators can describe hexagonal boron nitride (hBN) monolayers or lattice-matched graphene/hBN heterostructures (Giovannetti et al. 2007; Xiao et al. 2007), and quantum anomalous Hall insulators can be observed in magnetic topological insulators or optical lattices (Chang et al. 2013; Jotzu et al. 2014).

The Wallace, Semenoff and Haldane models are ideal to address basic notions of topological band theory in order of increasing complexity: a 2D Dirac semimetal like graphene has a non-zero quantum metric but the Berry curvature vanishes (except

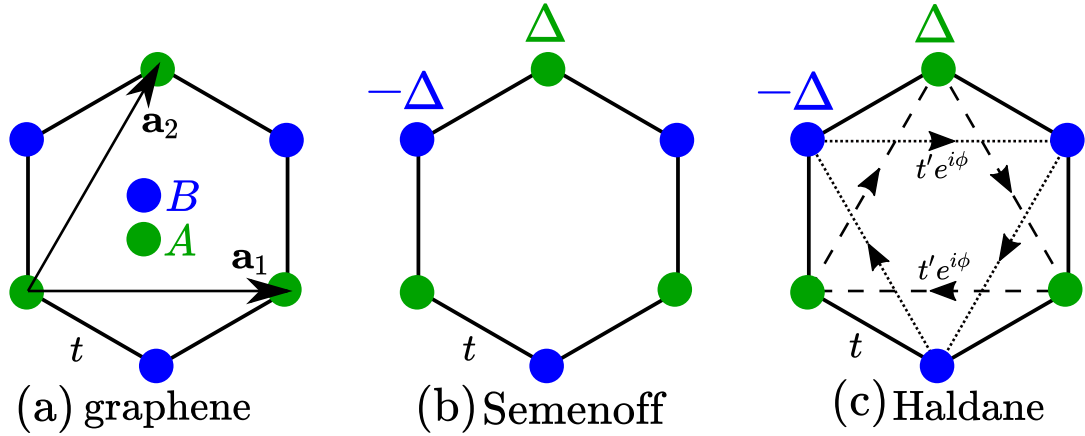


Fig. 1.3 – Sketch of the tight-binding models for (a) graphene. (b) Semenoff’s trivial insulator. (c) Haldane’s Chern insulator.

at singular points), and moreover there is no topology;³ a Semenoff insulator has a quantum metric and a finite Berry curvature, but no topology; finally, Haldane’s model has both non-vanishing quantum metric and Berry curvature, and moreover it is topologically non-trivial, as measured by the Chern invariant (1.23).

A further reason why we consider these 2D two-band models is that, in Chapter 5, we will introduce a class of 3D multiband systems (Hopf semimetals and insulators) that are quite analogous in a sense to be made more precise.

1.4.1 | Dirac semimetal: Graphene

Graphene is a monolayer of carbon atoms arrayed in a 2D honeycomb structure, characterized by a triangular Bravais lattice with two atoms A and B per unit cell, and with Bravais vectors $\mathbf{a}_1 = \sqrt{3}\hat{x}$ and $\mathbf{a}_2 = \frac{1}{2}(\sqrt{3}\hat{x} + 3\hat{y})$ in units of the carbon-carbon bond length $a_0 = 1$, cf. Fig. 1.3(a). The carbon atoms form covalent sp^2 bonds in the plane, leaving one valence electron per atom in a p_z orbital. The two energy bands formed from those orbitals are described within a tight-binding approach by the Bloch Hamiltonian (Cayssol and Fuchs 2021)

$$\begin{aligned} H(\mathbf{k}) &= h_1(\mathbf{k})\sigma_1 + h_2(\mathbf{k})\sigma_2, \\ h_1(\mathbf{k}) &= t[\cos(\mathbf{k} \cdot \boldsymbol{\delta}_1) + \cos(\mathbf{k} \cdot \boldsymbol{\delta}_2) + \cos(\mathbf{k} \cdot \boldsymbol{\delta}_3)], \\ h_2(\mathbf{k}) &= t[\sin(\mathbf{k} \cdot \boldsymbol{\delta}_1) + \sin(\mathbf{k} \cdot \boldsymbol{\delta}_2) + \sin(\mathbf{k} \cdot \boldsymbol{\delta}_3)]. \end{aligned} \quad (1.26)$$

Here, σ_i are Pauli matrices, t is the hopping amplitude between two adjacent carbon atoms (in the following $t = 1$) and the vectors $\boldsymbol{\delta}_{1,2} = \frac{1}{2}(\pm\sqrt{3}, 1)$, $\boldsymbol{\delta}_3 = (0, -1)$ connect a given B site to its three neighbors. The famous band structure associated to this Bloch Hamiltonian reads

$$\epsilon_\alpha(\mathbf{k}) = \alpha \sqrt{3 + 2 \cos(\sqrt{3}k_x) + 4 \cos(\sqrt{3}k_x/2) \cos(3k_y/2)}, \quad (1.27)$$

³By the absence of topology we mean the absence of a tenfold way bulk invariant. However, there are certain topological numbers that can be defined in graphene, for example to predict termination-dependent edge states of graphene ribbons (Delplace et al. 2011).

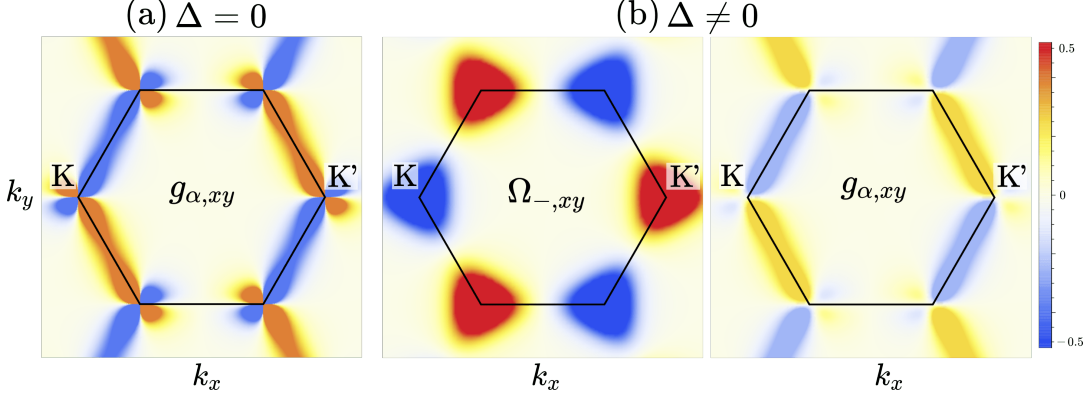


Fig. 1.4 – (a) Off-diagonal element of the quantum metric for graphene. It is the same for both bands. (b) Berry curvature for the valence band of the Semenoff insulator, and corresponding off-diagonal quantum metric. In the plot $\Delta = 1/2$.

where $\alpha = \pm 1$. Near the K ($\xi = +$) and K' ($\xi = -$) valleys of the Brillouin zone, located at

$$\mathbf{K}_\xi = -\xi \frac{4\pi}{3\sqrt{3}}(1, 0), \quad (1.28)$$

the low-energy expansion of $H(\mathbf{k})$ is given by

$$H^\xi(\mathbf{q}) = \xi q_x \sigma_1 + q_y \sigma_2, \quad (1.29)$$

with a low-energy dispersion $\epsilon_\alpha(\mathbf{q}) = \alpha|\mathbf{q}|$ that is dubbed “Dirac cone”. This name stems from the fact that the 4×4 matrix $H_D(\mathbf{q}) = \text{antidiag}(H^+(\mathbf{q}), H^-(\mathbf{q}))$ capturing both valleys is nothing else than a massless Dirac Hamiltonian. Hence, graphene is called a 2D Dirac semimetal.

Due to the presence of the Dirac cones, indicating strong coupling between the two bands, one expects interesting quantum geometric properties. While the Berry curvature vanishes everywhere in the Brillouin zone (except at the band crossing points where it is ill-defined) due to the simultaneous presence of time-reversal and inversion symmetry, the quantum metric is non-zero and strongly enhanced in the vicinity of the crossing points. For example, the off-diagonal element reads⁴

$$g_{\alpha,xy}(\mathbf{k}) = \frac{\sqrt{3}}{4\epsilon_\alpha^4(\mathbf{k})} \sin\left(\frac{\sqrt{3}k_x}{2}\right) \sin\left(\frac{3k_y}{2}\right) \times \left[\cos(\sqrt{3}k_x) - \cos\left(\frac{\sqrt{3}k_x}{2}\right) \cos\left(\frac{3k_y}{2}\right) \right], \quad (1.30)$$

which is plotted in Fig. 1.4(a). This quantum geometry hidden in the crossing points remains however rather obscure in the semimetallic case. It emerges more clearly upon gapping out the system, and indeed graphene can be viewed as a precursor for non-trivial insulators, as discussed in the following.

⁴The explicit expressions for quantum metric and Berry curvature presented in this section can in principle be obtained from Eqs. (1.13) or (1.21), but it is much more practical to use Eq. (2.41) introduced below.

1.4.2 | Semenoff insulator

Suppose the carbon atom on one of the graphene sublattices is exchanged by some other kind of atom. More generally, suppose a 2D hexagonal layer with two different kinds of atoms, for example boron nitride. A minimal model to describe such a layer consists in adding a staggered onsite potential to the Hamiltonian (1.26), such that

$$H(\mathbf{k}) = h_1(\mathbf{k})\sigma_1 + h_2(\mathbf{k})\sigma_2 + \Delta\sigma_3, \quad (1.31)$$

see Fig. 1.3(b). Again we focus on the quantum geometry. Since inversion symmetry is broken, the Berry curvature of the two bands is now allowed to be non-zero, and given by

$$\Omega_{\alpha,xy}(\mathbf{k}) = -\frac{\sqrt{3}\Delta}{\epsilon_\alpha^3(\mathbf{k})}w_\Delta(\mathbf{k}), \quad w_\Delta(\mathbf{k}) \equiv \sin(k_{12}/2)\sin(k_{23}/2)\sin(k_{31}/2), \quad (1.32)$$

where $\epsilon_\alpha(\mathbf{k})$ are the eigenvalues of the Hamiltonian (1.31) and $k_{ij} = \mathbf{k} \cdot \boldsymbol{\delta}_{ij}$ with $\boldsymbol{\delta}_{ij} \equiv (\boldsymbol{\delta}_i - \boldsymbol{\delta}_j)$. This Berry curvature field is plotted in Fig. 1.4(b). Clearly, it is peaked at the K and K' points and becomes singular in the limit $\Delta \rightarrow 0$. From Fig. 1.4(b), it can also be seen that the quantum metric is weakened as compared to the semimetallic case, as expected: In the limit $\Delta \rightarrow \infty$ the bands are decoupled and no interband effects can exist. Note further that while the Berry curvature map has the threefold rotation symmetry of the staggered graphene lattice, each component of the quantum metric does not.

Although the Berry curvature is non-zero and quite interesting, the Chern number (1.23) vanishes for the Semenoff insulator. This is because the time-reversal symmetry of the system imposes that the Berry curvature must be odd in \mathbf{k} . Hence, the Semenoff model describes an insulator that is topologically trivial.

1.4.3 | Chern insulator: Haldane's model

The tight-binding model presented in the following was not directly motivated by an experimentally accessible system. It was devised by Haldane (1988) as a proof of principle, demonstrating that the existence of conductance plateaus of the kind encountered in the quantum Hall effect does not necessarily require the presence of an external magnetic field; instead, the general condition is to obtain a non-zero Chern number by breaking time-reversal symmetry. In Haldane's model, this is achieved by adding certain complex second-neighbor hoppings $t'e^{i\phi}$ to the Semenoff insulator, see Fig. 1.3(c). They are designed such that a pattern of local magnetic fluxes of opposite signs emerges, which breaks time-reversal symmetry but corresponds to a vanishing net magnetic field. Accordingly, the quantum states giving rise to the Chern number (1.23) are simply standard Bloch states, unlike in the treatment of the quantum Hall effect where they are magnetic Bloch states (Thouless et al. 1982). For this reason, Haldane's model can be viewed as reproducing quantum Hall physics in a strongly simplified setup, and also as the first example of an intrinsic topological band insulator.

The Bloch Hamiltonian of Haldane's model is given by

$$H(\mathbf{k}) = h_0(\mathbf{k})1_2 + h_1(\mathbf{k})\sigma_1 + h_2(\mathbf{k})\sigma_2 + h_3(\mathbf{k})\sigma_3, \quad (1.33)$$

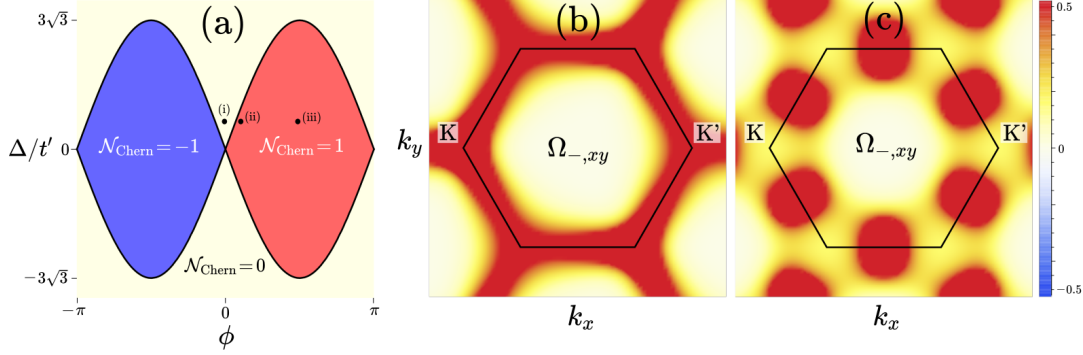


Fig. 1.5 – (a) Topological phase diagram for Haldane’s model. The Berry curvature for the valence band at point (i), $\phi = 0$, is essentially as in Fig. 1.4(b). At point (ii), $\phi = \pi/10$, it takes the form shown in panel (b), and at point (iii), $\phi = \pi/2$, it takes the form shown in (c). In both plots $t' = \Delta = 1/2$.

where $h_{1,2}(\mathbf{k})$ are the same as before, and additionally

$$\begin{aligned} h_0(\mathbf{k}) &= 2t' \cos \phi (\cos k_{12} + \cos k_{23} + \cos k_{31}), \\ h_3(\mathbf{k}) &= \Delta - 2t' \sin \phi (\sin k_{12} + \sin k_{23} + \sin k_{31}). \end{aligned} \quad (1.34)$$

The important term here is $h_3(\mathbf{k})$, which breaks inversion symmetry if $\Delta \neq 0$ and time-reversal symmetry if $t' \neq 0$, $\sin \phi \neq 0$. The Berry curvature reads

$$\begin{aligned} \Omega_{\alpha,xy}(\mathbf{k}) &= -\frac{\sqrt{3}}{\epsilon_{\alpha}^3(\mathbf{k})} [\Delta w_{\Delta}(\mathbf{k}) - t' \sin \phi w_{\phi}(\mathbf{k})], \\ w_{\phi}(\mathbf{k}) &= \cos k_{12} + \cos k_{23} + \cos k_{31} \\ &\quad - \frac{1}{2} (3 + \cos^2 k_{12} + \cos^2 k_{23} + \cos^2 k_{31}), \end{aligned} \quad (1.35)$$

where $\epsilon_{\alpha}(\mathbf{k})$ are the eigenvalues of the Hamiltonian (1.33). The first term is essentially the same as for the Semenoff insulator, while the second term, which is even in \mathbf{k} , is a signature of broken time-reversal symmetry. Computing the Chern number (1.23), one obtains a phase diagram as shown in Fig. 1.5(a). The system is an insulator for all parameter values except if $\Delta = \pm 3\sqrt{3}t' \sin \phi$. This critical line separates topologically trivial from non-trivial regions. The non-trivial regions have a Berry curvature distribution in the Brillouin zone that does not integrate to zero, see Fig. 1.5(b) and (c).

1.5 | Influence of geometry and topology on physics

Having outlined the basic aspects of quantum geometry and topology, we now want to illustrate that both play a crucial role for physical observables. Roughly speaking, one can say that (i) quantum geometric effects are much more ubiquitous than topological ones, but that (ii) topological effects are more striking. The former statement (i) is explained by the fact that quantum geometric densities are often non-trivial even if the associated topological number vanishes (as for the Semenoff insulator).

As a consequence, quantum geometric (interband) contributions to observables are ubiquitous even in the absence of topology. The latter statement (ii) is quite obvious from the fact that non-trivial topological numbers are intrinsically associated to quantization of some physical phenomenon, and thus to very clear experimental signatures (as for the quantum Hall effect). In contrast, non-topological quantum geometric contributions compete with conventional (single-band) contributions, and are not necessarily sizeable or easily distinguishable.

We start by discussing the edge states of topological systems and some of their physical consequences. We then shift attention to systems that are in general topologically trivial but still exhibit important physical signatures caused by quantum geometric effects. As examples we choose the orbital magnetism of crystals, the superfluid weight of superconductors, and magnetotransport (as described by semi-classical Boltzmann theory). We hope to convey how ubiquitous quantum geometric effects are, motivating the in-depth study of quantum geometry conducted later in this thesis.

1.5.1 | Topological edge states

In general, one considers the most relevant signature of a topologically non-trivial solid to be the existence of edge states. The particularity of such edge states consists in the topological protection, the details of which are determined by the symmetry class, recall the discussion in Section 1.3.1.

Topological edge states in insulators

The standard argument for the existence of topological edge states in band insulators⁵ is the following. By the rules of the tenfold way classification, any two insulating bulk Hamiltonians H and H' are topologically equivalent if there exists a continuous path $H(\lambda) = \lambda H + (1 - \lambda)H'$ connecting them such that the band gap (at the Fermi level) stays open and the same relevant symmetries are present for any λ . This equivalence is expressed in the existence of a topological number that is independent of λ . Conversely, if we start out with two bulk Hamiltonians H and H' with *different* topological numbers and interpolate between them, then the band gap necessarily has to close at some critical value $\lambda = \lambda_0$. For example, in agreement with this fact, the Haldane model (1.33) is a semimetal along the transition line in Fig. 1.5(a), as discussed in more detail by Thonhauser and Vanderbilt (2006).

Now, if we imagine a finite sample of a topological insulator embedded in a trivial insulator (say surrounded by the ambient atmosphere or vacuum), the real-space coordinate perpendicular to the edge/surface plays a role similar to λ , and the critical region where the topological character of the system changes is just the edge of the sample. Hence one expects the gap to close there, forming a (semi)metallic edge state.

⁵We here only address the well-established case of stable topological insulators. For very recent work on the bulk-boundary correspondence of fragile topological insulators, see Hwang et al. (2019) and Song et al. (2020). Similarly, for the bulk-boundary correspondence of delicate topological insulators, see the work of Alexandradinata et al. (2021), Lapierre et al. (2021), as well as Nelson et al. (2022).

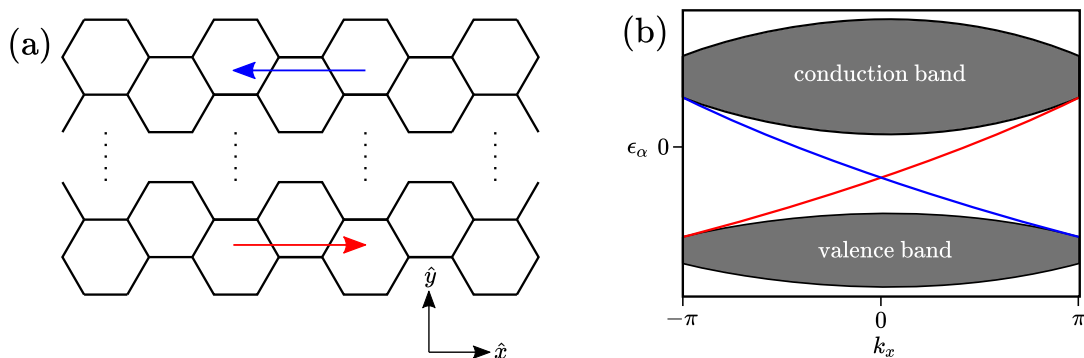


Fig. 1.6 – (a) Ribbon of a Haldane model in the $\mathcal{N}_{\text{Chern}} = 1$ phase, with zigzag edges. Colored arrows indicate propagation of the topological edge states. (b) Sketch of the corresponding energy spectrum, with helical topological in-gap modes. Such a spectrum can be easily obtained numerically, see Hao et al. (2008) for details.

This simple and general argument is known as *bulk-boundary correspondence*. However, while it tells us that something should happen at the edges of topological insulators, it does not immediately tell us any details about the number and properties of the boundary states. Therefore, the determination of the precise nature of the bulk-boundary correspondence has mostly been done in a case-by-case way, for example for quantum Hall insulators (Rammal et al. 1983; Niu and Thouless 1987; Hatsugai 1997), topological superconductors (Ryu and Hatsugai 2002), Chern insulators (Hao et al. 2008), quantum spin Hall insulators (Zhou et al. 2008), and 3D topological insulators (Isaev et al. 2011). Indeed, it is difficult to formulate a universal and precise bulk-boundary correspondence that works for any dimension and symmetries, but some efforts towards more universal definitions exist (Mong and Shivamoggi 2011; Essin and Gurarie 2011; Rhim et al. 2018).

As a concrete example, let us consider the consequences of the bulk-boundary correspondence for a Haldane insulator. Suppose we take a ribbon of the Haldane model which is infinite in the \hat{x} -direction, but finite in the \hat{y} -direction and terminated by an armchair edge, see Fig. 1.6(a). If the parameters are chosen such that the bulk Haldane model is in the $\mathcal{N}_{\text{Chern}} = 1$ phase, one can view the situation as a junction between a Chern insulator and a trivial insulator, such that the difference in the Chern number across the interface is $\Delta\mathcal{N}_{\text{Chern}} = 1$ ($\Delta\mathcal{N}_{\text{Chern}} = -1$) for the lower (upper) interface. One can show that this number is equal to the difference $n_{\text{R}} - n_{\text{L}}$ in the number of right- and left-moving topological edge states (Kane 2013). Indeed, this is confirmed by a numerical calculation of the ribbon energy spectrum (Hao et al. 2008), which exhibits one right-mover (left-mover) localized at the lower (upper) edge within the bulk gap, see Fig. 1.6(b).

Topological edge states in semimetals

In semimetals, one also encounters a close link between topological invariants and the presence of edge state (Matsuura et al. 2013). Here we content ourselves with giving an example that will be important to Chapter 5, namely 3D Weyl semimetals (Armitage et al. 2018). They exhibit pairs of band crossing points near the Fermi

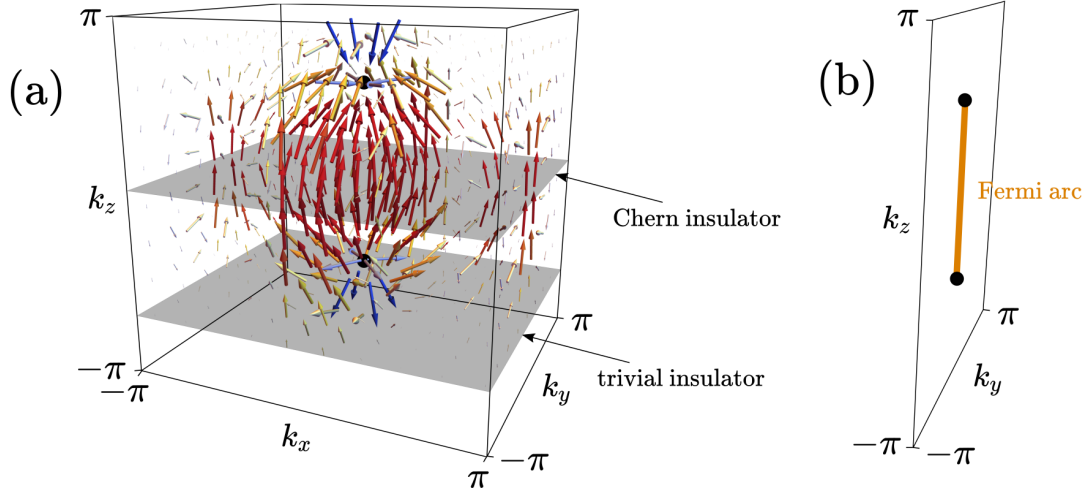


Fig. 1.7 – (a) A pair of Weyl points acts as a monopole/anti-monopole pair of Berry curvature. Parameters are taken as $t_i = 1$, $m = 2$ and $k_0 = \pi/2$. (b) Topological Fermi arc states connecting the Weyl node projection appear in the surface Brillouin zone.

level, where the low-energy theory for each crossing point can be written as

$$H_W^\gamma(\mathbf{q}) = \gamma \mathbf{q} \cdot \boldsymbol{\sigma} = \gamma(q_x \sigma_1 + q_y \sigma_2 + q_z \sigma_3), \quad (1.36)$$

which is known as a Weyl Hamiltonian (Weyl 1929) of chirality $\gamma = \pm$. The energy dispersion is conical [cf. Fig. 1.2(b)], dubbed “Weyl cone”, and the crossing points act as monopole sources or sinks of Berry curvature (Berry 1984; Berry 1985; Volovik 1987; Fang et al. 2003). Indeed, the Berry curvature pseudovector (1.9) around each crossing, computed in the parameter space $\mathbf{x} = \mathbf{q}$, is given by

$$\boldsymbol{\Omega}_\alpha(\mathbf{q}) = C_\alpha \frac{\mathbf{q}}{2|\mathbf{q}|^3}, \quad (1.37)$$

where $\alpha = \pm$ and where $C_\alpha = -\gamma\alpha$ is a Chern number in the sense of Eq. (1.24). To explain the occurrence of topological edge states, let us consider the simplest possible model⁶ of a Weyl semimetal, introduced by Yang et al. (2011), which breaks time-reversal symmetry and features a single pair of Weyl nodes at $\mathbf{k}_0 = \pm(0, 0, k_0)$, where $k_0 > 0$. The model is given by

$$\begin{aligned} H(\mathbf{k}) &= h_1(\mathbf{k})\sigma_1 + h_2(\mathbf{k})\sigma_2 + h_3(\mathbf{k})\sigma_3, \\ h_1(\mathbf{k}) &= [m(2 - \cos k_x - \cos k_y) - 2t_z(\cos k_z + \cos k_0)], \\ h_2(\mathbf{k}) &= 2t_x \sin k_x, \\ h_3(\mathbf{k}) &= 2t_y \sin k_y. \end{aligned} \quad (1.38)$$

The Berry curvature pseudovector field $\boldsymbol{\Omega}_+(\mathbf{k})$ of the conduction band is plotted in Fig. 1.7(a). Clearly, the lower Weyl point acts as a source, while the upper Weyl point acts as a sink of Berry curvature flux.

⁶It is not possible to have a single unpaired Weyl point, which can be viewed as a manifestation of a theorem by Nielsen and Ninomiya (1981).

Therefore, for any fixed $k_z = \Delta$ such that $|\Delta| < k_0$, the effective 2D Hamiltonian $H(k_x, k_y, \Delta)$ is a Chern insulator, while it is a trivial insulator if $k_0 < |\Delta| \leq \pi$. This is easily confirmed by computing the Chern number (1.23) of the model (1.38) for some arbitrary values of k_0 , t_i and m . For example, taking the parameters used for the plot in Fig. 1.7(a), we have $\mathcal{N}_\alpha^{\text{Chern}} = \alpha$, and thus the occupied subspace has $|\mathcal{N}_{\text{Chern}}| = 1$ whenever $|\Delta| < k_0$ and the Fermi level is not too far away from half filling. Recall now from Fig. 1.6 that, for a given Fermi level in the gap of a finite Chern insulator with $|\mathcal{N}_{\text{Chern}}| = 1$, there is a single edge state which corresponds to a point in the 1D surface Brillouin zone. Thus, for a finite sample of a Weyl semimetal, any surface that is not perpendicular to the direction connecting the Weyl points will exhibit topological surface states which form a 1D line connecting the projection of the Weyl points into the 2D surface Brillouin zone, cf. Fig. 1.7(b). These states are known as *Fermi arcs*, see Armitage et al. (2018) for more details.

1.5.2 | Physical consequences of topological edge states

One evident method to probe topological edge states consists in direct observation, for example using angle-resolved photoemission spectroscopy (Xia et al. 2009). However, here we want to focus on the perhaps most useful type of probe, namely electronic transport. It reveals striking signatures of the protected edge states. We restrict our attention to the (anomalous) Hall conductivity, which we will come back to later in this thesis.

Thouless et al. (1982) were the first to draw attention to the topological character of the quantum Hall phase, by computing the Hall conductivity of an infinite 2D electron gas subject to a magnetic field and a periodic potential from linear response theory. They found that the Hall conductivity at zero temperature can be written as (Kohmoto 1985)

$$\sigma_{xy}^{\text{H}} = -e^2 \sum_{\alpha \in \text{occ.}} \int_{\text{MBZ}} \frac{d^2 \tilde{\mathbf{k}}}{(2\pi)^2} \Omega_{\alpha, xy}(\tilde{\mathbf{k}}), \quad (1.39)$$

where the Fermi level is assumed to lie within a gap and the sum runs over occupied bands. The quantum numbers $\tilde{\mathbf{k}}$ live in an effective Brillouin zone determined by the number of magnetic flux quanta per unit cell, and integration is over this magnetic Brillouin zone. Accordingly, the Berry curvature is defined from magnetic Bloch states. One easily recognizes the formal agreement with the Chern number (1.23), such that the Hall conductivity is expected to be quantized in units⁷ of $e^2/(2\pi)$, and this is indeed observed experimentally (Klitzing et al. 1980).

At first glance, the excellent agreement of Eq. (1.39) with the experimental results is somewhat surprising for two reasons. First, in the experiments on 2D electron gases, there is typically no periodic potential. Second, the fact that any quantum Hall sample is necessarily finite is completely neglected in Eq. (1.39). The first issue may be resolved by arguing that one can take the magnitude of the periodic potential small while keeping the periodicity constant, which should essentially reproduce the 2D electron gas scenario. The second issue is resolved by the bulk-boundary correspondence.

⁷We use $\hbar = 1$ throughout the thesis, such that $h = 2\pi$.

Halperin (1982) first pointed out that edge currents should play a crucial role in a finite quantum Hall sample. More precisely, he argued that the number of filled Landau levels, determining the Hall plateaus, is equal to the number of edge channels, and that the latter carry the Hall current. Important improvements of Halperin’s theory (Niu and Thouless 1987; Büttiker 1988) take into account realistic device geometries and emphasize several characteristic length scales at play (magnetic length, elastic and inelastic scattering lengths, sample dimensions, etc.). This Halperin-Büttiker theory of edge channels has been qualitatively confirmed by many experiments. In its simplest form, the bulk-boundary correspondence implied by this theory can be written as

$$\# \text{ of filled bulk Landau levels} = \# \text{ of edge channels} = \mathcal{N}_{\text{Chern}}. \quad (1.40)$$

For more details on the bulk-boundary correspondence of quantum Hall systems, see the review article by Hatsugai (1997).

In the absence of an external magnetic field, the standard Hall effect and also the quantum Hall effect described above do not exist. However, if time-reversal symmetry is broken by some other means, for example, by magnetic textures, by magnetic impurities, or by the complex hoppings in Haldane’s model, a Hall effect can still occur. This is known as anomalous Hall effect (Nagaosa et al. 2010). The anomalous Hall effect has several contributions, which can be separated into intrinsic and extrinsic. The former are determined only by the band geometry of the perfect crystal, while the latter, known as skew-scattering and side-jump contributions, are disorder-related. At low temperature, intrinsic, skew-scattering and side-jump contributions are of comparable magnitude, while the intrinsic contribution tends to dominate at higher temperatures (Yue and Jin 2017).

In this thesis, we exclusively focus on the intrinsic contribution to the anomalous Hall (AH) conductivity, which in two dimensions and at zero temperature takes the simple form (Nagaosa et al. 2010)

$$\sigma_{xy}^{\text{AH}} = -e^2 \sum_{\alpha \in \text{occ.}} \int_{\text{BZ}} \frac{d^2 k}{(2\pi)^2} \Omega_{\alpha,xy}(\mathbf{k}) = -\frac{e^2}{2\pi} \mathcal{N}_{\text{Chern}}. \quad (1.41)$$

Here, \mathbf{k} is just the regular crystal momentum, the Berry curvature is constructed from standard Bloch states and integration is over the standard Brillouin zone. If $\mathcal{N}_{\text{Chern}} \neq 0$, the conductivity (1.41) clearly reproduces quantum Hall physics in the framework of a standard band insulator, explaining the equivalence of the terms “Chern insulator” and “quantum anomalous Hall insulator”. For realizations of such systems beyond Haldane’s model, see Weng et al. (2015) and He et al. (2018).

Importantly for our later purposes, the anomalous Hall effect also exists in 3D, where the anomalous Hall conductivity at zero temperature takes the tensorial form

$$\sigma_{ij}^{\text{AH}} = -e^2 \sum_{\alpha \in \text{occ.}} \int_{\text{BZ}} \frac{d^3 k}{(2\pi)^3} \Omega_{\alpha,ij}(\mathbf{k}), \quad (1.42)$$

with i and j representing any of the three spatial coordinates. Since integration is now over the 3D Brillouin zone, the integral does not represent a Chern number and is not quantized in general.

1.5.3 | Quantum geometry in orbital magnetism

We now turn our attention away from topology, and focus on physical phenomena caused by quantum geometry alone. As a first example, we here discuss the orbital magnetism of 2D crystals.

Orbital magnetism measures the response of a (spinless) electronic systems to an external magnetic field \mathbf{B} . For free electrons, one obtains the familiar cyclotron orbits, but for a crystalline system the collective response of the electron gas to the magnetic field is much more complicated to predict. While orbital magnetism is quite negligible in standard magnetic materials such as Fe, Co and Ni (Meyer and Asch 1961), this is not the case for all materials and a satisfying theory of magnetism obviously requires a thorough understanding of the orbital part (Thonhauser 2011).

A first important step to tackle the orbital magnetic response of crystals was taken by Peierls (1933), who generalized the work of Landau (1930) on the orbital susceptibility of free electrons to the case of electrons in a single Bloch band with dispersion $\epsilon(\mathbf{k})$. After many more efforts to generalize this, the orbital magnetization (Xiao et al. 2005; Thonhauser et al. 2005) and orbital susceptibility (Gómez-Santos and Stauber 2011; Raoux et al. 2015) of multiband systems are now rather well understood. Here we present the main results in the form obtained by Raoux et al. (2015).

Consider a 2D crystal in the presence of a perpendicular magnetic field B . The relevant thermodynamic state function of the (spinless) electron gas is the grand canonical potential

$$\Xi = -k_B T \int_{-\infty}^{\infty} dE \rho(E, B) \ln \left(1 + e^{-\frac{E-\mu}{k_B T}} \right), \quad (1.43)$$

where k_B is the Boltzmann constant, T absolute temperature, μ the chemical potential and ρ the density of states. The orbital magnetic responses are derivatives of the grand potential with respect to the magnetic field,

$$M = -\frac{1}{A} \frac{\partial \Xi}{\partial B} \Big|_{B \rightarrow 0}, \quad \chi = -\frac{\mu_0}{A} \frac{\partial^2 \Xi}{\partial B^2} \Big|_{B \rightarrow 0}, \quad (1.44)$$

where M and χ denote the orbital magnetization and orbital magnetic susceptibility of the system, respectively, A is the sample area, and μ_0 is the vacuum permeability. Since the density of states can be written as $\rho = -\frac{1}{\pi} \text{Im Tr } \mathcal{G}$ in terms of the system's retarded Green's function \mathcal{G} , one can develop a perturbation theory for M and χ by expanding \mathcal{G} , and thus the density of states, in powers of B . More precisely, in the case of an N -band system, \mathcal{G} is an $N \times N$ matrix whose diagonal elements can be written as

$$\mathcal{G}_{ii} = \mathcal{G}_{ii}^{(0)} + \mathcal{G}_{ii}^{(1)} B + \mathcal{G}_{ii}^{(2)} B^2 + \dots, \quad (1.45)$$

where $\mathcal{G}^{(0)} = G$ is the Green's function without magnetic field that is determined by the eigenvalues and eigenprojectors of the Bloch Hamiltonian:

$$G = \sum_{\alpha} D_{\alpha}(\mathbf{k}) P_{\alpha}(\mathbf{k}), \quad D_{\alpha}(\mathbf{k}) \equiv \frac{1}{E - \epsilon_{\alpha}(\mathbf{k}) + i\eta}. \quad (1.46)$$

With this approach, one can show that the orbital magnetization is given by

$$M = -\frac{ek_B T}{\pi} \int dE \int_{\text{BZ}} \frac{d^2 k}{(2\pi)^2} \ln \left(1 + e^{-\frac{E-\mu}{k_B T}} \right) \text{Im Tr}(G^2 H^x G H^y), \quad (1.47)$$

where the shorthand notation $H^i \equiv \partial_i H(\mathbf{k})$ is used. This can be rewritten as

$$M = \sum_{\alpha} \int_{\text{BZ}} \frac{d^2 k}{(2\pi)^2} \left[f(\epsilon_{\alpha}(\mathbf{k})) m_{\alpha}(\mathbf{k}) + ek_B T \ln \left(1 + e^{-\frac{\epsilon_{\alpha}(\mathbf{k})-\mu}{k_B T}} \right) \Omega_{\alpha}(\mathbf{k}) \right], \quad (1.48)$$

where $f(E)$ is the Fermi-Dirac distribution. Importantly, Eq. (1.48) allows one to realize that M is purely quantum geometrical, that is, it vanishes in a single-band system. Indeed, the Berry curvature $\Omega_{\alpha} \equiv \Omega_{\alpha,xy}$ appears explicitly, and moreover there is another geometric quantity, the *orbital magnetic moment* $m_{\alpha} \equiv m_{\alpha,xy}$, which can be computed using matrix elements of the velocity operator by a formula very similar to Eq. (1.21):

$$\begin{aligned} m_{\alpha,ij}(\mathbf{k}) &= e \text{Im} \langle \partial_i \psi_{\alpha}(\mathbf{k}) | [H(\mathbf{k}) - \epsilon_{\alpha}(\mathbf{k})] | \partial_j \psi_{\alpha}(\mathbf{k}) \rangle \\ &= -e \text{Im} \sum_{\beta \neq \alpha} \frac{\langle \psi_{\alpha}(\mathbf{k}) | \partial_i H(\mathbf{k}) | \psi_{\beta}(\mathbf{k}) \rangle \langle \psi_{\beta}(\mathbf{k}) | \partial_j H(\mathbf{k}) | \psi_{\alpha}(\mathbf{k}) \rangle}{\epsilon_{\alpha}(\mathbf{k}) - \epsilon_{\beta}(\mathbf{k})}. \end{aligned} \quad (1.49)$$

Note that from a semiclassical point of view, the first term of the magnetization (1.48) represents the rotation of the wave packet around its center of mass, while the second term stems from the movement of the center of mass.

Similarly, one can compute the orbital magnetic susceptibility from this perturbative approach. Let us first recall that, for a single-band system, the exact susceptibility is obtained from the Landau-Peierls formula (Peierls 1933)

$$\chi_{\text{LP}} = \frac{\mu_0 e^2}{12} \int_{\text{BZ}} \frac{d^2 k}{(2\pi)^2} f'(\epsilon(\mathbf{k})) \left[(\partial_x^2 \epsilon(\mathbf{k})) (\partial_y^2 \epsilon(\mathbf{k})) - (\partial_x \partial_y \epsilon(\mathbf{k}))^2 \right], \quad (1.50)$$

which is completely determined by the band dispersion. The appropriate generalization of the susceptibility to the multiband case is given by

$$\begin{aligned} \chi &= -\frac{\mu_0 e^2}{12\pi} \int_{\text{BZ}} \frac{d^2 k}{(2\pi)^2} \int_{-\infty}^{\infty} dE f(E) \text{Im Tr}(\mathcal{X}), \\ \mathcal{X} &= G H^{xx} G H^{yy} - (G H^{xy})^2 + 4(G H^x G H^y)^2 - 4(G H^x)^2 (G H^y)^2. \end{aligned} \quad (1.51)$$

Indeed, one recovers the Landau-Peierls formula when taking the one-band limit $H \rightarrow \epsilon$ and $G \rightarrow 1/(E - \epsilon + i\eta)$. While the decomposition of the susceptibility into geometrical quantities is much more involved than for the magnetization, one can derive, at least for the two-band case, an explicit decomposition of the susceptibility into contributions caused by quantum metric and Berry curvature (Raoux et al. 2015; Piéchon et al. 2016). This result, together with Eq. (1.48), shows the key role played by quantum geometry in orbital magnetism.

1.5.4 | Quantum geometry in the superfluid weight

The Meißner-Ochsenfeld effect describes the expulsion of an external magnetic field by a standard superconductor, corresponding to ideal diamagnetism. A first qualitative explanation of this phenomenon was given by London and London (1935), who formulated the equation

$$\mathbf{j}_s = -D_s \mathbf{A} \quad (1.52)$$

for the current density of a superconductor. Here, the proportionality constant D_s is known as the *superfluid weight*, which is related to the inverse square of the London penetration depth, and \mathbf{A} is the magnetic vector potential in the London gauge.

In a simplistic free electron theory, the superfluid weight is given by $D_s = n_s e^2 / m$, where n_s is the density of superfluid electrons and m the electron mass.⁸ In a more realistic approach, however, D_s is a material-dependent tensor to be determined from microscopic considerations and experiments. In particular, for a quantum mechanical description taking into account the periodic lattice potential of the superconducting crystal, one expects a situation rather analogous to the orbital magnetism discussed above: the external field induces a response whose characteristics (here D_s) are determined by the zero-field properties of the Bloch Hamiltonian, and in particular there should be quantum geometric contributions caused by the Bloch states.

Indeed, discussing multiband superconductors within the standard framework of Bardeen-Cooper-Schrieffer (BCS) theory and a mean-field approximation, Peotta and Törmä (2015) and especially Liang et al. (2017) recently emphasized the importance of such quantum geometric contributions to D_s . We here state some of their key results to illustrate that the QGT encoded in the Bloch states is ubiquitous not only in single-particle physics but also in many-body quantum phases.⁹

Consider a tight-binding Hamiltonian $H = H_{\text{kin}} + H_{\text{Hub}} + H_{\text{chem}}$ on a lattice with N inequivalent orbitals per unit cell, where the first term denotes the kinetic energy corresponding to hopping between orbitals, the second term covers on-site Hubbard interaction of strength U , and the last term is determined by the chemical potential μ . Applying a mean-field approximation to the Hubbard term, the Hamiltonian can be rewritten as $H = \sum_{\mathbf{k}} \Psi^\dagger(\mathbf{k}) H(\mathbf{k}) \Psi(\mathbf{k})$, with a Nambu spinor $\Psi(\mathbf{k})$ and a Bogoliubov-de Gennes (BdG) Hamiltonian

$$H(\mathbf{k}) = \begin{pmatrix} H_\uparrow(\mathbf{k}) - \mu 1_N & M_\Delta \\ M_\Delta^\dagger & -H_\downarrow^*(-\mathbf{k}) + \mu 1_N \end{pmatrix}, \quad (1.53)$$

which is a $2N \times 2N$ matrix. Here, $H_\sigma(\mathbf{k})$ is the Bloch Hamiltonian for spin $\sigma = \uparrow, \downarrow$ and the order parameters in $M_\Delta = \text{diag}(\Delta_1, \dots, \Delta_N)$ are proportional to U .

The superfluid weight can be derived either from the thermodynamic grand potential (similar in spirit to the orbital magnetism above) or from linear response theory.

⁸Note the analogy to Ohm's law $\mathbf{j} = \sigma \mathbf{E}$ where the conductivity takes the form $\sigma = ne^2 \tau / m$ in a simplistic Drude approach.

⁹Of course, since the mean-field approach essentially reduces the many-body problem to an effective single-particle problem, it is not surprising that interband effects appear in the same way as in a non-superconducting crystal. Nevertheless, the effects captured by the mean-field approach are expected to persist to some degree in an exact treatment.

One finds the elements of the superfluid weight tensor to be given by (Liang et al. 2017)

$$D_{s,ij} = \sum_{\mathbf{k}} \sum_{\alpha\beta\gamma\delta} C_{\alpha\beta\gamma\delta}(\mathbf{k}) [v_{i\uparrow}(\mathbf{k})]_{\alpha\beta} [v_{j\downarrow}(-\mathbf{k})]_{\gamma\delta}, \quad (1.54)$$

where $[v_{i\sigma}(\mathbf{k})]_{\alpha\beta} = \langle \psi_{\alpha\sigma}(\mathbf{k}) | \partial_i H_{\sigma}(\mathbf{k}) | \psi_{\beta\sigma}(\mathbf{k}) \rangle$ are matrix elements of the velocity operator for a given spin sector. The coefficients $C_{\alpha\beta\gamma\delta}(\mathbf{k})$ depend on the Fermi-Dirac distribution, the eigenenergies of the BdG Hamiltonian, and the expansion coefficients of the BdG eigenstates into Bloch eigenstates. The conventional (intraband) contribution to the superfluid weight, which is the only one that survives in a single-band system, is given by all terms such that $\alpha = \beta$ and $\gamma = \delta$. Note that, in the limit of a flat band, the intraband contribution vanishes. This is similar to the orbital magnetic susceptibility, whose intraband (Landau-Peierls) part is zero for a flat band. All terms with $\alpha \neq \beta$ or $\gamma \neq \delta$ are quantum geometric contributions, as can be easily realized by recalling the identity (1.20), which relates off-diagonal elements of the velocity operator to a non-Abelian Berry connection. One can make the dependence of the superfluid weight on geometrical quantities even more explicit in certain special cases. For example in the two-band case, the superfluid weight can be explicitly related to the quantum metric (Liang et al. 2017).

1.5.5 | Quantum geometry in magnetotransport

We have seen that the quantized Hall effects are determined by (topologically non-trivial) band geometry, but more generally transport phenomena contain quantum geometric contributions also in the absence of topology. This is especially relevant to 3D systems with strong interband coupling, such as Weyl and Dirac semimetals (Armitage et al. 2018).

Consider a multiband system (1.3). Our goal is to obtain the linear response electrical current $j_i = \sum_j \sigma_{ij} E_j$ in the presence of a magnetic field. A quantum mechanical treatment of the magnetoconductivity σ_{ij} is quite involved and no complete theory clearly illustrating the role of band geometry exists. Therefore, it is very popular to adopt a semiclassical approach, which indeed often yields very valuable insights. The approach is based on the Boltzmann equation in the relaxation time approximation (Ziman 1960):

$$\left(\partial_t + \dot{\mathbf{r}} \cdot \nabla_{\mathbf{r}} + \dot{\mathbf{k}} \cdot \nabla_{\mathbf{k}} \right) f_{\alpha}(\mathbf{k}, \mathbf{r}, t) = -\frac{1}{\tau} [f_{\alpha}(\mathbf{k}, \mathbf{r}, t) - f_{\alpha}^{\text{eq}}(\mathbf{k}, \mathbf{r}, t)]. \quad (1.55)$$

Here, \mathbf{r} and \mathbf{k} are the position and crystal momentum of a semiclassical wave packet in the band α , $f_{\alpha}(\mathbf{k}, \mathbf{r}, t)$ is the distribution function and $f_{\alpha}^{\text{eq}}(\mathbf{k}, \mathbf{r}, t)$ its equilibrium part in the absence of an electric field. The second and third terms on the left-hand side of Eq. (1.55) describe diffusion and drift of the wave packet, respectively, while the right-hand side takes account of scattering with a phenomenological scattering rate $1/\tau$.

To take account of geometrical effects, it is well known (Xiao et al. 2010; Cortijo 2016) that the semiclassical equations of motion entering the Boltzmann equation (1.55) should be extended by terms due to the Berry curvature $\mathbf{\Omega}_{\alpha}(\mathbf{k})$ and the orbital magnetic moment $\mathbf{m}_{\alpha}(\mathbf{k})$. Here we assume a 3D system with $\mathbf{\Omega}_{\alpha}(\mathbf{k}) =$

$(\Omega_{\alpha,yz}, \Omega_{\alpha,zx}, \Omega_{\alpha,xy})$, and with an orbital magnetic moment pseudovector $\mathbf{m}_\alpha(\mathbf{k}) = (m_{\alpha,yz}, m_{\alpha,zx}, m_{\alpha,xy})$ whose components are given by Eq. (1.49). The semiclassical equations of motion augmented by these quantities take the form

$$\dot{\mathbf{r}} = \mathbf{w}_\alpha(\mathbf{k}) - \dot{\mathbf{k}} \times \boldsymbol{\Omega}_\alpha(\mathbf{k}), \quad \dot{\mathbf{k}} = -e(\mathbf{E} + \dot{\mathbf{r}} \times \mathbf{B}), \quad (1.56)$$

where e is the electron charge, $\mathbf{w}_\alpha(\mathbf{k}) = \mathbf{v}_\alpha(\mathbf{k}) - \nabla_{\mathbf{k}}(\mathbf{m}_\alpha(\mathbf{k}) \cdot \mathbf{B})$ is the band velocity in the presence of a Zeeman-like energy shift $\epsilon_\alpha(\mathbf{k}) \rightarrow \tilde{\epsilon}_\alpha(\mathbf{k}) = \epsilon_\alpha(\mathbf{k}) - \mathbf{m}_\alpha(\mathbf{k}) \cdot \mathbf{B}$, and $\mathbf{v}_\alpha = \nabla_{\mathbf{k}}\epsilon_\alpha$ is the band velocity of the zero-field spectrum.

Upon inserting the equations of motion into the Boltzmann equation (1.55) and solving for the distribution function, one can find several contributions to the electrical conductivity tensor. In Appendix I.C, we conduct this procedure for a homogeneous system and to first order in \mathbf{B} . Under these conditions, one finds six contributions to the electrical conductivity:

- (i) The Drude conductivity (independent of \mathbf{B}), which depends only on the band velocity and is linear in the scattering time τ .
- (ii) The standard Hall conductivity created by the Lorentz force (linear in \mathbf{B}), which also depends only on the zero-field spectrum and scales as τ^2 .
- (iii) The anomalous Hall conductivity (independent of \mathbf{B}), which is a pure quantum geometric effect due to the Berry curvature and independent of the scattering time.
- (iv) A correction to the anomalous Hall effect which depends on both Berry curvature and orbital magnetic moment and is linear in \mathbf{B} .
- (v) A magnetoconductivity (linear in \mathbf{B}) induced by the Berry curvature, which scales as τ .
- (vi) Another magnetoconductivity (linear in \mathbf{B}), induced by the orbital magnetic moment, which also scales as τ .

All of these contributions except for the anomalous Hall conductivity are Fermi surface effects, that is, they vanish if the Fermi level resides in a band gap.

In particular, we highlight three contributions [(iii), (v), and (vi)] that clearly show the importance of quantum geometry in transport:

$$\sigma_{ij}^{\text{AH}} = -e^2 \sum_{\alpha} \int \frac{d^3k}{(2\pi)^3} f(\epsilon_{\alpha}) \epsilon_{ijk} (\Omega_{\alpha})_k, \quad (1.57a)$$

$$\begin{aligned} \sigma_{ij}^{\text{Berry}}(\mathbf{B}) = -e^3 \tau \sum_{\alpha} \int \frac{d^3k}{(2\pi)^3} f'(\epsilon_{\alpha}) \{ & -(\boldsymbol{\Omega}_{\alpha} \cdot \mathbf{B})(v_{\alpha})_i (v_{\alpha})_j \\ & + (\boldsymbol{\Omega}_{\alpha} \cdot \mathbf{v}_{\alpha}) [(v_{\alpha})_i B_j + (v_{\alpha})_j B_i] \}, \end{aligned} \quad (1.57b)$$

$$\begin{aligned} \sigma_{ij}^{\text{OMM}}(\mathbf{B}) = e^2 \tau \sum_{\alpha} \int \frac{d^3k}{(2\pi)^3} f'(\epsilon_{\alpha}) \{ & -(\mathbf{m}_{\alpha} \cdot \mathbf{B}) \partial_j (v_{\alpha})_i \\ & + [(v_{\alpha})_i \partial_j (\mathbf{m}_{\alpha} \cdot \mathbf{B}) + (v_{\alpha})_j \partial_i (\mathbf{m}_{\alpha} \cdot \mathbf{B})] / 2 \}. \end{aligned} \quad (1.57c)$$

Note that the anomalous Hall conductivity (1.57a) represents a finite-temperature generalization of Eq. (1.42) mentioned above. Note also that, interestingly, it appears that the exact same contributions can be found from a microscopic quantum mechanical approach (Könye and Ogata 2021), demonstrating the validity of the semiclassical formalism (at least for linear response and small \mathbf{B}). In Chapter 5, we will make explicit use of Eq. (1.57) to compute the magnetoconductivity of a class of multifold semimetals.

To close the chapter, we note that the quantum metric can also play a role in transport, but its effects are less striking than those caused by the Berry curvature. In a semiclassical treatment, the appearance of quantum metric effects requires an appropriate ad-hoc modification of the semiclassical equations of motion in addition to the modifications leading to Eq. (1.56). By a quantum mechanical derivation of the (linear response) electrical conductivity, it was recently shown that a dissipative correction to the longitudinal intraband (Drude-like) contribution is directly determined by the quantum metric (Mitscherling and Holder 2022). However this contribution is expected to be sizeable only if the Fermi level is close to a Dirac point or inside a very flat band. It is expected that the quantum metric will pop up in several other contributions when such theories of the electrical conductivity are generalized to the situation where a magnetic field is present.

Chapter 2

From two-band to multiband systems

Two-band models described by two-component equations of the form (1.3) or (1.5) have proved invaluable for illustrating key aspects of geometrically or topologically non-trivial semimetals and insulators. This is mostly because they are obviously the simplest systems that can capture interband effects, but also when confronted with the complicated band structure of a real crystal, it may be sufficient for certain purposes to consider only an effective two-band model formed from the highest valence band and lowest conduction band.

However, in many situations, it is required to go beyond the two-band scenario and consider multiband models for which Eqs. (1.3) and (1.5) become N -component linear algebra problems. This chapter motivates an in-depth study of such multiband ($N > 2$) systems, with special attention to flat bands, multifold band crossings, and their quantum geometry. This sets the stage for the original work on these topics presented in Chapters 3–5.

Our motivation is primarily a physical one, inspired by two main classes of systems that will be described in the following. Namely, first, we discuss paradigmatic flat-band systems such as Lieb, kagome, and pyrochlore lattices. They are relevant to many experiments on both artificial systems and real crystals, as we will detail further below. Second, we describe multifold band crossings characterized by an effective pseudospin Hamiltonian. They form the theoretical basis for understanding the behavior of a large number of crystals belonging to the family of 3D topological semimetals.

On the other hand, we also present a motivation from a more mathematical perspective by explaining why it is natural to expect rich and unconventional physics in multiband ($N > 2$) systems. Namely, we provide some insight into the complicated intrinsic structure of N -band systems encoded in the $\mathfrak{su}(N)$ algebra underlying the Hamiltonian, or alternatively in the Bloch spheres characterizing the internal parameter space. The mathematical insights and tools gained from this discussion will be put to use frequently in later chapters.

2.1 | Physical motivation (I) – Flat bands

Flat bands are completely dispersionless energy bands. They have long been known to develop in a two-dimensional electron gas in the presence of a magnetic field (Landau 1930), but can also occur in certain lattice systems, in which case there is at least

one band with $\epsilon_\alpha(\mathbf{k}) = \text{constant}$. While the first works on flat-band lattices were mostly interested in ferromagnetism induced by the Hubbard interaction, as reviewed by Tasaki (1998) and more recently by Derzhko et al. (2015), flat-band lattices are now being widely studied in many electronic and artificial systems (Liu et al. 2014; Leykam et al. 2018).

Flat bands are interesting because, on the one hand, band flatness signifies the absence of an intrinsic energy scale (a bandwidth), and on the other hand it implies the existence of macroscopically degenerate eigenstates. These two properties combined ensure that any perturbation may act non-perturbatively and profoundly modify the physics of the flat band. As an emblematic example, if Coulomb interactions are added to a Landau-quantized two-dimensional electron gas, the effect is known to be strongly non-perturbative, and the possibility for the existence of strongly correlated quantum phases arises, including fractional quantum Hall states (Girvin 2005) and Wigner crystals (Monarkha and Syvokon 2012).

Another important aspect of flat bands, which we will however not focus on during this thesis, concerns their topological character. For example, in the case of Landau quantization, the flat bands carry a non-zero first Chern number, as is evident in the quantum Hall effect. In contrast, in the scenario that we will mostly focus on (especially in Chapter 4), namely lattice models with finite-range hoppings, it is known that an exactly flat band cannot carry a finite Chern number (Green et al. 2010; Chen et al. 2014). Nevertheless, almost-flat bands obtained from finite-range hoppings may be topologically non-trivial, and so may exactly flat bands if one allows for infinite-range hoppings (Bergholtz and Liu 2013; Parameswaran et al. 2013).

We now proceed to introduce well-known flat-band models. An important message that we want to convey is that the simplest flat-band systems are multiband ($N > 2$) systems, indicating that a good understanding of the multiband scenario is essential for an appropriate analysis of flat-band physics. After discussing the simple models, we point out their relevance to experiments.

2.1.1 | Flat bands in simple lattice models

The simplest way to describe flat-band lattices consists in a tight-binding approach, which is the framework adopted in this thesis. The most well-known examples for flat-band lattices are two-dimensional and are visualized in Fig. 2.1: the Lieb lattice (Lieb 1989; Shen et al. 2010), the kagome lattice (Syôzi 1951; Guo and Franz 2009b), and the dice lattice (Horiguchi and Chen 1974; Sutherland 1986). The nearest-neighbor tight-binding models on these lattices are captured by Bloch Hamiltonians

$$\begin{aligned} H_{\text{Lieb}}(\mathbf{k}) &= 2 \cos k_x \lambda_1 + 2 \cos k_y \lambda_4, \\ H_{\text{kagome}}(\mathbf{k}) &= 2 \cos k_x \lambda_1 + 2 \cos(\mathbf{k} \cdot \boldsymbol{\delta}_1) \lambda_4 + 2 \cos(\mathbf{k} \cdot \boldsymbol{\delta}_2) \lambda_6, \\ H_{\text{dice}}(\mathbf{k}) &= \sum_i \cos(\mathbf{k} \cdot \boldsymbol{\delta}_i) (\lambda_1 + \lambda_6) + \sum_i \sin(\mathbf{k} \cdot \boldsymbol{\delta}_i) (\lambda_2 + \lambda_7), \end{aligned} \quad (2.1)$$

respectively, where we have taken the hopping amplitude $t = 1$ and the nearest-neighbor distance $a_0 = 1$. The λ_i designate $N = 3$ Gell-Mann matrices (Gell-Mann 1962), which are provided explicitly in Appendix II.A for the reader's convenience.

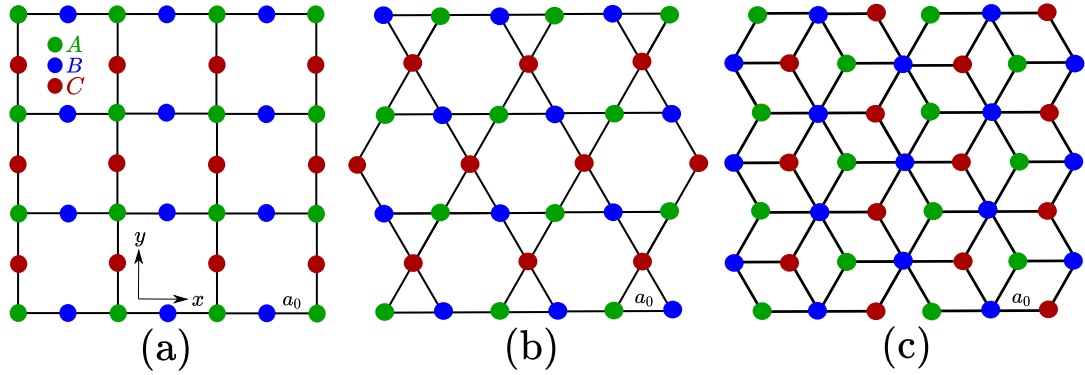


Fig. 2.1 – Paradigmatic flat-band systems. (a) Lieb lattice. (b) Kagome lattice. (c) Dice lattice. Nearest-neighbor tight-binding models on these lattices yield a perfectly flat band in the energy spectrum.

The vectors δ_i are given¹ by $\delta_{1,2} = \frac{1}{2}(1, \pm\sqrt{3})$, $\delta_3 = (-1, 0)$. The energy spectra of the Hamiltonians (2.1) are readily obtained as

$$\begin{aligned}\epsilon_{\alpha}^{\text{Lieb}}(\mathbf{k}) &= \alpha\sqrt{2}\sqrt{2 + \cos(2k_x) + \cos(2k_y)}, \\ \epsilon_{\alpha}^{\text{kagome}}(\mathbf{k}) &= 3\alpha^2 - 2 + \alpha\sqrt{3 + 2\cos(2k_x) + 4\cos k_x \cos(\sqrt{3}k_y)}, \\ \epsilon_{\alpha}^{\text{dice}}(\mathbf{k}) &= \alpha\sqrt{2}\sqrt{3 + 2\cos(\sqrt{3}k_y) + 4\cos(3k_x/2)\cos(\sqrt{3}k_y/2)},\end{aligned}\quad (2.2)$$

respectively, where $\alpha = 0, \pm$, and the existence of a flat band of energy ϵ_0 is evident. Since the corresponding band velocity $\mathbf{v}_0 = \nabla_{\mathbf{k}}\epsilon_0$ vanishes, it is natural to think of a flat band as being linked to some kind of non-propagating state. Indeed, as we will discuss in detail in Chapter 4, the presence of a flat band implies the existence of an infinite number of degenerate, strictly localized eigenstates of the real-space lattice Hamiltonian H .

Note that, while we have restricted our attention to 2D systems for simplicity, flat bands of course also exist in 3D. Well-known examples are the perovskite lattice (Weeks and Franz 2010) and the pyrochlore lattice (Reimers et al. 1991; Bergman et al. 2008; Guo and Franz 2009a). The former can be viewed as a 3D generalization of the Lieb lattice, while the latter is a generalization of the kagome lattice. In the simplest nearest-neighbor tight-binding description, both lattices feature four bands out of which two are degenerate flat bands.

We should like to stress again that all of the flat-band lattices mentioned here have $N > 2$ bands, suggesting that multiband systems provide a natural setup for realizing flat bands. Indeed, one of the most typical scenarios leading to the presence of flat bands is impossible to realize in a crystal with just two orbitals per unit cell. Namely, chiral flat bands arise from bipartite lattices with a different number of atoms in the two sublattices (Lieb 1989; Ramachandran et al. 2017), which clearly requires $N \geq 3$.

¹We have rotated these vectors as compared to the graphene case considered in Section 1.4.

For such bipartite systems, the Hamiltonian has a *chiral symmetry* (Ryu et al. 2010)

$$\mathcal{S}^{-1}H(\mathbf{x})\mathcal{S} = -H(\mathbf{x}), \quad (2.3)$$

where $\mathbf{x} = \mathbf{k}$ or $\mathbf{x} = \mathbf{q}$ for the lattice or continuum models, respectively. Actually, the flat bands of the Lieb, dice, and perovskite lattices are of this chiral type. Similarly, it is impossible to realize flat bands arising from frustration (as in the kagome or pyrochlore case) in an $N = 2$ lattice. Nevertheless, flat bands do exist in two-band systems, but this is only possible in the presence of second-neighbor hoppings, see Chapter 4 for more details.

2.1.2 | Flat bands in experiments

From an experimental point of view, the flat-band lattices mentioned above have attracted a lot of attention. While not known to exist in solids, Lieb lattices can be realized in photonic lattices, as has been demonstrated in several research groups (Guzmán-Silva et al. 2014; Vicencio et al. 2015; Mukherjee et al. 2015). Further, the Lieb geometry can be designed in artificial lattices, created by depositing carbon monoxide molecules onto a metal surface, as was suggested theoretically by Qiu et al. (2016) and shown experimentally by Slot et al. (2017).

The dice lattice has been of experimental relevance already two decades ago in the context of Aharonov-Bohm caging (Abilio et al. 1999; Naud et al. 2001), where three flat bands are induced by applying an appropriate magnetic flux. However, this situation is more complicated than and quite different from the simple hopping model (2.1). More recent experimental proposals to realize the standard dice lattice model involve ultracold atoms (Bercioux et al. 2009) or certain trilayer heterostructures (Wang and Ran 2011). Also, a cousin of the dice lattice, which interpolates between dice and honeycomb geometry (Raoux et al. 2014), might exist in $\text{Hg}_{0.83}\text{Cd}_{0.17}\text{Te}$ compounds for special parameter values (Malcolm and Nicol 2015).

The kagome lattice is by far the most pertinent to experiments, since, in contrast to the Lieb and dice lattices, it is known to exist in many crystals. For example, materials such as herbertsmithite, which exhibits a kagome layer of copper atoms, have been intensely investigated for quite some time. They are very relevant to quantum spin liquid research (Norman 2016; Zhou et al. 2017), because the kagome lattice affords strong magnetic frustration in the presence of an antiferromagnetic exchange coupling. Moreover, in magnetic Weyl semimetals such as Mn_3Sn (Yang et al. 2017) or $\text{Co}_3\text{Sn}_2\text{S}_2$ (Liu et al. 2018), which are of interest for their large anomalous Hall effects, the kagome layers formed from the manganese or cobalt atoms play a crucial role. Additionally, several materials with flat bands close to the Fermi level have been discovered (Lin et al. 2018; Kang et al. 2020; Liu et al. 2020), which contain kagome layers formed from iron or cobalt atoms. In such crystals, of course, a flat band is never perfectly flat, however for exotic physics to emerge it suffices if the band width of the quasi-flat band is a small energy scale compared to the relevant perturbation of interest. Yet more recently, a novel class of materials with kagome layers formed from vanadium atoms was discovered (Ortiz et al. 2019; Neupert et al. 2022), showing signatures of superconductivity and exotic charge density waves.

Concerning the 3D flat-band models, it should be mentioned that the pyrochlore lattice model is relevant, for example, to the description of pyrochlore oxides, where very flat bands near the Fermi level are predicted to exist via first-principles calculations (Hase et al. 2018; Hase et al. 2019).

Finally, beyond systems based on the lattices presented here, another field of enormous activity regarding flat bands has emerged in recent years. It concerns twisted bilayers and multilayers of graphene as well as other quasi-2D crystals, in particular transition metal dichalcogenides (Cheng et al. 2019; Andrei and MacDonald 2020). In this class of materials, an astonishing variety of different regimes emerges from the nearly flat bands, ranging from quantum Hall to Mott insulating and superconducting phases.

2.2 | Physical motivation (II) – multifold band crossings

A band crossing point is a point in the Brillouin zone where two or more energy bands meet. In the vicinity of the crossing point, the energy dispersion can take various forms, in particular it can be quadratic (parabolic) or linear (conical). The latter scenario is especially interesting since the crossing points act as defects that generically entail very peculiar geometrical and topological structures with a measurable impact on physical observables. For a general perspective on such defects, illustrating that they have been playing an important role in many domains of physics for decades, see for example the books by Volovik (2003) and Larson et al. (2020).

In the solid-state scenario, examples of such defects are encountered in graphene (Castro Neto et al. 2009) and Weyl semimetals (Armitage et al. 2018). They simulate concepts familiar from high-energy physics in a solid-state setup, and thus lead to a host of unconventional phenomena. In the case of graphene, the peculiar Dirac nature of the 2D crossings [recall Eq. (1.29)] allows for unconventional Landau levels, Klein tunneling through electrostatic barriers, and strongly termination-dependent edge physics, to name only a few interesting possibilities. In the case of Weyl semimetals, the Weyl character of the 3D crossings [recall Eq. (1.36)] allows to observe effects such as topological Fermi arc surface states, an anomalous Hall effect, as well as unconventional magnetotransport and optical responses.

So far, attention has mostly focused on crossings of two bands because they are easily accessible experimentally in graphene and Weyl semimetals. However, in recent years, crossings formed by $N > 2$ bands have come increasingly into focus, and this is the scenario we are interested in. We proceed as in the previous section, namely we first describe multiband crossings at the level of very simple models, before commenting on how they appear in experiments.

2.2.1 | Multifold crossings in simple models

Multifold crossings can exist in both 2D and 3D crystals. In the literature such crossings have been studied mainly in the spirit of generalizing 2D Dirac cones or 3D Weyl cones to $N > 2$. In both cases, the multiband crossings describe effective pseudospin- s fermions, where s can take both half-integer and integer values, and the

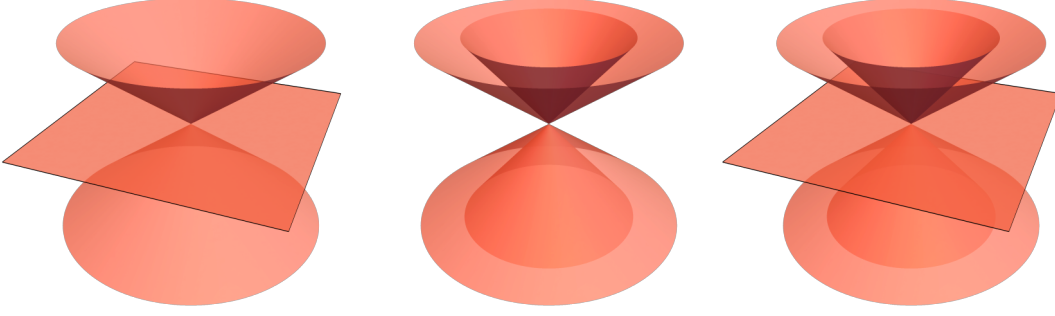


Fig. 2.2 – Energy spectrum for a pseudospin-1 (left), pseudospin-3/2 (middle), and pseudospin-2 system (right).

number N of bands is related to the spin quantum number as $N = 2s + 1$. In the present discussion of multifold crossings, we restrict our attention to this pseudospin case exclusively. It will be the purpose of Chapter 5 to show that not all linear multiband crossings are of the pseudospin type.

In the 2D case, the low-energy Hamiltonian describing a linear pseudospin- s crossing is given by (Lan et al. 2011; Dóra et al. 2011)

$$H(\mathbf{q}) = \gamma \mathbf{q} \cdot \mathbf{S} = \gamma(q_x S_x + q_y S_y), \quad (2.4)$$

where $\mathbf{q} = (q_x, q_y, 0)$ is the momentum as measured from the crossing point, $\gamma = \pm$ is the chirality (handedness), and $\mathbf{S} = (S_x, S_y, S_z)$ is the matrix representation of an arbitrary spin s . To qualify as spin matrices, the S_i need to satisfy a *spin algebra*

$$[S_i, S_j] = i\epsilon_{ijk} S_k, \quad (2.5)$$

as well as $\mathbf{S}^2 = s(s+1)1_N$. In the simplest case $s = 1/2$, one recovers from Eq. (2.4) the graphene Hamiltonian (1.29), since $\mathbf{S} = \boldsymbol{\sigma}/2$. For $s > 1/2$, one obtains multiband generalizations of graphene's low-energy model. For example, for $s = 1$ and $s = 3/2$, explicit expressions of the spin matrices in a standard representation are provided in Appendix II.A.

The energy spectrum of the pseudospin Hamiltonian (2.4) is easily obtained. It takes the form $\epsilon_\alpha(\mathbf{q}) = c_\alpha |\mathbf{q}| = c_\alpha (q_x^2 + q_y^2)^{1/2}$, where the band velocity c_α is simply given by the magnetic spin quantum number, $c_\alpha = m_s = -s, \dots, s$. This spectrum consists of a series of cones and flat bands, as visualized in Fig. 2.2 for $s = 1$ to $s = 2$. The fact that a zero-energy flat band occurs in the pseudospin model whenever s is an integer illustrates that flat bands and multifold crossings often accompany each other. Indeed, the Lieb and dice flat-band models discussed in Section 2.1.1 feature 2D pseudospin-1 crossing points.

Similarly, in 3D, the Hamiltonian describing a linear pseudospin- s crossing takes the form (Mañes 2012; Liang and Yu 2016; Bradlyn et al. 2016; Ezawa 2017)

$$H(\mathbf{q}) = \gamma \mathbf{q} \cdot \mathbf{S} = \gamma(q_x S_x + q_y S_y + q_z S_z), \quad (2.6)$$

where now $\mathbf{q} = (q_x, q_y, q_z)$. In the simplest case $s = 1/2$, one recovers the Weyl Hamiltonian (1.36). For $s > 1/2$, one obtains multiband generalizations of Weyl

	$s = 1/2$	$s = 1$	$s = 3/2$	$s = 2$
c_α	$-1/2, 1/2$	$-1, 0, 1$	$-3/2, -1/2, 1/2, 3/2$	$-2, -1, 0, 1, 2$
\mathcal{C}_α	$1, -1$	$2, 0, -2$	$3, 1, -1, -3$	$4, 2, 0, -2, -4$
ω_α	$1, 1$	$2, 4, 2$	$3, 7, 7, 3$	$4, 10, 12, 10, 4$

Table 2.1 – Coefficients c_α , \mathcal{C}_α and ω_α determining the energy spectrum, Berry curvature and orbital magnetic moment of the pseudospin- s continuum models (2.6), respectively (with $\gamma = +$). Each coefficient is listed from the lowest to the highest band.

fermions, often called *chiral multifold fermions*. The energy spectrum of the 3D pseudospin Hamiltonian is given by

$$\epsilon_\alpha(\mathbf{q}) = c_\alpha |\mathbf{q}| = c_\alpha \sqrt{q_x^2 + q_y^2 + q_z^2}, \quad (2.7)$$

where again $c_\alpha = m_s$, constituting a simple 3D generalization of the spectra plotted in Fig. 2.2. The band velocities c_α are explicitly listed in Table 2.1.

Pseudospin-like crossings are interesting mainly for their peculiar quantum geometry and topology. Indeed, the existence of an N -fold crossing implies strong interband coupling. In the 2D case (2.4), the quantum geometry can be unveiled by gapping out the crossing, similar to the discussion of graphene and Semenoff insulators in Section 1.4. Instead, here we are mostly interested in the 3D case. A crossing of the form (2.6) acts as a monopole source or sink of Berry curvature, with a Berry curvature pseudovector

$$\Omega_\alpha(\mathbf{q}) = \mathcal{C}_\alpha \frac{\mathbf{q}}{2|\mathbf{q}|^3}, \quad (2.8)$$

which generalizes the Berry curvature (1.37) of a Weyl fermion to arbitrary s . Thus, recalling Eq. (1.24), the crossing point clearly represents a topological defect, a *Berry monopole*, with a topological charge measured by the Chern number $\mathcal{C}_\alpha = -2\gamma c_\alpha = -2\gamma m_s$. This Chern number is explicitly listed in Table 2.1. For later purposes, we also state another geometric quantity of interest, namely the orbital magnetic moment. Summarizing its components in a pseudovector, we have

$$\mathbf{m}_\alpha = -\frac{e}{2}\omega_\alpha \frac{\mathbf{q}}{|\mathbf{q}|^2}, \quad \omega_\alpha = 2s(s+1) - \frac{\mathcal{C}_\alpha^2}{2} = 2[s(s+1) - c_\alpha^2]. \quad (2.9)$$

Interestingly, note that the coefficient ω_α is closely linked to the quantum metric (Lin and Hsiao 2021): $\omega_\alpha = 2|\mathbf{q}|^2 \text{Tr } g_\alpha(\mathbf{q})$. It is equally listed in Table 2.1.

From the symmetry point of view, the particle-hole symmetry of the spectrum (2.7) is due to a charge-conjugation parity (CP) symmetry

$$\mathcal{C}^\dagger H(\mathbf{x}) \mathcal{C} = -H^*(\mathbf{x}). \quad (2.10)$$

The CP symmetry is a combined symmetry of charge conjugation (C), defined by $\mathcal{V}^\dagger H(\mathbf{x}) \mathcal{V} = -H^*(-\mathbf{x})$, and inversion [or parity (P)], defined by $\mathcal{P}^\dagger H(\mathbf{x}) \mathcal{P} = H(-\mathbf{x})$ (Ryu et al. 2010); the CP symmetry operator is a unitary matrix $\mathcal{C} = \mathcal{P}\mathcal{V}$. For the

pseudospin systems, we have $\mathbf{x} = \mathbf{q}$ and $\mathcal{C} = \exp(i\pi S_y)$. Additionally, the isotropy of both spectrum (2.7) and Berry curvature (2.8) is caused by a full rotation symmetry

$$[\mathbf{L} + \mathbf{S}, H(\mathbf{q})] = 0, \quad (2.11)$$

where $\mathbf{L} = -i(\mathbf{q} \times \nabla_{\mathbf{q}})1_N$ is the orbital angular momentum operator.

We should further emphasize that, just like in the Weyl case, it is not possible to have a single unpaired pseudospin- s crossing (2.6) on a lattice (Nielsen and Ninomiya 1981). Therefore a minimal lattice model for a pseudospin- s semimetal must exhibit at least one pair of crossings of opposite chirality. We can easily construct such a model by writing

$$H(\mathbf{k}) = \mathbf{h}(\mathbf{k}) \cdot \mathbf{S} = h_1(\mathbf{k})S_x + h_2(\mathbf{k})S_y + h_3(\mathbf{k})S_z, \quad (2.12)$$

where the functions $h_i(\mathbf{k})$ are the same as in Eq. (1.38). Indeed, we have simply replaced the Pauli matrices by general spin matrices. This model has an energy spectrum

$$\epsilon_\alpha(\mathbf{k}) = c_\alpha \sqrt{h_1^2(\mathbf{k}) + h_2^2(\mathbf{k}) + h_3^2(\mathbf{k})}, \quad (2.13)$$

thus it is a semimetal with multifold crossings formed from $N = 2s + 1$ bands and located at $\mathbf{k}_0 = \pm(0, 0, k_0)$.

As in Fig. 1.7(a), we expect that one of the two crossing points acts as a source and the other as a sink of Berry curvature. This can be confirmed by computing the lattice Berry curvature for the model (2.12). As in Fig. 1.7(a), we want to measure the Berry flux between the crossing points by taking 2D slices for fixed k_z , and thus we only care about $\Omega_{\alpha,xy}(\mathbf{k})$, which takes the form

$$\Omega_{\alpha,xy}(\mathbf{k}) = -\frac{c_\alpha}{|\mathbf{h}(\mathbf{k})|^3} [4t_x t_y c_x c_y h_1(\mathbf{k}) - 2m t_y s_x c_y h_2(\mathbf{k}) - 2m t_x c_x s_y h_3(\mathbf{k})], \quad (2.14)$$

where we use shorthand notations $c_i = \cos k_i$ and $s_i = \sin k_i$. Taking the same parameters as in Fig. 1.7(a) for concreteness, this yields a Chern number $\mathcal{N}_\alpha^{\text{Chern}} = 2c_\alpha$ for any 2D slice such that $|k_z| < k_0$, while $\mathcal{N}_\alpha^{\text{Chern}} = 0$ otherwise. The total Chern number $\mathcal{N}^{\text{Chern}}$ at any fixed k_z is given by a sum over the Chern numbers of the occupied bands. For a pseudospin-1 semimetal at half filling, we thus have $|\mathcal{N}^{\text{Chern}}| = 2$, and for a pseudospin-3/2 semimetal $|\mathcal{N}^{\text{Chern}}| = 4$; there are thus two and four Fermi arcs connecting the projections of the multifold crossing points in the surface Brillouin zone, respectively. As we will see in the following, this has indeed been confirmed experimentally.

2.2.2 | Multifold crossings in experiments

The pseudospin fermions described above can be realized in many experimental setups. Early proposals for realizing the 2D Hamiltonian (2.4) suggest ultracold atoms in optical lattices (Bercioux et al. 2009; Shen et al. 2010; Lan et al. 2011). Later proposals also address electronic materials such as graphene antidot lattices (Ouyang et al. 2011), square graphene (Wang et al. 2013), an MoS₂ allotrope forming an octagon-square lattice (Li et al. 2014), or graphene on In₂Te₂ (Giovannetti et al.

2015). Successful experimental implementations of 2D pseudospin-1 fermions have been achieved recently in the experiments on artificial Lieb lattices already mentioned in Section 2.1.2.

The 3D case has attracted yet much more attention, since it is encountered in crystalline solids. Already shortly after the first prediction of a concrete material candidate for a Weyl semimetal (Wan et al. 2011), the possibility for multifold crossings in the band structure of certain crystals was pointed out by Mañes (2012). Since then, a huge field of research investigating a large number of topological semimetals has formed, mostly focussing on Weyl and Dirac semimetals (Armitage et al. 2018), but also increasingly investigating semimetals with multifold crossings (Lv et al. 2021). The latter are known under various names, such as *chiral topological semimetals*, *chiral multifold semimetals*, *generalized Weyl semimetals*, or just *topological semimetals*. As we have already mentioned, both Weyl semimetals and chiral topological semimetals are of great interest to a wide community, not only due to their topological Fermi arc surface states but also due to many other physical phenomena induced by the Berry monopoles. Most notably, they cause an anomalous Hall effect, peculiar behavior of the magnetoresistance, and unconventional optical responses.

Threefold fermions are known to exist in two types of crystals. One scenario involves a crossing of a non-degenerate band and a twofold degenerate band, which has been theoretically predicted for materials such as tantalum nitride and tungsten carbide (Weng et al. 2016b; Zhu et al. 2016; Weng et al. 2016a; Chang et al. 2017a), and experimentally observed shortly after (Lv et al. 2017; Ma et al. 2018). The other scenario involves a crossing of three fully nondegenerate bands, which corresponds to the pseudospin-1 scenario discussed above, with monopole charge $|\mathcal{C}| = 2$ and, accordingly, two Fermi arcs. This behavior has been predicted for crystals like $\text{Pd}_3\text{Bi}_2\text{S}_2$ and $\text{Ag}_3\text{Se}_2\text{Au}$ (Bradlyn et al. 2016), followed by experimental realizations in cobalt silicide and rhodium silicide (Takane et al. 2019; Rao et al. 2019; Sanchez et al. 2019).

Band degeneracies of higher degree are also known to exist in crystals. In particular, materials for which four-, six- or eightfold degenerate crossings have been predicted include Bi_2AuO_5 (Wieder et al. 2016), CoSi and RhSi (Chang et al. 2017b; Tang et al. 2017), and many more (Bradlyn et al. 2016; Cano et al. 2019). Some of those crystals exhibit fourfold nodal points of pseudospin-3/2 type, where $|\mathcal{C}| = 4$, leading to four Fermi arcs; or fourfold crossings of double Weyl type with $|\mathcal{C}| = 2$; or sixfold (double pseudospin-1) fermions, where also $|\mathcal{C}| = 4$; or eightfold (double Dirac) nodes. We wish to stress in particular that pseudospin-3/2 crossings and their associated Fermi arcs have been observed in several crystals, including PdBiSe (Lv et al. 2019), AlPt (Schröter et al. 2019), PtGa (Yao et al. 2020) and PdGa (Schröter et al. 2020).

2.3 | Mathematical motivation (I) – Hamiltonian and $\mathfrak{su}(N)$ algebra

We now proceed to describe the rich mathematical structure of N -band systems. In Chapters 4 and 5 we will explore some of that structure to design new kinds of flat-band lattices and multifold semimetals. We here consider first the $\mathfrak{su}(N)$

algebra underlying any N -band system, and then (in Section 2.4) the properties of the corresponding internal parameter space. In both cases, the complexity grows enormously for $N > 2$.

2.3.1 | Two-band systems

Let us start by reviewing the simple, familiar case of a two-band system ($N = 2$), for which the Hamiltonian of Eq. (1.6) can be written as

$$H(\mathbf{x}) = h_0(\mathbf{x})1_2 + \mathbf{h}(\mathbf{x}) \cdot \boldsymbol{\sigma} = \begin{pmatrix} h_0(\mathbf{x}) + h_3(\mathbf{x}) & h_1(\mathbf{x}) - ih_2(\mathbf{x}) \\ h_1(\mathbf{x}) + ih_2(\mathbf{x}) & h_0(\mathbf{x}) - h_3(\mathbf{x}) \end{pmatrix}. \quad (2.15)$$

Here, 1_2 is the identity and h_0 is a real scalar function. The real vector $\mathbf{h} = (h_1, h_2, h_3)$ will be called *Hamiltonian vector* and $\boldsymbol{\sigma}$ is a vector formed from Pauli matrices. The eigenvalues of Eq. (2.15) are

$$\epsilon_\alpha(\mathbf{x}) = h_0(\mathbf{x}) + \alpha|\mathbf{h}(\mathbf{x})|, \quad (2.16)$$

forming a band structure with two bands $\alpha = \pm$. Since the identity part of the Hamiltonian does not affect the eigenstates and hence quantum geometry and topology, we will often employ the rescaled energy

$$\varepsilon_\alpha(\mathbf{x}) \equiv \epsilon_\alpha(\mathbf{x}) - h_0(\mathbf{x}) = \alpha|\mathbf{h}(\mathbf{x})|. \quad (2.17)$$

Two-band systems admit a rather straightforward mathematical description, governed by the Lie algebra $\mathfrak{su}(2)$ (Pfeifer 2003). Indeed, the Pauli matrices σ_i form a basis for $\mathfrak{su}(2)$, and due to this fact we synonymously call Eq. (2.15) a two-band Hamiltonian, an $\mathfrak{su}(2)$ Hamiltonian, or an $SU(2)$ Hamiltonian, where $SU(2)$ is the corresponding Lie group. The simple structure of the $\mathfrak{su}(2)$ algebra is expressed in the product relations

$$\sigma_i \sigma_j = \delta_{ij} 1_2 + i\epsilon_{ijk} \sigma_k, \quad (\mathbf{m} \cdot \boldsymbol{\sigma})(\mathbf{n} \cdot \boldsymbol{\sigma}) = \mathbf{m} \cdot \mathbf{n} 1_2 + i(\mathbf{m} \times \mathbf{n}) \cdot \boldsymbol{\sigma}. \quad (2.18)$$

One also immediately obtains the (anti)commutation relations

$$[\sigma_i, \sigma_j] = 2i\epsilon_{ijk} \sigma_k, \quad \{\sigma_i, \sigma_j\} = 2\delta_{ij} 1_2. \quad (2.19)$$

According to the first and second identity of Eq. (2.19), the Pauli matrices are said to satisfy a *spin algebra* and a *Clifford algebra*, respectively. Such convenient properties will in general be absent in a multiband system.

2.3.2 | Multiband systems

Simple multiband systems: Dirac and pseudospin Hamiltonian

Moving beyond two-band systems, the simplest possible case is that of a *Dirac Hamiltonian*, given by

$$H_D(\mathbf{x}) = \mathbf{d}(\mathbf{x}) \cdot \boldsymbol{\Gamma}, \quad (2.20)$$

where $\mathbf{\Gamma} = (\Gamma_1, \dots, \Gamma_{\mathcal{D}})$ is a vector formed from $N \times N$ “gamma” matrices that satisfy a Clifford algebra:

$$\{\Gamma_i, \Gamma_j\} = 2\delta_{ij}1_N. \quad (2.21)$$

This is the same anticommutation relation as for the two-band case, cf. Eq. (2.19), explaining the simplicity of the Dirac Hamiltonian. A Dirac Hamiltonian can only exist for N even (with $\mathcal{D} = N$ or $\mathcal{D} = N + 1$) and has an energy spectrum

$$\varepsilon_{\pm}(\mathbf{x}) = \pm|\mathbf{d}(\mathbf{x})|, \quad (2.22)$$

where each band is $N/2$ -fold degenerate. Note that Eq. (2.20) is a generalization of Dirac’s Hamiltonian that describes relativistic electrons (and positrons) in empty space (Dirac 1928). In this paradigmatic case one has $N = \mathcal{D} = 4$, with three of the four gamma matrices coupled to the three momentum coordinates, and the last gamma matrix coupled to the electron/positron mass.

Another simple type of multiband system, which we have already encountered in Section 2.2, is a system for which the Hamiltonian can be written as

$$H(\mathbf{x}) = \mathbf{h}(\mathbf{x}) \cdot \mathbf{S}, \quad (2.23)$$

where the three matrices S_i fulfill a spin algebra (2.5). In other words, they maintain the same commutation relation as in the two-band case, explaining the simplicity of the pseudospin system.

Generic multiband systems: $SU(N)$ Hamiltonian

Our main focus in this thesis will be on completely generic multiband systems, for which the Hamiltonian matrix can be written as

$$H(\mathbf{x}) = h_0(\mathbf{x})1_N + \mathbf{h}(\mathbf{x}) \cdot \boldsymbol{\lambda}, \quad (2.24)$$

with a real scalar function h_0 and a real Hamiltonian vector $\mathbf{h} = (h_1, \dots, h_{N^2-1})$. Here, we have introduced a vector $\boldsymbol{\lambda} = (\lambda_1, \dots, \lambda_{N^2-1})$ composed of the $N^2 - 1$ elementary generator matrices λ_i of the Lie group $SU(N)$, which constitute a basis for the Lie algebra $\mathfrak{su}(N)$ (Pfeifer 2003). Throughout this thesis, we will choose the λ_i as (*generalized*) *Gell-Mann matrices*. For the reader’s convenience, they are explicitly listed for $N = 3$ and $N = 4$ in Appendix II.A. For example, it then follows that the three-band generalization of the Hamiltonian (2.15) takes the form

$$H(\mathbf{x}) = \begin{pmatrix} h_0 + h_3 + \frac{1}{\sqrt{3}}h_8 & h_1 - ih_2 & h_4 - ih_5 \\ h_1 + ih_2 & h_0 - h_3 + \frac{1}{\sqrt{3}}h_8 & h_6 - ih_7 \\ h_4 + ih_5 & h_6 + ih_7 & h_0 - \frac{2}{\sqrt{3}}h_8 \end{pmatrix}. \quad (2.25)$$

The eigenvalues of Eq. (2.24) cannot in general be written as a simple function of the Hamiltonian vector. Nevertheless, it again proves convenient to redefine the origin of energy to be h_0 , such that the identity part in the Hamiltonian vanishes and the eigenvalues are

$$\varepsilon_{\alpha}(\mathbf{x}) \equiv \epsilon_{\alpha}(\mathbf{x}) - h_0(\mathbf{x}). \quad (2.26)$$

We synonymously call Eq. (2.24) a multiband Hamiltonian, an N -band Hamiltonian, an $\mathfrak{su}(N)$ Hamiltonian or an $SU(N)$ Hamiltonian. Its mathematical structure is expressed in the product identity (Kaplan and Resnikoff 1967)

$$\lambda_i \lambda_j = \frac{2}{N} \delta_{ij} 1_N + (d_{ijk} + i f_{ijk}) \lambda_k, \quad (2.27)$$

as well as the (anti)commutation relations

$$[\lambda_i, \lambda_j] = 2i f_{ijk} \lambda_k, \quad \{\lambda_i, \lambda_j\} = \frac{4}{N} \delta_{ij} 1_N + 2d_{ijk} \lambda_k. \quad (2.28)$$

Since all generators λ_i are traceless, the convenient trace orthogonality

$$\text{Tr}(\lambda_i \lambda_j) = 2\delta_{ij} \quad (2.29)$$

holds. The (anti)commutation relations define totally antisymmetric and totally symmetric *structure constants* of $\mathfrak{su}(N)$, respectively:

$$f_{ijk} \equiv -\frac{i}{4} \text{Tr}([\lambda_i, \lambda_j] \lambda_k), \quad d_{ijk} \equiv \frac{1}{4} \text{Tr}(\{\lambda_i, \lambda_j\} \lambda_k). \quad (2.30)$$

These are a known set of real numbers once a matrix representation is chosen for the generators. Indeed, for $N = 2$, where $\boldsymbol{\lambda} = \boldsymbol{\sigma}$, the d_{ijk} vanish identically and $f_{ijk} = \epsilon_{ijk}$, such that Eq. (2.19) is recovered. For the explicit numerical values of d_{ijk} and f_{ijk} in the $N = 3$ case, see Table 2.2. Clearly, the complexity of the algebra is enormously increased as compared to the $\mathfrak{su}(2)$ case, indicating that multiband systems with $N \geq 3$ generally present a challenging mathematical problem.

Later on, we will also require dot, star and cross products of vectors defined from the structure constants:

$$\mathbf{m} \cdot \mathbf{n} \equiv m_i n_i, \quad (\mathbf{m} \star \mathbf{n})_i \equiv d_{ijk} m_j n_k, \quad (\mathbf{m} \times \mathbf{n})_i \equiv f_{ijk} m_j n_k, \quad (2.31)$$

where \mathbf{m} and \mathbf{n} are real and $(N^2 - 1)$ -dimensional. The star product is unfamiliar because it does not play any role in $N = 2$ situations (where $d_{ijk} = 0$), but it is crucial for $N > 2$ systems. Using Eq. (2.31), one can rewrite Eq. (2.27) in a vectorial form:

$$(\mathbf{m} \cdot \boldsymbol{\lambda})(\mathbf{n} \cdot \boldsymbol{\lambda}) = \frac{2}{N} \mathbf{m} \cdot \mathbf{n} 1_N + (\mathbf{m} \star \mathbf{n} + i \mathbf{m} \times \mathbf{n}) \cdot \boldsymbol{\lambda}, \quad (2.32)$$

which constitutes a multiband generalization of Eq. (2.18).

Finally, it will also prove useful to introduce the following notation for repeated star products of a vector with itself:

$$\mathbf{m}_\star^{(k)} = \mathbf{m} \star \mathbf{m}_\star^{(k-1)} \equiv \underbrace{\mathbf{m}_\star \star \dots}_k, \quad (2.33)$$

where $k \geq 1$ and $\mathbf{m}_\star^{(0)} = \mathbf{m}$. Thus $\mathbf{m}_\star = \mathbf{m} \star \mathbf{m}$, $\mathbf{m}_{\star\star} = \mathbf{m} \star \mathbf{m}_\star$, and so on.

	(i, j, k)	d_{ijk}	(i, j, k)	d_{ijk}	(i, j, k)	f_{ijk}
$\mathfrak{su}(2)$	–	–	–	–	(1, 2, 3)	1
$\mathfrak{su}(3)$	(1, 1, 8)	$1/\sqrt{3}$	(3, 5, 5)	1/2	(1, 2, 3)	1
	(1, 4, 6)	1/2	(3, 6, 6)	–1/2	(1, 4, 7)	1/2
	(1, 5, 7)	1/2	(3, 7, 7)	–1/2	(1, 5, 6)	–1/2
	(2, 2, 8)	$1/\sqrt{3}$	(4, 4, 8)	$-1/(2\sqrt{3})$	(2, 4, 6)	1/2
	(2, 4, 7)	–1/2	(5, 5, 8)	$-1/(2\sqrt{3})$	(2, 5, 7)	1/2
	(2, 5, 6)	1/2	(6, 6, 8)	$-1/(2\sqrt{3})$	(3, 4, 5)	1/2
	(3, 3, 8)	$1/\sqrt{3}$	(7, 7, 8)	$-1/(2\sqrt{3})$	(3, 6, 7)	–1/2
	(3, 4, 4)	1/2	(8, 8, 8)	$-1/\sqrt{3}$	(4, 5, 8)	$\sqrt{3}/2$
	–	–	–	–	(6, 7, 8)	$\sqrt{3}/2$

Table 2.2 – Comparison of inequivalent non-zero structure constants of the $\mathfrak{su}(2)$ and $\mathfrak{su}(3)$ algebra, as taken from Goyal et al. (2016).

2.4 | Mathematical motivation (II) – Internal parameters and Bloch spheres

A second way to become aware of the complexity of multiband ($N > 2$) systems consists in studying what we will call the *internal parameter space*. This is the space of parameters which are solely determined by the general mathematical structure of the $SU(N)$ Hamiltonian, independently of the physical realization. We distinguish such internal parameters from *external parameters*, which are the parameters of physical significance, such as \mathbf{k} or \mathbf{q} in band theory. We also relate internal to external parameters through the concept of Bloch spheres.

2.4.1 | Two-band systems

Internal parameter space

Different types of internal parameters are possible, arising from different ways to parametrize the eigenstates of the two-band Hamiltonian (2.15). Namely, first, we may consider the formal parametrization of a two-component complex vector, given by²

$$|\psi_\alpha\rangle = \begin{pmatrix} \cos \theta_\alpha \\ \sin \theta_\alpha e^{i\phi_\alpha} \end{pmatrix}, \quad (2.34)$$

²The state can always be brought to this form by fixing the global phase appropriately. For a completely general parametrization, one could leave the global phase arbitrary.

with two *eigenstate's angles* θ_α and ϕ_α . Second, it is straightforward to verify that the eigenstates can also be written as

$$|\psi_\alpha\rangle = \frac{1}{\sqrt{2\left(1 + \alpha\frac{h_3}{|\mathbf{h}}\right)}} \begin{pmatrix} \alpha + \frac{h_3}{|\mathbf{h}} \\ \frac{h_1 + ih_2}{|\mathbf{h}} \end{pmatrix} \quad (2.35)$$

in terms of the components h_i of the Hamiltonian vector. There is also a third possible parametrization. Namely, one can express the unit Hamiltonian vector \mathbf{u} in spherical coordinates,

$$\mathbf{u} \equiv \mathbf{h}/|\mathbf{h}| = (\sin\theta_h \cos\phi_h, \sin\theta_h \sin\phi_h, \cos\theta_h), \quad (2.36)$$

where we will call θ_h and ϕ_h the *Hamiltonian's angles*. Upon rewriting Eq. (2.35) in terms of those angles, one has

$$|\psi_+\rangle = \begin{pmatrix} \cos\frac{\theta_h}{2} \\ \sin\frac{\theta_h}{2} e^{i\phi_h} \end{pmatrix}, \quad |\psi_-\rangle = \begin{pmatrix} -\sin\frac{\theta_h}{2} \\ \cos\frac{\theta_h}{2} e^{i\phi_h} \end{pmatrix}. \quad (2.37)$$

This implies that the eigenstate's angles can be expressed in terms of the Hamiltonian's angles, for example as $\theta_+ = \theta_h/2$, $\theta_- = (\theta_h + \pi)/2$, $\phi_+ = \phi_- = \phi_h$. As we will see, such a simple relation between the different types of internal angles is only possible due to the extremely simple properties of two-band systems.

To get some insight into the structure of the different parameter spaces, it is instructive to consider the geometry of the quantum states with respect to the internal parameters. First, let us choose the parameter space of interest as $\mathbf{x} = (h_1, h_2, h_3)$. The corresponding quantum metric and Berry curvature tensors are 3×3 matrices with matrix elements³

$$g_{\alpha,ij} = \frac{1}{4|\mathbf{h}|^2} \left(\delta_{ij} - \frac{h_i h_j}{|\mathbf{h}|^2} \right), \quad \Omega_{\alpha,ij} = -\frac{\alpha}{2|\mathbf{h}|^3} \epsilon_{ijk} h_k. \quad (2.38)$$

This result means that any SU(2) Hamiltonian can be viewed as a monopole in the space of components h_i . More precisely, forming a 3D Berry curvature pseudovector, one has $\boldsymbol{\Omega}_\alpha(\mathbf{h}) = -\alpha\mathbf{h}/(2|\mathbf{h}|^3)$, which represents a Berry monopole. According to Eq. (1.24) we can thus associate a Chern number $\mathcal{C}_\alpha = -\alpha$ to any two-band system, measuring the flux of Berry curvature through a surface enclosing the point $\mathbf{h} = 0$ (a degeneracy of the two levels). This Berry monopole scenario does not in general hold true for a multiband system, except in the special case of a pseudospin system (2.23).

Second, let us choose the parameters of interest as $\mathbf{x} = (\theta_h, \phi_h)$. The corresponding QGT is a 2×2 matrix given by

$$g_\alpha = \frac{1}{4} \begin{pmatrix} 1 & 0 \\ 0 & \sin^2\theta_h \end{pmatrix}, \quad \Omega_\alpha = -\frac{\alpha}{2} \begin{pmatrix} 0 & \sin\theta_h \\ -\sin\theta_h & 0 \end{pmatrix}. \quad (2.39)$$

³This can be computed by inserting the eigenstates (2.35) into Eqs. (1.13) or (1.21), but it is more direct to employ Eq. (2.41) introduced below.

This is a well-known result (Kolodrubetz et al. 2017) and implies that any two-band system can be viewed as having the geometry of a unit two-sphere \mathbb{S}^2 . Indeed, the quantum metric is completely analogous to the Riemannian metric $ds^2 = d\theta^2 + \sin^2 \theta d\phi^2$ of a standard two-sphere.

External parameter space

In cases of physical relevance, one typically does not care too much about the space of internal parameters of the two-band system (2.15), but rather about the explicit dependency of the Hamiltonian vector $\mathbf{h}(\mathbf{x})$ on some vector of *external* parameters \mathbf{x} . In contrast to the internal parameters, which describe the abstract mathematical properties of the Hamiltonian, the external parameters have some specific physical meaning and describe the concrete physical realization of the two-band system. In particular, this scenario includes the case $\mathbf{x} = \mathbf{k}$ relevant to (topological) band theory.

The geometry of the quantum states in the space of external parameters strongly depends on the precise form of the Hamiltonian of interest. In general, the QGT $T_{\alpha,ij}(\mathbf{x})$ computed with respect to the external parameters can be obtained from the intrinsic geometric tensors by a simple composition rule:

$$T_{\alpha,ij}(\mathbf{x}) = \sum_{k,l} J_{ik} J_{jl} T_{\alpha,kl}(\mathbf{y}). \quad (2.40)$$

Here, $i, j \in \{\text{external parameters}\}$ and $k, l \in \{\text{internal parameters}\}$, with Jacobians $J_{ik} \equiv \partial_i y_k$ that encode the dependence of the internal parameters \mathbf{y} on the external parameters \mathbf{x} . As a very important application, we emphasize that Eq. (2.40) becomes especially useful when taking $\mathbf{y} = \mathbf{h}$. Namely, using the explicit expressions given in Eq. (2.38), one immediately has

$$g_{\alpha,ij}(\mathbf{x}) = \frac{1}{4} \left[\frac{\partial_i \mathbf{h}(\mathbf{x}) \cdot \partial_j \mathbf{h}(\mathbf{x})}{|\mathbf{h}(\mathbf{x})|^2} - \frac{(\mathbf{h}(\mathbf{x}) \cdot \partial_i \mathbf{h}(\mathbf{x})) (\mathbf{h}(\mathbf{x}) \cdot \partial_j \mathbf{h}(\mathbf{x}))}{|\mathbf{h}(\mathbf{x})|^4} \right], \quad (2.41)$$

$$\Omega_{\alpha,ij}(\mathbf{x}) = -\frac{\alpha}{2|\mathbf{h}(\mathbf{x})|^3} \mathbf{h}(\mathbf{x}) \cdot [\partial_i \mathbf{h}(\mathbf{x}) \times \partial_j \mathbf{h}(\mathbf{x})].$$

This provides the most general and the most straightforward way to compute the QGT for any two-band system (2.15); this QGT is a $\dim(\mathbf{x}) \times \dim(\mathbf{x})$ matrix. The simplicity and popularity of this QGT formula stems from the fact that it only involves the Hamiltonian vector \mathbf{h} , making it obsolete to explicitly construct eigenstates. This is in stark contrast to the standard formulas (1.13) and (1.21), which are based on eigenstates. It will be a major contribution of Chapter 3 to clarify and quantify the generalization of the convenient expressions (2.41) to arbitrary N .

Bloch spheres

For any given Hamiltonian, there is a particular dependency $\mathbf{y}(\mathbf{x})$ of internal on external parameters. This dependency can be visualized using a *Bloch sphere*. Here we consider three different Bloch spheres that can be associated to a two-band Hamiltonian. They are not always precisely distinguished because they happen to have the same shape, namely that of a unit two-sphere. However, we will see below that

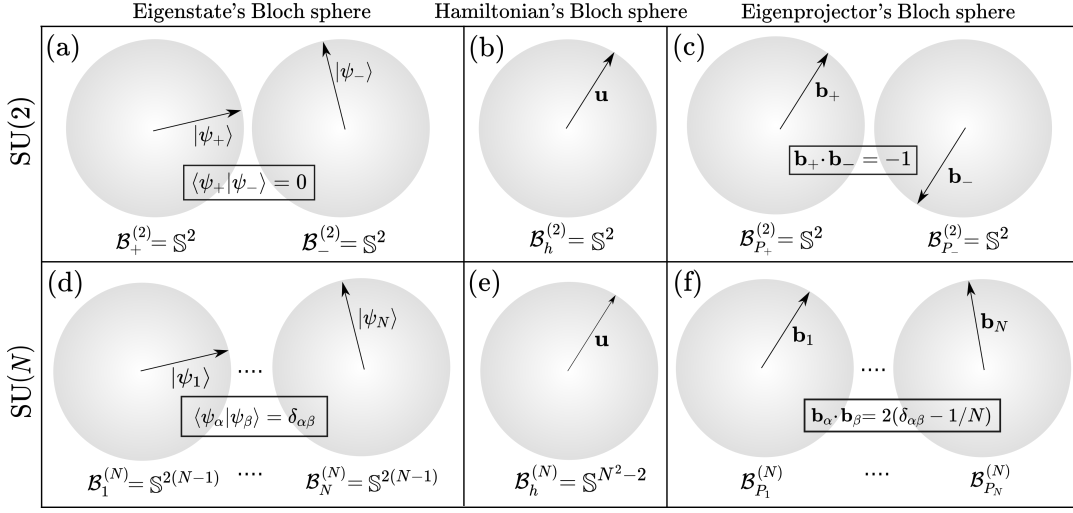


Fig. 2.3 – Schematic visualization of Bloch spheres appearing in the treatment of two-band [SU(2), first row] and multiband [SU(N), second row] Hamiltonians. The eigenstate’s Bloch sphere $\mathcal{B}_\alpha^{(N)}$ is a unit sphere for all N , but of different dimension than the Hamiltonian’s Bloch sphere if $N > 2$. The Hamiltonian’s Bloch sphere $\mathcal{B}_h^{(N)}$ corresponds to a unit sphere for any N . The eigenprojector’s Bloch sphere $\mathcal{B}_{P_\alpha}^{(N)}$ is a proper sphere for $N = 2$ only; for $N > 2$ it is of complicated shape.

when dealing with N -band Hamiltonians, the three Bloch spheres are in general very different, such that a precise distinction is necessary.

First, consider the eigenstates in the form (2.34), parametrized by the eigenstate’s angles $\theta_\alpha(\mathbf{x})$ and $\phi_\alpha(\mathbf{x})$. These angles define a map

$$|\psi_\alpha\rangle : X \rightarrow \mathcal{B}_\alpha^{(2)}, \quad \mathbf{x} \mapsto |\psi_\alpha(\mathbf{x})\rangle \quad (2.42)$$

from the (external) parameter space X to a space that may be called the *eigenstate’s Bloch sphere* $\mathcal{B}_\alpha^{(2)}$. Since $\theta_\alpha(\mathbf{x})$ and $\phi_\alpha(\mathbf{x})$ can be interpreted as spherical coordinates, $\mathcal{B}_\alpha^{(2)}$ is a unit two-sphere \mathbb{S}^2 , see Fig. 2.3(a). Second, consider the unit Hamiltonian vector (2.36), parametrized by the Hamiltonian’s angles $\theta_h(\mathbf{x})$ and $\phi_h(\mathbf{x})$. The unit vector defines a map

$$u : X \rightarrow \mathcal{B}_h^{(2)}, \quad \mathbf{x} \mapsto \mathbf{u}(\mathbf{x}) \quad (2.43)$$

from X to a space that may be called the *Hamiltonian’s Bloch sphere* $\mathcal{B}_h^{(2)}$. It is a unit two-sphere, too, see Fig. 2.3(b).

Finally, a third kind of Bloch sphere arises from the eigenprojectors P_α of the Hamiltonian (2.15). Namely, writing the projectors as

$$P_\alpha(\mathbf{x}) = |\psi_\alpha(\mathbf{x})\rangle\langle\psi_\alpha(\mathbf{x})| = \frac{1}{2}1_2 + \frac{1}{2}\mathbf{b}_\alpha(\mathbf{x}) \cdot \boldsymbol{\sigma}, \quad (2.44)$$

we can introduce a *Bloch vector* $\mathbf{b}_\alpha(\mathbf{x})$. It defines a map

$$\mathbf{b}_\alpha : X \rightarrow \mathcal{B}_{P_\alpha}^{(2)}, \quad \mathbf{x} \mapsto \mathbf{b}_\alpha(\mathbf{x}) \quad (2.45)$$

from parameter space to a space that may be called the *eigenprojector’s Bloch sphere* $\mathcal{B}_{P_\alpha}^{(2)}$. The peculiarity and simplicity of two-band systems, as compared to the more

general N -band case, consists in the fact that the eigenprojector's Bloch sphere is the same as the Hamiltonian's Bloch sphere, namely it is a unit two-sphere as well [see Fig. 2.3(c)]. This originates from the fact that the Bloch vector is parallel to the Hamiltonian vector, or equivalently that the eigenprojector is linear in the Hamiltonian matrix:

$$\mathbf{b}_\alpha(\mathbf{x}) = \alpha \mathbf{u}(\mathbf{x}) = \frac{\mathbf{h}(\mathbf{x})}{\varepsilon_\alpha(\mathbf{x})}, \quad P_\alpha(\mathbf{x}) = \frac{1}{2} \left[1_2 + \frac{1}{\varepsilon_\alpha(\mathbf{x})} \mathbf{h}(\mathbf{x}) \cdot \boldsymbol{\sigma} \right]. \quad (2.46)$$

Such a simple relation does not hold for a multiband system, and it will be undertaken in Chapter 3 to generalize Eq. (2.46) to any N .

The discussion of the Bloch spheres conducted here may seem somewhat superfluous in light of the fact that they all turn out to be simply unit two-spheres. However, we should like to stress again that the three Bloch spheres are *a priori distinct spaces*, which coincidentally all take the same shape for $N = 2$. Being aware of this distinction is necessary to avoid considerable confusion in the $SU(N > 2)$ case, where the three Bloch spheres are completely different from one another, see Fig. 2.3(d)–(f) and the discussion below.

2.4.2 | Multiband systems

We now briefly generalize the notions of internal parameter space and Bloch spheres to arbitrary N , which demonstrates the difficulty and complexity of the mathematical structure of multiband systems.

Internal parameter space

The formal parametrization of each eigenstate of an N -band system (2.24), generalizing Eq. (2.34), requires $N - 1$ pairs of eigenstate's angles $(\theta_\alpha^{(i)}, \phi_\alpha^{(i)})$, with $i = 1, \dots, N - 1$. This is because there are a priori N complex components, corresponding to $2N$ real parameters, of which two can be eliminated using the normalization condition and fixing the global phase. For example, for a three-band system, one can write⁴

$$|\psi_\alpha\rangle = \begin{pmatrix} \cos \theta_\alpha^{(1)} \\ \sin \theta_\alpha^{(1)} \cos \theta_\alpha^{(2)} e^{i\phi_\alpha^{(1)}} \\ \sin \theta_\alpha^{(1)} \sin \theta_\alpha^{(2)} e^{i\phi_\alpha^{(2)}} \end{pmatrix} \quad (2.47)$$

in terms of four eigenstate's angles. Thus, the complexity of the parameter space associated to the eigenstate's angles increases linearly in N .

Another possibility is to try to parametrize the eigenstates in terms of the Hamiltonian vector \mathbf{h} . This vector has $N^2 - 1$ real-valued components, and accordingly there are $N^2 - 2$ Hamiltonian's angles $\theta_h^{(i)}$ necessary to parametrize the unit vector $\mathbf{u} \equiv \mathbf{h}/|\mathbf{h}|$. For a three-band system, there are thus already seven Hamiltonian's angles. Clearly, the complexity of the parameter space associated to the Hamiltonian's

⁴Again one could add a global phase $\Gamma_\alpha(\mathbf{x})$ to have a completely general parametrization with an arbitrary gauge choice.

angles increases as N^2 . Moreover, unfortunately, already for $N = 3$ there is no simple generalization of Eqs. (2.35) or (2.37): the eigenvalues and eigenstates of the three-band Hamiltonian (2.25) in general involve cube roots and cannot easily be expressed in terms of the components h_i or the Hamiltonian's angles $\theta_h^{(i)}$.

As a consequence of these difficulties, the geometry of the internal parameter space is extremely complicated and opaque. This becomes evident, for example, when trying to compute the QGT in any of the parameter spaces

$$\mathbf{x} = \mathbf{h}, \quad \mathbf{x} = \left(\theta_h^{(1)}, \dots, \theta_h^{(N^2-2)} \right), \quad \mathbf{x} = \left(\theta_\alpha^{(1)}, \phi_\alpha^{(1)}, \dots, \theta_\alpha^{(N-1)}, \phi_\alpha^{(N-1)} \right).$$

Thus, no simple generalizations of Eqs. (2.38) or (2.39) exist. Also, the composition rule (2.40), while valid for any N , does not lead to a useful generalization of the powerful relation (2.41), due to the cumbersome form of the internal QGT $T_{\alpha,kl}(\mathbf{h})$. In fact, generalizing Eq. (2.41) to the multiband case is non-trivial, and part of Chapter 3 will be devoted to solving this problem with the help of eigenprojectors.

Bloch spheres

We now comment on different $SU(N)$ Bloch spheres that can be associated to a multiband system. First, the $2(N-1)$ eigenstate's angles define a map

$$|\psi_\alpha\rangle : X \rightarrow \mathcal{B}_\alpha^{(N)}, \quad \mathbf{x} \mapsto |\psi_\alpha(\mathbf{x})\rangle \quad (2.48)$$

from external parameter space X to an *eigenstate's Bloch sphere* $\mathcal{B}_\alpha^{(N)}$, which is a unit sphere $\mathcal{S}^{2(N-1)}$, as sketched in Fig. 2.3(d).

Second, the unit vector \mathbf{u} defines a map

$$u : X \rightarrow \mathcal{B}_h^{(N)}, \quad \mathbf{x} \mapsto \mathbf{u}(\mathbf{x}) \quad (2.49)$$

from X to a *Hamiltonian's Bloch sphere* $\mathcal{B}_h^{(N)}$, which is a unit sphere \mathcal{S}^{N^2-2} , as depicted in Fig. 2.3(e).

Again, the third Bloch sphere stems from the eigenprojectors. Upon using the same matrix basis as for the Hamiltonian (2.24), each eigenprojector can be written as (Hioe and Eberly 1981)

$$P_\alpha(\mathbf{x}) = |\psi_\alpha(\mathbf{x})\rangle\langle\psi_\alpha(\mathbf{x})| = \frac{1}{N}1_N + \frac{1}{2}\mathbf{b}_\alpha(\mathbf{x}) \cdot \boldsymbol{\lambda}, \quad (2.50)$$

where \mathbf{b}_α is a (*generalized*) *Bloch vector* or *coherence vector*, which is in one-to-one correspondence to the associated eigenprojector. We stress that the Bloch vector is a key quantity for the theory developed in Chapter 3.

Let us study the properties of the Bloch vector more closely. First we note that we have adopted the convention of a prefactor $\frac{1}{2}$ in front of \mathbf{b}_α , although various choices of this factor exist in the literature (Kimura 2003; Byrd and Khaneja 2003; Bertlmann and Krammer 2008). Note also that, since the $SU(N)$ generators $\boldsymbol{\lambda}$ are Hermitian, each Bloch vector is real. Now, since \mathbf{b}_α , just like the Hamiltonian vector, has $N^2 - 1$ real-valued components, the map $\mathbf{b}_\alpha(\mathbf{x})$ (for given α) would at first glance seem to define an $(N^2 - 2)$ -sphere, but in fact this is prevented by constraints on

the Bloch vectors. In particular, the orthogonality relation $P_\alpha(\mathbf{x})P_\beta(\mathbf{x}) = \delta_{\alpha\beta}P_\alpha(\mathbf{x})$ translates to the Bloch vector picture as⁵

$$\begin{aligned}\mathbf{b}_\alpha(\mathbf{x}) \cdot \mathbf{b}_\beta(\mathbf{x}) &= 2(\delta_{\alpha\beta} - 1/N), \\ \mathbf{b}_\alpha(\mathbf{x}) \star \mathbf{b}_\beta(\mathbf{x}) &= (\delta_{\alpha\beta} - 2/N)(\mathbf{b}_\alpha(\mathbf{x}) + \mathbf{b}_\beta(\mathbf{x})), \\ \mathbf{b}_\alpha(\mathbf{x}) \times \mathbf{b}_\beta(\mathbf{x}) &= 0,\end{aligned}\tag{2.51}$$

where dot, star, and cross products are to be understood in the sense of Eq. (2.31). While the first and last line in Eq. (2.51) are present for any N , the second line constitutes a constraint that is absent for $N = 2$. This star product constraint is mainly responsible for the complicated behavior of the vector $\mathbf{b}_\alpha(\mathbf{x})$, which defines a map

$$\mathbf{b}_\alpha : X \rightarrow \mathcal{B}_{P_\alpha}^{(N)}, \quad \mathbf{x} \mapsto \mathbf{b}_\alpha(\mathbf{x})\tag{2.52}$$

from parameter space not to an $(N^2 - 2)$ -sphere, but to a certain $2(N - 1)$ -dimensional subset thereof, which we may choose to call the *eigenprojector's Bloch sphere* $\mathcal{B}_{P_\alpha}^{(N)}$, or equivalently the *generalized Bloch sphere*, see Fig. 2.3(f). This implies that, in stark contrast to the $N = 2$ case, $\mathbf{u}(\mathbf{x})$ and $\mathbf{b}_\alpha(\mathbf{x})$ are completely distinct maps, and in particular $\mathbf{u}(\mathbf{x}) \nparallel \mathbf{b}_\alpha(\mathbf{x})$ for $N > 2$ [see also Eq. (3.32) derived below].

An intuitive understanding of the geometrical structure of the generalized Bloch sphere is not at all easy to acquire. Many efforts have been undertaken to figure out its properties for $N > 2$, which is a highly non-trivial issue. To mention only a few articles on the matter, we recommend to consult the work of Harriman (1978), Jakóbczyk and Siennicki (2001), Kimura (2003), Zyczkowski and Sommers (2003), Byrd and Khaneja (2003), Kimura and Kossakowski (2005), Mendaš (2006) and Goyal et al. (2016). For the interested reader, we outline some of the main results that have been established in Appendix II.B.

In summary, the Hamiltonian's, the eigenprojector's and the eigenstate's Bloch sphere are all isomorphic spaces for $N = 2$, but all different spaces for $N > 2$, illustrating the additional complexities that arise when passing from $N = 2$ to a higher number of bands.

⁵It is a simple exercise to verify this using the product identity (2.32).

Chapter 3

Bloch vector approach to observables

3.1 | Introduction

In quantum mechanics, it is common to construct measurable quantities by taking the matrix representation of the observables O of interest in the eigenbasis of H , with matrix elements $O_{\alpha\beta} = \langle \psi_\alpha | O | \psi_\beta \rangle$. For instance, the QGT (1.21), orbital magnetization (1.48) and superfluid weight (1.54) are constructed from matrix elements of the velocity operator $v_i = \partial_i H$ in the eigenbasis of H . However, especially when dealing with parameter-dependent systems, the energy eigenstates which are used to compute matrix elements $O_{\alpha\beta}$ prove rather cumbersome. Indeed, the following three issues present themselves.

- (i) The gauge dependency of the global phase of each eigenstate is unwieldy.
- (ii) Singularities of the wave function may occur in parameter space, and the location of the singularity points may be unpredictable.
- (iii) Even for a given gauge choice, there are many different ways to express an eigenstate, involving inconvenient trigonometric functions and phase angles with an intransparent parameter dependence. In other words, there is no unique closed-form expression of an eigenstate as a function of the Hamiltonian.

These issues are already annoying but tractable in the two-band case, however they become extremely hard to handle if not intractable when moving from two-band to multiband systems. In the multiband case, it is thus common to resort to (not always well-controlled) numerical construction of eigenstates and numerical computation of observables.

In this chapter, we formulate an alternative approach to observables. It is based on eigenprojectors $P_\alpha = |\psi_\alpha\rangle\langle\psi_\alpha|$, or, more precisely, on the corresponding Bloch vectors \mathbf{b}_α introduced in Eq. (2.50). Note that the Bloch vectors are just a vectorial representation of the projectors, in exactly the same way as the vector \mathbf{h} is a vectorial representation of the Hamiltonian H . This alternative approach has two advantages. First, at a practical level, it helps to avoid the issues associated with eigenstates in explicit computations and provides more analytical insight. Second, at a conceptual level, it offers a general strategy to decompose physical quantities into intraband and geometric contributions.

In the following, we first illustrate in more detail the three issues of eigenstates listed above. We hope to convince the reader that it may be useful for certain purposes to give up the eigenstates in favor of eigenprojectors, or, equivalently, Bloch vectors. We then write a number of well-known physical quantities in terms of Bloch vectors, in particular the quantum metric, Berry curvature and orbital magnetization. We proceed to explain how similar expressions can be obtained for any quantity of interest. Finally, we show how to obtain the Bloch vectors directly from the Hamiltonian and its eigenvalues. This provides a convenient means to explicitly compute physical quantities (especially simple ones such as the QGT and orbital magnetization) without constructing energy eigenstates. The exposition given here makes much use of the results of Graf and Piéchon (2021a), but also goes beyond. A related discussion can be found in the work of Pozo and Juan (2020).

3.2 | Motivation: Eigenstates versus eigenprojectors and Bloch vectors

The issues of gauge ambiguity, singularities in parameter space, and the difficulty to parametrize the eigenstates appear pretty clearly already in the two-band case. Namely, first, consider the formal parametrization (2.34) of a complex two-component unit vector. In fact, to be complete, one has to multiply it by a global phase factor $\exp[i\Gamma_\alpha(\mathbf{x})]$. In other words, the first evident problem of eigenstates is that they are gauge-dependent. Moreover, the global phase is parameter-dependent, which proves problematic when derivatives with respect to the parameters \mathbf{x} are to be carried out, for example when computing the QGT from Eq. (1.13).

Second, the expression for two-band eigenstates given in Eq. (2.35) illustrates the possible singular behavior of eigenstates in parameter space. A singularity is evidently to be expected when $h_3(\mathbf{x}_0)/|\mathbf{h}(\mathbf{x}_0)| = -\alpha$ for some point $\mathbf{x} = \mathbf{x}_0$. Similarly, if the eigenstate components are written in terms of the Hamiltonian's angles as in Eq. (2.37), then the relations $\tan \theta_h = \sqrt{h_1^2 + h_2^2}/h_3$ and $\tan \phi_h = h_2/h_1$ point towards further possible singular behavior when $h_3(\mathbf{x}_0) = 0$ or $h_1(\mathbf{x}_0) = 0$.

Third, there are at least three different ways to parametrize the eigenstates even for a given gauge choice, see Eqs. (2.34)–(2.37). It is not clear which one to use to construct matrix elements $O_{\alpha\beta}$, as one or the other may be advantageous depending on the particular circumstances. The closed-form expression (2.35) in terms of the Hamiltonian vector is perhaps the most transparent, but it does not appear very handy if one is dealing with classes of Hamiltonians beyond a specific Hamiltonian of interest.

While inconvenient, these issues are still tractable for a two-band system due to the inherent simplicity of its mathematical structure. However, in a multiband system, the issues get much worse and much more difficult to handle. To see this, recall, first, that the Hamiltonian vector \mathbf{h} has $N^2 - 1$ components. Thus, already for $N = 3$, a possible closed-form expression of the eigenstates in terms of those components, generalizing Eq. (2.35), would involve complicated functions of the eight parameter-dependent functions h_i , which makes such an expression essentially useless. This also implies that, unlike in the two-band case, we cannot even predict under which

	Gauge-dependency	Singularities	Unique parametrization
$ \psi_\alpha\rangle$	yes	yes	no
P_α	no	no	yes
\mathbf{b}_α	no	no	yes

Table 3.1 – Advantages of eigenprojectors and Bloch vectors as compared to eigenstates.

conditions singularities will occur in parameter space. Similarly, as mentioned earlier, the generalization of the widely used parametrization (2.37) to higher N must involve $N^2 - 2$ Hamiltonian’s angles whose singularities are completely unclear. Of course, the additional problem of the gauge ambiguity remains as well.

All these issues of eigenstates are eliminated by eigenprojectors, and equivalently by Bloch vectors, as summarized in Table 3.1. Namely, first, P_α and \mathbf{b}_α are evidently explicitly gauge-independent quantities. Second, they are well-behaved in parameter space, as singularities can only appear at band degeneracy points. In other words, for a multiband Hamiltonian of any size N , all singularities of the eigenprojectors and Bloch vectors can be predicted from the knowledge of the band structure alone. Third, we will see in Section 3.4 that, for any N , unique closed-form expressions $P_\alpha(H)$ of eigenprojectors in terms of the Hamiltonian matrix are easily obtained from the Cayley-Hamilton theorem (Cayley 1858; Horn and Johnson 2013). This also leads to closed-form expressions $\mathbf{b}_\alpha(\mathbf{h})$ of Bloch vectors in terms of the Hamiltonian vector. Eigenprojectors and Bloch vectors thus have a *unique* parametrization, involving only the parameters already present in the Hamiltonian. Unlike when dealing with eigenstates, there is no need to introduce new degrees of freedom with unclear interrelations. As a simple example, it is clear that the two-band projector (2.46) exhibits all of the convenient features advertised here.

3.3 | Writing observables in terms of Bloch vectors

Consider a multiband system described by a Hamiltonian (2.24). Our goal here is to show that any physical quantity constructed from operators O in the Hilbert space of H can be expressed in terms of Bloch vectors, and to illustrate the utility of such a procedure via simple examples. Note that throughout this chapter we will assume $\text{Tr } H = h_0 = 0$, such that H has eigenvalues ε_α as given by Eq. (2.26).

3.3.1 | First examples

As a first simple example, it is clear from Eq. (2.50) that the Hamiltonian itself can be written in terms of Bloch vectors as

$$H = \sum_{\alpha} \varepsilon_{\alpha} P_{\alpha} = \frac{1}{2} \sum_{\alpha} \varepsilon_{\alpha} \mathbf{b}_{\alpha} \cdot \boldsymbol{\lambda}, \quad \mathbf{h} = \frac{1}{2} \sum_{\alpha} \varepsilon_{\alpha} \mathbf{b}_{\alpha}. \quad (3.1)$$

In other words, the Hamiltonian vector can be viewed geometrically as being composed of Bloch vectors pointing in different directions and weighted by the respective energy eigenvalues. This is of course completely equivalent to the spectral decomposition in terms of eigenprojectors. It immediately follows that we can view each energy eigenvalue geometrically as the component of \mathbf{h} along the corresponding Bloch vector:

$$\varepsilon_\alpha = \mathbf{b}_\alpha \cdot \mathbf{h}. \quad (3.2)$$

More generally, any function of the Hamiltonian can be written as

$$f(H) = \frac{1}{N} \sum_\alpha f(\varepsilon_\alpha) + \frac{1}{2} \sum_\alpha f(\varepsilon_\alpha) \mathbf{b}_\alpha \cdot \boldsymbol{\lambda}. \quad (3.3)$$

Next, it is clear that an arbitrary operator in the Hilbert space of H can be written as

$$O = o_0 1_N + \mathbf{o} \cdot \boldsymbol{\lambda} \quad (3.4)$$

in terms of Gell-Mann matrices, where \mathbf{o} is an $(N^2 - 1)$ -dimensional vector (from now on we will assume $o_0 = 0$ for simplicity). Several important aspects of such operators can be expressed geometrically in terms of Bloch vectors. For example, the time evolution is encoded in the cross product of the vector \mathbf{o} and the Bloch vectors:

$$\dot{O} = i[H, O] = \sum_\alpha \varepsilon_\alpha (\mathbf{o} \times \mathbf{b}_\alpha) \cdot \boldsymbol{\lambda}, \quad \dot{\mathbf{o}} = \sum_\alpha \varepsilon_\alpha (\mathbf{o} \times \mathbf{b}_\alpha). \quad (3.5)$$

3.3.2 | Berry curvature, quantum metric and orbital magnetization

Let us now consider some more interesting cases, which are less trivial than the examples above and where the Bloch vector approach provides a real advantage. In particular, let us consider expectation values of operators that one often encounters in solid-state physics, and which are of the form

$$\mathcal{T}_\alpha \equiv \text{Tr}(P_\alpha O), \quad \mathcal{T}_{\alpha\beta} \equiv \text{Tr}(P_\alpha O P_\beta O'), \quad \mathcal{T}_{\alpha\beta\gamma} \equiv \text{Tr}(P_\alpha O P_\beta O' P_\gamma O''), \quad (3.6)$$

et cetera. For example, \mathcal{T}_α with $O = H$ is just the energy eigenvalue (3.2). More interestingly, $\mathcal{T}_{\alpha\beta}$ with $O = \partial_i H$ and $O' = \partial_j H$ appears in the quantum metric, Berry curvature and orbital magnetization; indeed, Eq. (1.21) for the quantum geometric tensor can be written as

$$T_{\alpha,ij}(\mathbf{x}) = \sum_{\beta \neq \alpha} \frac{\text{Tr}(P_\alpha H^i P_\beta H^j)}{(\varepsilon_\alpha - \varepsilon_\beta)^2}, \quad (3.7)$$

and similarly Eq. (1.49) for the orbital magnetic moment can be written as

$$m_{\alpha,ij}(\mathbf{x}) = -e \text{Im} \sum_{\beta \neq \alpha} \frac{\text{Tr}(P_\alpha H^i P_\beta H^j)}{\varepsilon_\alpha - \varepsilon_\beta}. \quad (3.8)$$

Here the superscript denotes a parametric derivative, $H^i \equiv \partial_i H$. Similar traces $\mathcal{T}_{\alpha\beta}$ appear in the anomalous Hall conductivity, spin Hall conductivity, or magnetoconductivities. Higher-order traces $\mathcal{T}_{\alpha\beta\gamma}$ or $\mathcal{T}_{\alpha\beta\gamma\delta}$ appear for example in the electrical

polarizability (Chen and Lee 2011) or orbital magnetic susceptibility (Raoux et al. 2015).

To illustrate the utility of the Bloch vector approach, we now present Bloch vector based expressions for the quantum metric, Berry curvature and orbital magnetization of an arbitrary multiband system. We also comment on how to derive similar expressions for more complicated quantities such as the orbital magnetic susceptibility, although this is not carried out in detail and left for future work.

Quantum metric and Berry curvature

Consider the quantum geometric tensor as given by Eq. (3.7). Inserting the Hamiltonian's spectral decomposition $H = \sum_{\alpha} \varepsilon_{\alpha} P_{\alpha}$ leads to the intermediate result

$$T_{\alpha,ij}(\mathbf{x}) = \text{Tr} [P_{\alpha}^i (1_N - P_{\alpha}) P_{\alpha}^j]. \quad (3.9)$$

Then, by inserting Eq. (2.50) for the eigenprojectors, one obtains the quantum metric and Berry curvature in terms of Bloch vectors as

$$g_{\alpha,ij}(\mathbf{x}) = \frac{1}{4} \mathbf{b}_{\alpha}^i \cdot \mathbf{b}_{\alpha}^j, \quad \Omega_{\alpha,ij}(\mathbf{x}) = -\frac{1}{2} \mathbf{b}_{\alpha} \cdot (\mathbf{b}_{\alpha}^i \times \mathbf{b}_{\alpha}^j), \quad (3.10)$$

for *arbitrary* values of N . Be aware that the Bloch vectors are $(N^2 - 1)$ -dimensional and the dot and cross products have to be interpreted in the $SU(N)$ sense of Eq. (2.31). For $N = 1$, one has $\mathbf{b}_{\alpha} = 0$ and of course no quantum metric or Berry curvature exists. For $N = 2$, it is straightforward to verify that the well-known expressions (2.41) are recovered upon inserting Eq. (2.46) for the Bloch vector. For $N = 3$, a similar way of writing the Berry curvature was already encountered by Barnett et al. (2012) and Lee et al. (2015), and for the quantum metric by Bauer et al. (2016). For general N , Eq. (3.10) is a new result, although Pozo and Juan (2020) recently found an equivalent formula in terms of so-called 1-generators.

We should like to emphasize the conceptual importance of Eq. (3.9) and especially of Eq. (3.10). These expressions show very clearly that the conventional eigenstate-based point of view on quantum geometry, as expressed in Chapter 1, can be replaced by viewing quantum geometry as encoded in the eigenprojectors or Bloch vectors. In particular, the QGT for a system with an arbitrary number of bands is fully encoded in very simple symmetric (quantum metric) and antisymmetric (Berry curvature) products of Bloch vectors. From a practical point of view, we shall see that Eq. (3.10) provides a very convenient means to explicitly compute the QGT for any given N -band Hamiltonian. This only requires to express the Bloch vectors in terms of \mathbf{h} , see Section 3.4.

Orbital magnetization

Next, consider the orbital magnetization. An expression in terms of Bloch vectors can be easily derived from the formula (1.48) that is already explicitly written in terms of geometric quantities. Since we already know the Berry curvature in terms of Bloch vectors, we simply have to find a Bloch vector expression for the orbital magnetic

moment. Inserting the Hamiltonian's spectral decomposition into Eq. (3.8) we arrive at the intermediate result

$$m_{\alpha,ij}(\mathbf{x}) = -e \operatorname{Im} \operatorname{Tr} [P_{\alpha}^i (\varepsilon_{\alpha} 1_N - H) P_{\alpha}^j] \quad (3.11)$$

for the orbital magnetic moment in terms of eigenprojectors. Substituting the eigenprojectors (2.50) leads to the desired result

$$m_{\alpha,ij}(\mathbf{x}) = -\frac{e}{2} \mathbf{h} \cdot (\mathbf{b}_{\alpha}^i \times \mathbf{b}_{\alpha}^j) \quad (3.12)$$

in terms of Bloch vectors. Note the close formal similarity to the Berry curvature (3.10). In particular, for $N = 2$, one has $\mathbf{h} = \varepsilon_{\alpha} \mathbf{b}_{\alpha}$ for both $\alpha = \pm$, such that the orbital magnetic moment is proportional to the Berry curvature, $m_{\alpha,ij} = e \varepsilon_{\alpha} \Omega_{\alpha,ij}$, as is well known. In contrast, for $N > 2$, Eq. (3.12) indicates that this proportionality is not in general maintained.

In summary, substituting Berry curvature and orbital magnetic moment into Eq. (1.48), one may write the full orbital magnetization for a 2D system with an arbitrary number N of bands in Bloch vector form as

$$M = \int_{\alpha} (f(\varepsilon_{\alpha}) \mathbf{h} + g(\varepsilon_{\alpha}) \mathbf{b}_{\alpha}) \cdot (\mathbf{b}_{\alpha}^x \times \mathbf{b}_{\alpha}^y), \quad (3.13)$$

where we use shorthand notations

$$\int_{\alpha} \equiv -\frac{e}{2} \int_{\text{BZ}} \frac{d^2 k}{(2\pi)^2} \sum_{\alpha}, \quad g(\varepsilon_{\alpha}) \equiv k_B T \ln \left(1 + e^{-\frac{\varepsilon_{\alpha} - \mu}{k_B T}} \right). \quad (3.14)$$

The expression (3.13), which can be viewed as an integral over a kind of ‘‘skyrmion density’’, neatly illustrates the geometrical origin of the orbital magnetization. It is also very useful in practice, since the Bloch vectors can be related in a unique way to the Hamiltonian vector (Section 3.4).

Orbital magnetic susceptibility

Physical quantities more complicated than the simple ones considered above are often formulated in terms of kernels such as

$$K_{ijk} = \operatorname{Tr} (GH^i GH^j GH^k), \quad K_{ijkl} = \operatorname{Tr} (GH^i GH^j GH^k GH^l), \quad (3.15)$$

see for example Chen and Lee (2011) or Raoux et al. (2015). More generally, the relevant kernels involve any combination of the Hamiltonian H , the corresponding Green's function G , and their parametric derivatives $H^i = \partial_i H$ and $G^i = \partial_i G$. For all such quantities, one can insert the Green's function (1.46) and aim for a maximally compact formula in terms of Bloch vectors, much in the same way as we have done to obtain the QGT (3.10) and the orbital magnetic moment (3.12). A general recipe for this is provided in Appendix III.A.

A quantity of immediate interest in this context is the orbital magnetic susceptibility (1.51). An expression of it in terms of Bloch vectors – and hence in terms of

geometrical quantities such as Berry curvature, quantum metric and orbital magnetic moment – is unknown, except for the two-band case (Raoux et al. 2015; Piéchon et al. 2016). Although we do not carry this out here, it is clear that a general Bloch vector expression for any N can be obtained by applying the general procedure of Appendix III.A to the relevant kernel $K_S = \text{Tr}(\mathcal{X}) = K_S^{(1)} - 4K_S^{(2)}$, where

$$\begin{aligned} K_S^{(1)} &\equiv \mathcal{K}_{xxyy} - \mathcal{K}_{xyxy}, & \mathcal{K}_{ijkl} &= \text{Tr}\left(GH^{ij}GH^{kl}\right), \\ K_S^{(2)} &\equiv K_{xxyy} - K_{xyxy}, & K_{ijkl} &= \text{Tr}\left(GH^iGH^jGH^kGH^l\right). \end{aligned} \quad (3.16)$$

This should enable one to clearly separate intraband from interband contributions to the orbital susceptibility, which allows in particular to compare the importance of geometric contributions and the (intraband) Landau-Peierls contribution.

3.3.3 | General observables

We now point out that it is in fact easy to see that a Bloch vector expression must exist for any observable quantity of interest. Let us assume we are interested in some quantity χ constructed from matrix elements of a certain set of operators in the eigenbasis of H :

$$\chi = f(O_{\alpha\beta}, O'_{\alpha\beta}, \dots). \quad (3.17)$$

Here an important constraint has to be respected: $O_{\alpha\beta}$ is not gauge-invariant, thus for χ to be observable it can only depend on diagonal matrix elements $O_{\alpha\alpha}$, as well as higher-order gauge-invariant products such as $O_{\alpha\beta}O'_{\beta\alpha}$, $O_{\alpha\beta}O'_{\beta\gamma}O''_{\gamma\alpha}$, and so on [Pozo and Juan (2020) provide a similar reasoning in terms of what they call *R-generators*]. It is thus more precise to write Eq. (3.17) as

$$\chi = f(O_{\alpha\alpha}, O_{\alpha\beta}O'_{\beta\alpha}, \dots). \quad (3.18)$$

It is now easy to realize that all gauge-invariant combinations of matrix elements of O are functions of the Bloch vectors. Indeed, by definition of an expectation value we have $O_{\alpha\alpha} = \text{Tr}(P_\alpha O)$ as well as $O_{\alpha\beta}O'_{\beta\alpha} = \text{Tr}(P_\alpha O P_\beta O')$, and so on. Note that these are exactly the kinds of traces mentioned above in Eq. (3.6). By substituting Eq. (2.50) for the eigenprojectors and Eq. (3.4) for the (traceless) operators, we arrive at the desired expression

$$\chi = f(\mathbf{o}, \mathbf{o}', \dots; \mathbf{b}_\alpha, \mathbf{b}_\beta, \dots), \quad (3.19)$$

which states that any observable quantity can be written in terms of Bloch vectors. As we have mentioned, the interest of such an expression is twofold. First, it allows to decompose χ into intraband and interband contributions; second, once the Bloch vectors are related to the Hamiltonian (Section 3.4), it can be used for explicit computations without worrying about the annoying features of energy eigenstates.

The explicit expressions of $O_{\alpha\alpha}$, $O_{\alpha\beta}O'_{\beta\alpha}$ and so on in terms of Bloch vectors are established by using Eq. (2.50) and simplifying the trace using the identity (2.32). First, it is trivial to find

$$O_{\alpha\alpha} = \text{Tr}(P_\alpha O) = \mathbf{b}_\alpha \cdot \mathbf{o}. \quad (3.20)$$

Next, we obtain

$$O_{\alpha\beta}O'_{\beta\alpha} = \text{Tr}(P_\alpha O P_\beta O') = (\mathcal{R}_{\alpha\beta} + \mathcal{R}_{\beta\alpha}) + i(\mathcal{I}_{\alpha\beta} - \mathcal{I}_{\beta\alpha}), \quad (3.21)$$

where

$$\begin{aligned} \mathcal{R}_{\alpha\beta} &= \frac{1}{N} \left(\frac{2}{N} - \delta_{\alpha\beta} \right) (\mathbf{o} \cdot \mathbf{o}') + \frac{1}{N} (\mathbf{b}_\alpha \cdot \mathbf{o})(\mathbf{b}_\beta \cdot \mathbf{o}') \\ &\quad + \frac{1}{2} (\mathbf{b}_\alpha \star \mathbf{o}) \cdot (\mathbf{b}_\beta \star \mathbf{o}') + \left(\frac{2}{N} - \frac{1}{2} \delta_{\alpha\beta} \right) \mathbf{b}_\alpha \cdot (\mathbf{o} \star \mathbf{o}'), \\ \mathcal{I}_{\alpha\beta} &= \frac{1}{N} \mathbf{b}_\alpha \cdot (\mathbf{o} \times \mathbf{o}') + \frac{1}{4} [(\mathbf{b}_\alpha \star \mathbf{o}) \cdot (\mathbf{b}_\beta \times \mathbf{o}') + (\mathbf{b}_\alpha \times \mathbf{o}) \cdot (\mathbf{b}_\beta \star \mathbf{o}')]. \end{aligned} \quad (3.22)$$

Establishing this expression requires a bit of algebra using the $\text{SU}(N)$ Jacobi identities that we provide in Appendix III.B. In the same way, one can proceed to obtain higher-order gauge-invariant combinations of matrix elements of the operators of interest, which will be increasingly complicated functions of the Bloch vectors.

To close this section, it should be noted that by applying Eq. (3.21) to the QGT (3.7), such that $\mathbf{o} = \mathbf{h}^i$ and $\mathbf{o}' = \mathbf{h}^j$, one finds an expression for the QGT in terms of Bloch vectors which is different from Eq. (3.10). This formula is provided in Appendix III.C, and its advantage consists in the absence of parametric derivatives of the Bloch vectors. A similar formula for the orbital magnetization could be derived by applying Eq. (3.21) to the expression (3.8).

3.4 | Eigenprojectors and Bloch vectors from the Hamiltonian

The Bloch vector expressions obtained above are conceptually interesting, but to make them useful in practice we need to connect the eigenprojectors P_α and Bloch vectors \mathbf{b}_α to the Hamiltonian. More precisely, the goal is to obtain a generalization of Eq. (2.46) to arbitrary N .

3.4.1 | Eigenprojectors as a function of the Hamiltonian matrix

The Cayley-Hamilton theorem (Cayley 1858; Horn and Johnson 2013) states that any square matrix satisfies its own characteristic equation. In particular, this holds for the $N \times N$ Hamiltonian matrix H . For example, for $N = 2$ the characteristic equation is

$$\epsilon^2 - (\epsilon_+ + \epsilon_-)\epsilon + \epsilon_+\epsilon_- = 0, \quad (3.23)$$

and thus the Hamiltonian satisfies the matrix identity

$$H^2 - (\epsilon_+ + \epsilon_-)H + \epsilon_+\epsilon_-1_2 = 0 \quad (3.24)$$

according to the Cayley-Hamilton theorem. This is an extremely powerful statement, because it means that H^2 and all higher powers can be written as linear functions of H . More generally, it is clear from the Cayley-Hamilton theorem that any analytic

k	0	1	2	3	4	5
c_k	1	0	$-C_2/2$	$-C_3/3$	$C_2^2/8 - C_4/4$	$C_2C_3/6 - C_5/5$

Table 3.2 – Coefficients c_k determining the polynomial $q_n(z)$.

function of the Hamiltonian, which is a priori an infinite-order polynomial $f(H) = \sum_{n=0}^{\infty} a_n H^n$, can be rewritten as a polynomial of degree $N - 1$ in H :

$$f(H) = \sum_{n=0}^{N-1} \tilde{a}_n H^n. \quad (3.25)$$

The main idea here is to apply this principle to the eigenprojector. As demonstrated in detail in Appendix III.D, each eigenprojector can indeed be written in the form

$$P_\alpha = \frac{\sum_{n=0}^{N-1} q_{N-1-n}(\varepsilon_\alpha) H^n}{\sum_{n=0}^{N-1} q_{N-1-n}(\varepsilon_\alpha) \varepsilon_\alpha^n} = \frac{\sum_{n=0}^{N-1} q_{N-1-n}(\varepsilon_\alpha) H^n}{\sum_{n=0}^{N-1} q_{N-1-n}(\varepsilon_\alpha) C_n}, \quad (3.26)$$

where the polynomials

$$q_n(z) \equiv \sum_{k=0}^n c_k z^{n-k} \quad (3.27)$$

are closely related to the Hamiltonian's characteristic polynomial and the coefficients c_k are determined by exponential Bell polynomials (Bell 1934; Comtet 1974). For our purposes here, it suffices to list these coefficients for $k \leq 5$, see Table 3.2. We have also introduced (*classical*) *Casimir invariants* (Kusnezov 1995)

$$C_n \equiv \text{Tr}(H^n) = \sum_{\alpha=1}^N \varepsilon_\alpha^n. \quad (3.28)$$

The utility of Eq. (3.26) becomes apparent if we write down the explicit eigenprojectors for $N = 2$ to $N = 5$, respectively:

$$\begin{aligned} P_\alpha &= \frac{1}{2\varepsilon_\alpha} (\varepsilon_\alpha 1_2 + H), \\ P_\alpha &= \frac{1}{3\varepsilon_\alpha^2 - \frac{C_2}{2}} \left[\left(\varepsilon_\alpha^2 - \frac{C_2}{2} \right) 1_3 + \varepsilon_\alpha H + H^2 \right], \\ P_\alpha &= \frac{1}{4\varepsilon_\alpha^3 - C_2\varepsilon_\alpha - \frac{C_3}{3}} \\ &\quad \times \left[\left(\varepsilon_\alpha^3 - \frac{C_2}{2}\varepsilon_\alpha - \frac{C_3}{3} \right) 1_4 + \left(\varepsilon_\alpha^2 - \frac{C_2}{2} \right) H + \varepsilon_\alpha H^2 + H^3 \right], \\ P_\alpha &= \frac{1}{5\varepsilon_\alpha^4 - \frac{3C_2}{2}\varepsilon_\alpha^2 - \frac{2C_3}{3}\varepsilon_\alpha + \frac{C_2^2 - 2C_4}{8}} \\ &\quad \times \left[\left(\varepsilon_\alpha^4 - \frac{C_2}{2}\varepsilon_\alpha^2 - \frac{C_3}{3}\varepsilon_\alpha + \frac{C_2^2 - 2C_4}{8} \right) 1_5 \right. \\ &\quad \left. + \left(\varepsilon_\alpha^3 - \frac{C_2}{2}\varepsilon_\alpha - \frac{C_3}{3} \right) H + \left(\varepsilon_\alpha^2 - \frac{C_2}{2} \right) H^2 + \varepsilon_\alpha H^3 + H^4 \right]. \end{aligned} \quad (3.29)$$

This represents the N -band generalization of the two-band projectors (2.46). Given the Hamiltonian, the only ingredient required for explicitly computing the eigenprojector P_α is the corresponding eigenenergy ε_α . Note that, in this context, one can make a certain distinction between $N < 5$ and $N \geq 5$. In the former case, it is in principle always possible to find the eigenvalues, since closed-form solutions for the characteristic polynomial exist, see Appendix III.E. In the latter case ($N \geq 5$), there are no closed-form solutions in general, but Eq. (3.26) loses none of its convenience as long as the eigenvalues ε_α are known.

Beyond the computation of eigenprojectors, Eq. (3.26) has two interesting applications. First, we can explicitly write down the coefficients of the polynomial expansion (3.25) of any function $f(H)$, yielding an alternative version of *Sylvester's formula* (Horn and Johnson 2013):

$$\tilde{a}_n = \sum_{\alpha=1}^N f(\varepsilon_\alpha) \frac{q_{N-1-n}(\varepsilon_\alpha)}{\sum_{n=0}^{N-1} q_{N-1-n}(\varepsilon_\alpha) \varepsilon_\alpha^n}. \quad (3.30)$$

Second, the eigenprojector is in some sense a more fundamental object than the eigenstate, namely Eq. (3.26) may be employed for constructing energy eigenstates as

$$|\psi_\alpha\rangle = \frac{1}{\sqrt{\langle \psi_g | P_\alpha | \psi_g \rangle}} P_\alpha |\psi_g\rangle, \quad (3.31)$$

by projecting onto a *gauge freedom state* $|\psi_g\rangle$ that can be chosen arbitrarily (for more details, see Appendix III.F). The eigenstates (3.31) can then be used further as desired.

3.4.2 | Bloch vectors as a function of the Hamiltonian vector

The above key results (3.26) and (3.29) on the eigenprojectors can equivalently be formulated in the language of Bloch vectors. In particular, by inserting Eqs. (2.24) and (2.50) into Eq. (3.26), one obtains the analog of the function $P_\alpha(\varepsilon_\alpha, H)$ in the vectorial language, namely $\mathbf{b}_\alpha(\varepsilon_\alpha, \mathbf{h})$, as demonstrated in detail in Appendix III.G. The usefulness of this procedure is most apparent when considering the explicit Bloch vector expressions resulting from it, provided here for $N = 2$ to $N = 5$:

$$\begin{aligned} \mathbf{b}_\alpha &= \frac{1}{\varepsilon_\alpha} \mathbf{h}, \\ \mathbf{b}_\alpha &= \frac{2}{3\varepsilon_\alpha^2 - \frac{C_2}{2}} (\varepsilon_\alpha \mathbf{h} + \mathbf{h}_\star), \\ \mathbf{b}_\alpha &= \frac{2}{4\varepsilon_\alpha^3 - C_2\varepsilon_\alpha - \frac{C_3}{3}} \left[\left(\varepsilon_\alpha^2 - \frac{C_2}{4} \right) \mathbf{h} + \varepsilon_\alpha \mathbf{h}_\star + \mathbf{h}_{\star\star} \right], \\ \mathbf{b}_\alpha &= \frac{2}{5\varepsilon_\alpha^4 - \frac{3C_2}{2}\varepsilon_\alpha^2 - \frac{2C_3}{3}\varepsilon_\alpha + \frac{C_2^2 - 2C_4}{8}} \\ &\quad \times \left[\left(\varepsilon_\alpha^3 - \frac{3C_2}{10}\varepsilon_\alpha - \frac{2C_3}{15} \right) \mathbf{h} + \left(\varepsilon_\alpha^2 - \frac{3C_2}{10} \right) \mathbf{h}_\star + \varepsilon_\alpha \mathbf{h}_{\star\star} + \mathbf{h}_{\star\star\star} \right]. \end{aligned} \quad (3.32)$$

This is the N -band generalization of the two-band Bloch vectors (2.46), and contains exactly the same information as Eq. (3.29).

The peculiar vectors \mathbf{h}_* , \mathbf{h}_{**} , et cetera appearing here are star products of the Hamiltonian vector with itself, where we use the notation introduced in Eq. (2.33). Such vectors appear because, for given N , each Bloch vector (3.32) is a kind of “vector polynomial” in \mathbf{h} , just like each eigenprojector is a matrix polynomial in H . Note also that, since the Casimir invariants are traces of powers of the Hamiltonian matrix, cf. Eq. (3.28), they can be directly expressed as

$$C_2 = 2|\mathbf{h}|^2, \quad C_3 = 2\mathbf{h} \cdot \mathbf{h}_*, \quad C_4 = \frac{4}{N}|\mathbf{h}|^4 + 2|\mathbf{h}_*|^2 \quad (3.33)$$

in terms of the Hamiltonian vector.

3.4.3 | Observables in terms of the Hamiltonian

As we have seen, the Bloch vectors are uniquely determined in terms of the Hamiltonian and its eigenvalues. Using this result, all physical quantities (3.19) expressed in terms of Bloch vectors can be explicitly evaluated for any given Hamiltonian without resorting to eigenstates. This is illustrated here for the QGT and the orbital magnetization.

Quantum geometric tensor

Consider the general expression (3.10) valid for arbitrary values of N , where we now substitute the explicit formula (3.32) for the Bloch vector. Let us first focus on the Berry curvature, for which we obtain a closed-form expression for arbitrary N (see Appendix III.H for a detailed discussion). We illustrate it here for $N = 3, 4, 5$, for comparison with the simple $N = 2$ expression (2.41). We find that, in the $N = 3$ case, the Berry curvature tensor is given by

$$\begin{aligned} \Omega_{\alpha,ij} &= -\frac{4}{(3\varepsilon_\alpha^2 - |\mathbf{h}|^2)^3} \boldsymbol{\nu}_\alpha \cdot \left(\boldsymbol{\nu}_\alpha^{(i)} \times \boldsymbol{\nu}_\alpha^{(j)} \right), \\ \boldsymbol{\nu}_\alpha &= \varepsilon_\alpha \mathbf{h} + \mathbf{h}_*, \\ \boldsymbol{\nu}_\alpha^{(i)} &= \varepsilon_\alpha \mathbf{h}^i + \mathbf{h}_*^i, \end{aligned} \quad (3.34)$$

where again $\mathbf{m}^i \equiv \partial_i \mathbf{m}$ for any vector \mathbf{m} . Note that if one inserts the particular energy parametrization (III.28), one recovers the $\text{SU}(3)$ Berry curvature formula found by Barnett et al. (2012). Similarly, for arbitrary $N = 4$ systems, we have

$$\begin{aligned} \Omega_{\alpha,ij} &= -\frac{4}{(4\varepsilon_\alpha q_\alpha - \frac{2}{3}\mathbf{h} \cdot \mathbf{h}_*)^3} \boldsymbol{\nu}_\alpha \cdot \left(\boldsymbol{\nu}_\alpha^{(i)} \times \boldsymbol{\nu}_\alpha^{(j)} \right), \\ \boldsymbol{\nu}_\alpha &= q_\alpha \mathbf{h} + \varepsilon_\alpha \mathbf{h}_* + \mathbf{h}_{**}, \\ \boldsymbol{\nu}_\alpha^{(i)} &= q_\alpha \mathbf{h}^i + \varepsilon_\alpha \mathbf{h}_*^i + \mathbf{h}_{**}^i, \end{aligned} \quad (3.35)$$

with $q_\alpha \equiv \varepsilon_\alpha^2 - \frac{1}{2}|\mathbf{h}|^2$. For arbitrary $N = 5$ systems, the Berry curvature is given by

$$\begin{aligned}\Omega_{\alpha,ij} &= -\frac{4}{(5\varepsilon_\alpha r_\alpha + \frac{3}{10}|\mathbf{h}|^4 - \frac{1}{2}|\mathbf{h}_\star|^2)^3} \boldsymbol{\nu}_\alpha \cdot \left(\boldsymbol{\nu}_\alpha^{(i)} \times \boldsymbol{\nu}_\alpha^{(j)} \right), \\ \boldsymbol{\nu}_\alpha &= r_\alpha \mathbf{h} + \tilde{q}_\alpha \mathbf{h}_\star + \varepsilon_\alpha \mathbf{h}_{\star\star} + \mathbf{h}_{\star\star\star}, \\ \boldsymbol{\nu}_\alpha^{(i)} &= r_\alpha \mathbf{h}^i + \tilde{q}_\alpha \mathbf{h}_\star^i + \varepsilon_\alpha \mathbf{h}_{\star\star}^i + \mathbf{h}_{\star\star\star}^i,\end{aligned}\tag{3.36}$$

where $r_\alpha \equiv \varepsilon_\alpha \tilde{q}_\alpha - \frac{4}{15} \mathbf{h} \cdot \mathbf{h}_\star$ and $\tilde{q}_\alpha \equiv \varepsilon_\alpha^2 - \frac{3}{5}|\mathbf{h}|^2$. In the same way, one may obtain expressions for $N > 5$.

For the quantum metric, writing down explicit formulas in terms of \mathbf{h} and ε_α proves problematic for $N > 2$, since cumbersome formulas follow from the chain rule when differentiating the Bloch vectors (3.32). For the Berry curvature above, this issue is circumvented by appropriate orthogonality relations (see Appendix III.H). Nevertheless, there are two simple ways to compute the quantum metric without using eigenstates. One can use either the formula provided in Appendix III.C, or, for any given Hamiltonian, one can simply calculate the Bloch vectors (3.32) explicitly, and then substitute the result into Eq. (3.10).

Orbital magnetization

We now conduct the same procedure for the orbital magnetization, by inserting Eq. (3.32) into Eq. (3.13). For the simplest case, $N = 2$, it follows

$$M = \int_\alpha \left(\frac{f(\varepsilon_\alpha)}{\varepsilon_\alpha^2} + \frac{g(\varepsilon_\alpha)}{\varepsilon_\alpha^3} \right) \mathbf{h} \cdot (\mathbf{h}^x \times \mathbf{h}^y).\tag{3.37}$$

For $N = 3$, it follows

$$M = \int_\alpha \left[\frac{4f(\varepsilon_\alpha)}{(3\varepsilon_\alpha^2 - |\mathbf{h}|^2)^2} \mathbf{h} + \frac{8g(\varepsilon_\alpha)}{(3\varepsilon_\alpha^2 - |\mathbf{h}|^2)^3} \boldsymbol{\nu}_\alpha \right] \cdot \left(\boldsymbol{\nu}_\alpha^{(x)} \times \boldsymbol{\nu}_\alpha^{(y)} \right),\tag{3.38}$$

where $\boldsymbol{\nu}_\alpha$ and $\boldsymbol{\nu}_\alpha^{(i)}$ are the same as in Eq. (3.34). Similar results are obtained for any desired N , allowing to compute the orbital magnetization without the need for energy eigenstates.

3.5 | Example: Pseudospin- s fermions

In this last section, we present a simple pedagogical example of how the formalism developed above, especially with regard to computing quantum metric and Berry curvature from Bloch vectors, can be applied to concrete Hamiltonians of interest. For simplicity, we consider continuum models (2.6) of pseudospin- s type, with $\gamma = 1$. Later, in Chapter 5, we will frequently make use of Eq. (3.10) to compute the quantum geometric structure of multiband systems beyond the pseudospin scenario.

Pseudospin-1 fermions. The spin Hamiltonian (2.6) can be easily rewritten in the general form of Eq. (2.24) by using the relation between spin matrices and Gell-Mann matrices (Appendix II.A). Thus, for $s = 1$, the Hamiltonian vector reads

$$\mathbf{h}(\mathbf{q}) = \frac{1}{2}(\sqrt{2}q_x, \sqrt{2}q_y, q_z, 0, 0, \sqrt{2}q_x, \sqrt{2}q_y, \sqrt{3}q_z).$$

Upon using the spectrum (2.7) with band velocity $c_\alpha = m_s$ and $C_2 = 2|\mathbf{q}|^2$, the eigenprojectors for a pseudospin-1 fermion are obtained from Eq. (3.29) as

$$P_\alpha(\mathbf{q}) = \frac{1}{3c_\alpha^2 - 1} \left[(c_\alpha^2 - 1)1_3 + \frac{c_\alpha}{|\mathbf{q}|}(\mathbf{h} \cdot \boldsymbol{\lambda}) + \frac{1}{|\mathbf{q}|^2}(\mathbf{h} \cdot \boldsymbol{\lambda})^2 \right].$$

It is readily verified that all expected properties of eigenprojectors are satisfied. Similarly, the Bloch vectors follow from Eq. (3.32) as

$$\mathbf{b}_\alpha(\mathbf{q}) = \frac{2}{3c_\alpha^2 - 1} \left(c_\alpha \frac{\mathbf{h}}{|\mathbf{q}|} + \frac{\mathbf{h}_\star}{|\mathbf{q}|^2} \right),$$

where

$$\mathbf{h}_\star(\mathbf{q}) = \left(\frac{q_x q_z}{\sqrt{2}}, \frac{q_y q_z}{\sqrt{2}}, \frac{3q_z^2 - |\mathbf{q}|^2}{4}, \frac{q_x^2 - q_y^2}{2}, q_x q_y, -\frac{q_x q_z}{\sqrt{2}}, -\frac{q_y q_z}{\sqrt{2}}, \frac{|\mathbf{q}|^2 - 3q_z^2}{4\sqrt{3}} \right).$$

The Berry curvature may now be obtained from Eq. (3.10) [or from Eq. (3.34)], and one recovers Eq. (2.8) as expected. Similarly, the quantum metric follows from Eq. (3.10) [or from Eq. (III.15)] as

$$g_{\alpha,ij}(\mathbf{q}) = \frac{2 - c_\alpha^2}{2|\mathbf{q}|^2} \left(\delta_{ij} - \frac{q_i q_j}{|\mathbf{q}|^2} \right),$$

in agreement with the results of Lin and Hsiao (2021).

Pseudospin-3/2 fermions. Exploiting the relation between spin matrices and Gell-Mann matrices (Appendix II.A), the Hamiltonian vector for $s = 3/2$ reads

$$\mathbf{h}(\mathbf{q}) = \frac{1}{2}(\sqrt{3}q_x, \sqrt{3}q_y, q_z, 0, 0, 2q_x, 2q_y, \sqrt{3}q_z, 0, 0, 0, 0, \sqrt{3}q_x, \sqrt{3}q_y, \sqrt{6}q_z).$$

The star product vectors \mathbf{h}_\star and $\mathbf{h}_{\star\star}$ can then be computed from Eq. (2.33). Using the spectrum (2.7) as well as $C_2 = 5|\mathbf{q}|^2$ and $C_3 = 0$, the eigenprojectors for a spin-3/2 fermion are obtained as

$$P_\alpha(\mathbf{q}) = \frac{1}{4c_\alpha(c_\alpha^2 - \frac{5}{4})} \times \left[c_\alpha \left(c_\alpha^2 - \frac{5}{2} \right) 1_4 + \frac{c_\alpha^2 - \frac{5}{2}}{|\mathbf{q}|}(\mathbf{h} \cdot \boldsymbol{\lambda}) + \frac{c_\alpha}{|\mathbf{q}|^2}(\mathbf{h} \cdot \boldsymbol{\lambda})^2 + \frac{1}{|\mathbf{q}|^3}(\mathbf{h} \cdot \boldsymbol{\lambda})^3 \right].$$

Similarly, the Bloch vectors are given by

$$\mathbf{b}_\alpha(\mathbf{q}) = \frac{1}{2c_\alpha(c_\alpha^2 - \frac{5}{4})} \left[\left(c_\alpha^2 - \frac{5}{4} \right) \frac{\mathbf{h}}{|\mathbf{q}|} + c_\alpha \frac{\mathbf{h}_\star}{|\mathbf{q}|^2} + \frac{\mathbf{h}_{\star\star}}{|\mathbf{q}|^3} \right].$$

Note that the coefficient of the linear term (in H) of the eigenprojector is in general not the same as the coefficient of the linear term (in \mathbf{h}) of the Bloch vector, and similarly for the higher-order terms. This is due to the fact that $H^{n+1} \neq \mathbf{h}_\star^{(n)} \cdot \boldsymbol{\lambda}$ for

$n \geq 0$. The Berry curvature follows from Eq. (3.10) [or from Eq. (3.35)], and again takes the expected form (2.8). The quantum metric reads

$$g_{\alpha,ij}(\mathbf{q}) = \frac{15/4 - c_{\alpha}^2}{2|\mathbf{q}|^2} \left(\delta_{ij} - \frac{q_i q_j}{|\mathbf{q}|^2} \right),$$

again in agreement with Lin and Hsiao (2021). Indeed, we can write the general quantum metric for an arbitrary pseudospin- s as

$$g_{\alpha,ij}(\mathbf{q}) = \frac{\omega_{\alpha}}{4|\mathbf{q}|^2} \left(\delta_{ij} - \frac{q_i q_j}{|\mathbf{q}|^2} \right), \quad (3.39)$$

where ω_{α} is the coefficient of the orbital magnetic moment given in Eq. (2.9).

3.6 | Conclusions

For a quantum system described by a parametric Hamiltonian matrix (2.24), observables are conventionally constructed from matrix elements $O_{\alpha\beta}$ that require explicit knowledge of energy eigenstates. Here we have argued that it can prove rewarding to get rid of the eigenstates and aim for a reformulation (3.19) in terms of Bloch vectors. Such a Bloch vector approach is motivated by the fact that Bloch vectors (like the corresponding eigenprojectors) offer several advantages over eigenstates, namely they are gauge-invariant, non-singular and possess a unique parametrization, see Table 3.1. A Bloch vector formulation can be done for any observable, and the present chapter illustrated how it works using simple examples such as the quantum geometric tensor and orbital magnetization, see in particular Eqs. (3.10) and (3.13).

At a conceptual level, the Bloch vector form (3.19) of a given quantity makes explicit the intraband or interband character of individual contributions, since Bloch vectors are identically zero in a single-band system (or in a multiband system with trivially decoupled bands). Moreover, one can draw the interesting conclusion that any observable can (at least in principle) be computed using only the Hamiltonian vector and the energy eigenvalues, in agreement with recent results of Pozo and Juan (2020). This becomes evident when combining Eqs. (3.19) and (3.32). The resulting expressions $\chi = f(\varepsilon_{\alpha}, \mathbf{h})$ are extremely convenient for explicit computation of Berry curvature and orbital magnetic moment, and indeed in the following Chapters 4 and 5 we will frequently make use of this fact. In particular, we emphasize that we have generalized the well-known Berry curvature expression (2.41) to arbitrary N , see Section 3.4.3. It is desirable to extend the ideas exposed here to quantities more complicated than the QGT and orbital magnetization, and to obtain Bloch vector based expressions e.g. for magnetoconductivities [beyond the Boltzmann result (1.57)] or the orbital magnetic susceptibility.

To close this chapter, we note that the validity of the formalism developed here goes beyond the case of Hermitian Hamiltonian matrices. In particular, the key expressions Eq. (3.29) for the eigenprojector and Eq. (3.32) for the Bloch vector stay valid for systems where the Hermiticity condition is relaxed (Bender 2007; Brody 2013).

Chapter 4

Designing flat-band models with multifold band crossings

4.1 | Introduction

In Chapter 2 we have pointed out the interest of flat bands as a basis for creating strongly correlated quantum phases. Additionally, we have emphasized the interest of (pseudospin- s) multifold band crossings in 3D, which lie at the heart of topological semimetals. Interestingly, as we have seen, both the paradigmatic flat-band models (such as the Lieb or dice lattice) and the pseudospin- s systems frequently exhibit a band crossing and a flat band simultaneously.

Motivated by this curious fact, in the present chapter we develop a systematic method to design tight-binding models that exhibit *both* a flat band and one or several multifold band touching points¹ residing at the flat-band energy. The flat-band systems obtained in this way are expected to exhibit very interesting quantum geometric properties, as we will indeed confirm later on.

The procedure is based on the notion of a compact localized state (CLS) (Aoki et al. 1996) – that is, a wave function strictly localized to some finite region of the lattice – and has several very convenient features. First, it allows to obtain (in principle infinitely many) novel flat-band tight-binding models *on any periodic lattice*, thus vastly extending the family of known flat-band systems. Second, the method offers extensive control over the number, location, degeneracy, and low-energy dispersion of multifold band touching points. Moreover, it is intuitive, fully analytic, and provides short-range hopping models that do not require any fine-tuning. Finally, the method can be viewed as a new classification scheme for flat-band networks, providing a common framework for known models (Mielke, Tasaki, Lieb, dice, breathing Kagome, and so on) and the additional models introduced here.

Previously, many different schemes to generate flat-band models have been developed, but they mostly do not pay special attention to band crossings. For example, Miyahara et al. (2005), Röntgen et al. (2018), or Morfonios et al. (2021) recently suggested flat-band construction procedures based on graph theory, an approach that has a long history (Mielke 1991a; Mielke 1991b). Various other approaches include Origami rules (Dias and Gouveia 2015), repeated miniarrays (Morales-Inostroza and Vicencio 2016), or generic existence conditions (Toikka and Andreanov 2018). An im-

¹Note that we employ the terms *band crossing* and *band touching* synonymously whenever the nature of the low-energy dispersion is not specified. However, when the low-energy dispersion is linear (quadratic), we usually employ the term band crossing (band touching).

portant class of flat bands is obtained in the presence of a bipartite lattice structure (Ramachandran et al. 2017; Călugăru et al. 2021), and also the direct extension of known flat-band lattices may lead to new flat-band models, see for example Mizoguchi and Hatsugai (2019), Lee et al. (2019), or Ogata et al. (2021).

Moreover, over the last years, the close relation between flat bands and CLSs, which we will equally make use of, has been increasingly exploited. For example, Nishino et al. (2003) and Nishino and Goda (2005) have discussed CLSs for tight-binding models on hexagonal, cubic or diamond lattices. Flach et al. (2014) have proposed to classify flat bands by the number of unit cells occupied by the corresponding CLS, which is also the strategy used by a series of follow-up articles (Maimaiti et al. 2017; Maimaiti et al. 2019; Maimaiti et al. 2021). Additionally, Sathe et al. (2021) have analyzed general conditions necessary to construct CLSs.

Apart from an early article by Bergman et al. (2008), work on flat-band systems that also focuses more specifically on the role of band crossings has emerged only quite recently, see for example Rhim and Yang (2019) or Mizoguchi and Hatsugai (2019). In particular, Rhim and Yang (2019) introduced a flat-band classification scheme based on singularity properties of the flat-band eigenstate at band crossing points. An extension of these ideas has led the same authors to propose a flat-band construction scheme starting from CLSs (Hwang et al. 2021), which is similar to the method described in this chapter.

We begin this chapter by reminding some known facts about flat-band systems (Section 4.2), in particular the important notion of a CLS. In Section 4.3, we turn to the description of our flat-band construction method, where the exposition is mostly based on Graf and Piéchon (2021b). We describe how flat-band Hamiltonians can be engineered from any given CLS, and this idea is developed in detail in Sections 4.4 and 4.5. After some further remarks regarding our flat-band design principle (Section 4.6) we highlight some interesting perspectives opened by our results (Section 4.7). This includes, in particular, the quantum geometry of the multifold touching points, which will naturally guide us to the concept of a Berry dipole, essential for Chapter 5. We further briefly address magnetic flat bands and multiple flat bands, all of which appear as promising topics for future work. Conclusions are given in Section 4.8.

4.2 | Basics of flat-band physics

4.2.1 | Compact localized states and associated Bloch states

Definition of a compact localized state

Consider a periodic lattice treated in the tight-binding approximation, with N (atomic) orbitals per unit cell, that is, with N sublattices labeled by $a = A, B, C, \dots$. On such a lattice, a *compact localized state* (CLS) centered at some localization center \mathbf{R}_C can be formed as a linear combination

$$|\Psi_{\text{CLS}}^{\mathbf{R}_C}\rangle = \sum_{a_i \in \text{CLS}} w_{a_i} |a_i\rangle \quad (4.1)$$

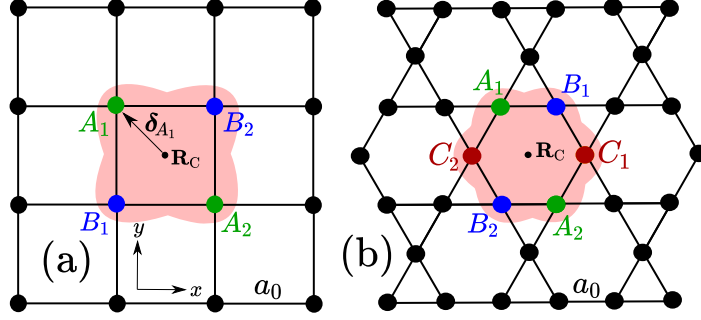


Fig. 4.1 – Example for a CLS (a) on a square lattice ($N = 2$) and (b) on a Kagome lattice ($N = 3$). The orbitals included in the CLS are colored and labeled. The CLS wave function is represented by the light red region.

of orbitals $|a_i\rangle$, where the complex number w_{a_i} – the *CLS amplitude* on the respective orbital – takes a non-zero value only for a finite number of lattice sites around \mathbf{R}_C . The subindex i takes account of the fact that more than one orbital of a given type a will in general appear in the CLS (orbitals a_i and $a_{j \neq i}$ are in different unit cells). Since only a finite number of orbitals contributes to the CLS, the CLS wave function

$$\Psi_{\text{CLS}}^{\mathbf{R}_C}(\mathbf{r}) \propto \langle \mathbf{r} | \Psi_{\text{CLS}}^{\mathbf{R}_C} \rangle \quad (4.2)$$

is restricted to a finite region of the lattice, with strictly zero probability amplitude outside this region.

As an example, consider the CLS built on the square lattice ($N = 2$) shown in Fig. 4.1(a). It involves four orbitals labeled by $a = A, B$ and $i = 1, 2$, that is,

$$|\Psi_{\text{CLS}}^{\mathbf{R}_C}\rangle = w_{A_1} |A_1\rangle + w_{A_2} |A_2\rangle + w_{B_1} |B_1\rangle + w_{B_2} |B_2\rangle. \quad (4.3)$$

Similarly, the CLS on the Kagome lattice ($N = 3$) shown in Fig. 4.1(b) involves six orbitals, namely

$$|\Psi_{\text{CLS}}^{\mathbf{R}_C}\rangle = w_{A_1} |A_1\rangle + w_{A_2} |A_2\rangle + w_{B_1} |B_1\rangle + w_{B_2} |B_2\rangle + w_{C_1} |C_1\rangle + w_{C_2} |C_2\rangle. \quad (4.4)$$

The orbitals with non-zero amplitude ($w_{a_i} \neq 0$) are located at positions δ_{a_i} as measured from \mathbf{R}_C . For the CLS of Fig. 4.1(a), we have $\delta_{A_{1,2}} = \mp \frac{1}{2}(1, -1)$ as well as $\delta_{B_{1,2}} = \mp \frac{1}{2}(1, 1)$. For the CLS of Fig. 4.1(b), the positions are $\delta_{A_{1,2}} = \mp \frac{1}{2}(1, -\sqrt{3})$, $\delta_{B_{1,2}} = \pm \frac{1}{2}(1, \sqrt{3})$, and $\delta_{C_{1,2}} = \pm(1, 0)$. Note that the nearest-neighbor distance is taken as $a_0 = 1$ here and throughout.

Bloch state of a compact localized state

For any CLS (4.1) centered at some \mathbf{R}_C , there exists a macroscopic number of equivalent copies translated by some Bravais vector. Thus, for any given CLS, we can introduce a *Bloch state of the CLS (BCLS)* $|f(\mathbf{k})\rangle$, which is obtained as an unnormalized superposition of the CLS and all its translated copies:

$$|f(\mathbf{k})\rangle = \sum_{\mathbf{R}_C} e^{-i\mathbf{k} \cdot \mathbf{R}_C} |\Psi_{\text{CLS}}^{\mathbf{R}_C}\rangle. \quad (4.5)$$

Note that this (reciprocal-space) BCLS is simply the Fourier transform of the (real-space) CLS.

To work with Eq. (4.5), it is further useful to adopt the Bloch basis. In particular, we can expand the BCLS as

$$|f(\mathbf{k})\rangle = \sum_a f_a(\mathbf{k}) |a, \mathbf{k}\rangle, \quad (4.6)$$

where the kets $|a, \mathbf{k}\rangle$ denote Bloch basis states (they are discussed in more detail in Appendix I.A). The coefficients of the BCLS take the form

$$f_a(\mathbf{k}) \equiv \sum_{i \in \text{CLS}} w_{a_i} e^{i\mathbf{k} \cdot \delta_{a_i}}, \quad (4.7)$$

meaning that they are completely specified by the positions and amplitudes of the orbitals contained in the real-space CLS.²

In the Bloch basis, which we adopt hereafter, the BCLS takes the form of a column vector:

$$|f(\mathbf{k})\rangle = (f_A(\mathbf{k}), f_B(\mathbf{k}), \dots)^T. \quad (4.8)$$

For example, the CLS of Fig. 4.1(a) gives rise to a BCLS

$$|f(\mathbf{k})\rangle = \begin{pmatrix} w_{A_1} e^{-\frac{i}{2}(k_x - k_y)} + w_{A_2} e^{\frac{i}{2}(k_x - k_y)} \\ w_{B_1} e^{-\frac{i}{2}(k_x + k_y)} + w_{B_2} e^{\frac{i}{2}(k_x + k_y)} \end{pmatrix}, \quad (4.9)$$

and the CLS of Fig. 4.1(b) corresponds to a BCLS

$$|f(\mathbf{k})\rangle = \begin{pmatrix} w_{A_1} e^{-ik_-} + w_{A_2} e^{ik_-} \\ w_{B_1} e^{ik_+} + w_{B_2} e^{-ik_+} \\ w_{C_1} e^{ik_x} + w_{C_2} e^{-ik_x} \end{pmatrix}, \quad (4.10)$$

where $k_{\pm} \equiv \frac{1}{2}(k_x \pm \sqrt{3}k_y)$. In the same way, each arbitrarily designed CLS on any lattice uniquely corresponds to some BCLS $|f(\mathbf{k})\rangle$.

4.2.2 | Link between compact localized states and flat bands

Here we discuss the well-known fact that, whenever there is a flat band in some band structure, it implies the existence of highly degenerate CLSs in real space.

²The BCLS was introduced in a similar way by Rhim and Yang (2019), however these authors work in the "tight-binding basis I", where the Bloch Hamiltonian has the periodicity of the first Brillouin zone. In contrast, here and throughout this thesis we work in the "tight-binding basis II" (Bena and Montambaux 2009). The functional form of the coefficients $f_a(\mathbf{k})$ depends on this choice of basis.

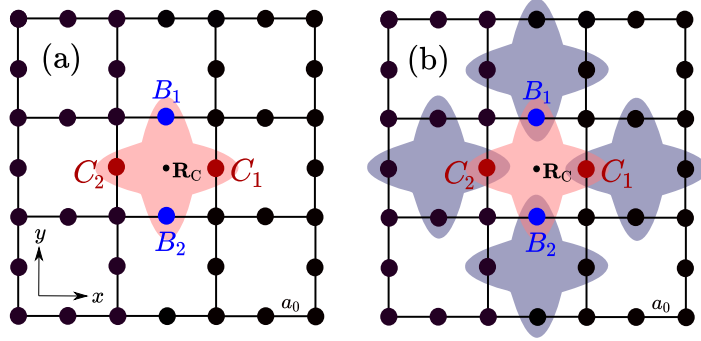


Fig. 4.2 – (a) A compact localized state which is a zero-energy eigenstate of the (real-space) Lieb Hamiltonian. (b) The CLS is not orthogonal to its neighbors.

Example: Lieb lattice

As a simple example illustrating this, let us consider the Lieb model (2.1) discussed previously. Writing its Bloch Hamiltonian explicitly in matrix form, we have

$$H_{\text{Lieb}}(\mathbf{k}) = 2 \begin{pmatrix} 0 & \cos k_x & \cos k_y \\ \cos k_x & 0 & 0 \\ \cos k_y & 0 & 0 \end{pmatrix}. \quad (4.11)$$

This Hamiltonian clearly has an eigenstate

$$|\psi_0(\mathbf{k})\rangle = \frac{1}{(c_x^2 + c_y^2)^{1/2}} (0, c_y, -c_x)^T \quad (4.12)$$

of strictly zero energy, where we use shorthand notations $c_i = \cos k_i$. Let us now consider a CLS on the Lieb lattice as shown in Fig. 4.2(a), with amplitudes $w_{B_i} = 1/2$ and $w_{C_i} = -1/2$, such that

$$|\Psi_{\text{CLS}}^{\mathbf{R}_C}\rangle = \frac{1}{2} (|B_1\rangle + |B_2\rangle - |C_1\rangle - |C_2\rangle). \quad (4.13)$$

From Eq. (4.7) it is evident that the BCLS associated to this CLS is exactly given by $|f(\mathbf{k})\rangle = (c_x^2 + c_y^2)^{1/2} |\psi_0(\mathbf{k})\rangle$. Since this BCLS is a flat-band eigenstate of the Bloch Hamiltonian (4.11), it is clear that the CLS (4.13) is an eigenstate of the (real-space) Hamiltonian H . This can be straightforwardly verified by writing the explicit real-space tight-binding Schrödinger equation for the Lieb lattice.³ It is now crucial to realize that not only the particular CLS shown in Fig. 4.2(a), but also *all its copies* translated by some Bravais vector are eigenstates of the Lieb Hamiltonian, with the same zero-energy eigenvalue. Clearly, the system permits a highly (indeed macroscopically) degenerate set of eigenstates.

³For a similar discussion concerning the CLS associated to the flat band of the dice lattice model (2.1), see for example the beautiful article by Sutherland (1986).

General method to obtain compact localized states

For flat-band Hamiltonians more complicated than the Lieb lattice, it is not necessarily trivial to directly deduce the form of the corresponding CLSs. However there is a systematic way to find the CLSs given the knowledge of the Bloch wave functions. In particular, assume we are given any tight-binding model with a flat band, with known Bloch eigenstates $|\Psi_0(\mathbf{k})\rangle$. Then it is clear that these eigenstates are degenerate for all \mathbf{k} and thus they can be freely mixed to construct another eigenstate of the real-space Hamiltonian as

$$|\xi(\mathbf{R}_C)\rangle = c_0 \sum_{\mathbf{k}} c_{\mathbf{k}} e^{i\mathbf{k}\cdot\mathbf{R}_C} |\Psi_0(\mathbf{k})\rangle. \quad (4.14)$$

This state is centered at \mathbf{R}_C ; $c_{\mathbf{k}}$ is an arbitrary function and c_0 a normalization constant. Upon expanding the Bloch state $|\Psi_0(\mathbf{k})\rangle$ using Eq. (I.1), one obtains

$$|\xi(\mathbf{R}_C)\rangle = \sum_{i,a} A_{\mathbf{R}_C\mathbf{R}_{a_i}} |a, i\rangle, \quad A_{\mathbf{R}_C\mathbf{R}_{a_i}} = \frac{c_0}{\sqrt{\mathcal{N}}} \sum_{\mathbf{k}} c_{\mathbf{k}} c_{0,a}(\mathbf{k}) e^{i\mathbf{k}\cdot(\mathbf{R}_C - \mathbf{R}_{a_i})}, \quad (4.15)$$

where $\mathbf{R}_{a_i} \equiv \mathbf{R}_i + \mathbf{r}_a$; \mathbf{R}_i is the position of unit cell i and \mathbf{r}_a the position of orbital a relative to that unit cell, \mathcal{N} is the total number of unit cells (see Appendix I.A). In other words, the flat-band eigenstate $|\xi(\mathbf{R}_C)\rangle$ occupies the orbitals $|a, i\rangle$ with amplitudes $A_{\mathbf{R}_C\mathbf{R}_{a_i}}$. These amplitudes depend on the components $c_{0,a}(\mathbf{k})$ of the state $|\psi_0(\mathbf{k})\rangle = (c_{0,A}(\mathbf{k}), c_{0,B}(\mathbf{k}), \dots)^T$, which is simply the flat-band eigenstate of the Bloch Hamiltonian matrix $H(\mathbf{k})$. They further depend on the choice of the arbitrary function $c_{\mathbf{k}}$.

From a physical point of view, we can now make an important distinction (Rhim and Yang 2019). Since $|\psi_0(\mathbf{k})\rangle$ is normalized, its components are necessarily of the form $c_{0,a} = \tilde{c}_{0,a} / \langle \tilde{\psi}_0 | \tilde{\psi}_0 \rangle^{1/2}$, where the normalization factor in the denominator is typically a square root of a \mathbf{k} -dependent function. For example, for the flat-band eigenstate (4.12) of the Lieb model we have $\tilde{c}_{0,A} = 0$, $\tilde{c}_{0,B} = c_y$, $\tilde{c}_{0,C} = -c_x$ and $\langle \tilde{\psi}_0 | \tilde{\psi}_0 \rangle = c_x^2 + c_y^2$. Thus, if $c_{\mathbf{k}}$ is chosen such as to cancel the normalization factor, then the coefficients $A_{\mathbf{R}_C\mathbf{R}_{a_i}}$ become simple sums of Bloch phases, which is an essential requirement for compact localization. Indeed, such a choice guarantees that $A_{\mathbf{R}_C\mathbf{R}_{a_i}} \neq 0$ only for a finite number of orbitals $|a, i\rangle$, such that $|\xi(\mathbf{R}_C)\rangle$ becomes a compact localized state (4.1). By shifting \mathbf{R}_C , we thus obtain a set of \mathcal{N} different CLSs, all of which are flat-band eigenstates by design.

If instead $c_{\mathbf{k}}$ is chosen such that the denominator is not canceled, one obtains a state infinitely extended in real space, which is not what we are looking for. Indeed, if we were to take $c_{\mathbf{k}} = 1$ in Eq. (4.14), then $|\xi(\mathbf{R}_C)\rangle$ would become equivalent to the Wannier state $|\Phi_0(\mathbf{R}_C)\rangle$ of the flat band [see Eq. (4.16) below]. Such Wannier states typically exhibit an exponential decay away from their center (He and Vanderbilt 2001) but are not compactly localized.

As an example, we now show that this general method allows to recover the CLS (4.13), which we obtained earlier “by inspection”. Starting from the flat-band eigenstate (4.12) of the Lieb model, we may use Eq. (4.15) to construct a state $|\xi(\mathbf{R}_C = 0)\rangle$. Clearly, the sublattice A is unoccupied, and the B and C sites are

occupied as

$$A_{0,\mathbf{R}_{B_i}} = \frac{c_0}{\sqrt{\mathcal{N}}} \sum_{\mathbf{k}} c_{\mathbf{k}} \frac{c_y}{\sqrt{c_x^2 + c_y^2}} e^{-i\mathbf{k}\cdot\mathbf{R}_{B_i}}, \quad A_{0,\mathbf{R}_{C_i}} = \frac{c_0}{\sqrt{\mathcal{N}}} \sum_{\mathbf{k}} c_{\mathbf{k}} \frac{-c_x}{\sqrt{c_x^2 + c_y^2}} e^{-i\mathbf{k}\cdot\mathbf{R}_{C_i}}.$$

To get a CLS, we now cancel the denominator by choosing $c_{\mathbf{k}} = (c_x^2 + c_y^2)^{1/2}$. Taking the normalization constant as $c_0 = \mathcal{N}^{-1/2}$, we then indeed find non-zero amplitudes $A_{R_{B_1}} = A_{R_{B_2}} = 1/2$ and $A_{R_{C_1}} = A_{R_{C_2}} = -1/2$ for the four labeled sites in Fig. 4.2(a), while the amplitudes vanish on all other lattice sites. Thus we recover the CLS (4.13). For more examples, we recommend to consult Rhim and Yang (2019).

4.2.3 | Wannier states versus compact localized states

Here we briefly comment on the relation between CLSs and Wannier states, since the latter may be more familiar to the reader. Wannier states are a set of mutually orthogonal states that can be used as a complete basis to express electronic states in a crystal (Wannier 1937). They can be defined as a Fourier transform of the Bloch states (1.2), namely

$$|\Phi_{\alpha}(\mathbf{R})\rangle = \frac{1}{\sqrt{\mathcal{N}}} \sum_{\mathbf{k}} e^{i\mathbf{k}\cdot\mathbf{R}} |\Psi_{\alpha}(\mathbf{k})\rangle. \quad (4.16)$$

Here \mathbf{R} denotes the position of the unit cell where the Wannier state is centered, and α is the sublattice index. Using the orthonormality $\langle \Psi_{\alpha}(\mathbf{k}) | \Psi_{\beta}(\mathbf{k}') \rangle = \delta_{\alpha\beta} \delta_{\mathbf{k}\mathbf{k}'}$ of the Bloch states one readily verifies that $\langle \Phi_{\alpha}(\mathbf{R}) | \Phi_{\beta}(\mathbf{R}') \rangle = \delta_{\alpha\beta} \delta_{\mathbf{R}\mathbf{R}'}$. For any dispersive band in a crystal, one can choose to work with the Bloch or Wannier states as appropriate. While the Bloch states are eigenstates of the lattice Hamiltonian (1.1), the Wannier states are in general not.

For a flat band, however, it is clear from the definition (4.16) that both Bloch and Wannier states are eigenstates of H . Moreover, as we have seen, any flat band implies the existence of \mathcal{N} different CLSs. Thus, for a flat band the set of CLSs can be viewed as a third possible type of basis, in addition to the Bloch and Wannier bases. However, the \mathcal{N} different CLSs do not in general form an orthogonal set. For example, it is clear from Fig. 4.2(a) that in the Lieb model the most compactly localized flat-band eigenstate possible occupies two unit cells. This state overlaps with all four copies translated by one unit cell in the \hat{x} or \hat{y} direction, see Fig. 4.2(b), and the overlap is such that the CLSs are not mutually orthogonal.

At the same time, the N different CLSs also do not necessarily form a complete set. That is, they are not necessarily linearly independent, in which case they cannot span the flat band completely. Rhim and Yang (2019) recently made use of this fact to separate flat bands into two very general classes:

- (i) Flat bands for which a complete set of CLSs cannot be found; these are called *singular flat bands*, and they exhibit a singular band touching with a dispersive band. Technically, this is the case whenever $c_{\mathbf{k}}$ – which needs to be chosen such that compact localization is achieved – has a root $c_{\mathbf{k}_0} = 0$ for at least one \mathbf{k}_0 in the Brillouin zone. Equivalently, this happens whenever the BCLS associated to the flat band vanishes for some \mathbf{k}_0 , that is $|f(\mathbf{k}_0)\rangle = 0$. For such

systems, additional states (known as non-contractible loop states) are necessary to complement the basis of CLSs.

- (ii) Flat bands that can be spanned by a complete set of CLSs; these are the *non-singular flat bands*, including in particular flat bands that are gapped away from all other bands, or flat bands touching a dispersive band in a non-singular way. In this case there does not exist a point \mathbf{k}_0 such that $c_{\mathbf{k}_0} = 0$ or $|f(\mathbf{k}_0)\rangle = 0$.

For example, for the case of the Lieb lattice considered above, the function $c_{\mathbf{k}} = (c_x^2 + c_y^2)^{1/2}$ and the BCLS $|f(\mathbf{k})\rangle = c_{\mathbf{k}}|\psi_0(\mathbf{k})\rangle$ clearly vanish for $k_x = \pm\pi/2$, $k_y = \pm\pi/2$. Thus the crossing point between the two dispersive bands and the flat band is singular.

These two classes of flat bands are also topologically distinct: when a non-singular touching is lifted, the flat band remains exactly flat and thus carries no Chern number (Chen et al. 2014); however when a singular touching is lifted, the flat band gets distorted and is allowed to acquire a Chern number.

In summary, CLSs can be used as a basis for flat bands (with some restrictions if the flat band is singular), but represent a class of eigenstates fundamentally different from Wannier states, which are always linearly independent and mutually orthogonal.

4.3 | Building flat-band models from compact localized states

Drawing on the knowledge about CLSs summarized above, we are now in the position to develop a powerful construction scheme for flat-band models. The main idea is to *invert* the line of reasoning used above. More precisely, we have illustrated that whenever there is a flat band in a given tight-binding model, then there is a set of \mathcal{N} degenerate CLSs; we have also described how to find those CLSs. In contrast, in the following we will start out from the CLS and are looking for flat-band models.

Assume we are given any arbitrarily shaped CLS $|\Psi_{\text{CLS}}\rangle$ on any periodic lattice of choice, which we shall call an *input CLS*, see Fig. 4.3(a). We are now going to show that it is always possible to construct families of tight-binding Hamiltonians H such that this input CLS and all its translated copies constitute a macroscopically degenerate set of eigenstates:

$$H|\Psi_{\text{CLS}}^{\mathbf{R}_C}\rangle = \epsilon_0|\Psi_{\text{CLS}}^{\mathbf{R}_C}\rangle, \quad \forall \mathbf{R}_C. \quad (4.17)$$

In order to find these tight-binding Hamiltonians H , we first construct the BCLS $|f(\mathbf{k})\rangle$ associated to the input CLS. In a second step, see Fig. 4.3(b), we *impose* Bloch Hamiltonians $H(\mathbf{k})$ for which $|f(\mathbf{k})\rangle$ automatically represents a flat-band eigenstate:

$$H(\mathbf{k})|f(\mathbf{k})\rangle = \epsilon_0|f(\mathbf{k})\rangle. \quad (4.18)$$

In particular, as explained below, $H(\mathbf{k})$ is chosen as a function of $|f(\mathbf{k})\rangle$, and can exhibit a quadratic or linear dependency on $|f(\mathbf{k})\rangle$. This generically leads to models with quadratic or linear band touchings, respectively. Finally, once appropriate matrices $H(\mathbf{k})$ are found, it is straightforward to obtain the real-space models H from them, see Fig. 4.3(c), which will be flat-band models by construction. We should

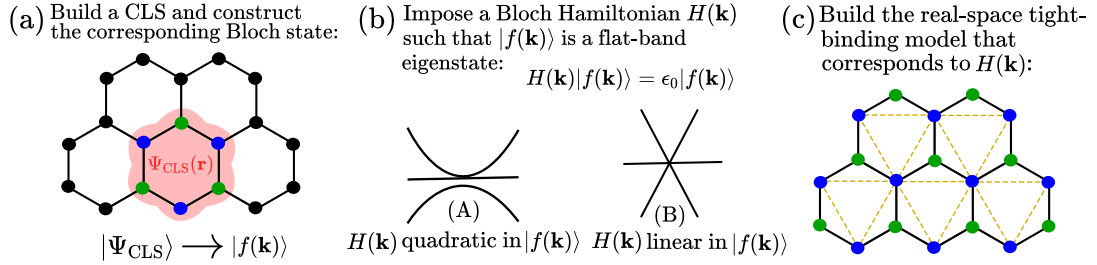


Fig. 4.3 – Basics of our method to build flat-band lattice models. In (a), the CLS wave function in real space is illustrated by the red shading. In (b), ϵ_0 denotes the energy of the flat band. An example for a band structure with a quadratic (linear) band touching is sketched on the left (right). In (c), a schematic visualization of the final flat-band hopping model is shown.

like to emphasize again that this strategy is opposite to basically all known methods to create flat bands, which usually attempt to design appropriate hoppings of the real-space Hamiltonian. Note also that hereafter $\epsilon_0 = 0$ without loss of generality.

To see how the Bloch Hamiltonian design [Fig. 4.3(b)] can be done, let us write Eq. (4.18) explicitly in matrix form:

$$\begin{pmatrix} H_{AA}(\mathbf{k}) & H_{AB}(\mathbf{k}) & \dots \\ H_{BA}(\mathbf{k}) & H_{BB}(\mathbf{k}) & \dots \\ \dots & \dots & \dots \end{pmatrix} \begin{pmatrix} f_A(\mathbf{k}) \\ f_B(\mathbf{k}) \\ \dots \end{pmatrix} = 0. \quad (4.19)$$

Evidently, *a flat band will automatically exist* if the Bloch Hamiltonian is *imposed* to be an appropriate function $H(\mathbf{k}) = H(|f(\mathbf{k})\rangle)$ of the BCLS. More concretely, the matrix elements $H_{ab}(\mathbf{k})$ should depend on the components $f_a(\mathbf{k})$ in such a way that $\sum_b H_{ab}(\mathbf{k})f_b(\mathbf{k}) = 0$ is fulfilled for every a , independently of the detailed functional form of the components $f_a(\mathbf{k})$. Thus, the task at hand consists in finding matrices $H(|f(\mathbf{k})\rangle)$ that fulfill Eq. (4.19).

As will become clear throughout this chapter, in addition to the mathematical constraint (4.19) we have to be aware of an additional physical constraint:

$$H(\mathbf{k}) \text{ must be a } \textit{reasonable} \text{ Bloch Hamiltonian.} \quad (4.20)$$

This means that $H(|f(\mathbf{k})\rangle)$ has to be chosen such that the real-space tight-binding Hamiltonian H constructed from it makes sense on a lattice. The latter property is not automatically guaranteed for all matrices $H(|f(\mathbf{k})\rangle)$ that fulfill Eq. (4.19). More concretely, for $H(\mathbf{k})$ to be reasonable, the matrix elements $H_{ab}(\mathbf{k})$ should be made of finite sums of Bloch phases that are compatible with the underlying lattice geometry (see Appendix IV.A for more details).

As it turns out, there are two different simple choices for matrices that fulfill condition (4.19):

- $H(\mathbf{k})$ is a *quadratic* function of the $f_a(\mathbf{k})$
 - flat-band models with quadratic band touching points, Section 4.4.
- $H(\mathbf{k})$ is a *linear* function of the $f_a(\mathbf{k})$
 - flat-band models with linear band crossing points, Section 4.5.

Designing quadratic flat-band Hamiltonians is possible for $N \geq 2$ bands and, conveniently, condition (4.20) is automatically fulfilled for any input CLS. In contrast, designing linear Hamiltonians requires $N \geq 3$ and the condition (4.20) is only fulfilled for special input CLSs. For this reason, the quadratic case may be regarded as simpler and will be treated first.

4.4 | Flat-band models with quadratic band touching

The simplest scenario for a quadratic flat-band model is encountered in two-band ($N = 2$) systems. The procedure can then straightforwardly be generalized to $N = 3$, and finally to any N .

4.4.1 | Two-band models

Consider some CLS built on a lattice with two orbitals per unit cell:

$$|\Psi_{\text{CLS}}^{\text{RC}}\rangle = \sum_{i \in \text{CLS}} (w_{A_i} |A_i\rangle + w_{B_i} |B_i\rangle). \quad (4.21)$$

The corresponding BCLS has two components,

$$|f(\mathbf{k})\rangle = (f_A, f_B)^T, \quad (4.22)$$

where hereafter $f_a \equiv f_a(\mathbf{k})$ for brevity. We now want to construct a matrix $H(\mathbf{k})$ that vanishes on $|f(\mathbf{k})\rangle$, that is, $H(\mathbf{k})|f(\mathbf{k})\rangle = 0$. The only generic way to do this consists in introducing a state

$$|f^{AB}\rangle \equiv (-f_B^*, f_A^*)^T \quad (4.23)$$

orthogonal to $|f(\mathbf{k})\rangle$, as well as the corresponding matrix

$$F_{\mathbf{k}}^{AB} \equiv |f^{AB}\rangle \langle f^{AB}|. \quad (4.24)$$

Then a Bloch Hamiltonian defined as

$$H(\mathbf{k}) \equiv \lambda_{\mathbf{k}}^{AB} F_{\mathbf{k}}^{AB} = \lambda_{\mathbf{k}}^{AB} \begin{pmatrix} |f_B|^2 & -f_A f_B^* \\ -f_A^* f_B & |f_A|^2 \end{pmatrix} \quad (4.25)$$

will obviously have $|f(\mathbf{k})\rangle$ as an eigenstate of zero energy; in other words, Eq. (4.19) is fulfilled for *any* $|f(\mathbf{k})\rangle$. The band structure associated to Eq. (4.25) reads

$$\epsilon_0(\mathbf{k}) = 0, \quad \epsilon_1(\mathbf{k}) = \lambda_{\mathbf{k}}^{AB} (|f_A|^2 + |f_B|^2). \quad (4.26)$$

Here, $\lambda_{\mathbf{k}}^{AB}$ is an arbitrary real function with the periodicity of the Brillouin zone. If it is taken positive (or negative) throughout, the flat band is gapped away from the dispersive band at all \mathbf{k} -points where $|f(\mathbf{k})\rangle$ does not vanish. In this case, a band touching at \mathbf{k}_0 can only occur if $|f(\mathbf{k}_0)\rangle = 0$, that is, all band touchings are singular. In contrast, if $\lambda_{\mathbf{k}}^{AB}$ changes sign in the Brillouin zone, non-singular band touchings

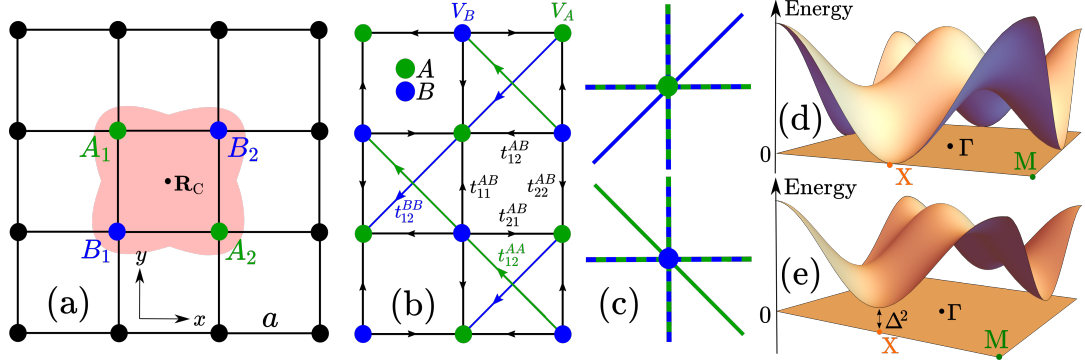


Fig. 4.4 – (a) CLS on the square lattice. (b) Flat-band tight-binding model built from it. Hopping parameters are in general complex, as indicated by the arrows. (c) The hopping directions are determined by the CLS shape. (d) Band structure for $w_{A_i} = -w_{B_i} = 1$. (e) Band structure for the same amplitudes except $w_{B_2} = -1 - \Delta$.

are possible. Since we are predominantly interested in non-trivial touching points created by the singularity of the flat-band eigenstate, we will take $\lambda_{\mathbf{k}}^{AB} = 1$ from now on.

Let us now see how flat-band tight-binding models can be designed from Eq. (4.25). As a first example, consider the CLS (4.3) used previously, which is again visualized in Fig. 4.4(a) for convenience. We now simply insert the corresponding BCLS (4.9) into Eq. (4.25), to obtain a Bloch Hamiltonian of the form

$$H(\mathbf{k}) = \begin{pmatrix} H_{AA}(\mathbf{k}) & H_{AB}(\mathbf{k}) \\ H_{AB}^*(\mathbf{k}) & H_{BB}(\mathbf{k}) \end{pmatrix}, \quad (4.27)$$

where

$$\begin{aligned} H_{AA}(\mathbf{k}) &= V_A + t_{12}^{BB} e^{-i(k_x+k_y)} + t_{21}^{BB} e^{i(k_x+k_y)}, \\ H_{BB}(\mathbf{k}) &= V_B + t_{12}^{AA} e^{-i(k_x-k_y)} + t_{21}^{AA} e^{i(k_x-k_y)}, \\ H_{AB}(\mathbf{k}) &= t_{11}^{AB} e^{ik_y} + t_{12}^{AB} e^{-ik_x} + t_{21}^{AB} e^{ik_x} + t_{22}^{AB} e^{-ik_y}. \end{aligned} \quad (4.28)$$

The hopping directions present in the real-space tight-binding model H described by this Bloch Hamiltonian are depicted in Fig. 4.4(b). They can be directly understood from the shape of the CLS, as illustrated in Fig. 4.4(c): hoppings from site A to site B (B to A) are determined by all vectors that connect orbitals A to orbitals B (B to A) within the CLS. Similarly, hoppings from site A to site A (B to B) are determined by all vectors that connect orbitals B to orbitals B (A to A) within the CLS. See also Appendix IV.A for more details on the origin of this behavior.

The onsite energies of the Hamiltonian (4.27) take the values $V_A \equiv |w_{B_1}|^2 + |w_{B_2}|^2$ and $V_B \equiv |w_{A_1}|^2 + |w_{A_2}|^2$. The inter-sublattice hopping parameters are given by $t_{ij}^{ab} \equiv -w_{a_i} w_{b_j}^*$, and the intra-sublattice hopping parameters are $t_{ij}^{aa} \equiv w_{a_i} w_{a_j}^*$. All of these parameters strongly depend on the amplitudes of the input CLS. As a consequence, the band structure can be *engineered* by the choice of the CLS amplitudes. In particular, the existence of a (singular) band touching can be ensured by choosing $|f(\mathbf{k})\rangle$ singular. For example, if the CLS amplitudes are such that $|f(\mathbf{k}_X)\rangle = 0$, a

band touching at the X point of the Brillouin zone appears, see Fig. 4.4(d). Similarly, there would be a band touching at the Γ point if $w_{a_1} = -w_{a_2} \in \mathbb{R}$. In contrast, if $|f(\mathbf{k})\rangle$ is chosen non-singular, the bands are gapped away from each other, see Fig. 4.4(e).

As a second example, consider the CLS on the honeycomb lattice shown in Fig. 4.5(a). It is straightforward to obtain the BCLS

$$|f(\mathbf{k})\rangle = \begin{pmatrix} w_{A_1} e^{-ik_+} + w_{A_2} e^{ik_x} \\ w_{B_1} e^{ik_+} + w_{B_2} e^{ik_-} \end{pmatrix}, \quad (4.29)$$

where again $k_{\pm} \equiv \frac{1}{2}(k_x \pm \sqrt{3}k_y)$. Inserting into Eq. (4.25), one obtains a tight-binding model of the form (4.27), where now

$$\begin{aligned} H_{AA}(\mathbf{k}) &= V_A + t_{12}^{BB} e^{i\sqrt{3}k_y} + t_{21}^{BB} e^{-i\sqrt{3}k_y}, \\ H_{BB}(\mathbf{k}) &= V_B + t_{12}^{AA} e^{-i(k_x+k_+)} + t_{21}^{AA} e^{i(k_x+k_+)}, \\ H_{AB}(\mathbf{k}) &= t_{11}^{AB} e^{-2ik_+} + t_{12}^{AB} e^{-ik_x} + t_{21}^{AB} e^{ik_-} + t_{22}^{AB} e^{ik_+}, \end{aligned} \quad (4.30)$$

with onsite energies and hoppings as defined above. This model is shown in Fig. 4.5(b). Due to the asymmetric shape of the input CLS, the hoppings are also distributed asymmetrically, as illustrated in Fig. 4.5(c). By an appropriate choice of the CLS amplitudes, the band structure can be freely designed to exhibit a band touching at the Γ point or at the K points, see Fig. 4.5(d) and (e), or to be gapped by taking $|f(\mathbf{k})\rangle$ non-singular.

Proceeding in the same way, *infinitely many* different $N = 2$ flat-band models and their band structures can be designed. For *any imaginable CLS* of the form (4.21), if one inserts the corresponding BCLS (4.22) into Eq. (4.25), one obtains a flat-band tight-binding model. Its hopping directions are determined by the shape of the input CLS (that is, the set of all vectors δ_{a_i}), and hopping parameters as well as onsite energies that are determined by the amplitudes w_{a_i} of the input CLS.

To illustrate that the procedure outlined above indeed works for arbitrary input CLSs, we may consider the (absurdly complicated) snowflake-shaped CLS displayed in Fig. 4.5(f). Of course, for such an extended input CLS, the real-space model that one obtains involves many further-neighbor hoppings and it is not useful to draw it explicitly. However, conveniently, the band structure (4.26) can be analyzed and designed *without* considering the real-space model. For example, taking $w_{a_i} = 1$ for all 42 orbitals involved in the CLS, the dispersive band $\epsilon_1(\mathbf{k})$ strongly oscillates and exhibits a large peak at the Γ point (not shown). If the amplitudes are flipped to $w_{a_i} = -1$ on three out of the six branches of the snowflake, see Fig. 4.5(g), then $\epsilon_1(\mathbf{k})$ exhibits six peaks arrayed hexagonally in the Brillouin zone.

We emphasize that the Bloch Hamiltonian (4.25) is indeed always *reasonable* [cf. condition (4.20)] due to its quadratic character, as explained in more detail in Appendix IV.A. In fact, it is not only a reasonable flat-band Hamiltonian, but the *only possible form* for the Bloch Hamiltonian of any $N = 2$ flat-band model. This can be easily understood from the spectral theorem, see Appendix IV.B.

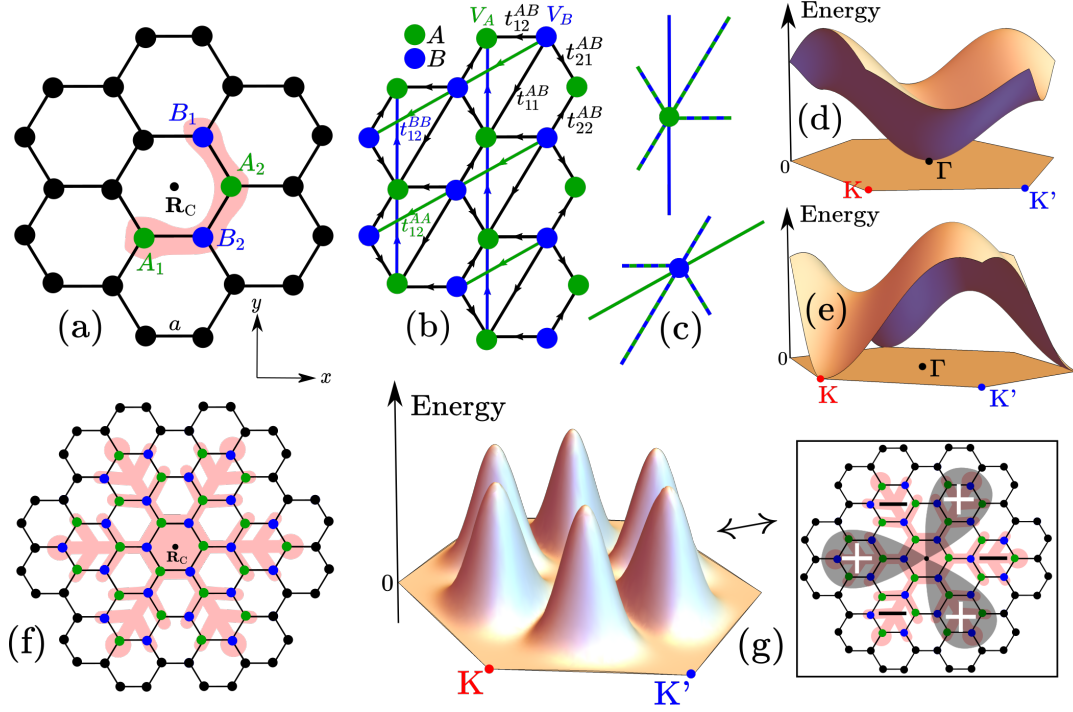


Fig. 4.5 – (a) CLS on the honeycomb lattice. (b) Flat-band model built from it. (c) The hopping directions are determined by the CLS shape. (d) Band structure for $w_{a_1} = -w_{a_2} = 1$. (e) Band structure for $w_{a_1} = 1$, $w_{a_2} = -e^{2\pi i/3}$. (f) Snowflake-shaped CLS. (g) Band structure of the corresponding flat-band model (left), with amplitudes as shown in the right inset: $w_{a_i} = 1$ inside the dark-shaded branches, and $w_{a_i} = -1$ outside.

As we will show below, an analogous procedure of flat-band model and band structure design is possible for $N > 2$. Additionally, the tunability turns out to be considerably increased.

4.4.2 | Three-band models

Consider now a CLS built on a lattice with three orbitals per unit cell:

$$|\Psi_{\text{CLS}}^{\mathbf{R}_C}\rangle = \sum_{i \in \text{CLS}} (w_{A_i} |A_i\rangle + w_{B_i} |B_i\rangle + w_{C_i} |C_i\rangle). \quad (4.31)$$

The corresponding BCLS has three components,

$$|f(\mathbf{k})\rangle = (f_A, f_B, f_C)^T. \quad (4.32)$$

We can now introduce *three different* states orthogonal to $|f\rangle$, namely

$$\begin{aligned} |f^{AB}\rangle &= (-f_B^*, f_A^*, 0)^T, \\ |f^{AC}\rangle &= (-f_C^*, 0, f_A^*)^T, \\ |f^{BC}\rangle &= (0, -f_C^*, f_B^*)^T, \end{aligned} \quad (4.33)$$

with corresponding matrices $F_{\mathbf{k}}^{ab} \equiv |f^{ab}\rangle\langle f^{ab}|$, where

$$F_{\mathbf{k}}^{AB} = \begin{pmatrix} |f_B|^2 & -f_A f_B^* & 0 \\ -f_A^* f_B & |f_A|^2 & 0 \\ 0 & 0 & 0 \end{pmatrix}, \quad F_{\mathbf{k}}^{AC} = \begin{pmatrix} |f_C|^2 & 0 & -f_A f_C^* \\ 0 & 0 & 0 \\ -f_A^* f_C & 0 & |f_A|^2 \end{pmatrix}, \quad (4.34)$$

$$F_{\mathbf{k}}^{BC} = \begin{pmatrix} 0 & 0 & 0 \\ 0 & |f_C|^2 & -f_B f_C^* \\ 0 & -f_B^* f_C & |f_B|^2 \end{pmatrix}.$$

A class of flat-band Bloch Hamiltonians is then obtained as a linear combination:

$$H(\mathbf{k}) = \lambda_{\mathbf{k}}^{AB} F_{\mathbf{k}}^{AB} + \lambda_{\mathbf{k}}^{AC} F_{\mathbf{k}}^{AC} + \lambda_{\mathbf{k}}^{BC} F_{\mathbf{k}}^{BC}, \quad (4.35)$$

where $\lambda_{\mathbf{k}}^{AB}$, $\lambda_{\mathbf{k}}^{AC}$, $\lambda_{\mathbf{k}}^{BC}$ are arbitrary real functions with the periodicity of the Brillouin zone. It will suffice to choose them as constants, $\lambda_{\mathbf{k}}^{ab} = \lambda_{ab}$. The Hamiltonian (4.35) is analogous to Eq. (4.25) in that it *automatically* verifies the desired conditions (4.19) and (4.20) for any conceivable input CLS, that is, for any $|f(\mathbf{k})\rangle$. Therefore, infinitely many flat-band models on any $N = 3$ lattice can be obtained from Eq. (4.35).

Moreover, there is an additional advantage compared to the $N = 2$ case, namely there are now three *relative* parameters λ_{ab} , while the single parameter λ_{AB} in the two-band Hamiltonian (4.25) only acts globally. As a consequence, the Hamiltonian (4.35) can be strongly tuned even if an input CLS *completely fixed with regard to both shape and amplitudes* is used. This represents an additional degree of freedom absent in the two-band case. In this context, it is also crucial to realize that the states (4.33) are not eigenstates of the Hamiltonian (4.35). In fact, they form an overcomplete basis of the space orthogonal to $|f(\mathbf{k})\rangle$. This redundancy is at the origin of the tunability provided by the λ_{ab} . In contrast to the flat-band eigenstate $|f(\mathbf{k})\rangle$, the dispersive-band eigenstates of the Hamiltonian (4.35) do depend on the parameters λ_{ab} .

The dependency on the choice of the input CLS (that is, of the functions f_a) and the tunability by the λ_{ab} are clearly reflected in the Hamiltonian's band structure

$$\epsilon_0(\mathbf{k}) = 0, \quad \epsilon_{1,2}(\mathbf{k}) = \frac{1}{2} \left(C_1 \pm \sqrt{2C_2 - C_1^2} \right), \quad (4.36)$$

where C_n are Casimir invariants (3.28) which in the present case take the form

$$C_1 = \sum_{a,b>a} \lambda_{ab} (|f_a|^2 + |f_b|^2),$$

$$C_2 = \sum_b \left(\sum_{a \neq b} \lambda_{ab} |f_a|^2 \right)^2 + 2 \sum_{a,b>a} \lambda_{ab}^2 |f_a|^2 |f_b|^2. \quad (4.37)$$

As an example, consider again the six-site CLS on the Kagome lattice used previously, shown in Fig. 4.6(a), with corresponding BCLS (4.10). Inserting into Eq. (4.35), one

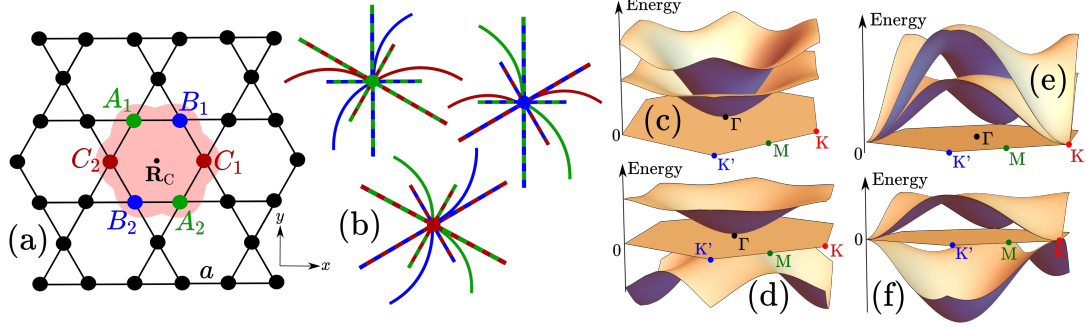


Fig. 4.6 – (a) CLS on the Kagome lattice. (b) Hopping directions occurring in the flat-band model built from it, as determined by the CLS shape. The corresponding band structure is shown for $w_{a_1} = -w_{a_2} = 1$ in (c) with $\lambda_{AB} = \lambda_{AC} = \lambda_{BC}/2 = 1$ and in (d) with $\lambda_{AB} = \lambda_{AC} = -\lambda_{BC}/2 = 1$; for $w_{a_1} = 1$, $w_{A_2} = e^{\pi i/3}$, $w_{B_2} = e^{-\pi i/3}$, $w_{C_2} = -e^{-2\pi i/3}$ in (e) with $\lambda_{AB} = \lambda_{AC} = \lambda_{BC}/2 = 1$ and in (f) with $\lambda_{AB} = \lambda_{AC} = -\lambda_{BC}/2 = 1$.

obtains a flat-band tight-binding model

$$H(\mathbf{k}) = \begin{pmatrix} H_{AA}(\mathbf{k}) & H_{AB}(\mathbf{k}) & H_{AC}(\mathbf{k}) \\ H_{AB}^*(\mathbf{k}) & H_{BB}(\mathbf{k}) & H_{BC}(\mathbf{k}) \\ H_{AC}^*(\mathbf{k}) & H_{BC}^*(\mathbf{k}) & H_{CC}(\mathbf{k}) \end{pmatrix}, \quad (4.38)$$

with diagonal matrix elements

$$\begin{aligned} H_{AA} &= V_A + t_{12}^{A,BB} e^{2ik_+} + t_{21}^{A,BB} e^{-2ik_+} + t_{12}^{A,CC} e^{2ik_x} + t_{21}^{A,CC} e^{-2ik_x}, \\ H_{BB} &= V_B + t_{12}^{B,AA} e^{-2ik_-} + t_{21}^{B,AA} e^{2ik_-} + t_{12}^{B,CC} e^{2ik_x} + t_{21}^{B,CC} e^{-2ik_x}, \\ H_{CC} &= V_C + t_{12}^{C,AA} e^{-2ik_-} + t_{21}^{C,AA} e^{2ik_-} + t_{12}^{C,BB} e^{2ik_+} + t_{21}^{C,BB} e^{-2ik_+}, \end{aligned} \quad (4.39)$$

and off-diagonal elements

$$\begin{aligned} H_{AB} &= t_{11}^{AB} e^{-ik_x} + t_{12}^{AB} e^{i\sqrt{3}k_y} + t_{21}^{AB} e^{-i\sqrt{3}k_y} + t_{22}^{AB} e^{ik_x}, \\ H_{AC} &= t_{11}^{AC} e^{-i(k_x+k_-)} + t_{12}^{AC} e^{ik_+} + t_{21}^{AC} e^{-ik_+} + t_{22}^{AC} e^{i(k_x+k_-)}, \\ H_{BC} &= t_{11}^{BC} e^{-ik_-} + t_{12}^{BC} e^{i(k_x+k_+)} + t_{21}^{BC} e^{-i(k_x+k_+)} + t_{22}^{BC} e^{ik_-}. \end{aligned} \quad (4.40)$$

Again, the hopping directions are determined by the CLS shape, as illustrated in Fig. 4.6(b), and the tight-binding model thus involves at most third-neighbor hoppings.

The onsite energies $V_a \equiv \sum_{b \neq a} \lambda_{ab} (|w_{b_1}|^2 + |w_{b_2}|^2)$ as well as the inter-sublattice hoppings $t_{ij}^{ab} \equiv -\lambda_{ab} w_{a_i} w_{b_j}^*$ and intra-sublattice hoppings $t_{ij}^{a,bb} \equiv \lambda_{ab} w_{b_i} w_{b_j}^*$ are strongly tunable by the six CLS amplitudes w_{a_i} and the three parameters λ_{ab} . This affords considerable control over the behavior of the dispersive bands, and in particular over the occurrence of band touching points. For example, the band structure can be chosen to exhibit a threefold touching at the Γ point, and the position of the flat band with respect to the dispersive bands can be controlled by the λ_{ab} , see Fig. 4.6(c) and (d). Similarly, the touching can be placed at the K points, and again the position of the flat band can be controlled, see Fig. 4.6(e) and (f). Of course, the flat band can also be gapped out completely by an imbalance in the CLS amplitudes.

More generally, for three-band models of the form (4.35), a band touching point of any degeneracy, and at various positions in the Brillouin zone, can be designed without destroying the flat band. At $\mathbf{k} = \mathbf{k}_0$, there will be a twofold touching if $2C_2(\mathbf{k}_0) = C_1(\mathbf{k}_0)[1 + C_1(\mathbf{k}_0)]$, and a threefold touching if $C_1(\mathbf{k}_0) = C_2(\mathbf{k}_0) = 0$. Clearly, this can be achieved in several different ways, with or without fine-tuning of the λ_{ab} . All possible scenarios are listed in Appendix IV.C.

4.4.3 | N -band models

The arguments made above can be readily extended to any N . Consider a generic CLS (4.1) built on a lattice with N orbitals per unit cell, with corresponding BCLS (4.8). We may now introduce $\binom{N}{2}$ states

$$|f^{ab}\rangle \equiv (0, \dots, 0, -f_b^*, 0, \dots, 0, f_a, 0, \dots, 0)^T \quad (4.41)$$

orthogonal to $|f\rangle$, and the $N \times N$ matrices

$$F_{\mathbf{k}}^{ab} \equiv |f^{ab}\rangle\langle f^{ab}| \quad (4.42)$$

constructed from them. A generic quadratic flat-band Bloch Hamiltonian is then obtained by forming a linear combination of these $\binom{N}{2}$ matrices:

$$H(\mathbf{k}) = \sum_{a,b>a} \lambda_{\mathbf{k}}^{ab} F_{\mathbf{k}}^{ab}, \quad (4.43)$$

where $a, b \in \{A, B, C, \dots\}$ and $\lambda_{\mathbf{k}}^{ab}$ is an arbitrary real function with the periodicity of the Brillouin zone. We will assume $\lambda_{\mathbf{k}}^{ab} = \lambda_{ab}$ to be constants, such that the off-diagonal and diagonal matrix elements of the Hamiltonian (4.43) explicitly read

$$H_{ab}(\mathbf{k}) = -\lambda_{ab} f_a f_b^*, \quad H_{aa}(\mathbf{k}) = \sum_{b \neq a} \lambda_{ab} |f_b|^2. \quad (4.44)$$

The Hamiltonian (4.43), which generalizes Eqs. (4.25) and (4.35) to any N , is the first main result of this chapter. One can insert into it *any arbitrary CLS* built on any lattice, for any spatial dimension and any number of sites per unit cell. Since conditions (4.19) and (4.20) are automatically fulfilled, each such input CLS gives rise to a reasonable real-space tight-binding model with a flat band. One thus obtains arbitrarily many flat-band models on any lattice.⁴

Besides having the property of exhibiting a flat band automatically, the Hamiltonian (4.43) has two convenient properties. Namely, first, it is strongly tunable by two independent knobs: the functions f_a and the $N(N-1)/2$ parameters λ_{ab} . The latter tunability stems from the fact that the states (4.41) are not eigenstates of the Hamiltonian (4.43) and form an overcomplete basis of the space orthogonal to $|f(\mathbf{k})\rangle$. Second, it allows to design band touching points of any degeneracy. Although, for $N > 3$, there is no elegant closed-form solution for the energy bands, the two most

⁴Of course, while Eq. (4.43) provides infinitely many flat-band models, it does not capture all possible flat-band models except in the $N = 2$ limit. In particular, flat-band models with a linear function $H(|f(\mathbf{k})\rangle)$ exist for $N \geq 3$, see Section 4.5.

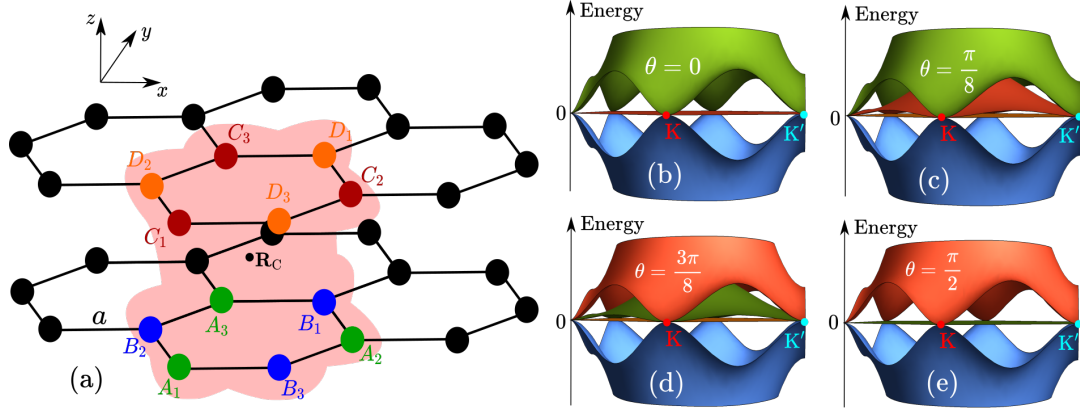


Fig. 4.7 – (a) CLS on a bilayer honeycomb lattice. (b)–(e) Band structure (4.47) for the tight-binding model built from it, for different values of θ and with $\lambda_{AB} = 1$.

interesting classes of such band touchings (which do not require fine-tuning of the λ_{ab}) can be determined as follows. (1) If $|f(\mathbf{k}_0)\rangle = 0$ for some \mathbf{k}_0 , there will be an N -fold (singular) band touching at \mathbf{k}_0 . We have already seen examples for this in the two-band and three-band case, see Figs. 4.4–4.6. (2) If, at \mathbf{k}_0 , all except one component of $|f(\mathbf{k}_0)\rangle$ vanish, say $f_{a_0}(\mathbf{k}_0) \neq 0$ and $f_{a \neq a_0}(\mathbf{k}_0) = 0$, then the Hamiltonian (4.43) becomes locally diagonal with eigenvalues $\{0, \lambda_{a_0, a \neq a_0} |f_{a_0}(\mathbf{k}_0)|^2\}$. In other words, a d -fold band touching at \mathbf{k}_0 , with $1 \leq d \leq N - 1$, can be created as desired by setting $d - 1$ parameters $\lambda_{a_0, a \neq a_0}$ to zero.

As an example for the $N > 3$ case, consider a CLS on an $N = 4$ bilayer honeycomb lattice, shown in Fig. 4.7(a). For simplicity, we take all CLS amplitudes to be identical, $w_{a_i} = 1$. The corresponding BCLS is given by

$$|f(\mathbf{k})\rangle = (g_{\mathbf{k}}, g_{\mathbf{k}}^*, g_{\mathbf{k}}, g_{\mathbf{k}}^*)^T, \quad g_{\mathbf{k}} \equiv 2e^{-\frac{i}{2}k_x} \cos\left(\frac{\sqrt{3}k_y}{2}\right) + e^{ik_x}. \quad (4.45)$$

Even though the CLS is completely fixed (shape and amplitudes), the flat-band Bloch Hamiltonian (4.43) built from it is still tunable by six parameters $\lambda_{AB}, \lambda_{AC}, \lambda_{AD}, \lambda_{BC}, \lambda_{BD}, \lambda_{CD}$. To reduce the number of parameters, it is reasonable to set $\lambda_{CD} = \lambda_{AB}, \lambda_{BC} = \lambda_{AD}$ and $\lambda_{BD} = \lambda_{AC}$ for reasons of symmetry [cf. Fig. 4.7(a)]. We may then further set $\lambda_{AC} = -\cos^2 \theta \lambda_{AB}$ and $\lambda_{AD} = -\sin^2 \theta \lambda_{AB}$ to ensure a tight-binding model with zero onsite energies and no intra-sublattice hopping:

$$H(\mathbf{k}) = \lambda_{AB} \begin{pmatrix} 0 & -g_{\mathbf{k}}^2 & \cos^2 \theta |g_{\mathbf{k}}|^2 & \sin^2 \theta g_{\mathbf{k}}^2 \\ -(g_{\mathbf{k}}^*)^2 & 0 & \sin^2 \theta (g_{\mathbf{k}}^*)^2 & \cos^2 \theta |g_{\mathbf{k}}|^2 \\ \cos^2 \theta |g_{\mathbf{k}}|^2 & \sin^2 \theta g_{\mathbf{k}}^2 & 0 & -g_{\mathbf{k}}^2 \\ \sin^2 \theta (g_{\mathbf{k}}^*)^2 & \cos^2 \theta |g_{\mathbf{k}}|^2 & -(g_{\mathbf{k}}^*)^2 & 0 \end{pmatrix}. \quad (4.46)$$

Physically, the parameter θ quantifies the ratio between vertical (AC and BD) and diagonal (AD and BC) inter-layer hoppings. In addition to a zero-energy flat band $\epsilon_0 = 0$, the band structure of the model (4.46) contains three dispersive bands

$$\epsilon_1(\mathbf{k}) = -2|g_{\mathbf{k}}|^2, \quad \epsilon_2(\mathbf{k}) = 2\sin^2 \theta |g_{\mathbf{k}}|^2, \quad \epsilon_3(\mathbf{k}) = 2\cos^2 \theta |g_{\mathbf{k}}|^2, \quad (4.47)$$

in units of λ_{AB} . The upper two (lower two) bands are tunable by θ if λ_{AB} is taken to be positive (negative), as shown in Fig. 4.7(b)–(e). Note that the system has a chiral symmetry (2.3) for $\theta = n\pi/2$, $n \in \mathbb{Z}$. In this case there is a doubly degenerate flat band, of which one is essential (ϵ_0) while the other one is accidental (ϵ_2 or ϵ_3).

Finally, to illustrate that our flat-band model construction scheme indeed works for any dimension, an $N = 4$ flat-band model built from a CLS on the (3D) cubic lattice is discussed in Appendix IV.D.

4.5 | Flat-band models with linear band crossing

In the previous section we have seen that appropriate Bloch Hamiltonians which are purely quadratic functions of the components f_a of the flat-band eigenstate give rise to quadratic band touching points. It is then natural to study Bloch Hamiltonians that are purely linear functions of the components f_a . As might be expected, this will give rise to models with linear band crossing points.

A generic Bloch Hamiltonian linear in the f_a and respecting Hermiticity can be constructed as⁵

$$H(\mathbf{k}) = \sum_i \lambda_{i,\mathbf{k}} \left(|e_i\rangle \langle f_i^\perp(\mathbf{k})| + |f_i^\perp(\mathbf{k})\rangle \langle e_i| \right). \quad (4.48)$$

Here $\lambda_{i,\mathbf{k}}$ is any real function with the periodicity of the first Brillouin zone, assumed to be constant ($\lambda_{i,\mathbf{k}} = \lambda_i$) in the following; $|e_i\rangle$ are \mathbf{k} -independent vectors; $|f_i^\perp(\mathbf{k})\rangle$ are vectors perpendicular to the BCLS $|f(\mathbf{k})\rangle$ and, importantly, linear in the components f_a . Note that the number of terms in the sum is equal to the number of different vectors $|f_i^\perp\rangle$.

Several important statements about the Hamiltonian (4.48) can be made.

- A linear flat-band model cannot exist in a two-band system. Intuitively, it is reasonable that a linearly dispersing band (“half a Dirac cone”) touching a flat band should be impossible. Recall also that we have proven in Appendix IV.B that any two-band system with a flat band must be of the quadratic form (4.25). Thus, the simplest models of the form (4.48) have three bands.
- For the construction of a linear model (4.48), one cannot use a completely arbitrary input CLS, in contrast to the quadratic scenario. Instead, the input CLS needs to have special symmetry properties, as we will detail below.
- While the first term of the summand in Eq. (4.48) always vanishes on the BCLS by definition, there are two possible scenarios for the second term:

(A) All vectors $|e_i\rangle$ are individually orthogonal to the BCLS, that is, $\langle e_i|f(\mathbf{k})\rangle = 0$ for each i .

(B) The vectors $|e_i\rangle$ are not individually orthogonal to the BCLS, but the sum is, namely $\sum_i \lambda_i |f_i^\perp\rangle \langle e_i|f(\mathbf{k})\rangle = 0$.

⁵Note that the method exposed here is a more comprehensive and more general version of that previously presented by Graf and Piéchon (2021b).

As we will see, different input CLSs can be classified according to whether they give rise to flat-band Hamiltonians of type \mathcal{A} or type \mathcal{B} .

In the following, the three-band case will be studied in detail (Section 4.5.1) before generalizing to higher N (Section 4.5.2).

4.5.1 | Three-band models

Consider again some CLS (4.31) built on a lattice with three orbitals per unit cell, with corresponding BCLS (4.32). Our goal is now to construct $N = 3$ flat-band Bloch Hamiltonians of the form (4.48). We can identify four different generic types of input CLSs that work. They will be called \mathcal{A}_I -CLS, \mathcal{A}_{II} -CLS, \mathcal{B}_I -CLS and \mathcal{B}_{II} -CLS, respectively, a notation motivated by the scenarios (\mathcal{A}) and (\mathcal{B}) introduced above, as will become clear shortly.

These CLSs are also distinguished by important symmetry properties of the flat-band Bloch Hamiltonians built from them. Namely, starting out from an \mathcal{A}_I -CLS, one obtains a flat-band Hamiltonian characterized by a (global) chiral symmetry (2.3), with $\mathbf{x} = \mathbf{k}$ and a unitary matrix \mathcal{S} that fulfills $\mathcal{S}^2 = 1_3$. Accordingly, the Hamiltonian has a particle-hole symmetric spectrum. Starting out from an \mathcal{A}_{II} -CLS, the spectrum of the resulting flat-band Hamiltonian is not particle-hole symmetric in general but a chiral symmetry can be recovered in special cases. In contrast, CLSs of type \mathcal{B} (both \mathcal{B}_I and \mathcal{B}_{II}) give rise to flat-band Bloch Hamiltonians that exhibit a (global) CP symmetry (2.10) with $\mathbf{x} = \mathbf{k}$ and \mathcal{C} such that $\mathcal{C}^2 = 1_3$. For such CP-symmetric Hamiltonians, the spectrum is also particle-hole symmetric. The four distinct generic types of CLSs along with the resulting flat-band models are presented in detail in the following.

Flat-band models from type- \mathcal{A} compact localized states

It is easy to see that for a completely generic BCLS of a three-band system, $|f(\mathbf{k})\rangle = (f_A, f_B, f_C)^T$, there is no constant vector $|e_i\rangle$ orthogonal to it. However, such an orthogonal constant vector can exist if either one component of the BCLS vanishes (type \mathcal{A}_I) or if two components are proportional to each other (type \mathcal{A}_{II}), as discussed in detail in the following.

Flat-band models from \mathcal{A}_I -CLSs. The first possibility for building an $N = 3$ linear flat-band Hamiltonian arises if the input CLS (4.31) occupies two sublattices in an arbitrary fashion, while vanishing on the third. Let $u \in \{A, B, C\}$ denote the unoccupied sublattice, then $f_u = 0$, $f_{a \neq u} \neq 0$, and $f_A f_B f_C = 0$. A CLS of this kind will be called type \mathcal{A}_I . Any \mathcal{A}_I -CLS gives rise to a corresponding \mathcal{A}_I -BCLS

$$\begin{aligned} |f(\mathbf{k})\rangle &= |m_u^{ABC}\rangle, \\ |m_A^{ABC}\rangle &\equiv (0, f_B, f_C)^T, \\ |m_B^{ABC}\rangle &\equiv (f_A, 0, f_C)^T, \\ |m_C^{ABC}\rangle &\equiv (f_A, f_B, 0)^T. \end{aligned} \tag{4.49}$$

According to Eq. (4.48), we now need to write down all vectors linear in the f_a that are orthogonal to the BCLS. For any given unoccupied sublattice u there is only one

such vector $|f_{1,u}^\perp\rangle$, which takes the form

$$|f_{1,A}^\perp\rangle = |f^{BC}\rangle, \quad |f_{1,B}^\perp\rangle = |f^{AC}\rangle, \quad |f_{1,C}^\perp\rangle = |f^{AB}\rangle, \quad (4.50)$$

where the $|f^{ab}\rangle$ are given by Eq. (4.33). Additionally, there is a constant vector $|e_{1,u}\rangle$ that is also orthogonal to the BCLS, namely $|e_{1,A}\rangle = |v_1\rangle$, $|e_{1,B}\rangle = |v_2\rangle$, $|e_{1,C}\rangle = |v_3\rangle$, where simply $|v_1\rangle = (1, 0, 0)^T$, $|v_2\rangle = (0, 1, 0)^T$, and $|v_3\rangle = (0, 0, 1)^T$. The existence of such an orthogonal constant vector characterizes the CLS as type \mathcal{A} .

Clearly, a matrix orthogonal to the BCLS $|m_u^{ABC}\rangle$ is then constructed as

$$M_{u,\mathbf{k}}^{ABC} = |e_{1,u}\rangle\langle f_{1,u}^\perp| + |f_{1,u}^\perp\rangle\langle e_{1,u}|, \quad (4.51)$$

which takes the explicit form

$$\begin{aligned} M_{A,\mathbf{k}}^{ABC} &\equiv \begin{pmatrix} 0 & -f_C & f_B \\ -f_C^* & 0 & 0 \\ f_B^* & 0 & 0 \end{pmatrix}, & M_{B,\mathbf{k}}^{ABC} &\equiv \begin{pmatrix} 0 & -f_C^* & 0 \\ -f_C & 0 & f_A \\ 0 & f_A^* & 0 \end{pmatrix}, \\ M_{C,\mathbf{k}}^{ABC} &\equiv \begin{pmatrix} 0 & 0 & -f_B^* \\ 0 & 0 & f_A^* \\ -f_B & f_A & 0 \end{pmatrix} \end{aligned} \quad (4.52)$$

for $u = A, B, C$, respectively. Consequently, any \mathcal{A}_I -CLS can be used to build a linear flat-band Bloch Hamiltonian

$$H(\mathbf{k}) = \lambda_{\mathbf{k}}^{ABC} M_{u,\mathbf{k}}^{ABC}, \quad (4.53)$$

where $\lambda_{\mathbf{k}}^{ABC}$ is any function with the periodicity of the first Brillouin zone. This Hamiltonian has a band structure

$$\epsilon_0(\mathbf{k}) = 0, \quad \epsilon_{1,2}(\mathbf{k}) = \pm \lambda_{\mathbf{k}}^{ABC} \sqrt{\langle m_u^{ABC} | m_u^{ABC} \rangle}. \quad (4.54)$$

The bands are particle-hole symmetric due to a chiral symmetry (2.3) with $\mathcal{S} = \text{diag}(\tau_A, \tau_B, \tau_C)$, where $\tau_{a \neq u} = 1$ and $\tau_{a=u} = -1$. Note that $\lambda_{\mathbf{k}}^{ABC} = 1$ in the following.

Examples. CLSs of type \mathcal{A}_I can be easily found on any $N = 3$ lattice, since the functions $f_{a \neq u}$ are completely unconstrained. As an example, consider the CLS on the Kagome lattice shown in Fig. 4.8(a). Evidently, we have $u = B$, and the associated BCLS (4.49) is given by

$$f_A = w_{A_1} e^{-ik_-} + w_{A_2} e^{ik_-}, \quad f_C = w_{C_1} e^{ik_x} + w_{C_2} e^{-ik_x}. \quad (4.55)$$

Inserting into Eq. (4.53), we obtain a flat-band tight-binding model

$$H(\mathbf{k}) = \begin{pmatrix} 0 & H_{AB}(\mathbf{k}) & 0 \\ H_{AB}^*(\mathbf{k}) & 0 & H_{BC}(\mathbf{k}) \\ 0 & H_{BC}^*(\mathbf{k}) & 0 \end{pmatrix}, \quad (4.56)$$

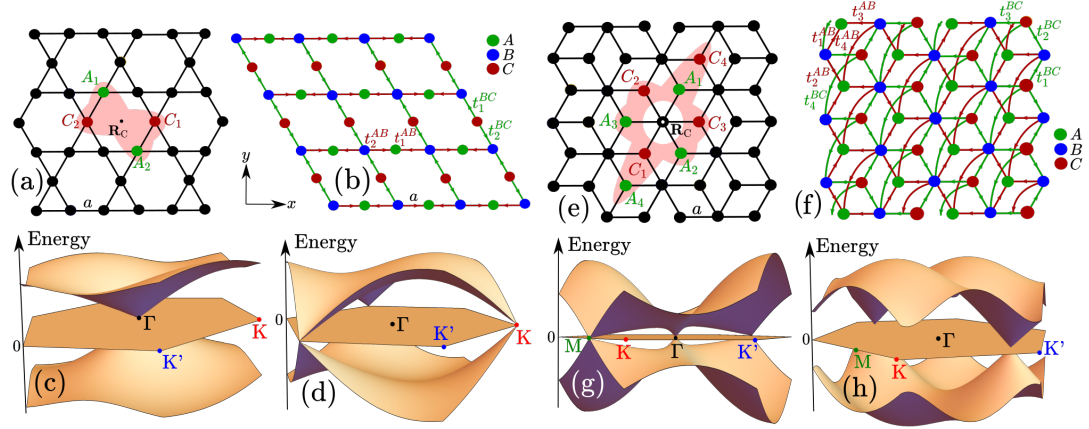


Fig. 4.8 – (a) An \mathcal{A}_I -CLS on the Kagome lattice. (b) Flat-band tight-binding model built from it. Hopping directions are determined by the CLS shape as indicated by the colors. The corresponding band structure is shown in (c) for $w_{a_1} = -w_{a_2} = 1$ and in (d) for $w_{a_1} = 1, w_{a_2} = e^{i\pi/3}$. (e) A more complicated \mathcal{A}_I -CLS on the dice lattice. (f) Tight-binding model built from it. The corresponding band structure is shown in (g) for $w_{a_1} = -w_{a_4} = w_{A_2} = w_{C_2}/2 = -w_{A_3} = -w_{C_3}/2 = 1$ and in (h) for $w_{a_{1,2,3}} = -w_{a_4} = 1$.

where

$$H_{AB}(\mathbf{k}) = t_1^{AB} e^{-ik_x} + t_2^{AB} e^{ik_x}, \quad H_{BC}(\mathbf{k}) = t_1^{BC} e^{-ik_-} + t_2^{BC} e^{ik_-}. \quad (4.57)$$

This model has the topology of a Lieb lattice [cf. Fig. 2.1(a)] and is depicted in Fig. 4.8(b). The hopping directions are determined by the shape of the input CLS, that is, by the vectors δ_{a_i} , although in a different fashion than for the quadratic models (see Appendix IV.A for details). Similarly, the hopping parameters $t_i^{AB} \equiv -w_{C_i}^*$ and $t_i^{BC} \equiv w_{A_i}$ again depend on the CLS amplitudes, which allows to design the band structure. For instance, a (singular) band crossing may be created at the Γ point [Fig. 4.8(c)] or at the K points [Fig. 4.8(d)].

As a more complicated example, consider the CLS on the dice lattice shown in Fig. 4.8(e). The corresponding BCLS (4.49) is given by

$$\begin{aligned} f_A &= w_{A_1} e^{ik_+} + w_{A_2} e^{ik_-} + w_{A_3} e^{-ik_x} + w_{A_4} e^{-2ik_+}, \\ f_C &= w_{C_1} e^{-ik_+} + w_{C_2} e^{-ik_-} + w_{C_3} e^{ik_x} + w_{C_4} e^{2ik_+}, \end{aligned} \quad (4.58)$$

and inserting into Eq. (4.53) leads to a flat-band model of the form (4.56), where now

$$\begin{aligned} H_{AB}(\mathbf{k}) &= t_1^{AB} e^{ik_+} + t_2^{AB} e^{ik_-} + t_3^{AB} e^{-ik_x} + t_4^{AB} e^{-2ik_+}, \\ H_{BC}(\mathbf{k}) &= t_1^{BC} e^{ik_+} + t_2^{BC} e^{ik_-} + t_3^{BC} e^{-ik_x} + t_4^{BC} e^{-2ik_+}, \end{aligned} \quad (4.59)$$

with hopping parameters as defined above. This model is depicted in Fig. 4.8(f) and allows for different kinds of band crossings depending on the CLS amplitudes. For example, crossings may appear at the Γ and M points [Fig. 4.8(g)], but also away from high-symmetry points [Fig. 4.8(h)]. Finally, note that a similar construction works in *any spatial dimension*, since \mathcal{A}_I -CLSs can be easily built just by leaving one sublattice empty.

Flat-band models from \mathcal{A}_{II} -CLSs. The second possibility for building an $N = 3$ linear flat-band Hamiltonian arises if the input CLS (4.31) occupies all sublattices, but with the constraint that the orbitals of two sublattices need to be located at the same positions with respect to the localization center. The orbitals of the third sublattice (indicated by u) are unconstrained. We will call a CLS of this kind type \mathcal{A}_{II} . Any \mathcal{A}_{II} -CLS corresponds to an \mathcal{A}_{II} -BCLS of the form

$$\begin{aligned} |f(\mathbf{k})\rangle &= |n_u^{ABC}\rangle, \\ |n_A^{ABC}\rangle &\equiv (f_A, \gamma_1 f_C, \gamma_2 f_C)^T, \\ |n_B^{ABC}\rangle &\equiv (\gamma_2 f_A, f_B, \gamma_1 f_A)^T, \\ |n_C^{ABC}\rangle &\equiv (\gamma_1 f_B, \gamma_2 f_B, f_C)^T, \end{aligned} \quad (4.60)$$

where $\gamma_{1,2}$ are complex numbers determined by the CLS amplitudes. Again, for any given u , we can construct all vectors orthogonal to the BCLS, of which there are two ($|f_{1,u}^\perp\rangle$ and $|f_{2,u}^\perp\rangle$) in the present case:

$$\begin{aligned} |f_{1,A}^\perp\rangle &= (-\gamma_1^* f_C^*, f_A^*, 0)^T, & |f_{2,A}^\perp\rangle &= (\gamma_2^* f_C^*, 0, -f_A^*)^T, \\ |f_{1,B}^\perp\rangle &= (0, -\gamma_1^* f_A^*, f_B^*)^T, & |f_{2,B}^\perp\rangle &= (-f_B^*, \gamma_2^* f_A^*, 0)^T, \\ |f_{1,C}^\perp\rangle &= (f_C^*, 0, -\gamma_1^* f_B^*)^T, & |f_{2,C}^\perp\rangle &= (0, -f_C^*, \gamma_2^* f_B^*)^T. \end{aligned} \quad (4.61)$$

Additionally, there is a constant vector $|e_{1,u}\rangle$ orthogonal to the BCLS, which takes the form $|e_{1,A}\rangle = (0, \gamma_2^*, -\gamma_1^*)^T$, $|e_{1,B}\rangle = (-\gamma_1^*, 0, \gamma_2^*)^T$, or $|e_{1,C}\rangle = (\gamma_2^*, -\gamma_1^*, 0)^T$. Again, the existence of such an orthogonal constant vector characterizes the CLS as type \mathcal{A} . Now we can construct a matrix that vanishes on the BCLS as a linear combination

$$N_{u,\mathbf{k}}^{ABC} = \sum_{i=1,2} \lambda_i \left(|e_{1,u}\rangle \langle f_{i,u}^\perp| + |f_{i,u}^\perp\rangle \langle e_{1,u}| \right), \quad (4.62)$$

where more explicitly

$$\begin{aligned} N_{A,\mathbf{k}}^{ABC} &\equiv \begin{pmatrix} 0 & \gamma_2(-\lambda_1\gamma_1^* + \lambda_2\gamma_2^*)f_C^* & \gamma_1(\lambda_1\gamma_1^* - \lambda_2\gamma_2^*)f_C^* \\ \dots & 2\lambda_1 \operatorname{Re}(\gamma_2^* f_A) & -\lambda_1\gamma_1 f_A^* - \lambda_2\gamma_2^* f_A \\ \dots & \dots & 2\lambda_2 \operatorname{Re}(\gamma_1^* f_A) \end{pmatrix}, \\ N_{B,\mathbf{k}}^{ABC} &\equiv \begin{pmatrix} 2\lambda_2 \operatorname{Re}(\gamma_1^* f_B) & \gamma_1^*(\lambda_1\gamma_1 - \lambda_2\gamma_2) f_A & -\lambda_1\gamma_1^* f_B - \lambda_2\gamma_2 f_B^* \\ \dots & 0 & \gamma_2(-\lambda_1\gamma_1^* + \lambda_2\gamma_2^*) f_A^* \\ \dots & \dots & 2\lambda_1 \operatorname{Re}(\gamma_2^* f_B) \end{pmatrix}, \\ N_{C,\mathbf{k}}^{ABC} &\equiv \begin{pmatrix} 2\lambda_1 \operatorname{Re}(\gamma_2^* f_C) & -\lambda_1\gamma_1 f_C^* - \lambda_2\gamma_2^* f_C & \gamma_2^*(-\lambda_1\gamma_1 + \lambda_2\gamma_2) f_B \\ \dots & 2\lambda_2 \operatorname{Re}(\gamma_1^* f_C) & \gamma_1^*(\lambda_1\gamma_1 - \lambda_2\gamma_2) f_B \\ \dots & \dots & 0 \end{pmatrix}, \end{aligned}$$

where the dotted elements are obtained by Hermiticity. It is easy to check that indeed $N_{u,\mathbf{k}}^{ABC} |n_u^{ABC}\rangle = 0$.

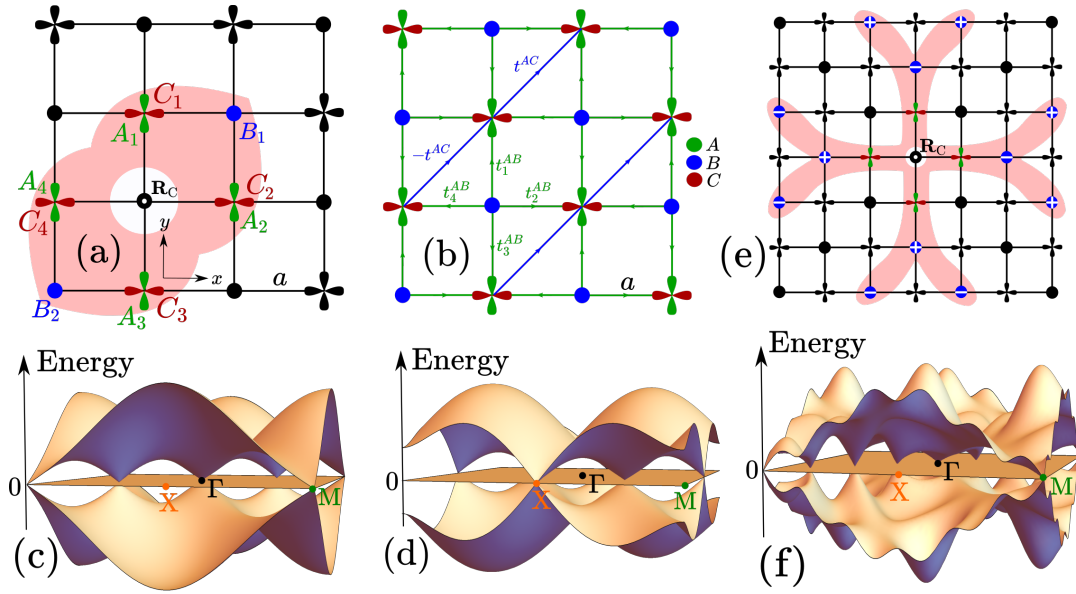


Fig. 4.9 – (a) An \mathcal{A}_{II} -CLS on a multiorbital square lattice. (b) Flat-band tight-binding model built from it. The corresponding band structure with $w_{B_1} = 1$ is shown in (c) for $w_{A_1} = -w_{A_2} = w_{A_3}/2 = -w_{A_4}/2 = 1$ and in (d) for $w_{A_1} = w_{A_2} = -w_{A_3}/2 = -w_{A_4}/2 = 1$. (e) A more complicated \mathcal{A}_{II} -CLS with $w_{A_1} = -w_{A_2} = w_{A_3}/2 = -w_{A_4}/2 = 1$ and $w_{B_i} = \pm 1$ as shown. (f) Band structure for the tight-binding model built from it.

Consequently, any \mathcal{A}_{II} -CLS can be used to build a linear flat-band Bloch Hamiltonian

$$H(\mathbf{k}) = \lambda_{\mathbf{k}}^{ABC} N_{u,\mathbf{k}}^{ABC}, \quad (4.63)$$

where $\lambda_{\mathbf{k}}^{ABC}$ is any function with the periodicity of the Brillouin zone. Again $\lambda_{\mathbf{k}}^{ABC} = 1$ in the following. This Hamiltonian has a band structure of the form (4.36), where now

$$\begin{aligned} C_1 &= 2 \operatorname{Re}[(\lambda_1 \gamma_2^* + \lambda_2 \gamma_1^*) f_u], \\ C_2 &= C_1^2 + 2|\lambda_1 \gamma_1 - \lambda_2 \gamma_2|^2 \langle n_u^{ABC} | n_u^{ABC} \rangle. \end{aligned} \quad (4.64)$$

Clearly, the system is tunable by choice of the CLS amplitudes, but also for fixed CLS amplitudes via the parameters $\lambda_{1,2}$. Note also that if $C_1 = 0$, for example by taking $\lambda_1 = \lambda_2$ and $\gamma_1 = -\gamma_2$, then the bands become particle-hole symmetric due to the presence of a chiral symmetry (2.3) with diagonal matrix elements $\mathcal{S}_{aa} = -\delta_{au}$ and off-diagonal elements $\mathcal{S}_{ab} = 1 - \delta_{au} - \delta_{bu}$.

Examples. CLSs of type \mathcal{A}_{II} cannot be found on all $N = 3$ lattices, due to the constraints on the CLS mentioned above. However it is easy to devise an arbitrary number of \mathcal{A}_{II} -CLSs for instance on multiorbital lattices. Out of the many possibilities, we here present two examples on a square lattice. For simplicity, we ensure chiral symmetry by fixing $\gamma_2 = -\gamma_1 = 1$ and $\lambda_1 = \lambda_2 = 1/2$, and take the unconstrained sublattice as $u = b$.

The first example is obtained from the CLS shown in Fig. 4.9(a). In order for the CLS to be of \mathcal{A}_{II} -type with γ_i as specified above, we have to take $w_{A_i} = -w_{C_i}$. Further we choose $w_{B_1} = -w_{B_2}$ with w_{B_i} real for concreteness. The corresponding

BCLS, $|n_B^{ABC}\rangle$, cf. Eq. (4.60), is then given by

$$\begin{aligned} f_A &= w_{A_1} e^{ik_y} + w_{A_2} e^{ik_x} + w_{A_3} e^{-ik_y} + w_{A_4} e^{-ik_x}, \\ f_B &= 2iw_{B_1} \sin(k_x + k_y). \end{aligned} \quad (4.65)$$

Note that by our choice of the CLS amplitudes we have ensured that f_B is purely imaginary, which guarantees the absence of intra-sublattice hopping. Indeed, inserting the BCLS into Eq. (4.63), we obtain a flat-band tight-binding model

$$H(\mathbf{k}) = \begin{pmatrix} 0 & H_{AB}(\mathbf{k}) & H_{AC}(\mathbf{k}) \\ H_{AB}^*(\mathbf{k}) & 0 & H_{BC}(\mathbf{k}) \\ H_{AC}^*(\mathbf{k}) & H_{BC}^*(\mathbf{k}) & 0 \end{pmatrix}, \quad (4.66)$$

where

$$\begin{aligned} H_{AB}(\mathbf{k}) &= H_{BC}^*(\mathbf{k}) = t_1^{AB} e^{ik_y} + t_2^{AB} e^{ik_x} + t_3^{AB} e^{-ik_y} + t_4^{AB} e^{-ik_x}, \\ H_{AC}(\mathbf{k}) &= t^{AC} e^{i(k_x+k_y)} - t^{AC} e^{-i(k_x+k_y)}, \end{aligned} \quad (4.67)$$

with hopping parameters $t_i^{AB} \equiv w_{A_i}$ and $t^{AC} \equiv w_{B_1}$, as shown in Fig. 4.9(b). By choice of the numerical values of the CLS amplitudes a threefold band crossing may be created for example at the Γ and M points [Fig. 4.9(c)] or at the X point [Fig. 4.9(d)].

A more complicated example for an \mathcal{A}_{II} -CLS, where again $w_{A_i} = -w_{C_i}$ and $w_{B_i} = \pm 1$, is shown in Fig. 4.9(e). Inserting into Eq. (4.63) leads to a flat-band tight-binding model with linear band crossings at the Γ and M points, as well as additional crossings along the (1,1)-direction, as shown in Fig. 4.9(f). Note finally that \mathcal{A}_{II} -CLSs can of course also be constructed in 3D, for example on a multiorbital cubic lattice.

Flat-band models from type- \mathcal{B} compact localized states

As we have seen above, a constant orthogonal vector $|e_i\rangle$ exists only if one component of the BCLS vanishes (type \mathcal{A}_I) or if two components are proportional to each other (type \mathcal{A}_{II}). We cannot find any other kind of CLSs that allow for a constant orthogonal vector (except trivial uninteresting cases where two or all three sublattices are unoccupied). We thus believe to have described the scenario (\mathcal{A}) exhaustively. However, a flat-band Bloch Hamiltonian can also be constructed if the scenario (\mathcal{B}) applies. Two possible cases are presented here, though it remains unclear if the scenario (\mathcal{B}) is exhaustively captured by them.

Flat-band models from \mathcal{B}_I -CLSs. A third possibility for building an $N = 3$ linear flat-band Hamiltonian arises if the input CLS (4.31) occupies all sublattices, but with the following constraints: the orbitals of each given type $a \in \{A, B, C\}$ need to be arranged pairwise at equal distance from the localization center, and the signs of the CLS amplitudes w_{a_i} within each pair have to be identical or opposite. We may denote such a CLS as type \mathcal{B}_I . These constraints are formulated more precisely in terms of the corresponding \mathcal{B}_I -BCLS, which takes the form

$$|f(\mathbf{k})\rangle = |o^{ABC}\rangle \equiv (f_A, f_B, f_C)^T, \quad f_a^* = \kappa_a f_a, \quad \kappa_A \kappa_B \kappa_C = -1, \quad (4.68)$$

that is, each component f_a is either real ($\kappa_a = 1$) or imaginary ($\kappa_a = -1$), and the three signs κ_a are correlated such that $f_A f_B f_C = -(f_A f_B f_C)^*$. It is easy to find three vectors $|f_i^\perp\rangle$ orthogonal to the BCLS, namely

$$\begin{aligned} |f_1^\perp\rangle &= (0, -\kappa_C f_C, \kappa_B f_B)^T, \\ |f_2^\perp\rangle &= (-f_C, 0, -\kappa_B f_A)^T, \\ |f_3^\perp\rangle &= (f_B, \kappa_C f_A, 0)^T. \end{aligned} \quad (4.69)$$

However, there is clearly no constant vector orthogonal to the BCLS, so it cannot be of type \mathcal{A} . Interestingly, we can nevertheless construct a linear Hermitian matrix orthogonal to the BCLS as

$$O_{\mathbf{k}}^{ABC} \equiv \sum_i |e_i\rangle \langle f_i^\perp| = \sum_i |f_i^\perp\rangle \langle e_i| = \begin{pmatrix} 0 & -f_C & f_B \\ -\kappa_C f_C & 0 & \kappa_C f_A \\ \kappa_B f_B & -\kappa_B f_A & 0 \end{pmatrix}, \quad (4.70)$$

where $i = 1, 2, 3$ and $|e_i\rangle = |v_i\rangle$, with $|v_i\rangle$ three-component unit basis vectors as introduced earlier. Clearly, the matrix $O_{\mathbf{k}}^{ABC}$ is of the desired form (4.48) with $\lambda_i = 1/2$, and satisfies the property (\mathcal{B}).

Thus, any \mathcal{B}_I -CLS can be used to build a linear flat-band Bloch Hamiltonian

$$H(\mathbf{k}) = \lambda_{\mathbf{k}}^{ABC} O_{\mathbf{k}}^{ABC}. \quad (4.71)$$

This Hamiltonian has a band structure

$$\epsilon_0(\mathbf{k}) = 0, \quad \epsilon_{1,2}(\mathbf{k}) = \pm \lambda_{\mathbf{k}}^{ABC} \sqrt{\langle o^{ABC} | o^{ABC} \rangle}, \quad (4.72)$$

which is particle-hole symmetric due to the presence of a CP symmetry (2.10) with $\mathbf{x} = \mathbf{k}$ and $\mathcal{C} = \text{diag}(\kappa_A, \kappa_B, \kappa_C)$. Again $\lambda_{\mathbf{k}}^{ABC} = 1$ hereafter.

Examples. CLSs of type \mathcal{B}_I cannot be found on all $N = 3$ lattices, due to the above-mentioned constraints. For instance, a \mathcal{B}_I -CLS cannot exist on the dice lattice, but it can exist on the Kagome lattice. As an example, consider the CLS shown in Fig. 4.10(a), where we take the amplitudes w_{a_1} to be real for concreteness. In order for the CLS to qualify as \mathcal{B}_I , the three amplitudes w_{a_2} have to be chosen as $w_{a_2} = \kappa_a w_{a_1}$, with $\kappa_A \kappa_B \kappa_C = -1$. The corresponding BCLS (4.68) is determined by

$$\begin{aligned} f_A &= w_{A_1} \left(e^{-ik_-} + \kappa_A e^{ik_-} \right), \\ f_B &= w_{B_1} \left(e^{ik_+} + \kappa_B e^{-ik_+} \right), \\ f_C &= w_{C_1} \left(e^{ik_x} + \kappa_C e^{-ik_x} \right). \end{aligned} \quad (4.73)$$

Inserting into Eq. (4.71), we find a flat-band tight-binding model of the form (4.66), where

$$\begin{aligned} H_{AB}(\mathbf{k}) &= t^{AB} \left(e^{ik_x} + \kappa_C e^{-ik_x} \right), \\ H_{AC}(\mathbf{k}) &= t^{AC} \left(e^{ik_+} + \kappa_B e^{-ik_+} \right), \\ H_{BC}(\mathbf{k}) &= t^{BC} \left(e^{-ik_-} + \kappa_A e^{ik_-} \right). \end{aligned} \quad (4.74)$$

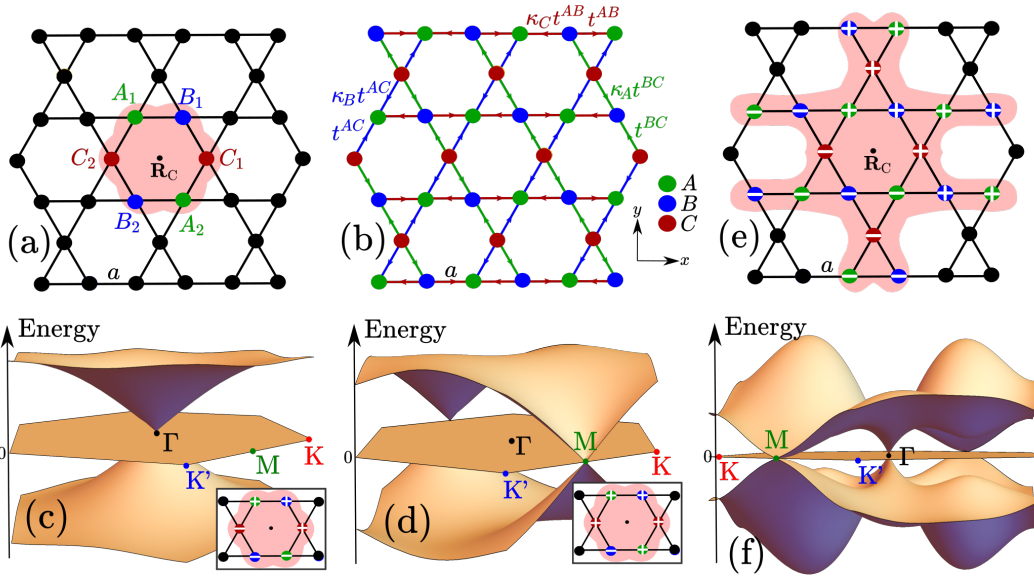


Fig. 4.10 – (a) A CLS on the Kagome lattice that is type \mathcal{B}_I if the amplitudes are properly correlated. (b) Tight-binding model built from the CLS. The corresponding band structure with $w_{a_1} = 1$ is shown in (c) for $\kappa_a = -1$ and in (d) for $\kappa_A = -\kappa_B = \kappa_C = 1$. (e) A more extended \mathcal{B}_I -CLS on the Kagome lattice, with $w_{a_i} = \pm 1$ as shown. (f) Band structure for the corresponding tight-binding model.

Here, the hopping parameters are $t^{AB} \equiv -w_{C_1}$, $t^{AC} \equiv w_{B_1}$ and $t^{BC} \equiv \kappa_C w_{A_1}$. This model is shown in Fig. 4.10(b). Again, the band structure can be designed using the CLS amplitudes. An example with a band crossing at the Γ point is shown in Fig. 4.10(c) – this is equivalent to a “breathing Kagome” lattice (Green et al. 2010) – and one with a band crossing at the M point in Fig. 4.10(d).

As a more complicated example, consider the extended \mathcal{B}_I -CLS shown in Fig. 4.10(e). Inserting into Eq. (4.71) leads to a flat-band tight-binding model with linear band crossings at the Γ and M points, as shown in Fig. 4.10(f). Finally, an example for a \mathcal{B}_I -CLS on a 3D lattice is given in Appendix IV.D.

Flat-band models from \mathcal{B}_{II} -CLSs. The last possibility for building an $N = 3$ linear flat-band Hamiltonian that we will consider arises if the input CLS (4.31) occupies all sublattices, with the following constraints: under inversion, the orbital positions of one sublattice are mapped to those of a second sublattice (with the localization center being the center of inversion), and the CLS amplitudes are related by complex conjugation. At the same time, the third sublattice (indicated by u) has orbitals (position and amplitude) that are correlated in a symmetric fashion with respect to the localization center. We may define such a CLS as type \mathcal{B}_{II} . More precisely, any \mathcal{B}_{II} -CLS has a corresponding \mathcal{B}_{II} -BCLS

$$\begin{aligned}
 |f(\mathbf{k})\rangle &= |q_u^{ABC}\rangle, \\
 |q_A^{ABC}\rangle &\equiv (f_A, -f_C^*, f_C)^T, \\
 |q_B^{ABC}\rangle &\equiv (f_A, f_B, -f_A^*)^T, \\
 |q_C^{ABC}\rangle &\equiv (-f_B^*, f_B, f_C)^T,
 \end{aligned} \tag{4.75}$$

where the component f_u is real, and thus $f_A f_B f_C = (f_A f_B f_C)^*$. For any given u , there are three vectors $|f_{i,u}^\perp\rangle$ orthogonal to the BCLS, namely

$$\begin{aligned} |f_{1,A}^\perp\rangle &= (0, f_C^*, f_C)^T, & |f_{2,A}^\perp\rangle &= (f_C, f_A, 0)^T, & |f_{3,A}^\perp\rangle &= (f_C^*, 0, -f_A)^T, \\ |f_{1,B}^\perp\rangle &= (-f_B, f_A^*, 0)^T, & |f_{2,B}^\perp\rangle &= (f_A, 0, f_A^*)^T, & |f_{3,B}^\perp\rangle &= (0, f_A, f_B)^T, \\ |f_{1,C}^\perp\rangle &= (f_C, 0, f_B)^T, & |f_{2,C}^\perp\rangle &= (0, -f_C, f_B^*)^T, & |f_{3,C}^\perp\rangle &= (f_B^*, f_B, 0)^T. \end{aligned}$$

Again, there is no constant vector orthogonal to the BCLS, but a Hermitian matrix that vanishes on $|q_u^{ABC}\rangle$ can be constructed as

$$Q_{u,\mathbf{k}}^{ABC} = \sum_i |e_i\rangle \langle f_{i,u}^\perp| = \sum_i |f_{i,u}^\perp\rangle \langle e_i|, \quad (4.76)$$

where $i = 1, 2, 3$ and $|e_i\rangle = |v_i\rangle$, or more explicitly

$$\begin{aligned} Q_{A,\mathbf{k}}^{ABC} &= \begin{pmatrix} 0 & f_C & f_C^* \\ f_C^* & f_A & 0 \\ f_C & 0 & -f_A \end{pmatrix}, & Q_{B,\mathbf{k}}^{ABC} &= \begin{pmatrix} -f_B & f_A & 0 \\ f_A^* & 0 & f_A \\ 0 & f_A^* & f_B \end{pmatrix}, \\ Q_{C,\mathbf{k}}^{ABC} &= \begin{pmatrix} f_C & 0 & f_B^* \\ 0 & -f_C & f_B \\ f_B & f_B^* & 0 \end{pmatrix}. \end{aligned} \quad (4.77)$$

Again, the matrix $Q_{u,\mathbf{k}}^{ABC}$ is of the desired form (4.48) with $\lambda_i = 1/2$, and satisfies the property (\mathcal{B}) . Thus, any \mathcal{B}_{II} -CLS can be used to build a linear flat-band Bloch Hamiltonian

$$H(\mathbf{k}) = \lambda_{\mathbf{k}}^{ABC} Q_{u,\mathbf{k}}^{ABC}. \quad (4.78)$$

This Hamiltonian is in fact a pseudospin-1 Hamiltonian, that is, it can be written in the form $H_{\mathbf{k}} = h_x(\mathbf{k})S_x + h_y(\mathbf{k})S_y + h_z(\mathbf{k})S_z$, with pseudospin-1 operators that fulfill the algebra (2.5). It has a band structure

$$\epsilon_0(\mathbf{k}) = 0, \quad \epsilon_{1,2}(\mathbf{k}) = \pm \lambda_{\mathbf{k}}^{ABC} \sqrt{\langle q_u^{ABC} | q_u^{ABC} \rangle}, \quad (4.79)$$

whose particle-hole symmetric character is protected by a CP symmetry (2.10) with $\mathbf{x} = \mathbf{k}$ and $\mathcal{C} = e^{i\pi S_y}$, with diagonal matrix elements $\mathcal{C}_{aa} = -\delta_{au}$ and off-diagonal elements $\mathcal{C}_{ab} = 1 - \delta_{au} - \delta_{bu}$. Again $\lambda_{\mathbf{k}}^{ABC} = 1$ in the examples below.

Examples. CLSs of type \mathcal{B}_{II} cannot be found on all $N = 3$ lattices due to the requirement of two sublattices being the conjugate of each other. For instance, a \mathcal{B}_{II} -CLS cannot exist on the Kagome lattice, but it can exist on the dice lattice. As an example, consider the CLS shown in Fig. 4.11(a), where we fix w_{B_i} to be imaginary for concreteness. In order for the CLS to qualify as \mathcal{B}_{II} , we now have to take $w_{B_2} = -w_{B_1}$, implying $u = B$, and additionally $w_{C_i} = -w_{A_i}^*$. The corresponding BCLS $|q_B^{ABC}\rangle$, cf. Eq. (4.75), is then determined by

$$f_A = w_{A_1} e^{ik_+} + w_{A_2} e^{ik_-} + w_{A_3} e^{-ik_x}, \quad f_B = 2iw_{B_1} \sin(k_x + k_+). \quad (4.80)$$

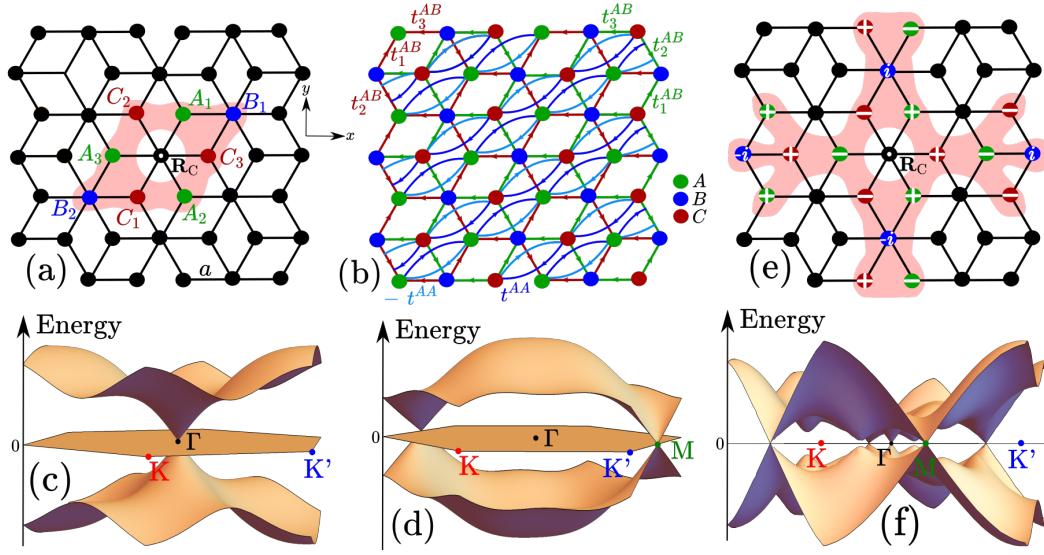


Fig. 4.11 – (a) A CLS on the dice lattice that is \mathcal{B}_{II} if the amplitudes are properly correlated. (b) Tight-binding model built from the CLS. The corresponding band structure is shown in (c) for $w_{A_1} = w_{A_2} = -w_{A_3}/2 = 1$, $w_{B_1} = i$ and in (d) for $w_{A_1} = w_{A_2} = w_{A_3}/2 = 1$, $w_{B_1} = i$. (e) A more extended \mathcal{B}_{II} -CLS on the dice lattice, with $w_{A_i} = \pm 1$ and $w_{B_i} = \pm i$ as shown. (f) Band structure for the corresponding tight-binding model.

Inserting into Eq. (4.78), we find a flat-band tight-binding model

$$H(\mathbf{k}) = \begin{pmatrix} H_{AA}(\mathbf{k}) & H_{AB}(\mathbf{k}) & 0 \\ H_{AB}^*(\mathbf{k}) & 0 & H_{BC}(\mathbf{k}) \\ 0 & H_{BC}^*(\mathbf{k}) & H_{CC}(\mathbf{k}) \end{pmatrix}, \quad (4.81)$$

where

$$\begin{aligned} H_{AA}(\mathbf{k}) &= -H_{CC}(\mathbf{k}) = 2it^{AA} \sin(k_x + k_+), \\ H_{AB}(\mathbf{k}) &= H_{BC}(\mathbf{k}) = t_1^{AB} e^{ik_+} + t_2^{AB} e^{ik_-} + t_3^{AB} e^{-ik_x}, \end{aligned} \quad (4.82)$$

with hopping parameters $t^{AA} \equiv -w_{B_1}$ and $t_i^{AB} \equiv w_{A_i}$. The corresponding real-space tight-binding model is shown in Fig. 4.11(b), and its band structure can be designed using the CLS amplitudes. An example with a band crossing at the Γ point is shown in Fig. 4.11(c), and one with a crossing at the M point in Fig. 4.11(d). Note that band crossings at the K points could be created by taking an input CLS with six B orbitals arrayed hexagonally.

As a more complicated example, consider the extended \mathcal{B}_{II} -CLS shown in Fig. 4.11(e). Inserting into Eq. (4.78) leads to a flat-band tight-binding model with linear crossings at the Γ and M points, as shown in Fig. 4.11(f). Finally, an example for a \mathcal{B}_{II} -CLS in 3D is given in Appendix IV.D.

4.5.2 | N -band models

Here we outline how to extend the construction of a linear flat-band Hamiltonian to any N , without developing the theory in full detail. Consider again a generic CLS

(4.1) built on a lattice with N orbitals per unit cell, associated to a BCLS (4.8). Two general procedures for building a linear flat-band Hamiltonian from such a CLS can be adopted.

The first consists in looking for a Hamiltonian of the form (4.48), just like we did in the three-band case. Such a linear flat-band Hamiltonian cannot be built from a completely arbitrary CLS, however it can be built if the CLS is subject to some constraints. For example, for $N = 4$, if the D sublattice is unoccupied by the input CLS, $|f(\mathbf{k})\rangle = (f_A, f_B, f_C, 0)$, one can find three vectors that are linear in the f_a and orthogonal to the BCLS: $|f_{1,D}^\perp\rangle = |f^{AB}\rangle$, $|f_{2,D}^\perp\rangle = |f^{AC}\rangle$, $|f_{3,D}^\perp\rangle = |f^{BC}\rangle$, as given by Eq. (4.41). Additionally there is a constant vector $|e_1\rangle = |v_4\rangle$ which is also orthogonal to the BCLS. A CLS of this kind is easily identified as type \mathcal{A} , and a flat-band Hamiltonian (4.48) consisting of a linear combination of three matrices can be built from it:

$$H(\mathbf{k}) = \begin{pmatrix} 0 & 0 & 0 & \lambda_1 f_B^* + \lambda_2 f_C^* \\ 0 & 0 & 0 & -\lambda_1 f_A^* + \lambda_3 f_C^* \\ 0 & 0 & 0 & -\lambda_2 f_A^* - \lambda_3 f_B^* \\ \lambda_1 f_B + \lambda_2 f_C & -\lambda_1 f_A + \lambda_3 f_C & -\lambda_2 f_A - \lambda_3 f_B & 0 \end{pmatrix}.$$

Clearly, while a type \mathcal{A}_I Hamiltonian is not tunable for $N = 3$, cf. Eq. (4.53), it is tunable by three parameters $\lambda_{1,2,3}$ for $N = 4$. This reflects the general fact that more tunability is present when the number of bands increases. While we have only addressed the example of an \mathcal{A}_I -CLS here, for any given $N > 3$ it would be interesting to classify all possible types of CLSs that exhibit appropriate internal symmetries that make them suitable for the construction of linear flat-band models (4.48).

The second possible procedure is very similar in spirit to what was done in Section 4.4 for the quadratic flat-band models. There, we identified the $N = 2$ quadratic Hamiltonian (4.25) as a *building block* that allowed to construct $N \times N$ matrices $F_{\mathbf{k}}^{ab}$ that vanish on $|f(\mathbf{k})\rangle$; the N -band quadratic Hamiltonian (4.43) was then formed as a linear combination of these matrices. In exactly the same way, we can now regard the $N = 3$ linear Hamiltonians (4.53), (4.63), (4.71) and (4.78) as *building blocks* that will allow to construct $N \times N$ matrices $F_{\mathbf{k}}^{abc}$ that vanish on $|f(\mathbf{k})\rangle$. An N -band linear flat-band Hamiltonian can then be formed as a linear combination of these matrices,

$$H(\mathbf{k}) = \sum_{a,b>a,c>b} \lambda_{\mathbf{k}}^{abc} F_{\mathbf{k}}^{abc}, \quad (4.83)$$

where $\lambda_{\mathbf{k}}^{abc}$ is an arbitrary function with the periodicity of the Brillouin zone (again $\lambda_{\mathbf{k}}^{abc} = \lambda_{abc}$ hereafter). The $N \geq 4$ linear models obtained from Eq. (4.83) are, just like the $N \geq 3$ quadratic models, tunable by the input CLS *and* the parameters λ_{abc} that arise from the linear combination. For more details about this method and for explicit examples, we refer the reader to Graf and Piéchon (2021b). Here we only mention that in order to give rise to a flat-band model (4.83) the input CLS must be decomposable into type \mathcal{A} or type \mathcal{B} sub-CLSs, each of which involves three sublattices (a, b, c) out of the N sublattices.

4.6 | Further remarks on the flat-band design method

4.6.1 | Scarcity of linear flat-band models

We should comment on an important difference between the quadratic flat-band Hamiltonians of Section 4.4 and the linear ones of Section 4.5. Namely, there are two fundamental reasons that make the linear flat-band models much rarer than the quadratic models. The first is the following:

- Only for certain classes of input CLSs it is possible to construct a linear matrix $H(\mathbf{k})$ that fulfills $H(\mathbf{k})|f(\mathbf{k})\rangle = 0$.

We have seen this in detail in Section 4.5.1 above, where we found that a given CLS has to possess special properties (type \mathcal{A} or type \mathcal{B}) to allow for the construction of a linear flat-band model.

However, even if some given CLS possesses such properties, it is not automatically guaranteed that the flat-band Hamiltonian constructed from it will be *reasonable*, that is, make sense when transformed to real space [cf. condition (4.20)]. For example, while we have only studied \mathcal{A}_I -CLSs for which the corresponding linear flat-band Hamiltonian (4.53) does make sense on a lattice (cf. Fig. 4.8), it is easy to find a counterexample. Indeed, consider the CLS shown in Fig. 4.12(a). It perfectly qualifies as an \mathcal{A}_I -CLS with $u = B$, however we can convince ourselves that the Bloch Hamiltonian obtained by inserting its BCLS into Eq. (4.53) does not correspond to a reasonable lattice model. Similarly, while we have only studied \mathcal{B}_{II} -CLSs for which Eq. (4.78) makes sense on a lattice (cf. Fig. 4.11), the CLS shown in Fig. 4.12(b) constitutes a counterexample. It perfectly qualifies as a \mathcal{B}_{II} -CLS with $u = A$ if $w_{A_1} = w_{A_2}$ is real and $w_{C_i} = -w_{B_i}^*$, but will not lead to a reasonable real-space model when its BCLS is inserted into Eq. (4.78).

Thus, we can formulate a second constraint that reduces the number of possible linear flat-band models:

- Even if the input CLS belongs to a special class (such as \mathcal{A} or \mathcal{B}), the position of the localization center and the arrangement of the sites around it need to be compatible with the underlying lattice (Appendix IV.A), else the linear matrix $H(\mathbf{k})$ will not make sense in real space.

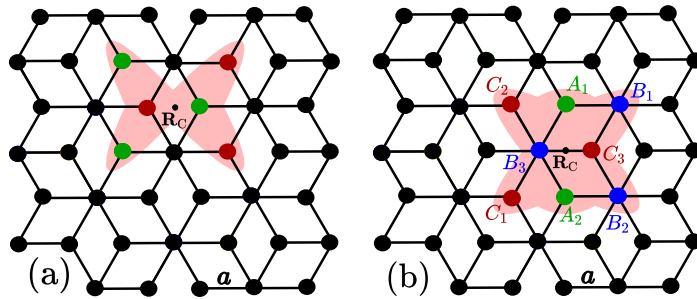


Fig. 4.12 – (a) An \mathcal{A}_I -CLS on the dice lattice for which the linear Hamiltonian (4.53) is not physically reasonable. (b) A \mathcal{B}_{II} -CLS on the dice lattice for which the linear Hamiltonian (4.78) is not physically reasonable.

4.6.2 | Interpolating between linear and quadratic band touching

From the previous discussion we know that all CLSs allow to build quadratic flat-band models, while only special CLSs allow to build linear ones. In other words, each such special CLS can be used to create both a linear *and* a quadratic flat-band model; both models will have a zero-energy flat band and an *identical* flat-band eigenstate. In this way, we can construct tight-binding models that allow to *interpolate smoothly* between multifold linear and quadratic band touchings, without moving the touching point or destroying the flat band.

As a simple example, consider again a six-site CLS on the Kagome lattice, where we fix $w_{A_1} = -w_{B_1} = w_{C_1} = -w_{A_2} = w_{B_2} = -w_{C_2} = 1$ for simplicity, as shown in Fig. 4.13(a). This CLS is clearly of \mathcal{B}_I -type, with BCLS $|f(\mathbf{k})\rangle = (f_A, f_B, f_C)^T = -2i(\sin k_-, \sin k_+, -\sin k_x)^T$, and can thus be used to create a linear Bloch Hamiltonian H_{lin} via Eq. (4.71). But it can also be used to create a quadratic Bloch Hamiltonian H_{quad} via Eq. (4.35). We may now interpolate between the two,

$$H(\mathbf{k}) = (1 - \lambda)H_{\text{lin}} + \lambda H_{\text{quad}}, \quad (4.84)$$

which gives rise to a tight-binding model that can be smoothly tuned from linear to quadratic by the parameter $\lambda \in [0, 1]$, *without* the flat band and its eigenstate being affected in any way. This is illustrated in Fig. 4.13(b)–(d).

In the same way, for any N , any linear band crossing point created via the methods exposed in Section 4.5 can be smoothly tuned to become quadratic, simply by interpolating the respective linear flat-band model with the quadratic model (4.43) built from the same CLS. It should also be mentioned that, from a practical point of view, such tuning processes are often very useful to extract information on a certain physical phenomenon. In the $\alpha - T_3$ model, for example, quantum geometry can be tuned without changing the spectrum, which helps to isolate interband contributions to the orbital magnetic susceptibility from conventional (Landau-Peierls) contributions (Raoux et al. 2014). Here we are in the opposite limit, where the spectrum can be tuned without changing the flat-band eigenstate, which may equally be used to separate quantum geometric from spectral information. Indeed, for exactly this reason, our Hamiltonian (4.84) was recently put to use to study the behavior of the superfluid weight in flat-band systems with band touchings (Huhtinen et al. 2022).

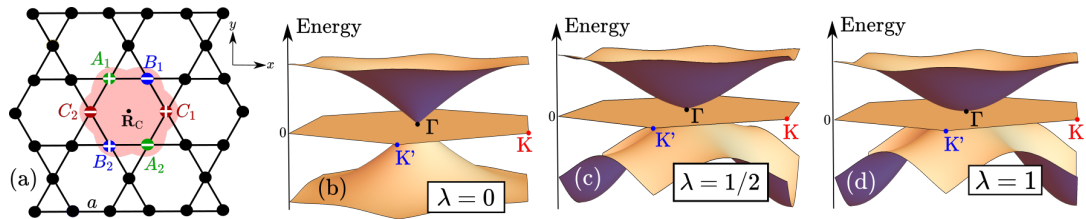


Fig. 4.13 – (a) A CLS on the Kagome lattice. (b)–(d) Band structure of the mixed linear-quadratic tight-binding model (4.84) built from it, for different values of λ . For the linear contribution we use $\lambda_{ABC} = 1$ and for the quadratic one the parameters λ_{ab} are as in Fig. 4.6(d).

4.6.3 | Flat-band models beyond the linear or quadratic class

While the method exposed in this chapter yields infinitely many flat-band tight-binding models, it is clear that not all flat-band models are governed by Bloch Hamiltonians that are simply linear or quadratic functions of the BCLS $|f(\mathbf{k})\rangle$. In fact, it is possible to define matrices $H(\mathbf{k})$ whose elements are higher-order polynomials (e.g. of degree three or four) in the components f_a , and that still verify $H(\mathbf{k})|f(\mathbf{k})\rangle = 0$. Furthermore, some flat-band Hamiltonians may actually be viewed as *infinite-order* polynomials of the BCLS's components. As a prominent example for this, consider the ordinary nearest-neighbor tight-binding model on the ($N = 3$) Kagome lattice [cf. Fig. 2.1(b)]. According to Eq. (2.1), it is captured by a Bloch Hamiltonian

$$H(\mathbf{k}) = 2 \begin{pmatrix} 0 & \cos k_x & \cos k_+ \\ \cos k_x & 0 & \cos k_- \\ \cos k_+ & \cos k_- & 0 \end{pmatrix}, \quad (4.85)$$

where $k_{\pm} = k_x/2 \pm \sqrt{3}k_y/2$, and the unnormalized flat-band eigenstate (BCLS) associated to the flat band at energy $\epsilon_0 = -2$ reads

$$|f(\mathbf{k})\rangle = (f_A, f_B, f_C)^T = (\sin k_-, \sin k_+, -\sin k_x)^T. \quad (4.86)$$

At least in some sectors of the Brillouin zone one may thus be tempted to write the Bloch Hamiltonian as

$$H(\mathbf{k}) = 2 \begin{pmatrix} 0 & \sqrt{1-f_C^2} & \sqrt{1-f_B^2} \\ \sqrt{1-f_C^2} & 0 & \sqrt{1-f_A^2} \\ \sqrt{1-f_B^2} & \sqrt{1-f_A^2} & 0 \end{pmatrix}, \quad (4.87)$$

such that the matrix elements are infinite-order polynomials in the BCLS components. Clearly, the Kagome model lies outside of our flat-band classification scheme.

Another way to see that the Kagome Hamiltonian cannot be covered by our approach is the following. At the Γ point, the flat-band eigenstate (4.86) vanishes, and the band structure exhibits a twofold band touching point. A situation of this kind cannot be captured by the Hamiltonians discussed in this chapter, since they always satisfy $H(\mathbf{k}_0) = 0$ whenever $|f(\mathbf{k}_0)\rangle = 0$, forcing *all bands* to touch simultaneously.

In view of the discussion of this important example, it would be rewarding to establish all possible relations between $H(\mathbf{k})$ and $|f(\mathbf{k})\rangle$, involving both finite- and infinite-order polynomials.

4.7 | Perspectives of flat-band systems

As a last contribution to this chapter, we outline several perspectives connected to the results presented above, which might be worthwhile exploring in more detail.

4.7.1 | Quantum geometry of flat-band models

The quantum geometry of 2D flat-band systems has recently attracted considerable attention. First, there is a wide community interested in the quantum geometry of quasi-flat bands, as they appear for example in twisted bilayer graphene. These quasi-flat bands are often topologically non-trivial, and both the quantum geometry and topology of these bands has profound effects on superconductivity, see for example Törmä et al. (2022) for a very recent review. Second, there is also much work on the quantum geometric properties of touching points between flat and dispersive bands in 2D. Topics that have been addressed include the Berry phase of threefold crossings, for example in a lattice that can be smoothly tuned from a honeycomb to a dice geometry (Raoux et al. 2014); the non-contractible loop states arising from singular band crossings, which were observed in photonic kagome lattices (Ma et al. 2020b); the Landau levels of a singular flat-band crossing (Rhim et al. 2020), and many more.

Here we want to focus on the quantum geometric properties of the flat-band systems that can be obtained by our construction scheme. In principle, we could consider flat-band models with any number of bands N , any spatial dimension d , any degree D of degeneracy for the band crossing point, and any type of low-energy dispersion, and then conduct a systematic investigation of the quantum geometric properties of the corresponding continuum models around the crossing points.

Instead of carrying out this task in full depth, we here showcase the perhaps most interesting case: the four fundamental types of linear crossing points ($N = D = 3$) introduced in Section 4.5.1, with the number of spatial dimensions fixed to $d = 3$. Indeed, given the different symmetry properties of the Hamiltonians (4.53), (4.63), (4.71) and (4.78), it may be expected that the quantum geometry of the corresponding low-energy models should be very different. To obtain a generic continuum model for each given type of crossing point (\mathcal{A}_I , \mathcal{A}_{II} , \mathcal{B}_I or \mathcal{B}_{II}), we assume the crossing to be located at the Γ point without loss of generality, $\mathbf{k} = \mathbf{q}$, and then make an ansatz

$$f_a(\mathbf{q}) = \mathbf{v}_a \cdot \mathbf{q} \quad (4.88)$$

for the BCLS components, where \mathbf{v}_a is a three-component complex vector. To obtain the simplest generic models, we will also constrain $H(\mathbf{q})$ to exhibit an isotropic energy spectrum.

Using the expansion (4.88), we obtain a representative continuum model of type \mathcal{A}_I from Eq. (4.53):

$$H(\mathbf{q}) = \begin{pmatrix} 0 & -\mathbf{v}_C \cdot \mathbf{q} & \mathbf{v}_B \cdot \mathbf{q} \\ -\mathbf{v}_C^* \cdot \mathbf{q} & 0 & 0 \\ \mathbf{v}_B^* \cdot \mathbf{q} & 0 & 0 \end{pmatrix}. \quad (4.89)$$

An isotropic spectrum can be ensured by imposing the constraint $\text{Re}(v_{B,i}^* v_{B,j} + v_{C,i}^* v_{C,j}) = c\delta_{ij}$, where c is a constant. For example, taking $\mathbf{v}_B = (0, 0, -i)$ and $\mathbf{v}_C = (-1, i, 0)$, we get $\epsilon_\alpha = c_\alpha |\mathbf{q}|$, where $c_\alpha = 0, \pm 1$. Note that this spectrum is exactly the same as for a pseudospin-1. To address quantum geometry, we compute

the Berry curvature from Bloch vectors [e.g. by combining Eqs. (3.32) and (3.10)], which yields a pseudovector that takes the form of a *Berry dipole*,

$$\boldsymbol{\Omega}_\alpha(\mathbf{q}) = \kappa_\alpha(\mathbf{d} \cdot \mathbf{q}) \frac{\mathbf{q}}{|\mathbf{q}|^4}, \quad (4.90)$$

with geometric charges $\kappa_0 = 2$, $\kappa_\pm = -1$ and a dipole orientation $\mathbf{d} = (0, 0, 1)$. As a second example, we may take $\mathbf{v}_B = (0, 1, -i \cos \theta)$ and $\mathbf{v}_C = -(1, 0, i \sin \theta)$, which leads to a Berry dipole with the same geometric charges but with a tunable orientation $\mathbf{d} = (\cos \theta, \sin \theta, 0)$. A lattice realization of such a tunable model would be interesting as it would allow to rotate the Berry dipole simply by varying the hopping strengths, but without changing the lattice topology. This is quite reminiscent of the 2D $\alpha - \mathcal{T}_3$ model interpolating between honeycomb and dice lattices (Raoux et al. 2014). For the moment, we do not delve any deeper into this topic, since the Berry dipole and its physical consequences will be the main subject of Chapter 5.

From Eq. (4.63) we get a representative continuum model of type \mathcal{A}_{II} as

$$H(\mathbf{q}) = \begin{pmatrix} 0 & \gamma_2(-\lambda_1\gamma_1^* + \lambda_2\gamma_2^*)\mathbf{v}_C^* \cdot \mathbf{q} & \gamma_1(\lambda_1\gamma_1^* - \lambda_2\gamma_2^*)\mathbf{v}_C^* \cdot \mathbf{q} \\ \dots & 2\lambda_1 \operatorname{Re}(\gamma_2^*\mathbf{v}_A) \cdot \mathbf{q} & (-\lambda_1\gamma_1\mathbf{v}_A^* - \lambda_2\gamma_2^*\mathbf{v}_A) \cdot \mathbf{q} \\ \dots & \dots & 2\lambda_2 \operatorname{Re}(\gamma_1^*\mathbf{v}_A) \cdot \mathbf{q} \end{pmatrix}. \quad (4.91)$$

To impose an isotropic spectrum, we first need to ensure $C_1 = \operatorname{Tr}(H) = 0$, which can be done either (i) by fixing $\lambda_1\gamma_2^* + \lambda_2\gamma_1^* = 0$ while keeping \mathbf{v}_A arbitrary, or (ii) by taking γ_i real and \mathbf{v}_A imaginary. In both cases one obtains an effective chiral symmetry. Under the constraint of an isotropic spectrum, the model (4.91) becomes thus equivalent to the model (4.89) upon transforming to the chiral basis.

From Eq. (4.71) we get a generic continuum model of type \mathcal{B}_I ,

$$H(\mathbf{q}) = \begin{pmatrix} 0 & -\mathbf{v}_C \cdot \mathbf{q} & \mathbf{v}_B \cdot \mathbf{q} \\ -\kappa_C \mathbf{v}_C \cdot \mathbf{q} & 0 & \kappa_C \mathbf{v}_A \cdot \mathbf{q} \\ \kappa_B \mathbf{v}_B \cdot \mathbf{q} & -\kappa_B \mathbf{v}_A \cdot \mathbf{q} & 0 \end{pmatrix}, \quad (4.92)$$

where the \mathbf{v}_a are constrained to be real (in which case $\kappa_a = 1$) or imaginary (then $\kappa_a = -1$), and to fulfill $\kappa_A\kappa_B\kappa_C = -1$. Under these conditions the spectrum is particle-hole symmetric due to CP symmetry, and is guaranteed to be isotropic if $\kappa_A v_{A,i} v_{A,j} + \kappa_B v_{B,i} v_{B,j} + \kappa_C v_{C,i} v_{C,j} = c \delta_{ij}$ with a constant c . A simple example would be $\mathbf{v}_A = (1, 0, 0)$, $\mathbf{v}_B = (0, 1, 0)$ and $\mathbf{v}_C = (0, 0, i)$, which gives rise to a pseudospin-1 Hamiltonian with Berry monopole (2.8). The same happens for any other allowed choice of the \mathbf{v}_a . Similarly, from Eq. (4.78) we obtain a representative continuum model of type \mathcal{B}_{II} as

$$H(\mathbf{q}) = \begin{pmatrix} 0 & \mathbf{v}_C \cdot \mathbf{q} & \mathbf{v}_C^* \cdot \mathbf{q} \\ \mathbf{v}_C^* \cdot \mathbf{q} & \mathbf{v}_A \cdot \mathbf{q} & 0 \\ \mathbf{v}_C \cdot \mathbf{q} & 0 & -\mathbf{v}_A \cdot \mathbf{q} \end{pmatrix}, \quad (4.93)$$

where \mathbf{v}_C is arbitrary and \mathbf{v}_A is real. The spectrum is isotropic whenever $\text{Re}(v_{A,i}v_{A,j} + 2v_{C,i}^*v_{C,j}) = c\delta_{ij}$. This Hamiltonian also describes a pseudospin-1 fermion and is thus equivalent to Eq. (4.92); for example a standard representation of a pseudospin-1 is obtained for $\mathbf{v}_A = (0, 0, 1)$ and $\mathbf{v}_C = (1, -i, 0)/\sqrt{2}$.

In summary, the continuum models $H_{\mathcal{B}}(\mathbf{q})$ derived from the type- \mathcal{B} flat-band Hamiltonians introduced in Section 4.5.1 exhibit a CP symmetry (2.10) and the quantum geometric structure is that of a *Berry monopole* (2.8), more precisely that of a pseudospin-1. Such crossings are known from chiral multifold semimetals. In contrast, the continuum models $H_{\mathcal{A}}(\mathbf{q})$ derived from the type- \mathcal{A} lattice models, despite having the same spectrum as a pseudospin-1, exhibit a chiral symmetry (2.3) instead of a CP symmetry, and the quantum geometric structure associated to the threefold crossing is that of a *Berry dipole* (4.90) instead of a Berry monopole. Such systems have, to our knowledge, not been described in the literature. It will be the purpose of Chapter 5 to carry out an in-depth study of semimetals with chiral symmetry that exhibit such Berry dipole crossings. It would certainly also be rewarding to systematically investigate the quantum geometric properties of other kinds of nodal points (with different N , D or d) that can be obtained from our flat-band construction scheme.

4.7.2 | Designing magnetic flat-band models

So far, we have exclusively considered systems without spin-orbit coupling, where the spin-up and spin-down electrons are uncoupled and can individually be treated as spinless electrons. However, it would be very interesting to construct flat-band models with spin-orbit coupling, where the spin degree of electrons can flip and thus has to be taken into account, as explained in the following.

The main idea is to repeat exactly the same procedure as in Fig. 4.3, but where the input CLS (4.1) now exhibits a spin texture. More precisely, it can be written in the form

$$|\Psi_{\text{CLS}}^{\mathbf{R}_C}\rangle = \sum_{a_i \in \text{CLS}} (w_{a_i \uparrow} |a_i \uparrow\rangle + w_{a_i \downarrow} |a_i \downarrow\rangle), \quad (4.94)$$

and the CLS amplitude on any given site can be written as a spinor

$$\begin{pmatrix} w_{a_i \uparrow} \\ w_{a_i \downarrow} \end{pmatrix} = e^{i\Gamma_{a_i}} \begin{pmatrix} \cos \frac{\theta_{a_i}}{2} \\ \sin \frac{\theta_{a_i}}{2} e^{i\phi_{a_i}} \end{pmatrix}. \quad (4.95)$$

For a lattice with N inequivalent geometric sites $a = A, B, \dots$ per unit cell, it is then clear that the BCLS has $2N$ components, and can be written as

$$|f(\mathbf{k})\rangle = (f_{A\uparrow}, f_{A\downarrow}, f_{B\uparrow}, f_{B\downarrow}, \dots)^T \quad (4.96)$$

in the Bloch basis, where $f_{a\sigma} = \sum_{i \in \text{CLS}} w_{a_i \sigma} e^{i\mathbf{k} \cdot \delta_{a_i}}$. As an example, consider the CLS built on the simple square lattice ($N = 1$) shown in Fig. 4.14(a). It corresponds to a BCLS

$$|f(\mathbf{k})\rangle = 2i(\sin[(k_x - k_y)/2], \sin[(k_x + k_y)/2])^T. \quad (4.97)$$

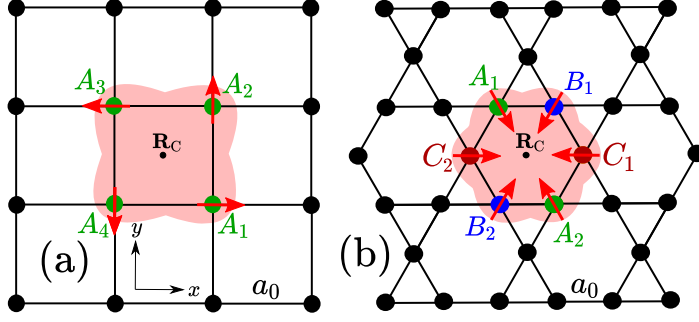


Fig. 4.14 – Examples for CLSs with spin texture. The CLS amplitude spinor is visualized by a red arrow. (a) CLS on a square lattice ($N = 1$) with $\theta_{A_i} = (i - 1)\pi$ and $\phi_{A_i} = 0$. (b) CLS on a Kagome lattice ($N = 3$) with $\theta_{A_1} = -\theta_{B_2} = -2\pi/3$, $\theta_{A_2} = -\theta_{B_1} = 4\pi/3$, $\theta_{C_1} = 2\pi$, $\theta_{C_2} = 0$ and $\phi_{A_i} = 0$.

As another example, the CLS built on the Kagome lattice ($N = 3$) visualized in Fig. 4.14(b), corresponds to a BCLS

$$|f(\mathbf{k})\rangle = -i(\sin k_-, -\sqrt{3} \sin k_-, \sin k_+, \sqrt{3} \sin k_+, 2 \sin k_x, 0)^T. \quad (4.98)$$

It is straightforward to build flat-band models from such CLSs by directly applying the results established previously, simply by reinterpreting the sense of the sublattices. For example, for any CLS built on a lattice with $N = 1$, we can construct a flat-band Hamiltonian as

$$H(\mathbf{k}) \equiv \lambda_{\mathbf{k}}^{\uparrow\downarrow} F_{\mathbf{k}}^{\uparrow\downarrow} = \lambda_{\mathbf{k}}^{\uparrow\downarrow} \begin{pmatrix} |f_{A\downarrow}|^2 & -f_{A\uparrow} f_{A\downarrow}^* \\ -f_{A\uparrow}^* f_{A\downarrow} & |f_{A\uparrow}|^2 \end{pmatrix}, \quad (4.99)$$

which is just a reinterpretation of Eq. (4.25). The real-space interpretation of such a Hamiltonian is straightforward. The off-diagonal matrix elements that previously described inter-sublattice hoppings (A to B) now describe spin flips during hopping ($A \uparrow$ to $A \downarrow$). This is nothing else than a tight-binding description of an *effective spin-orbit coupling*. We stress that this spin-orbit coupling is an intrinsic feature of the flat-band model that cannot be eliminated, and that does not destroy the perfect flat band. This is in contrast to approaches that add spin-orbit coupling to spinless flat-band models, which often results in topological quasi-flat bands, see for example Ma et al. (2020a). Similarly, the diagonal matrix elements that previously described on-site energies V_a and intra-sublattice hoppings (e.g. A to A) now correspond to spin-dependent on-site energies $V_{A\sigma}$ and spin-preserving hoppings (e.g. $A \uparrow$ to $A \uparrow$).

More generally, any Hamiltonian with an even matrix dimension presented earlier in this chapter can be directly used to create a flat-band model from a CLS with spin texture. Such models will in general have non-trivial magnetic properties. For example, for any geometric sublattice $a = A, B, C, \dots$ one obtains the spin magnetic moment of the band α as

$$\mathbf{s}_{\alpha}^{(a)}(\mathbf{k}) = \frac{1}{2} \frac{\langle \psi_{\alpha}^{(a)} | \boldsymbol{\sigma} | \psi_{\alpha}^{(a)} \rangle}{\langle \psi_{\alpha}^{(a)} | \psi_{\alpha}^{(a)} \rangle}, \quad (4.100)$$

where $|\psi_\alpha^{(a)}\rangle = (c_{\alpha,a\uparrow}, c_{\alpha,a\downarrow})^T$ is the part of the full eigenstate $|\psi_\alpha\rangle$ that is associated to the sublattice a . The spin magnetization (of a 2D system) is then obtained by integrating over filled bands as

$$M_s^{(a)} = \sum_\alpha \int_{\text{BZ}} \frac{d^2k}{(2\pi)^2} f(\epsilon_\alpha(\mathbf{k})) \mathbf{s}_\alpha^{(a)}(\mathbf{k}). \quad (4.101)$$

Let us now assume zero temperature for simplicity. If the Fermi level is such that the flat band is completely filled or completely empty, the spin magnetization (per sublattice) is uniform across the whole lattice, which is an evident consequence of the periodicity. However, if the flat band is partially filled, it is not clear if this is necessarily the case. In particular, it appears very intriguing to study the precise manner of how the flat band is filled, in other words how the N different available CLSs are sequentially populated. The spatial profile of the spin magnetization should strongly depend on the details of this process (Ferro and Piéchon n.d.).

In addition to the spin magnetization, the orbital magnetization (1.48) will also contribute to the total magnetization of such spin-orbit coupled flat-band systems. Many open questions remain as to the interplay between magnetism and quantum geometry in such systems.

4.7.3 | Designing models with more than one flat band

Throughout this chapter we have been content with the construction of a single flat band, but an intriguing possibility is to design tight-binding models with two or more flat bands. For creating a system with two flat bands, according to our general method, one could start out with two CLSs represented by BCLSs $|f_1(\mathbf{k})\rangle$ and $|f_2(\mathbf{k})\rangle$, respectively. One should then construct a Hamiltonian that verifies

$$H(\mathbf{k})|f_1(\mathbf{k})\rangle = \epsilon_1|f_1(\mathbf{k})\rangle, \quad H(\mathbf{k})|f_2(\mathbf{k})\rangle = \epsilon_2|f_2(\mathbf{k})\rangle, \quad (4.102)$$

where ϵ_1 and ϵ_2 are the flat-band energies. If one wants to have two non-degenerate flat bands, the corresponding input CLSs have to be chosen orthogonal to each other. A major problem that arises in this case is that one cannot construct the desired flat-band Hamiltonian as a matrix orthogonal to both BCLSs. While it can always be chosen orthogonal to the first BCLS, the flatness of the energy eigenvalue belonging to the second BCLS needs to be ensured by some other means.

This is difficult to achieve in general, however we can illustrate how this might work using the example of a two-band system. Indeed, since the Hamiltonian (4.25) covers all possible $N = 2$ flat-band systems, we know that two flat bands are only possible if $|f_{1,A}|^2 + |f_{1,B}|^2 = |f_{2,A}|^2 + |f_{2,B}|^2 = \text{const}$. This can be satisfied, for example, on a square lattice with two orbitals per site by choosing two CLSs as shown in Fig. 4.15, such that $|f_1(\mathbf{k})\rangle = (c_x + is_y, is_x + c_y)$ and $|f_2(\mathbf{k})\rangle = (is_x - c_y, c_x - is_y)$. Inserting, say, $|f_1(\mathbf{k})\rangle$ into Eq. (4.25), one obtains a Bloch Hamiltonian

$$H(\mathbf{k}) = \begin{pmatrix} s_x^2 + c_y^2 & -(c_x + is_y)(c_y - is_x) \\ -(c_x - is_y)(c_y + is_x) & c_x^2 + s_y^2 \end{pmatrix} \quad (4.103)$$

with two completely flat eigenvalues $\epsilon_1 = 0$ and $\epsilon_2 = 2$. This Hamiltonian describes a tight-binding model with at most third-neighbor hoppings.

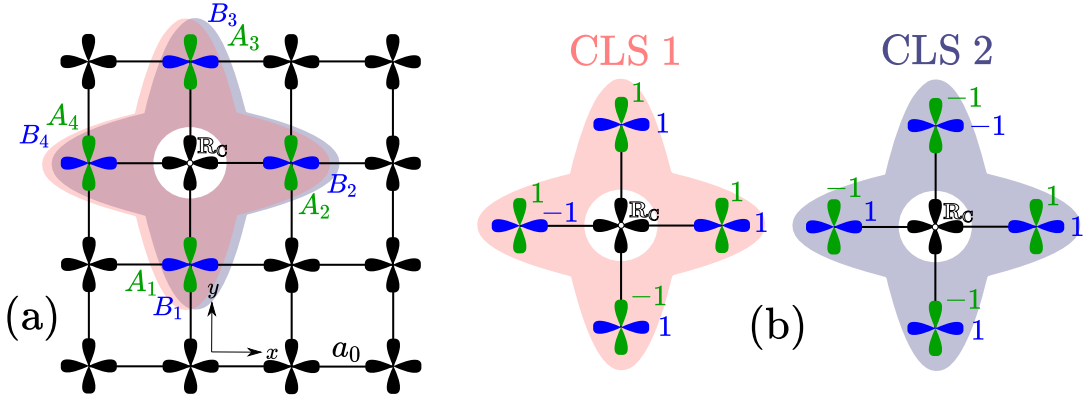


Fig. 4.15 – (a) Two CLSs on a two-orbital square lattice. (b) Distribution of CLS amplitudes that gives rise to a model with two flat bands.

4.8 | Conclusions

It has been known for a long time that, for any given flat-band tight-binding model H on a periodic lattice, it is possible to find a macroscopic number of compact localized states (CLSs) as eigenstates of H . Conversely, in the present chapter, we have shown that for *any given (input) CLS* $|\Psi_{\text{CLS}}^{\text{RC}}\rangle$ on any periodic lattice, it is possible to engineer one or several families of tight-binding Hamiltonians H for which this CLS and all its translated copies are eigenstates. We have provided a precise procedure to find such tight-binding Hamiltonians, which are *flat-band models* by construction. Since infinitely many different CLSs can be constructed on any lattice, this represents an efficient flat-band construction scheme: it yields infinitely many flat-band tight-binding models on any periodic lattice.

This procedure is most conveniently carried out in reciprocal space, and relies on the one-to-one correspondence between any given CLS $|\Psi_{\text{CLS}}^{\text{RC}}\rangle$, see Eq. (4.1), and its Fourier transform, the BCLS $|f(\mathbf{k})\rangle$, see Eq. (4.6). Flat-band Bloch Hamiltonians $H(\mathbf{k})$ can be conveniently engineered as a function of the BCLS, from which the real-space model H is naturally deduced.

For any arbitrarily designed input CLS, it is always possible to construct a flat-band model $H(\mathbf{k})$ as a quadratic function of the BCLS. This generic quadratic Hamiltonian, which works for any number of bands $N \geq 2$, is provided in Eq. (4.43) and gives rise to models with quadratic multifold band touching points at the flat-band energy. In contrast, if the input CLS has certain special properties, it can be used not only to build quadratic models, but also to construct a Bloch Hamiltonian $H(\mathbf{k})$ as a linear function of the BCLS. Such a generic linear Hamiltonian, can be constructed using Eq. (4.48) for any given $N \geq 3$, or using a superposition (4.83) of 3×3 blocks. It provides tight-binding models with linear multifold band crossings at the flat-band energy.

Due to the underlying superposition principle, our models can not only be designed by choice of the input CLS, but are also widely tunable by a set of completely free parameters. Importantly, the flat band and its eigenstate are *independent* of these free parameters. This tunability in terms of the input CLS and the free parameters

equips us with a huge playground to vary the existence, degeneracy, location and (non-)singularity of multifold band touching points.

While our method allows to build infinitely many flat-band models, and while it captures most models known in the literature, it can be generalized in several ways. For example, a more general version of the quadratic Hamiltonian (4.43) reads $H_{\mathbf{k}} = \sum_{\alpha, \beta > \alpha} \sum_{\gamma, \delta > \gamma} \lambda_{\alpha\beta\gamma\delta} |f_{\mathbf{k}}^{\alpha\beta}\rangle \langle f_{\mathbf{k}}^{\gamma\delta}|$, where $\lambda_{\alpha\beta\gamma\delta}^* = \lambda_{\gamma\delta\alpha\beta}$. Moreover, as we have mentioned, some important flat-band systems such as the standard nearest-neighbor hopping model on the Kagome lattice reside outside of our classification scheme.

Beyond the mere construction of flat bands, we have presented several interesting perspectives. First, we have shown that the quantum geometry of three-band linear band crossings in 3D is essentially governed by a Berry dipole if chiral symmetry is imposed. This is in contrast to more well-known linear three-band crossings of pseudospin-1 type, which have exactly the same energy spectrum but a quantum geometry governed by a CP symmetry and a Berry monopole. The physical properties of Berry dipole crossings will be the main subject of the next chapter. It would certainly be of interest to conduct a more detailed investigation of the different kinds of multifold crossings that can be obtained by our method, and to establish a kind of classification table of the quantum geometric properties in terms of spatial dimension, number of bands involved in the crossing, and symmetries. Second, we have argued that it is a promising route to create magnetic flat-band models from CLSs with spin texture. Their magnetic and quantum geometric properties are quite unexplored terrain.

Additional perspectives can be envisaged. For example, we have only used strictly localized states as an input for our Hamiltonians, in order to obtain short-range tight-binding models with an exactly flat band. This implies that all flat bands presented in this work have a first Chern number $\mathcal{C}_0 = 0$. It might be worthwhile to use our construction scheme assuming that flat-band eigenstates could now be represented by power-law localized states instead of CLSs – in particular with regard to a possible topological character of the flat bands.

Chapter 5

Multifold fermions beyond Berry monopoles

5.1 | Introduction

As discussed in Section 2.2, three-dimensional topological semimetals are materials with energy band crossing points that act as sources or sinks of Berry curvature, so-called Berry monopoles, see Eq. (2.8). These monopoles always come in pairs [Fig. 5.1(a)]. As also mentioned, such materials are of enormous interest in the condensed matter community because they host exotic phenomena such as Fermi arcs, anomalous Hall effect, and many more (Armitage et al. 2018; Lv et al. 2021).

Motivated by the importance of these materials, in this chapter we would like to address a fundamental issue of linear band crossings in three dimensions. Namely, it is known that any linear two-band ($N = 2$) crossing in 3D necessarily is of the Weyl form (1.36), and thus creates a Berry monopole. A common belief is that any linear multiband ($N > 2$) crossing also acts as a Berry monopole. At first glance, this seems to be confirmed by the existence of the pseudospin- s Hamiltonians (2.6), which have linear multifold crossings with Berry monopole, the only difference to the Weyl case being the higher Chern numbers. The purpose of this chapter is to illustrate that this common belief is actually wrong, and to draw attention to the existence of *other* linear multiband crossings, which are not of the Berry monopole type.

In the following, we first explain the above claim that any linear two-band crossing is a Berry monopole, and disprove the assumption that any linear multiband ($N > 2$) crossing is also a Berry monopole (Section 5.2). Then, as an explicit example, we propose a class of systems that exhibit linear multifold crossings, just like a chiral multifold semimetal, but with the peculiar property that each crossing point carries a *dipolar* Berry curvature

$$\Omega_\alpha(\mathbf{q}) = \kappa_\alpha(\mathbf{d} \cdot \mathbf{q}) \frac{\mathbf{q}}{|\mathbf{q}|^4}. \quad (5.1)$$

Notice that while it is possible to view each monopole-antimonopole pair of a topological semimetal as forming a Berry curvature dipole \mathbf{d}_0 in the Brillouin zone [Fig. 5.1(a)], such a dipole is extended, that is, the two poles are separated in momentum space. In stark contrast, Eq. (5.1) describes a *point-like* Berry dipole \mathbf{d} [Fig. 5.1(b)], that is, a point that acts as source and sink of Berry curvature flux simultaneously. Accordingly, \mathbf{d} represents an anisotropy axis fixing the dipole direction, but not a distance in momentum space. The Berry dipole (5.1) really emerges from the multifold band crossing point, as shown in Fig. 5.1(c)–(e). The *dipole charge* κ_α , which is

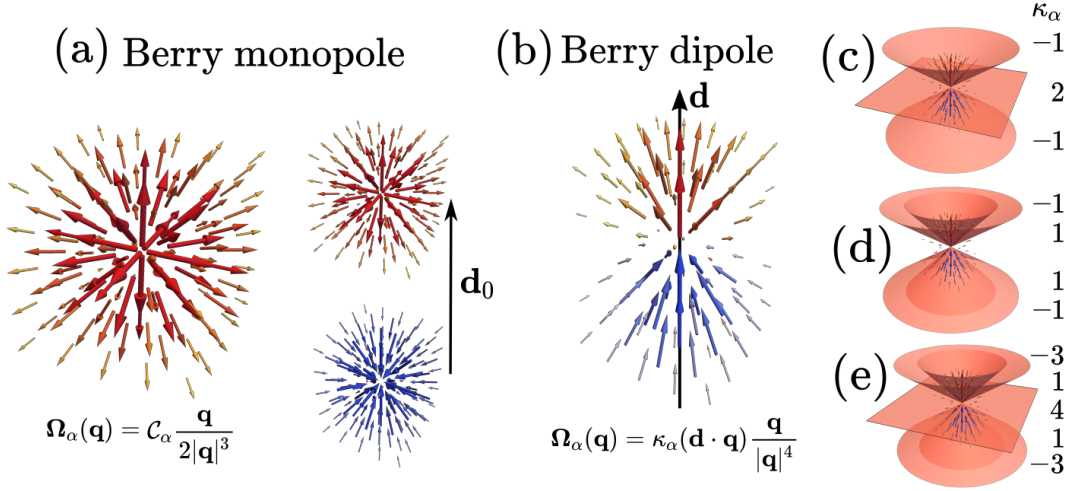


Fig. 5.1 – (a) Known topological semimetals are based on linear crossings each of which is a Berry monopole (left). Those appear in monopole-antimonopole pairs (right). (b) Multifold Hopf semimetals are based on linear crossings each of which is a Berry dipole. (c)–(e) Energy spectrum and dipole charges of the models (5.4a)–(5.4c).

an integer associated to each band, plays a similar role as the Chern number for the Berry monopole (2.8). We will come back to its importance in more detail below.

Systems with Berry dipole crossings (5.1) will be referred to as *multifold Hopf semimetals (MHSs)*. In Sections 5.3 and 5.4 we introduce explicit continuum and lattice models for such semimetals, with $N = 3, 4, 5$ bands.¹ We further discuss in detail the physical properties of these models; they are strongly affected by the Berry dipoles and thus very different from those of conventional topological semimetals, despite the exact same low-energy spectrum. In particular, we illustrate this for the Landau level spectrum, anomalous Hall effect, and magnetoconductivity, all of which have been extensively studied in Weyl and chiral multifold semimetals.

While the terms “multifold” and “semimetal” are self-explanatory from the nature of the energy spectrum [Fig. 5.1(c)–(e)], the term “Hopf” is for the moment unclear. It will be justified in Section 5.5, where we demonstrate that the multifold Hopf semimetals are closely related to a certain class of *delicate* topological insulators (Nelson et al. 2021), namely the Hopf insulators (Moore et al. 2008; Deng et al. 2013). To be more precise, we propose lattice models for multiband Hopf insulators (Lapierre et al. 2021) and show that multifold Hopf semimetals appear at their topological phase transitions. This justifies the word “Hopf”, extends recent results regarding topological phase transitions of two-band Hopf insulators (Alexandradinata et al. 2021; Nelson et al. 2022) to the multiband case, and provides an interesting platform to study delicate topology. During this discussion, we will also find that a second class of semimetals with Berry dipole is possible, characterized by quadratic band touchings; this class is however fundamentally different from the linear crossings with

¹Recall that we have already seen in Section 4.7.1 that Berry dipoles can exist in flat-band systems with linear band crossings in the presence of chiral symmetry; in agreement with this, chiral symmetry will play an important role for the multifold Hopf semimetal models.

Berry dipole, in particular it can be obtained from merging the monopoles of a chiral multifold semimetal.

At the end of the chapter, we suggest intriguing perspectives in the realm of Hopf semimetals and insulators (Section 5.6). Notably, we show that linear multiband crossings can carry quantum geometric structures yet more exotic than the Berry dipole, such as Berry quadrupoles and octupoles. Moreover, we point out an analogy between the systems considered here and the 2D Haldane model described in Section 1.4. Finally, Hopf semimetals appear to be related to 4D semimetals with tensor monopoles by a dimensional reduction procedure.

5.2 | Motivation: Exploring the matrix space of linear Hamiltonians

Consider a linear crossing of two bands ($N = 2$) in three dimensions, as visualized in Fig. 5.2(a). In addition to being linear, we demand the crossing to be isotropic for simplicity, that is, we assume that the energy of each band is directly proportional to the distance from the crossing point, $\epsilon_\alpha(\mathbf{q}) \sim |\mathbf{q}|$. Imposing these constraints, there is only a single possibility to write down a continuum Hamiltonian, which can be seen as follows. Taking the crossing point as the origin of energy, any linear two-band Hamiltonian has to be of the form

$$H(\mathbf{q}) = \mathbf{h}(\mathbf{q}) \cdot \boldsymbol{\sigma}, \quad \mathbf{h}(\mathbf{q}) = q_x \mathbf{v}_x + q_y \mathbf{v}_y + q_z \mathbf{v}_z, \quad (5.2)$$

according to Eq. (2.15), where \mathbf{v}_i are three-component real vectors. Imposing isotropy implies $|\mathbf{h}|^2 = \sum_{ij} \mathbf{v}_i \cdot \mathbf{v}_j q_i q_j \sim |\mathbf{q}|^2$ and thus $\mathbf{v}_i \cdot \mathbf{v}_j = c \delta_{ij}$ with some constant c . Thus, there is a unique Hamiltonian describing a linear isotropic two-band crossing in 3D: the Weyl Hamiltonian (1.36) that acts as a Berry monopole [Fig. 5.2(a)].

Consider now a linear 3D crossing of more than two bands ($N \geq 3$), as shown in Fig. 5.2(b). According to Eq. (2.24), a generic Hamiltonian describing such a crossing is of the form

$$H(\mathbf{q}) = \mathbf{h}(\mathbf{q}) \cdot \boldsymbol{\lambda}, \quad \mathbf{h}(\mathbf{q}) = q_x \mathbf{v}_x + q_y \mathbf{v}_y + q_z \mathbf{v}_z, \quad (5.3)$$

where \mathbf{v}_i are $(N^2 - 1)$ -component real vectors. Again we impose an isotropic energy spectrum $\epsilon_\alpha(\mathbf{q}) \sim |\mathbf{q}|$. A simple choice to achieve this would be to take $\mathbf{v}_i \cdot \boldsymbol{\lambda} = S_i$, which recovers the pseudospin- s Hamiltonian (2.6). However, other choices for the vectors \mathbf{v}_i are allowed in the vast space \mathbb{R}^{N^2-1} , so that there is *no unique Hamiltonian* for a linear isotropic multiband ($N > 2$) crossing in 3D. For example, for $N = 3$, taking $\mathbf{v}_x = \mathbf{e}_1$, $\mathbf{v}_y = \mathbf{e}_2$, and $\mathbf{v}_z = \mathbf{e}_5$, where \mathbf{e}_i are basis vectors of \mathbb{R}^8 , one obtains a Hamiltonian with an isotropic spectrum *identical* to that of a pseudospin-1, but with a Berry dipole (5.1) instead of a Berry monopole.² In fact, this is exactly the same

²Note that it can be very instructive to try to get some intuition about the behavior of the vectors \mathbf{v}_i , which encode all of the quantum geometric structure of the respective Hamiltonians. For example, the difference in the quantum geometry of a pseudospin- s and that of the models (5.4) introduced below appears to be reflected in the vectorial identities $\mathbf{v}_i \times \mathbf{v}_j = \frac{1}{2} \epsilon_{ijk} \mathbf{v}_k$ and $(\mathbf{v}_i \times \mathbf{v}_j) \cdot \mathbf{v}_k = 0$. The former constitutes a vectorial formulation of the spin algebra (2.5) and is satisfied by the multifold crossings with Berry monopole, while the latter is satisfied by the multifold crossings with chiral symmetry and Berry dipole.

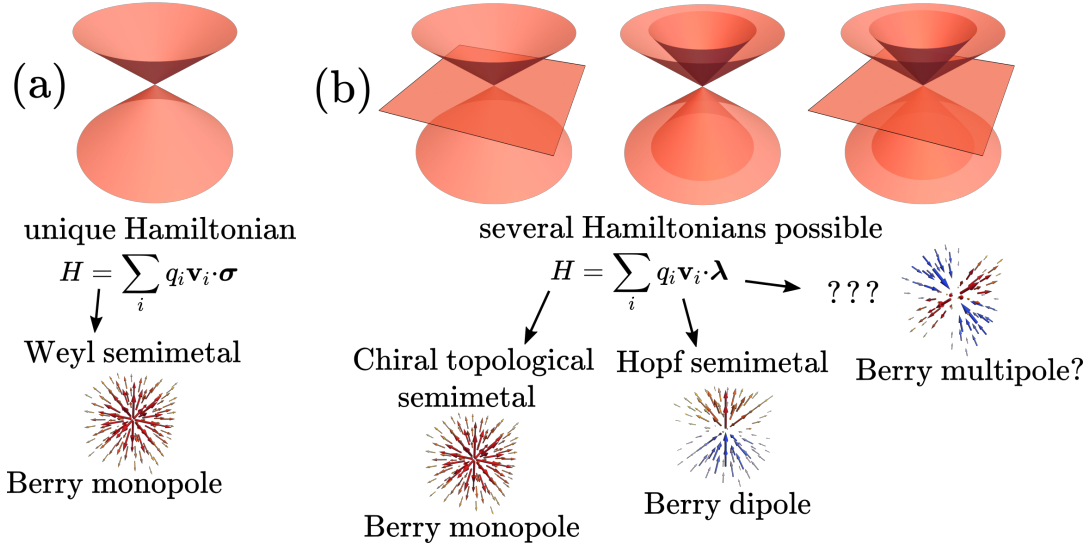


Fig. 5.2 – (a) A linear two-band crossing in 3D is captured by a unique Hamiltonian. (b) Linear N -band crossings in 3D (where $N > 2$) can be obtained from several different Hamiltonians, with different geometric and topological properties.

scenario as already studied in Section 4.7.1.

In summary, by exploring the matrix space of $N > 2$ Gell-Mann matrices, one can construct various models for 3D linear band crossings whose quantum geometry drastically differs [Fig. 5.2(b)]. The bulk of this chapter presents one particular class obtained from this main idea: the multifold Hopf semimetals. However other classes, e.g. with Berry multipole structure, are possible, as discussed later.

5.3 | Continuum models for multifold Hopf semimetals

5.3.1 | Models and symmetries

Consider the following continuum models $H_N^\xi(\mathbf{q})$, with $N = 3, 4, 5$ bands:

$$H_3^\xi(\mathbf{q}) = \begin{pmatrix} 0 & Q_3^\xi \\ (Q_3^\xi)^\dagger & 0_2 \end{pmatrix}, \quad Q_3^\xi = \begin{pmatrix} q_-^\xi & -iq_z \end{pmatrix}, \quad (5.4a)$$

$$H_4^\xi(\mathbf{q}) = \begin{pmatrix} 0_2 & Q_4^\xi \\ (Q_4^\xi)^\dagger & 0_2 \end{pmatrix}, \quad Q_4^\xi = \begin{pmatrix} aq_-^\xi & iaq_z \\ ibq_z & bq_+^\xi \end{pmatrix}, \quad (5.4b)$$

$$H_5^\xi(\mathbf{q}) = \begin{pmatrix} 0_3 & Q_5^\xi \\ (Q_5^\xi)^\dagger & 0_2 \end{pmatrix}, \quad Q_5^\xi = \begin{pmatrix} 0 & i\sqrt{2}q_z \\ iq_z & q_+^\xi \\ \sqrt{2}q_+^\xi & 0 \end{pmatrix}. \quad (5.4c)$$

	Threefold HS	Fourfold HS	Fivefold HS
c_α	$-1, 0, 1$	$-a, -b, b, a$	$-\sqrt{2}, -1, 0, 1, \sqrt{2}$
κ_α	$-1, 2, -1$	$-1, 1, 1, -1$	$-3, 1, 4, 1, -3$
ω_α	$1, 0, -1$	$a, -b, b, -a$	$\sqrt{2}, 3, 0, -3, -\sqrt{2}$

Table 5.1 – Coefficients c_α , κ_α and ω_α determining the energy spectrum, Berry curvature and orbital magnetic moment of the continuum models (5.4), respectively. Each coefficient is listed from the lowest to the highest band.

Here we have defined a term $q_\pm^\xi \equiv \xi q_x \pm i q_y$ familiar from graphene or Weyl semimetals, where $\xi = \pm$ can be viewed as a valley index. For the four-band model, we have introduced two real parameters a and b , where we assume $a > b > 0$. The models (5.4) are constructed to have a linear isotropic spectrum³

$$\epsilon_\alpha(\mathbf{q}) = c_\alpha |\mathbf{q}|, \quad (5.5)$$

with band velocities c_α as listed in the first row of Table 5.1. Clearly, this spectrum is as visualized in the previous Figs. 5.1 and 5.2: there is a cone along with a flat band for $N = 3$, two cones with different slopes for $N = 4$, and two cones along with a flat band for $N = 5$. The particle-hole symmetric character of the spectrum (5.5) is obviously due to a chiral symmetry (2.3) with $\mathcal{S}^2 = 1_N$, where \mathcal{S} is just a diagonal matrix.

The continuum models are further constructed to exhibit a dipolar Berry curvature (5.1). Here the Berry dipole vector is given by $\mathbf{d} = (0, 0, \xi)$.⁴ The fact that the quantum geometry is anisotropic can be understood from the fact that the Hamiltonians (5.4), as opposed to pseudospin models, do not exhibit a full rotation symmetry. Instead, they only have an axial rotation symmetry

$$[L_d + \Sigma_d, H_N^\xi(\mathbf{q})] = 0. \quad (5.6)$$

Here $L_d = \mathbf{d} \cdot \mathbf{L}$ is the projection of angular momentum onto the Berry dipole axis, and Σ_d is a diagonal matrix acting as an effective spin projection.⁵

Aside from the Berry dipole orientation \mathbf{d} , an important ingredient of Eq. (5.1) is the dipole charge κ_α , which is an integer for each band. For the models (5.4), these dipole charges take values as listed in the second row of Table 5.1 [see also Fig. 5.1(c)–(e)]. Importantly, they are distributed *symmetrically* with respect to zero energy, $\kappa_\alpha = \kappa_{-\alpha}$, and thus $\mathbf{\Omega}_\alpha = \mathbf{\Omega}_{-\alpha}$. This is a consequence of the chiral symmetry, and it implies that large dipole charges are carried by the flat bands: $\kappa_0 = 2$ for the threefold and $\kappa_0 = 4$ for the fivefold Hopf semimetal. We emphasize that, in stark

³Constructing models with this property is not trivial for $N > 3$. We found the models by mapping the Hamiltonian to a pseudomolecule, as explained in Appendix V.A for the interested reader.

⁴For simplicity, we restrict to models with a fixed dipole axis (up to the ξ degree of freedom). Recall however from Section 4.7.1 that it is also possible to construct models with tunable \mathbf{d} .

⁵To be concrete, we have $\Sigma_d = \frac{1}{3} \text{diag}(1, -2, 1)$, $\Sigma_d = \frac{1}{2} \text{diag}(1, -1, -1, 1)$, and $\Sigma_d = \frac{1}{5} \text{diag}(4, -1, -6, -1, 4)$ for the models (5.4a)–(5.4c), respectively.

contrast, one has $\mathbf{\Omega}_\alpha = -\mathbf{\Omega}_{-\alpha}$ for any two-band system, and also for any pseudospin- s Hamiltonian (2.6); accordingly, the flat band carries no geometric charge (Chern number).

In addition to the Berry curvature, below we will also have need of the orbital magnetic moment. It also takes a dipolar form:

$$\mathbf{m}_\alpha(\mathbf{q}) = \frac{e}{2}\omega_\alpha(\mathbf{d} \cdot \mathbf{q})\frac{\mathbf{q}}{|\mathbf{q}|^3}. \quad (5.7)$$

The coefficients ω_α are listed in the third row of Table 5.1. Comparing to the orbital magnetic moment (2.9) of a pseudospin- s Hamiltonian, one can see that, just like for the Berry curvature, the symmetry of the coefficients ω_α is opposite: they satisfy $\omega_\alpha = \omega_{-\alpha}$ for a pseudospin, while $\omega_\alpha = -\omega_{-\alpha}$ for a Hopf semimetal.

We now illustrate via three scenarios that the Berry dipole charge κ_α and orientation \mathbf{d} have a strong impact on physical properties of the continuum models (5.4). Namely, we consider (i) the Landau level spectrum in the presence of a strong magnetic field; (ii) the anomalous Hall conductivity in the presence of an electric field; (iii) the magnetoconductivity in the presence of an electric and a weak magnetic field. For the moment, we consider these effects for a single continuum model $H_N^\xi(\mathbf{q})$. Later we will introduce tight-binding models for multifold Hopf semimetals, with one or more Berry dipole crossings in the Brillouin zone, and discuss the same physical effects from a lattice perspective.

5.3.2 | Physical properties (I) – Landau levels

Consider electrons modeled by Eq. (5.4) in the presence of a strong magnetic field $\mathbf{B} = B\hat{\mathbf{B}}$. A generic magnetic field orientation can be expressed as

$$\hat{\mathbf{B}} = (0, \sin \theta, \cos \theta) \quad (5.8)$$

without loss of generality, due to the axial rotation symmetry (5.6). In order to find the energy spectrum under the magnetic field, we replace the canonical momentum \mathbf{q} by the gauge-invariant kinetic momentum (Jackson 2012), as $\mathbf{q} \rightarrow \mathbf{\Pi} = \mathbf{q} + e\mathbf{A}$, with the gauge choice $\mathbf{A} = Bx(0, \cos \theta, -\sin \theta)$. Note that the momentum

$$q_0 = \hat{\mathbf{B}} \cdot \mathbf{q} = \sin \theta q_y + \cos \theta q_z \quad (5.9)$$

along the magnetic field is conserved. Using the canonical commutation relations $[x_j, q_k] = i\delta_{jk}$, one finds

$$[\Pi_x, \Pi_y] = -i \cos \theta / l_B^2, \quad [\Pi_y, \Pi_z] = 0, \quad [\Pi_z, \Pi_x] = -i \sin \theta / l_B^2, \quad (5.10)$$

where $l_B \equiv 1/(eB)$ is the magnetic length. Moreover, it is convenient to introduce ladder operators as (Li et al. 2016)

$$\begin{aligned} \hat{d} &= \frac{l_B}{\sqrt{2}}(\Pi_x - i \cos \theta \Pi_y + i \sin \theta \Pi_z), \\ \hat{d}^\dagger &= \frac{l_B}{\sqrt{2}}(\Pi_x + i \cos \theta \Pi_y - i \sin \theta \Pi_z). \end{aligned} \quad (5.11)$$

They act on number states $|n\rangle$ as $\hat{d}^\dagger |n\rangle = \sqrt{n+1} |n+1\rangle$ and $\hat{d} |n\rangle = \sqrt{n} |n-1\rangle$, and satisfy the bosonic commutation relation $[\hat{d}, \hat{d}^\dagger] = 1$. Reversing the above relations, we can express the kinetic momentum in terms of the ladder operators as

$$\begin{aligned}\Pi_x &= \frac{1}{\sqrt{2}l_B}(\hat{d} + \hat{d}^\dagger), \\ \Pi_y &= q_0 \sin \theta + \frac{i}{\sqrt{2}l_B} \cos \theta(\hat{d} - \hat{d}^\dagger), \\ \Pi_z &= q_0 \cos \theta - \frac{i}{\sqrt{2}l_B} \sin \theta(\hat{d} - \hat{d}^\dagger), \\ \Pi_\pm^\xi &= \xi \Pi_x \pm i \Pi_y = \frac{1}{\sqrt{2}l_B} \left[(\xi \pm \cos \theta) \hat{d}^\dagger + (\xi \mp \cos \theta) \hat{d} \right] \pm i \sin \theta q_0.\end{aligned}\tag{5.12}$$

The Hamiltonian in the presence of the magnetic field can now fully be written in terms of ladder operators.

Using the above procedure, the Landau level spectrum of the Hopf semimetals (5.4) can be easily computed analytically, as carried out in detail in Appendix V.B. The Landau levels are expected to form a quasi-1D dispersion in terms of the conserved momentum q_0 , and are further expected to be particle-hole symmetric due to the fact that the magnetic field does not break the chiral symmetry of the zero-field Hamiltonian.

We find the exact Landau levels for a three-band crossing (5.4a) to be given by

$$\epsilon_\alpha^{n,\xi} = c_\alpha \sqrt{2eB \left(n + \frac{1 - \kappa_\alpha \xi \cos \theta}{2} \right) + q_0^2}, \quad n = 0, 1, \dots\tag{5.13}$$

with $c_\alpha = 0, \pm 1$ and n the Landau level index. As expected, the flat band is maintained under the magnetic field. More importantly, the dispersive bands carry a clear signature of the Berry dipole's charge (κ_α) and orientation ($\xi \cos \theta \equiv \hat{\mathbf{B}} \cdot \mathbf{d}$). As a consequence, the Landau level spectrum strongly depends on the magnetic field direction: it is gapped for $\mathbf{B} \uparrow \uparrow \mathbf{d}$, and gapless for $\mathbf{B} \uparrow \downarrow \mathbf{d}$, see Fig. 5.3(a). We should like to emphasize that this tunability is a *pure quantum geometric effect*. Indeed, the magnetic field couples to the eigenstates of the Hopf semimetal and thus unveils the Berry dipole via the magnetic energy levels; in contrast, the existence of the Berry dipole is invisible in the fully isotropic zero-field energy spectrum.

Similarly, we find the exact Landau levels of a four-band crossing (5.4b):

$$\begin{aligned}\epsilon_\alpha^{n,\xi} &= \alpha_1 \sqrt{\eta_+ + \eta_- + \alpha_2 \sqrt{(\eta_+ - \eta_-)^2 + \nu^2}}, \quad n = 0, 1, \dots \\ \eta_\pm &= \frac{c_\pm^2}{2} \left[2eB \left(n + \frac{1 - \kappa_\pm \xi \cos \theta}{2} \right) + q_0^2 \right].\end{aligned}\tag{5.14}$$

Here, we use a band index tuple $\alpha = (\alpha_1, \alpha_2)$ with $\alpha_i = \pm$; $c_+ = a$ and $c_- = b$ are the band velocities of the two cones, and $\kappa_\pm = \mp 1$ the corresponding dipole charges; moreover, $\nu = c_+ c_- e(\mathbf{B} \times \mathbf{d})_x = abeB\xi \sin \theta$. Again, the Berry dipole (5.1) explicitly appears and the Landau levels can be tuned by rotating \mathbf{B} , see Fig. 5.3(b). The precise character of this tunability, however, is now quite different, in particular the Landau level spectrum remains gapless for any orientation of \mathbf{B} .

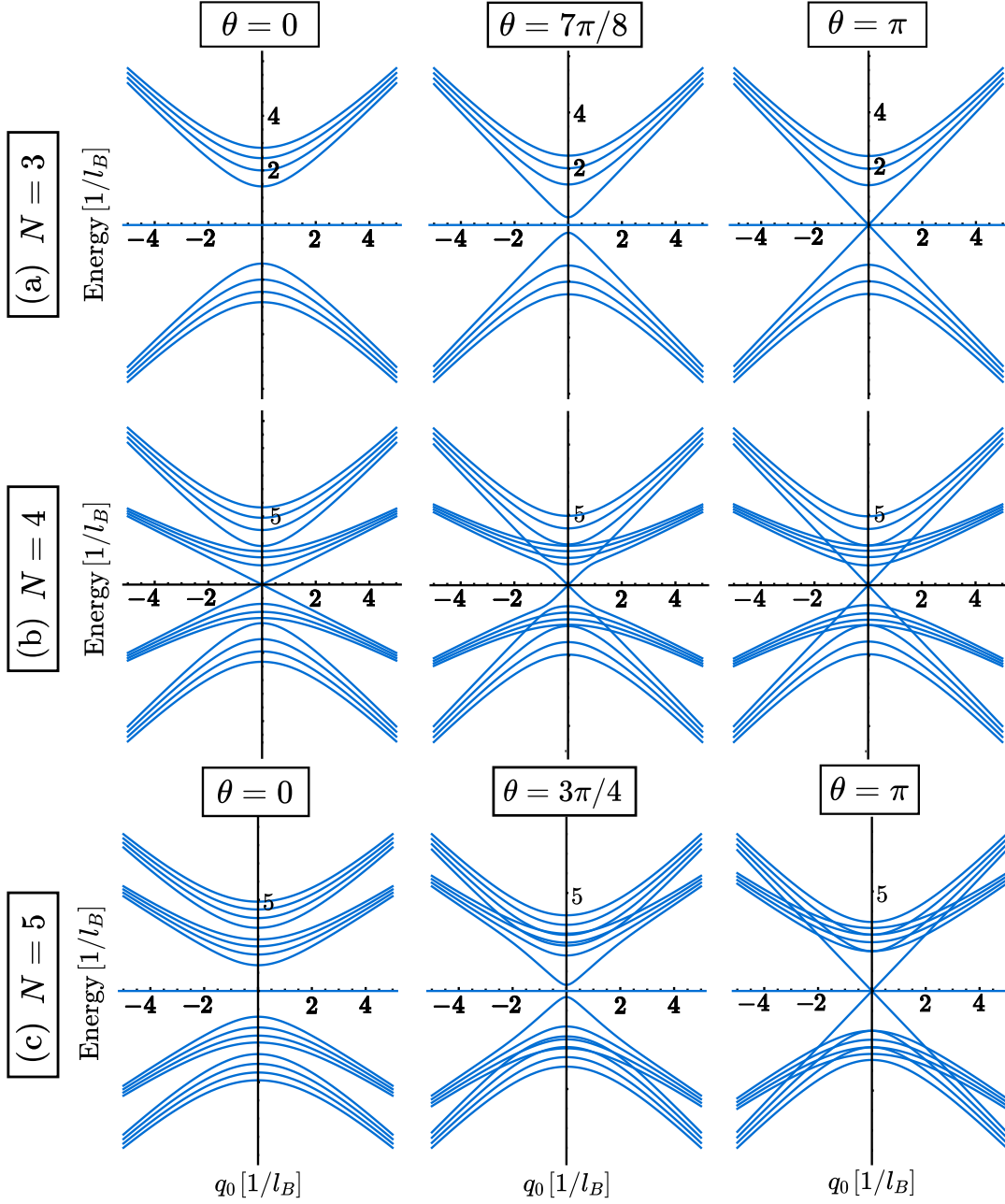


Fig. 5.3 – (a) Landau level spectrum (5.13) for $\xi = +$ for three different θ , in units of the inverse magnetic length $1/l_B$. It can be tuned from gapped to gapless by rotating \mathbf{B} . (b) Landau levels (5.14) for $\xi = +$, $a/2 = b = 1$. They are gapless for any θ . (c) Landau levels (5.15) for $\xi = +$. They behave similarly to the three-band case.

Finally, the Landau levels of the fivefold crossing (5.4c) are given by

$$\begin{aligned} \epsilon_\alpha^{n,\xi} &= \alpha_1 \sqrt{\eta_+ + \eta_- + \alpha_2 \sqrt{(\eta_+ - \eta_-)^2 + \tilde{\nu}^2}}, \quad n = 1, 2, \dots \\ \eta_\pm &= \frac{c_\pm^2}{2} \left[2eB \left(n + \frac{1 - \kappa_\pm \xi \cos \theta}{2} \right) + q_0^2 \right]. \end{aligned} \quad (5.15)$$

Now we have $\alpha_1 = 0, \pm$ and $\alpha_2 = \pm$. The band velocities of the two cones are $c_+ = \sqrt{2}$ and $c_- = 1$, the corresponding dipole charges are $\kappa_+ = -3$ and $\kappa_- = 1$, and $\tilde{\nu} = 2\sqrt{3}(\mathbf{B} \times \mathbf{d})_x = 2\sqrt{3}\xi eB \sin \theta$. This five-band spectrum behaves similarly to the three-band spectrum above, notably it can be tuned from gapped to gapless by rotating the magnetic field relative to the Berry dipole direction.

To contextualize these results, it is useful to compare to the Landau level spectrum of several known systems with ‘‘Dirac-like’’ band crossings. First, there is clearly a big difference with the Landau levels of pseudospin- s systems (2.6), which are *independent* of the magnetic field orientation $\hat{\mathbf{B}}$ due to the full rotation symmetry (2.11). Moreover, for a pseudospin-like crossing, the topological character of the Berry monopole (2.8) is reflected in the Landau level spectrum via the existence of chiral Landau levels. These are modes connecting two families of Landau levels with different band index α , similar to what happens for chiral modes in the absence of a magnetic field (see for example the chiral edge states of the Chern insulator in Fig. 1.6). The number of chiral Landau levels is directly determined by the Chern number \mathcal{C}_α , see for example Bradlyn et al. (2016) for the pseudospin-1 case, and Ezawa (2017) or Delplace (2022) for the case of general s . Also, for a pseudospin- s crossing with integer s , the flat band of the zero-field spectrum is destroyed since \mathbf{B} breaks the CP symmetry. More details on the Landau levels of pseudospin- s fermions are given in Appendix V.C.

There is also a big difference with the Landau levels of Dirac fermions (Dirac 1928). Since the Dirac Hamiltonian has full rotation symmetry, the Landau levels are independent of $\hat{\mathbf{B}}$. However, in contrast to pseudospin fermions, Dirac fermions feature chiral symmetry and thus the Landau level spectrum remains particle-hole symmetric. Indeed, if we allow the case $a = b$ (that we have so far excluded) in the model (5.4b), then this model becomes a Dirac semimetal $H_D(\mathbf{q}) = \mathbf{q} \cdot \mathbf{\Gamma}$ with anticommuting matrices $\Gamma_{x,y,z}$. Accordingly, in the limit $a = b$ we recover from Eq. (5.14) the famous Landau level spectrum of Dirac fermions $\epsilon_\pm^n = \pm(2eBn + q_0^2)^{1/2}$, established a long time ago by Rabi (1928).

Finally, one can also compare the Landau levels of the Hopf semimetals to those of an extended Berry dipole \mathbf{d}_0 formed from two Weyl nodes (or more generally two Berry monopoles in a chiral multifold semimetal). Those obviously depend on the direction of $\hat{\mathbf{B}}$ since the dipole axis \mathbf{d}_0 induces an anisotropy (Saykin et al. 2018). However, this dependence is quite distinct from the one of Eqs. (5.13)–(5.15), in particular due to the broken particle-hole symmetry of the spectrum and the presence of connected chiral Landau levels originating from the two valleys.

To close this discussion on the Landau levels of Hopf semimetals, we emphasize that some useful insight can also be obtained from a semiclassical analysis. Indeed, aside from the quantum approach described above, it is possible to establish Eq. (5.13) using Onsager’s semiclassical quantization condition (Onsager 1952). More precisely,

one needs to employ an extended Onsager condition that takes into account *intra-band* corrections due to Berry curvature and orbital magnetic moment (Roth 1966; Mikitik and Sharlai 1999; Fuchs et al. 2010; Gao and Niu 2017). More importantly, the semiclassical approach helps to understand the origin of the terms $\nu \sim |\mathbf{B} \times \mathbf{d}|$ in Eq. (5.14) and $\tilde{\nu} \sim |\mathbf{B} \times \mathbf{d}|$ in Eq. (5.15). These terms remain unexplained in the quantum approach but find an intuitive semiclassical interpretation in terms of *interband* coupling between degenerate orbits. Such coupling arises whenever a constant energy curve intersects more than one band, as is unavoidable for a zero-field spectrum consisting of two or more cones. For more details, see Appendix V.D, where we develop an original approach to semiclassical Landau quantization of degenerate orbits.

5.3.3 | Physical properties (II) – Anomalous Hall effect

Consider now electrons modeled by Eq. (5.4) in the presence of a weak electric field \mathbf{E} . To describe the linear response of the system, we adopt the semiclassical Boltzmann approach in the relaxation time approximation, as already described in Section 1.5.5. In the absence of an external magnetic field, this approach yields only two contributions to the electrical conductivity tensor: the standard Drude conductivity and the anomalous Hall conductivity. The former is not very interesting for our purposes, as it depends only on the zero-field spectrum; indeed, the Drude conductivity of the Hopf semimetals (5.4) is exactly the same as for the pseudospin Hamiltonians (2.6). In contrast, the anomalous Hall (AH) conductivity (1.57a) is expected to be very interesting, as it is strongly influenced by the dipolar Berry curvature.

Inserting the Berry dipole (5.1) into Eq. (1.57a), and assuming zero temperature, we obtain

$$\sigma_{xy}^{\text{AH}} = -\xi \frac{e^2}{6\pi^2} \sum_{\alpha} \kappa_{\alpha} \int_0^{q_c} dq \Theta(E_F - c_{\alpha}q), \quad (5.16)$$

where $\Theta(q)$ is the Heaviside function and $q = |\mathbf{q}|$. It is necessary to introduce a momentum cutoff $q_c \gg 0$ to the upper integration limit to avoid divergence. This is an artefact of the continuum model, induced by the infinite band width, and is absent in an actual lattice model, as we shall see below. For the three-band Hopf semimetal (5.4a), three regions can be distinguished when tuning E_F , see Fig. 5.4(a). The anomalous Hall conductivity in these regions becomes

$$\sigma_{xy}^{\text{AH}} = -\xi \frac{e^2}{6\pi^2} \begin{cases} 0 \\ \kappa_{-}(E_F + q_c) \\ \kappa_{+}(E_F - q_c) \end{cases} = \xi \frac{e^2}{6\pi^2} \begin{cases} 0, & |E_F| > q_c \\ E_F + q_c, & -q_c < E_F < 0 \\ E_F - q_c, & 0 < E_F < q_c \end{cases} \quad (5.17)$$

where the Berry dipole charges are $\kappa_{+} = \kappa_{-} = -1$ (Table 5.1). This conductivity is plotted in Fig. 5.4(b) and changes sign abruptly at the flat band, with a jump equal to the flat band Berry dipole charge $\kappa_0 = 2$. Similarly, for the four- and five-band Hopf semimetals, several regions can be distinguished when tuning E_F , as is clear from Fig. 5.4(a). The corresponding anomalous Hall conductivity (see Appendix V.E for explicit expressions) is plotted in Fig. 5.4(b). For the fourfold Hopf semimetal, the anomalous Hall conductivity is continuous at half filling since there is no flat band.

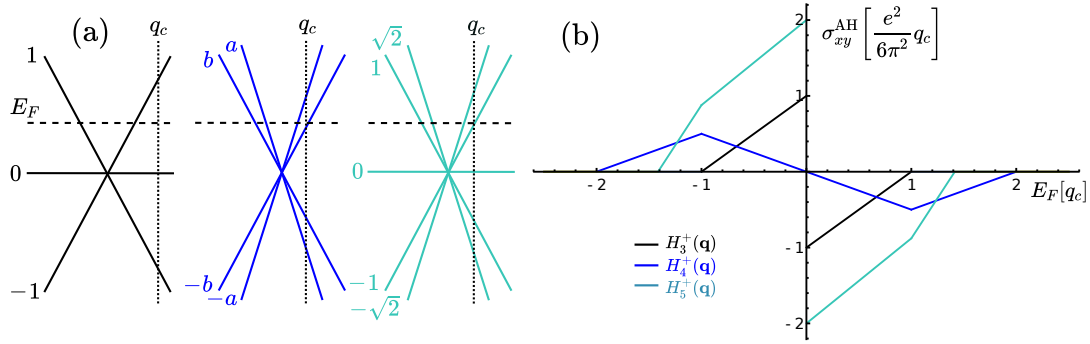


Fig. 5.4 – (a) Schematic energy spectrum of the Hopf semimetal continuum models (5.4), with Fermi energy E_F , momentum cutoff q_c and band velocities c_α indicated. (b) Corresponding anomalous Hall conductivity for $\xi = +$. For $N = 4$, we have used band velocities $a = 2$, $b = 1$. For N odd, there is an abrupt sign change at half filling, with a jump equal to the Berry dipole charge κ_0 of the flat band.

For the fivefold Hopf semimetal, the jump at half filling is again equal to the flat-band Berry dipole charge $\kappa_0 = 4$.

For all continuum models, we may therefore write the general anomalous Hall current \mathbf{j}_{AH} with components $j_i^{\text{AH}} = \sum_j \sigma_{ij}^{\text{AH}} E_j$ in the form

$$\mathbf{j}_{\text{AH}}(E_F) = \sigma_{\text{AH}}(E_F) \mathbf{E} \times \mathbf{d}, \quad (5.18)$$

where $\sigma_{\text{AH}}(E_F) = -\sigma_{\text{AH}}(-E_F)$ and $\mathbf{d} = (0, 0, \xi)$. This current flows perpendicular to both the electric field and the Berry dipole, and it flips sign when flipping the orientation ξ . This can be understood from the fact that the Berry curvature acts as a fictitious magnetic field. Moreover, the current (5.18) is clearly an *odd function* of the Fermi energy. This important parity property can be directly explained from the symmetries of the Hamiltonians (5.4): it is a combined effect of the particle-hole symmetric spectrum and the Berry curvature property $\Omega_\alpha = \Omega_{-\alpha}$. For a proof, see Appendix V.E.

The continuum treatment of the anomalous Hall effect may be considered somewhat unsatisfying, due to the necessity to introduce a cutoff and the discontinuous jumps at half filling. It is reasonable to regularize the problem by considering the anomalous Hall conductivity of an appropriate lattice model. In particular, we consider the Hopf semimetal lattice models $\mathfrak{h}_N(\mathbf{k})$ ($N = 3, 4, 5$) that will be defined in more detail in Eq. (5.26) below. In these models, we fix the parameter $\Delta_0 = -3$, such that a single Berry dipole crossing exists in the Brillouin zone at the Γ point. Using the Berry curvature of the lattice model, we then calculate the anomalous Hall conductivity at zero temperature numerically from Eq. (1.57a). The result is shown in Fig. 5.5(a). It agrees with both the qualitative predictions of the continuum theory and the general symmetry arguments presented in Appendix V.E. In particular, it is odd in E_F and its global sign can be flipped by inverting the direction of the Berry dipole at the Γ point. Also, as one can see, the discontinuous jump at half filling is replaced by a smooth behavior.

Let us compare the anomalous current (5.18) with that caused by an extended Berry dipole \mathbf{d}_0 [Fig. 5.1(a)], as in a Weyl semimetal. It is known that a pair of

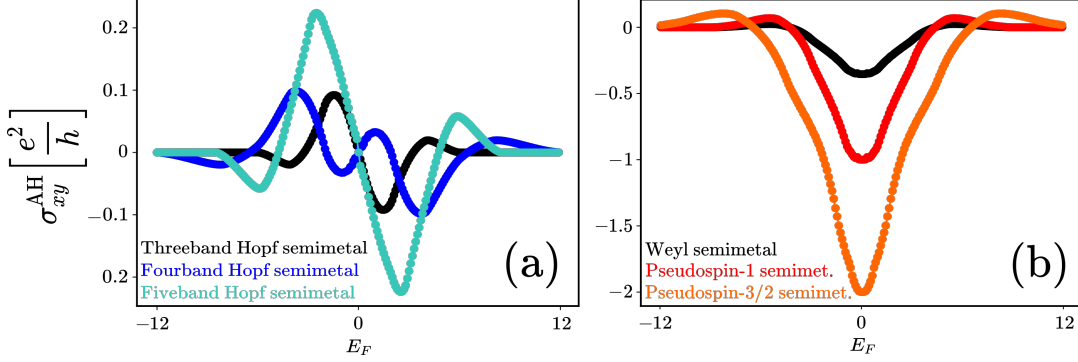


Fig. 5.5 – (a) Anomalous Hall conductivity for lattice models $\mathfrak{h}_N(\mathbf{k})$ [cf. Eq. (5.26)] of multifold Hopf semimetals. Choosing $\Delta_0 = -3$ ensures the existence of a single Berry dipole at the Γ point. The odd parity is due to the property $\kappa_\alpha = \kappa_{-\alpha}$ of the geometric charges of this Berry dipole. (b) Typical anomalous Hall conductivity for lattice models of chiral topological semimetals with a single pair of Berry monopoles [cf. Eq. (2.12)]. The even parity is due to the property $\mathcal{C}_\alpha = -\mathcal{C}_{-\alpha}$ of each Berry monopole.

coupled Weyl nodes causes an anomalous Hall current of the form

$$\mathbf{j}_{\text{AH}}^{\text{W}}(E_F) = \sigma_{\text{AH}}^{\text{W}}(E_F) \mathbf{E} \times \mathbf{d}_0, \quad (5.19)$$

see for example Klinkhamer and Volovik (2005), Burkov and Balents (2011), or Yang et al. (2011). Here \mathbf{d}_0 represents the distance between Weyl nodes (or a tilt direction). Importantly, the anomalous Hall conductivity $\sigma_{\text{AH}}^{\text{W}}(E_F)$ is now an *even function* of the Fermi energy, see again Appendix V.E for a simple proof. Again, to corroborate this claim, we numerically compute the anomalous Hall conductivity for lattice models featuring a pair of pseudospin- s crossings (Berry monopoles), where $s = 1/2$, $s = 1$, or $s = 2$. In particular, we take the model (2.12) considered previously, which describes a chiral multifold semimetal with a pair of nodes at $\mathbf{k}_0 = \pm(0, 0, k_0)$ [for $s = 1/2$ this is just the Weyl model (1.38)]. Taking the same parameters as for the Berry curvature plot in Fig. 1.7(a), namely $t_i = 1$, $m = 2$ and $k_0 = \pi/2$, one obtains the anomalous Hall conductivity shown in Fig. 5.5(b). As expected, it is even in E_F .

In summary, the anomalous Hall current (5.18) caused by a point-like Berry dipole crossing (5.4) is similar in form to the anomalous Hall current (5.19) caused by an extended Berry dipole formed from two topological monopoles of a Weyl or multifold topological semimetal. However, it is *opposite* in parity. This can be viewed as a pure quantum geometric effect, as it is a direct consequence of the symmetry of the Berry dipole charges ($\kappa_\alpha = \kappa_{-\alpha}$).

5.3.4 | Physical properties (III) – Magnetoconductivity

Finally, consider electrons modeled by Eq. (5.4) in the presence of both weak electric and magnetic fields \mathbf{E} and \mathbf{B} . We again adopt the Boltzmann approach of Section 1.5.5, and focus on the contributions to the electrical conductivity that are of linear order in \mathbf{B} . These contributions include (see also Appendix V.E): the classical Hall conductivity caused by the Lorentz force, which depends only on the zero-field spectrum; a correction to the anomalous Hall effect caused by the orbital magnetic

moment, which we will however not focus on; and, most importantly, a dissipative quantum geometric current $\mathbf{j}_{\text{geo}}(\mathbf{B})$, with components

$$j_i^{\text{geo}} = \sum_j \left[\sigma_{ij}^{\text{Berry}}(\mathbf{B}) + \sigma_{ij}^{\text{OMM}}(\mathbf{B}) \right] E_j. \quad (5.20)$$

This current is caused by Berry curvature [cf. Eq. (1.57b)] and orbital magnetic moment [cf. Eq. (1.57c)]. In the following we focus on this latter contribution, which is expected to be strongly affected by the Berry dipole.

Inserting the Berry dipole (5.1), the band velocity $\mathbf{v}_\alpha = c_\alpha \mathbf{q}/|\mathbf{q}|$, and the orbital magnetic moment (5.7) into Eqs. (1.57b) and (1.57c), and assuming zero temperature, a simple calculation shows that the geometric current takes the general form

$$\mathbf{j}_{\text{geo}} = A_1(\mathbf{E} \cdot \mathbf{B})\mathbf{d} + A_2(\mathbf{E} \cdot \mathbf{d})\mathbf{B} + A_3(\mathbf{B} \cdot \mathbf{d})\mathbf{E} \quad (5.21)$$

for all continuum models (5.4). In other words, there is a current along the Berry dipole direction (except if the applied magnetic field is perpendicular to the electric field), a current along the applied magnetic field (except if the electric field is perpendicular to the Berry dipole), and a longitudinal current (except if the magnetic field is applied perpendicular to the Berry dipole).

The explicit expressions for the coefficients A_i ($i = 1, 2, 3$), in units of $A_0 \equiv -e^3\tau/(12\pi^2)$, are as follows (see Appendix V.E for a derivation): $A_i = A_0$ for the continuum model (5.4a) describing a threefold Hopf semimetal; similarly $A_i = A_0(a - b)$ for the fourfold Hopf semimetal (5.4b); and $A_{1,2} = (21\sqrt{2} - 17)A_0/5$, $A_3 = (23 + \sqrt{2})A_0/5$ for the fivefold Hopf semimetal (5.4c). As we can see, these coefficients are independent of the Fermi level E_F . This is of course not true on the lattice, but it implies that the magnetoconductivity can be expected to be an *even function* of E_F . Indeed, as for the anomalous Hall current above, this parity property can be readily understood from general symmetry arguments, more precisely from the combined effect of a particle-hole symmetric spectrum and a Berry curvature $\boldsymbol{\Omega}_\alpha = \boldsymbol{\Omega}_{-\alpha}$. See Appendix V.E for a short proof.

As for the anomalous Hall current, we confirm the validity of the magnetocurrent (5.21) by conducting a numerical calculation of the tensors (1.57b) and (1.57c) for the lattice models $\mathfrak{h}_N(\mathbf{k})$ introduced in Eq. (5.26) below. Again we use conditions such that a single Berry dipole crossing is located at the Γ point. These calculations (not shown) confirm that $\mathbf{j}_{\text{geo}}(\mathbf{B})$ is indeed even in E_F .

Again, let us compare the current (5.21) to that caused by an extended Berry dipole \mathbf{d}_0 formed from a pair of Berry monopoles. As a matter of fact, it is well known that a pair of coupled Weyl nodes gives rise to a current $\mathbf{j}_{\text{CA}} \sim (\mathbf{E} \cdot \mathbf{B})\mathbf{d}_0$, which is attributed to the chiral anomaly (Nielsen and Ninomiya 1983; Zyuzin 2017; Sharma et al. 2017). Moreover, it gives rise to a current $\mathbf{j}_{\text{CME}} \sim \delta\epsilon\mathbf{B}$, where $\delta\epsilon$ is an energy difference between the valleys. This is known as the chiral magnetic effect (Vilenkin 1980; Fukushima et al. 2008; Zyuzin et al. 2012; Zyuzin 2017). Finally, a pair of Weyl nodes exhibits a current $\mathbf{j}_{\text{MCE}} \sim (\mathbf{B} \cdot \mathbf{d}_0)\mathbf{E}$, known as the magnetochiral effect (Cortijo 2016; Kundu et al. 2020). Similar kinds of currents exist for pairs of pseudospin crossings with $s > 1/2$. The three current contributions \mathbf{j}_{CA} , \mathbf{j}_{CME} , and \mathbf{j}_{MCE} are *odd functions* of E_F , due to the particle-hole symmetric spectrum and the

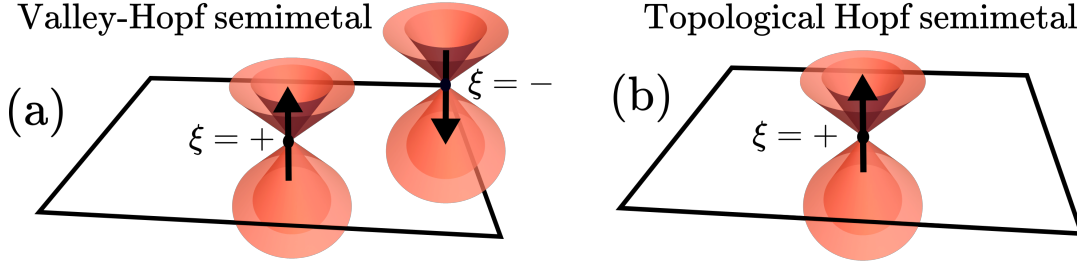


Fig. 5.6 – Valley-Hopf semimetals (topological Hopf semimetals) have an even (odd) number of linear multifold crossings with Berry dipole.

Berry curvature property $\Omega_\alpha = -\Omega_{-\alpha}$. Again a short proof is provided in Appendix V.E. To further confirm this, we have also conducted numerical calculations of the geometric current $\mathbf{j}_{\text{geo}}(\mathbf{B})$ for the lattice model (2.12).

In summary, each term of the linear magnetocurrent (5.21) caused by a point-like Berry dipole crossing (5.4) has a counterpart in the response of an extended Berry dipole formed from two topological monopoles. However, just like for the anomalous Hall effect, the currents have *opposite* parity as a function of the filling. This is again a direct consequence of the dipole charges ($\kappa_\alpha = \kappa_{-\alpha}$).

5.4 | Tight-binding models for multifold Hopf semimetals

We now demonstrate how the continuum models discussed above can be obtained as the low-energy theory of lattice models. In particular, we introduce two different classes of tight-binding models for multifold Hopf semimetals, both of which recover Eq. (5.4) in the vicinity of high-symmetry points of the Brillouin zone. The first class consists of semimetals that have an even number of crossing points with Berry dipole in the Brillouin zone. The crossings can be arranged in pairs $\xi = \pm$, with opposite dipole orientation in each valley [Fig. 5.6(a)]. These systems will be called *valley-Hopf semimetals*. The second class comprises semimetals with an odd number of Berry dipole crossings in the Brillouin zone. These systems will be called *topological Hopf semimetals*. We first present a selection of examples for the two classes, and then describe their physical properties.

5.4.1 | Valley-Hopf semimetals

Within this class, we can further distinguish between models $h_N(\mathbf{k})$ with preserved time-reversal symmetry and models $\tilde{h}_N(\mathbf{k})$ with broken time-reversal symmetry.

Valley-Hopf semimetals with time-reversal symmetry

As examples for this class of lattice models we choose Hamiltonians of the form

$$h_N(\mathbf{k}) = \begin{pmatrix} 0 & \mathcal{Q}_N \\ \mathcal{Q}_N^\dagger & 0 \end{pmatrix}, \quad (5.22)$$

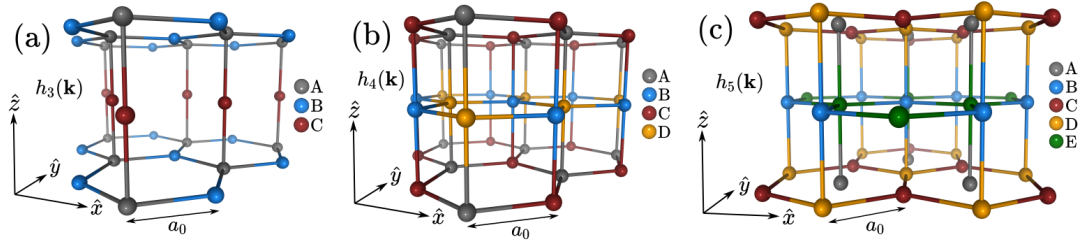


Fig. 5.7 – (a)–(c) Tight-binding models for threefold, fourfold and fivefold valley-Hopf semimetals with time-reversal symmetry on a 3D hexagonal lattice. Links are non-zero hoppings of the tight-binding Hamiltonian (5.22).

where

$$\mathcal{Q}_3 = \begin{pmatrix} w_{\mathbf{k}} & -is_z \end{pmatrix}, \quad \mathcal{Q}_4 = \begin{pmatrix} aw_{\mathbf{k}} & ias_z \\ ibs_z & bw_{\mathbf{k}}^* \end{pmatrix}, \quad \mathcal{Q}_5 = \begin{pmatrix} 0 & i\sqrt{2}s_z \\ is_z & w_{\mathbf{k}}^* \\ \sqrt{2}w_{\mathbf{k}}^* & 0 \end{pmatrix}.$$

Here $w_{\mathbf{k}} \equiv \frac{2}{3} \sum_j \exp(i\mathbf{k} \cdot \boldsymbol{\delta}_j)$, where $\boldsymbol{\delta}_{1,2} = \frac{1}{2}(\pm\sqrt{3}, 1, 0)$ and $\boldsymbol{\delta}_3 = (0, -1, 0)$, and we use shorthand notations $s_i \equiv \sin k_i$. The Hamiltonians (5.22) represent nearest-neighbor tight-binding models on a hexagonal Bravais lattice, with Bravais vectors $\mathbf{a}_1 = \sqrt{3}\hat{x}$, $\mathbf{a}_2 = \frac{1}{2}(\sqrt{3}\hat{x} + 3\hat{y})$, $\mathbf{a}_3 = 2\hat{z}$. Indeed, the models describe 2D honeycomb layers (as in graphene), stacked in a particular way along the \hat{z} direction, as visualized in Fig. 5.7. The tight-binding models have the following nearest-neighbor hoppings in real space. The three-band model $h_3(\mathbf{k})$ has isotropic hoppings $t_{AB} = 2/3$ in the A-B planes and alternating hoppings $t_{AC} = \pm 1/2$ along the A-C direction, see Fig. 5.7(a). The four-band model $h_4(\mathbf{k})$ has isotropic hoppings $t_{AC} = 2a/3$ and $t_{BD} = 2b/3$ in the A-C and B-D planes, respectively, as well as alternating hoppings $t_{AD} = \pm a/2$ and $t_{BC} = \pm b/2$ in the perpendicular direction, see Fig. 5.7(b). Finally, the five-band model $h_5(\mathbf{k})$ has isotropic hoppings $t_{BE} = 2/3$ and $t_{CD} = 2\sqrt{2}/3$, as well as alternating hoppings $t_{BD} = \pm 1/2$ and $t_{AE} = \pm 1/\sqrt{2}$ along the vertical direction, see Fig. 5.7(c).

The band structure of the models $h_N(\mathbf{k})$ is given by

$$\epsilon_{\alpha}(\mathbf{k}) = \frac{2}{3}c_{\alpha} \sqrt{f(k_x, k_y) + \frac{9}{4} \sin^2 k_z}. \quad (5.23)$$

It is particle-hole symmetric due to a chiral symmetry (2.3) with a diagonal matrix \mathcal{S} , and the coefficients c_{α} are the same as for the continuum models (5.4), see Table 5.1. The function $f(k_x, k_y) = 3 + 2 \cos(\sqrt{3}k_x) + 4 \cos(\sqrt{3}k_x/2) \cos(3k_y/2)$ describing in-plane hopping is exactly the same as for graphene, cf. Eq. (1.27).

Since, for all models $h_N(\mathbf{k})$, the Bravais period is doubled along the \hat{z} direction, such that the Brillouin zone extends from $k_z = -\pi/2$ to $k_z = \pi/2$, it is clear that nodal points in the spectrum (5.23) can appear only in the $k_z = 0$ plane. Indeed, the hexagonal Brillouin zone contains one N -fold nodal point at the K ($\xi = +$) and one at the K' ($\xi = -$) valley, with coordinates \mathbf{K}_{ξ} as given by Eq. (1.28). These nodal points are described exactly by the continuum models (5.4) at low energy, as can be

easily seen by noting that $w_{\mathbf{k}} \rightarrow \xi q_x - i q_y$ around these points. Thus, there is a Berry dipole pointing up in the K valley and one pointing down in the K' valley.

Valley-Hopf semimetals without time-reversal symmetry

As examples for this class of lattice models we choose Hamiltonians of the form

$$\tilde{h}_N(\mathbf{k}) = \begin{pmatrix} 0 & \tilde{Q}_N \\ \tilde{Q}_N^\dagger & 0 \end{pmatrix}, \quad (5.24)$$

where

$$\tilde{Q}_3 = \begin{pmatrix} s_- & -i s_z \end{pmatrix}, \quad \tilde{Q}_4 = \begin{pmatrix} a s_- & i a s_z \\ i b s_z & b s_+ \end{pmatrix}, \quad \tilde{Q}_5 = \begin{pmatrix} 0 & i\sqrt{2} s_z \\ i s_z & s_+ \\ \sqrt{2} s_+ & 0 \end{pmatrix}.$$

Here we use shorthand notations $s_{\pm} \equiv s_x \pm i s_y$. The Hamiltonians $\tilde{h}_N(\mathbf{k})$ represent nearest-neighbor tight-binding models on a tetragonal Bravais lattice, with Bravais vectors $\mathbf{a}_1 = \hat{x} + \hat{y}$, $\mathbf{a}_2 = \hat{x} - \hat{y}$, and $\mathbf{a}_3 = 2\hat{z}$. Indeed, the models describe 2D square layers stacked in a particular way along the \hat{z} direction, as shown in Fig. 5.8. Note that the five-band model has two types of orbitals (A and C) located at the same site.

The three-band model $\tilde{h}_3(\mathbf{k})$ has alternating hoppings $t_{AB} = \pm i/2$ ($t_{AB} = \pm 1/2$) in the \hat{x} -direction (\hat{y} -direction) within the A-B plane and alternating hoppings $t_{AC} = \pm 1/2$ along the A-C direction, see Fig. 5.8(a). Similarly, the model $\tilde{h}_4(\mathbf{k})$ has alternating hoppings $t_{AC} = \pm i a/2$ ($t_{AC} = \pm a/2$) in the \hat{x} direction (\hat{y} direction) within the A-C plane, alternating hoppings $t_{BD} = \pm i b/2$ ($t_{BD} = \pm b/2$) in the \hat{x} direction (\hat{y} direction) within the B-D plane, and alternating hoppings $t_{AD} = \pm a/2$ and $t_{BC} = \pm b/2$ in the perpendicular direction, see Fig. 5.8(b). Finally, the five-band model $\tilde{h}_5(\mathbf{k})$ has alternating hoppings $t_{BE} = \pm i/2$ ($t_{BE} = \pm 1/2$) in the \hat{x} direction (\hat{y} direction) within the B-E plane, alternating hoppings $t_{CD} = \pm i/\sqrt{2}$ ($t_{CD} = \pm 1/\sqrt{2}$) in the \hat{x} direction (\hat{y} direction) within the C-D plane, as well as alternating hoppings $t_{AE} = \pm 1/\sqrt{2}$ and $t_{BD} = \pm 1/2$ along the vertical direction, see Fig. 5.8(c).

The corresponding band structure of the models $\tilde{h}_N(\mathbf{k})$ is given by

$$\epsilon_{\alpha}(\mathbf{k}) = c_{\alpha} \sqrt{\sin^2 k_x + \sin^2 k_y + \sin^2 k_z}, \quad (5.25)$$

which is again particle-hole symmetric due to a chiral symmetry, and where the band velocities c_{α} are the same as for the continuum models (5.4), see Table 5.1. Again nodal points can appear only in the $k_z = 0$ plane. Indeed, the tetragonal Brillouin zone contains two N -fold nodal points, namely one located at the Γ point ($\xi = +$) and one at the M point ($\xi = -$), where $\mathbf{k}_{\Gamma} = 0$ and $\mathbf{k}_{\text{M}} = (\pi, 0, 0)$. It is straightforward to see that the low-energy theory around these points is exactly described by the continuum models (5.4).

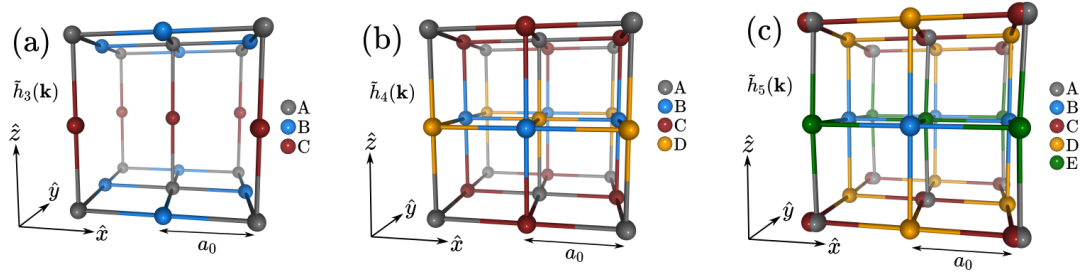


Fig. 5.8 – (a)–(c) Tight-binding models for threefold, fourfold and fivefold valley-Hopf semimetals with broken time-reversal symmetry on a 3D tetragonal lattice, as given by the tight-binding Hamiltonian (5.24).

5.4.2 | Topological Hopf semimetals

This class, characterized by an odd number of Berry dipoles in the Brillouin zone, is somewhat harder to realize than the previous one, in particular it appears that time-reversal symmetry always has to be broken. This is not surprising considering that these systems are closely related to Hopf insulators (see Section 5.5 below), which are also characterized by broken time-reversal symmetry. As examples for topological Hopf semimetals, we consider Hamiltonians of the form

$$\mathfrak{h}_N(\mathbf{k}) = \begin{pmatrix} 0 & \mathfrak{Q}_N \\ \mathfrak{Q}_N^\dagger & 0 \end{pmatrix}, \quad (5.26)$$

where

$$\mathfrak{Q}_3 = \begin{pmatrix} s_- & g_{\Delta_0} \end{pmatrix}, \quad \mathfrak{Q}_4 = \begin{pmatrix} as_- & -ag_{\Delta_0} \\ bg_{\Delta_0}^* & bs_+ \end{pmatrix}, \quad \mathfrak{Q}_5 = \begin{pmatrix} 0 & \sqrt{2}g_{\Delta_0}^* \\ g_{\Delta_0}^* & s_+ \\ \sqrt{2}s_+ & 0 \end{pmatrix},$$

and with

$$g_{\Delta_0} \equiv \Delta_0 + c_x + c_y + e^{-iz}, \quad (5.27)$$

where Δ_0 is a real parameter. These Hamiltonians are difficult to realize as pure hopping models with only one orbital per site, however since they contain only terms $\sim \sin k_i$ or $\sim \cos k_i$ they may be constructed assuming a simple cubic Bravais lattice with N orbitals per site and appropriate couplings, see Fig. 5.9.

The Hamiltonians $\mathfrak{h}_N(\mathbf{k})$ have an energy spectrum

$$\epsilon_\alpha(\mathbf{k}) = c_\alpha \sqrt{s_x^2 + s_y^2 + s_z^2 + (\Delta_0 + c_x + c_y + c_z)^2}, \quad (5.28)$$

where again a chiral symmetry is evident and the coefficients c_α are as in Table 5.1. This spectrum becomes gapless only for $\Delta_0 = \pm 1, \pm 3$. For the moment, since we are interested in the semimetallic phase, we only allow the parameter Δ_0 to take one of these discrete values.

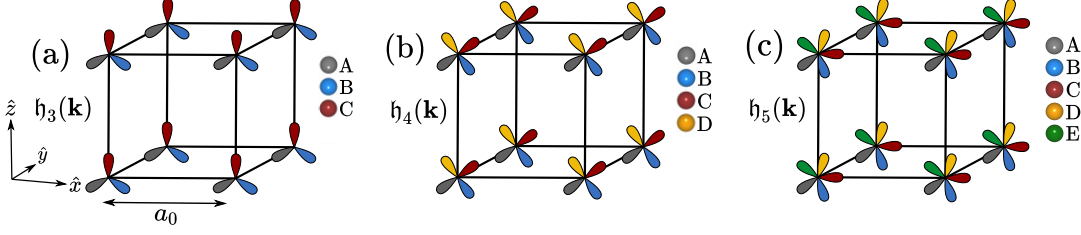


Fig. 5.9 – (a)–(c) Tight-binding models for threefold, fourfold and fivefold topological Hopf semimetals can be constructed on a multiorbital cubic lattice, with hoppings as given by the tight-binding Hamiltonian (5.26).

For $\Delta_0 = -3$, there is a single N -fold crossing at the Γ point of the cubic Brillouin zone, described by a low-energy theory $H_N^+(\mathbf{q})$, corresponding to a Berry dipole pointing up. Similarly, for $\Delta_0 = 3$, there is a single N -fold crossing at the R point, $\mathbf{k}_R = (\pi, \pi, \pi)$, described by $-H_N^+(\mathbf{q})$, and thus corresponding to a Berry dipole pointing down. For $\Delta_0 = -1$, there are three N -fold crossings at the inequivalent X points: $\mathbf{k}_{X1} = (\pi, 0, 0)$, $\mathbf{k}_{X2} = (0, \pi, 0)$, $\mathbf{k}_{X3} = (0, 0, \pi)$. They are described by $H_{N,X1}(\mathbf{q}) = H_N^+(-q_x, q_y, q_z)$, $H_{N,X2}(\mathbf{q}) = H_N^+(q_x, -q_y, q_z)$, and $H_{N,X3}(\mathbf{q}) = H_N^+(q_x, q_y, -q_z)$, respectively, thus corresponding to Berry dipoles pointing down, down and up. Finally, for $\Delta_0 = 1$, there are three N -fold crossings at the M points: $\mathbf{k}_{M1} = (0, \pi, \pi)$, $\mathbf{k}_{M2} = (\pi, 0, \pi)$, $\mathbf{k}_{M3} = (\pi, \pi, 0)$. They are described by $H_{N,Mi}(\mathbf{q}) = -H_{N,Xi}(\mathbf{q})$, thus corresponding to Berry dipoles pointing up, up, and down. The four types of high-symmetry points mentioned here (Γ , R, X, M) will play an important role below when we discuss topological phase transitions of Hopf insulators.

5.4.3 | Physical properties from a lattice perspective

For a Fermi level close to the nodal points, the physical properties of the semimetallic lattice models (5.22), (5.24) and (5.26) are simply obtained by summing the continuum results, as obtained in Sections 5.3.2–5.3.4, over all valleys. It is then clear that both the anomalous Hall current (5.18) and the magnetocurrent (5.21) cancel for a valley-Hopf semimetal, since there is an even number of crossings with opposite Berry dipoles, cf. Fig. 5.6(a). However, the currents are non-trivial for the topological Hopf semimetals (5.26), since there is one net Berry dipole in the Brillouin zone. To confirm this, as already mentioned, we have numerically calculated the anomalous Hall conductivity of $\mathfrak{h}_N(\mathbf{k})$ for parameters such that a single Berry dipole crossing exists at the Γ point, see Fig. 5.5(a). A similar lattice calculation (not shown) confirms the existence of weak-field magnetocurrents \mathbf{j}_{geo} for a topological Hopf semimetal (5.26).

Despite the fact that the anomalous Hall conductivity and magnetoconductivity cancel for the valley-Hopf semimetals, it is possible to conceive of other ways to unveil the presence of the Berry dipoles in these systems. For example, consider the lattice model $h_3(\mathbf{k})$ [shown in Fig. 5.7(a)], and assume the presence of a strong magnetic field (5.8). For $\theta = 0$, we know from Fig. 5.3(a) that the Landau level spectrum at the K valley ($\xi = +$) will be gapped out, while the Landau level spectrum at the K' valley ($\xi = -$) will be gapless. For $\theta = \pi$, the situation is reversed. Flipping the

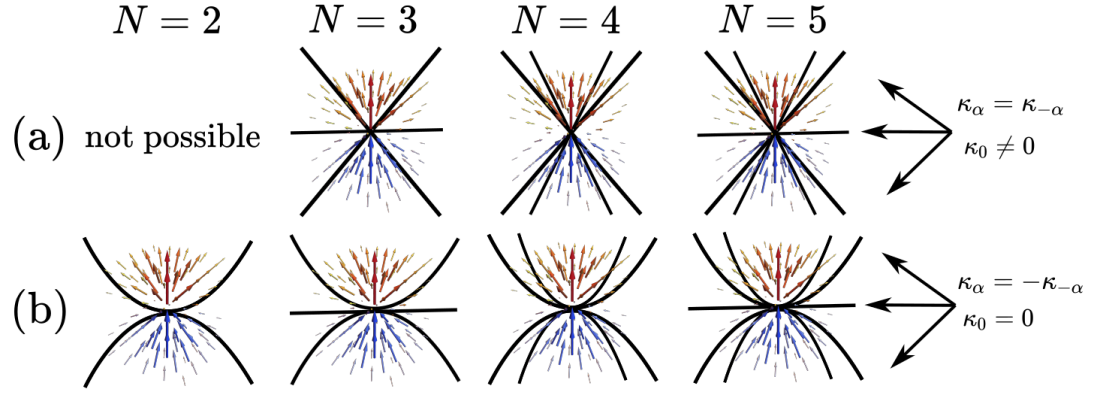


Fig. 5.10 – Two classes of multiband Hopf insulators and semimetals. (a) Multiband Hopf insulators as described by Eq. (5.34) exhibit linear multifold crossings with a Berry dipole such that $\kappa_\alpha = \kappa_{-\alpha}$. (b) Multiband Hopf insulators as described by a generalized Moore-Ran-Wen model (5.40) exhibit quadratic multifold touchings with a Berry dipole such that $\kappa_\alpha = -\kappa_{-\alpha}$.

magnetic field thus provides a means to completely switch the valley polarization of dispersive states in an energy window $E_F \in [-eB, eB]$ around the highly degenerate flat band. This effect is purely due to the Berry dipole. A similar effect exists for the lattice model $h_5(\mathbf{k})$. From a more general perspective, it appears interesting to study optical and magneto-optical responses of the valley-Hopf semimetals.

5.5 | Multiband Hopf semimetals and Hopf insulators

In this section we connect the semimetals introduced above to the theory of Hopf insulators. We start by describing the well-known concept of a two-band Hopf insulator, first introduced by Moore et al. (2008), as well as a generalization of the Hopf insulator to the multiband ($N > 2$) case, which was proposed very recently by Lapierre et al. (2021). We then propose the first concrete lattice models for multiband Hopf insulators, which can be separated into two fundamentally different classes. For the first class, the semimetallic phase obtained at a topological phase transition is exactly the (linear) multifold Hopf semimetal (5.4), characterized by a linear crossing with a Berry dipole (5.1) such that $\kappa_\alpha = \kappa_{-\alpha}$. For the second class, the semimetal at a topological phase transition may be called a *quadratic multifold Hopf semimetal*; it also carries a Berry dipole (5.1), however emerging from a quadratic touching and with $\kappa_\alpha = -\kappa_{-\alpha}$. As we shall see, the quadratic Hopf semimetals can be obtained from merging Berry monopoles, while the linear Hopf semimetals cannot. These results are summarized in Fig. 5.10 and explained in detail in the following.

5.5.1 | Two-band and multiband Hopf insulators

Two-band Hopf insulators

Consider a three-dimensional two-band system (2.15) and assume the two bands to be fully gapped. The Bloch Hamiltonian can be seen as a map $H(\mathbf{k}) : \mathbb{T}^3 \mapsto \mathbb{S}^2$ from the Brillouin zone 3-torus \mathbb{T}^3 to the two-sphere \mathbb{S}^2 . The possible topological character of

such a map can be determined from homotopy classification, as was first carried out by Pontrjagin (1941). The classification involves three Chern numbers (weak topological invariants) that classify maps $\mathbb{T}^2 \mapsto \mathbb{S}^2$ from the three possible sub-tori \mathbb{T}^2 to \mathbb{S}^2 . If $H(\mathbf{k})$ is such that all three Chern numbers vanish, the homotopy classification of maps $H(\mathbf{k}) : \mathbb{T}^3 \mapsto \mathbb{S}^2$ is the same as that of $H(\mathbf{k}) : \mathbb{S}^3 \mapsto \mathbb{S}^2$ (Lapierre et al. 2021), and the relevant topological invariant is the *Hopf invariant* or *Hopf number*, which takes integer values $\mathcal{N}_{\text{Hopf}} \in \mathbb{Z}$. This name originates from an important work of Hopf (1931) regarding mappings from the three-sphere \mathbb{S}^3 to the two-sphere \mathbb{S}^2 .

The above rather abstract notions were applied to the theory of band insulators by Moore et al. (2008), who proposed a class of topological insulators (3D two-band insulators in the absence of time-reversal symmetry) based on the Hopf map. They argued that this phase might be realizable in crystals for example when electrons move in a magnetic background. In particular, they constructed the following tight-binding model:⁶

$$\begin{aligned} H(\mathbf{k}) &= \mathbf{h}(\mathbf{k}) \cdot \boldsymbol{\sigma}, \\ h_1(\mathbf{k}) &= 2s_x s_z + 2s_y (c_x + c_y + c_z + \Delta), \\ h_2(\mathbf{k}) &= -2s_y s_z + 2s_x (c_x + c_y + c_z + \Delta), \\ h_3(\mathbf{k}) &= s_x^2 + s_y^2 - s_z^2 - (c_x + c_y + c_z + \Delta)^2, \end{aligned} \quad (5.29)$$

where Δ is a tunable parameter. This Hamiltonian will be referred to as the Moore-Ran-Wen model. To be precise, in the original paper Moore et al. (2008) considered only the particular value $\Delta = -3/2$; we here use a slightly more general version of the model, which was studied by Deng et al. (2013).

The Moore-Ran-Wen model is designed to exhibit a non-trivial Hopf number, which can be computed as a Brillouin zone integral

$$\mathcal{N}_{\text{Hopf}} = \frac{1}{4\pi^2} \int_{\text{BZ}} d^3k \mathcal{A}_\alpha(\mathbf{k}) \cdot \boldsymbol{\Omega}_\alpha(\mathbf{k}) \quad (5.30)$$

over the scalar product of Berry connection and curvature. Importantly, the Hopf invariant is *not* associated to an individual band [unlike, say, the Chern number (1.23)], but instead it is a characteristic of the whole band structure. Accordingly, it is irrelevant whether one chooses the valence or conduction band to compute it ($\alpha = \pm$). This fact becomes more transparent when writing $\mathcal{N}_{\text{Hopf}}$ in the form of Eq. (1.25). This equation, which is actually valid for arbitrary N (see below), is indeed equivalent to Eq. (5.30) for the two-band case.⁷ It should also be mentioned that the integral in Eq. (5.30), and more generally the Hopf number (1.25), is not obviously gauge-invariant. It can however be shown that gauge invariance is guaranteed if the three Chern numbers mentioned above vanish (Moore et al. 2008). It can indeed be

⁶This model is often written in the equivalent form

$$H(\mathbf{k}) = (z^\dagger \boldsymbol{\sigma} z) \cdot \boldsymbol{\sigma}, \quad z = (s_x + i s_y, s_z + i(c_x + c_y + c_z + \Delta))^T.$$

⁷To see this, insert the 2×2 matrix $U(\mathbf{k}) = (|\psi_+(\mathbf{k})\rangle, |\psi_-(\mathbf{k})\rangle)$ into Eq. (1.25), where $|\psi_\alpha(\mathbf{k})\rangle = (\psi_{\alpha,1}(\mathbf{k}), \psi_{\alpha,2}(\mathbf{k}))^T$. By explicit calculation one finds $\chi(\mathbf{k}) = 3\epsilon_{ijk} \mathcal{A}_{\alpha,i}(\mathbf{k}) \Omega_{\alpha,jk}(\mathbf{k}) = 6\mathcal{A}_\alpha(\mathbf{k}) \cdot \boldsymbol{\Omega}_\alpha(\mathbf{k})$.

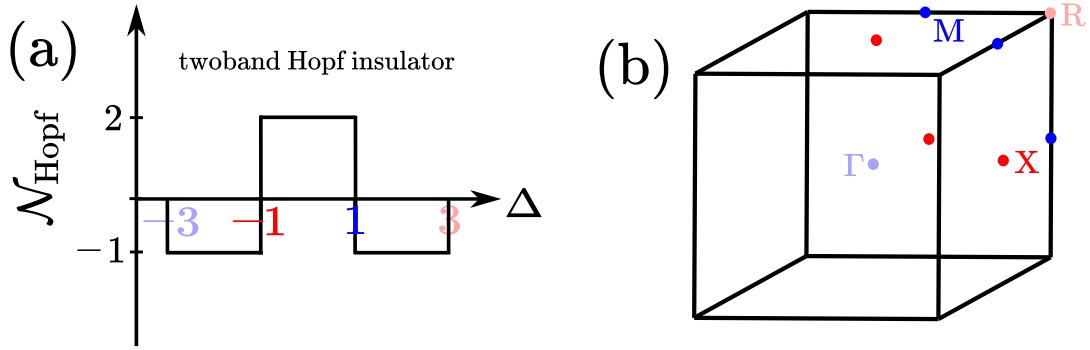


Fig. 5.11 – (a) Hopf invariant for the Moore-Ran-Wen model (5.29). Topological phase transitions occur for $\Delta = \Delta_0 \in \{\pm 1, \pm 3\}$, where gaps close at the Γ , X, M or R points of the cubic Brillouin zone, see (b). Red (blue) colors denote a positive (negative) change of $\mathcal{N}_{\text{Hopf}}$.

easily verified for the Moore-Ran-Wen model that the three Chern numbers

$$\mathcal{N}_\alpha^{\text{Chern},ij} = \frac{1}{2\pi} \int_{\mathbb{T}^2} dk_i dk_j \Omega_{\alpha,ij}(k_i, k_j; k_l = \text{const.}) \quad (5.31)$$

for $(i, j) = (x, y), (y, z), (z, x)$ are zero, which implies that Eq. (5.30) really yields a gauge-invariant \mathbb{Z} number.

In Fig. 5.11(a) we plot the Hopf number of the Moore-Ran-Wen model [as computed from Eqs. (1.25) or (5.30)] as a function of the parameter Δ . Clearly, the system is topologically non-trivial in the Hopf sense for $|\Delta| < 3$. Topological phase transitions occur whenever the energy spectrum

$$\epsilon_\pm(\mathbf{k}) = \pm(s_x^2 + s_y^2 + s_z^2 + (c_x + c_y + c_z + \Delta)^2) \quad (5.32)$$

becomes gapless, which happens at points Γ , R, X, M for $\Delta = -3, 3, -1, 1$, respectively, as visualized in Fig. 5.11(b). These transitions will be discussed in more detail below.

Multiband Hopf insulators

A multiband generalization of the Hopf insulator was recently established by Lapierre et al. (2021). Consider a three-dimensional N -band system (2.24) and assume *all* N bands to be fully gapped, such that there are no degenerate subspaces. Under these conditions, the Bloch Hamiltonian $H(\mathbf{k})$ can be seen as a map $H(\mathbf{k}) : \mathbb{T}^3 \mapsto \text{SU}(N)/\text{U}(1)^{N-1}$ from the Brillouin zone 3-torus \mathbb{T}^3 to the quotient group $\text{SU}(N)/\text{U}(1)^{N-1}$. In the $N = 2$ case this reduces to the scenario discussed above as $\text{SU}(2)/\text{U}(1)$ is isomorphic to \mathbb{S}^2 . Under the assumption that all three weak invariants (Chern numbers) vanish, it can be shown from homotopy classification that the map $H(\mathbf{k}) : \mathbb{T}^3 \mapsto \text{SU}(N)/\text{U}(1)^{N-1}$ is classified by a \mathbb{Z} invariant, which is known as the *Hopf invariant* or *Hopf number* of the N -band system. This name is chosen by analogy to the two-band case.

To compute the Hopf number of the N -band system, Lapierre et al. (2021) introduced Eq. (1.25). As we have seen, for $N = 2$ there is the equivalent expression

(5.30), but it relies on very specific properties which are no longer valid for $N > 2$. Indeed, in general the Hopf number cannot be written in terms of Abelian geometric quantities. Instead, an expression based on the non-Abelian Chern-Simons three-form (Ryu et al. 2010) is possible:⁸

$$\mathcal{N}_{\text{Hopf}} = \frac{1}{8\pi^2} \int_{\text{BZ}} d^3k \text{Tr} \left[\mathcal{A} \cdot (\nabla \times \mathcal{A}) - \frac{2i}{3} \mathcal{A} \cdot (\mathcal{A} \times \mathcal{A}) \right]. \quad (5.33)$$

Here, $\mathcal{A} = \mathcal{A}(\mathbf{k}) = (\mathcal{A}_x(\mathbf{k}), \mathcal{A}_y(\mathbf{k}), \mathcal{A}_z(\mathbf{k}))$ is a vector formed from $N \times N$ non-Abelian Berry connection matrices with matrix elements $\mathcal{A}_{i,\alpha\beta}(\mathbf{k}) = i\langle \psi_\alpha(\mathbf{k}) | \partial_i \psi_\beta(\mathbf{k}) \rangle$. While Eq. (5.33) is conceptually useful as a generalization of Eq. (5.30), we find Eq. (1.25) to be less cumbersome for practical purposes. We emphasize again that Eqs. (1.25) and (5.33) are gauge-invariant if the three weak invariants [Chern numbers (5.31)] vanish.

5.5.2 | Lattice models for multiband Hopf insulators

Aside from the Moore-Ran-Wen model (5.29), several similar Hamiltonians have been proposed for two-band Hopf insulators (Deng et al. 2013; Kennedy 2016; Liu et al. 2017; Schuster et al. 2019). Here we introduce the first known lattice models for multiband Hopf insulators. They can be separated into two classes (linear and quadratic) as shown in Fig. 5.10, and as discussed in more detail in the following.

Linear multiband Hopf insulators

Consider the tight-binding Hamiltonians

$$h_N^{\text{Hopf}}(\mathbf{k}) = \begin{pmatrix} 0 & Q_N^{\text{Hopf}} \\ (Q_N^{\text{Hopf}})^\dagger & 0 \end{pmatrix}, \quad (5.34)$$

where

$$Q_3^{\text{Hopf}} = \begin{pmatrix} s_- & g_\Delta \end{pmatrix}, \quad Q_4^{\text{Hopf}} = \begin{pmatrix} as_- & -ag_\Delta \\ bg_\Delta^* & bs_+ \end{pmatrix}, \quad Q_5^{\text{Hopf}} = \begin{pmatrix} 0 & \sqrt{2}g_\Delta^* \\ g_\Delta^* & s_+ \\ \sqrt{2}s_+ & 0 \end{pmatrix},$$

with $g_\Delta \equiv \Delta + c_x + c_y + e^{-iz}$ and with a continuous parameter Δ .⁹ They have an energy spectrum

$$\epsilon_\alpha(\mathbf{k}) = c_\alpha \epsilon, \quad \epsilon = \sqrt{s_x^2 + s_y^2 + s_z^2 + (\Delta + c_x + c_y + c_z)^2}, \quad (5.35)$$

⁸It appears that there is a wrong sign in the second term of Eq. (12) in the work of Lapierre et al. (2021).

⁹The attentive reader may have noticed that the Hamiltonians (5.34) are obtained from the models (5.26) upon simply replacing the discrete parameter Δ_0 by a continuous parameter Δ . This implies that the semimetals (5.26) occur at topological phase transitions of the insulators (5.34), as we will discuss further below.

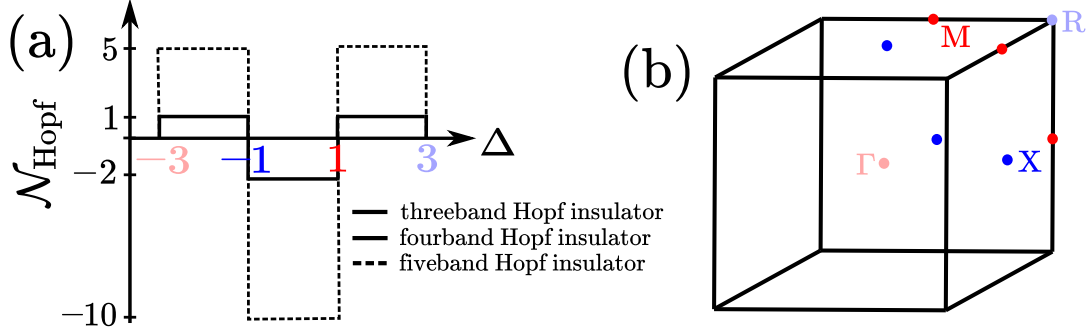


Fig. 5.12 – (a) Hopf invariant (1.25) for the models (5.34) with $N = 3, 4, 5$. Topological phase transitions occur for $\Delta = \pm 1, \pm 3$, where gaps close at the Γ , X , M or R points of the cubic Brillouin zone, see (b).

which is particle-hole symmetric due to chiral symmetry and has band velocities c_α as listed in Table 5.1. We now claim that these models are multiband Hopf insulators. More precisely, they may be called linear multiband Hopf insulators, in the sense that they exhibit linear crossing points at topological phase transitions, as discussed further below. The linear crossings originate from the fact that $h_N^{\text{Hopf}}(\mathbf{k})$ can be viewed as tight-binding models with only nearest-neighbor hoppings on a multiorbital cubic lattice, such as shown in Fig. 5.9.

To confirm that the Hamiltonians (5.34) are Hopf insulators, we first verify that the three Chern numbers (5.31) vanish, and then compute the Hopf number from Eq. (1.25); for the $N = 3$ and $N = 4$ case, using a convenient gauge choice we find a Hopf density

$$\chi(\mathbf{k}) = \frac{12}{\epsilon^4} (c_x c_y + c_y c_z + c_z c_x + \Delta c_x c_y c_z), \quad (5.36)$$

and from numerical integration one obtains

$$\mathcal{N}_{\text{Hopf}} = \begin{cases} 0 & |\Delta| > 3 \\ 1 & 1 < |\Delta| < 3, \\ -2 & 0 < |\Delta| < 1 \end{cases}, \quad (5.37)$$

as shown in Fig. 5.12(a). For the $N = 5$ model the Hopf density is more involved; for our gauge choice we have¹⁰

$$\begin{aligned} \chi(\mathbf{k}) = \frac{12}{\epsilon^4} \{ & -c_x c_y + 2c_x c_z + 2c_y c_z - 2(c_x^2 + c_y^2) \\ & - (c_x c_{2y} + c_y c_{2x}) c_z + 2(c_x - c_y) s_x s_y s_z \\ & + \Delta [c_x c_y c_z - (c_x c_{2y} + c_y c_{2x}) - 3(c_x + c_y)] - 2\Delta^2 c_x c_y \}, \end{aligned} \quad (5.38)$$

leading to higher Hopf numbers:

$$\mathcal{N}_{\text{Hopf}} = \begin{cases} 0 & |\Delta| > 3 \\ 5 & 1 < |\Delta| < 3. \\ -10 & 0 < |\Delta| < 1 \end{cases}. \quad (5.39)$$

¹⁰We recall that the Hopf density is not gauge-invariant, but the Hopf number is.

Topological phase transitions occur whenever the energy gap of the spectrum (5.36) closes, as will be discussed in more detail shortly.

It should also be mentioned that the model $h_3^{\text{Hopf}}(\mathbf{k})$ is actually well known as a *chiral topological insulator* in the literature (Wang et al. 2014; Lian et al. 2019). It was introduced for constructing fractional topological phases (Neupert et al. 2012), and we here identify it as a three-band Hopf insulator. Indeed, it appears that the topological invariant defined in Eq. (3.7) of Neupert et al. (2012) is just the Hopf number, however calculated from a simplified formula that makes explicit use of the fact that the system has $N = 3$ bands and chiral symmetry. However, when chiral symmetry is broken without a gap-closing, the topological invariant in Eq. (3.7) of Neupert et al. (2012) should become ill-defined. In contrast, the Hopf number (1.25) remains well-defined and the values (5.37) should remain unchanged.

Quadratic multiband Hopf insulators: generalized Moore-Ran-Wen model

We here introduce a second class of multiband insulators, generalizing the Moore-Ran-Wen model (5.29) to any N . This is done simply by replacing the Pauli matrices by pseudospin- s matrices, to obtain

$$\begin{aligned} h_s^{\text{Hopf}}(\mathbf{k}) &= \mathbf{h}(\mathbf{k}) \cdot \mathbf{S}, \\ h_1(\mathbf{k}) &= 2s_x s_z + 2s_y (c_x + c_y + c_z + \Delta), \\ h_2(\mathbf{k}) &= -2s_y s_z + 2s_x (c_x + c_y + c_z + \Delta), \\ h_3(\mathbf{k}) &= s_x^2 + s_y^2 - s_z^2 - (c_x + c_y + c_z + \Delta)^2. \end{aligned} \quad (5.40)$$

These models have an energy spectrum

$$\epsilon_\alpha(\mathbf{k}) = c_\alpha (s_x^2 + s_y^2 + s_z^2 + (c_x + c_y + c_z + \Delta)^2), \quad (5.41)$$

where $c_\alpha = m_s$ as listed in Table 2.1. The gap closings occur at the same values of Δ and at the same points in the Brillouin zone as for the two-band Hopf insulator (5.29) and the multiband Hopf insulator (5.34). Since these gap closings are characterized by quadratic touchings – which originates from the fact that Eq. (5.40) can be viewed as a tight-binding model with next-nearest-neighbor hoppings on a multiorbital cubic lattice –, we will call the models (5.40) quadratic multiband Hopf insulators.

To confirm the Hopf character, we again compute the Hopf invariant from Eq. (1.25). For $s = 1/2$ this is equivalent to the Moore-Ran-Wen model. For $s = 1$ we obtain

$$\mathcal{N}_{\text{Hopf}} = \begin{cases} 0 & |\Delta| > 3 \\ -5 & 1 < |\Delta| < 3, \\ 10 & 0 < |\Delta| < 1 \end{cases}, \quad (5.42)$$

as shown in Fig. 5.13. It would be interesting to compute the Hopf numbers for higher s and to try to establish the function $\mathcal{N}_{\text{Hopf}}(s)$; this gets however quite cumbersome for $s > 1$ due to the complicated expressions for the energy eigenstates.

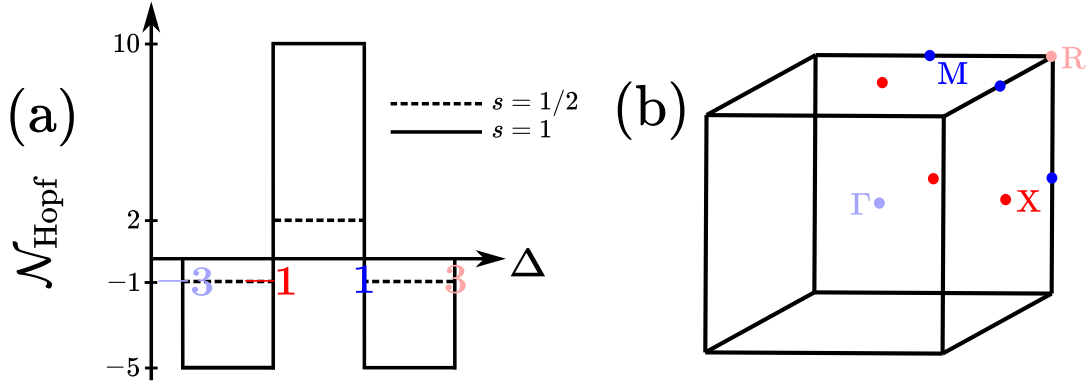


Fig. 5.13 – (a) Hopf invariant (1.25) for the models (5.40) with $s = 1/2$ and $s = 1$. The $s = 1/2$ case is equivalent to the Moore-Ran-Wen model (5.29). Topological phase transitions occur when gaps close at the Γ , X, M or R points of the cubic Brillouin zone, see (b).

5.5.3 | Hopf semimetals as topological phase transitions

We now demonstrate that at the topological phase transitions of each of the Hopf insulators (5.29), (5.34) and (5.40) there appear semimetallic phases with Berry dipole. Such phases will be called *Hopf semimetals*, which establishes the desired connection with the first four sections of this chapter.

Twofold Hopf semimetal in the Moore-Ran-Wen model

The band structure (5.32) of the Moore-Ran-Wen model (5.29) is in general insulating, but becomes gapless for $\Delta = \pm 1, \pm 3$. Accordingly, there occur topological phase transitions at these parameter values, see Fig. 5.11. We now investigate these transitions more closely by introducing a continuum model

$$H_\nu(\mathbf{q}) = \mathbf{h}_\nu(\mathbf{q}, \Delta_\nu) \cdot \boldsymbol{\sigma} \quad (5.43)$$

in the vicinity of each gap-closing value of Δ , where

$$\begin{aligned} \mathbf{h}_\Gamma(\mathbf{q}, \Delta_\Gamma) &= (2q_x q_z + 2q_y \Delta_\Gamma, -2q_y q_z + 2q_x \Delta_\Gamma, q_x^2 + q_y^2 - q_z^2 - \Delta_\Gamma^2), \\ \mathbf{h}_R(\mathbf{q}, \Delta_R) &= \mathbf{h}_\Gamma(\mathbf{q}, \Delta_\Gamma \rightarrow -\Delta_R), \\ \mathbf{h}_{X_i}(\mathbf{q}, \Delta_X) &= \mathbf{h}_\Gamma(q_i \rightarrow -q_i, \Delta_\Gamma \rightarrow \Delta_X), \\ \mathbf{h}_{M_i}(\mathbf{q}, \Delta_M) &= \mathbf{h}_{X_i}(\mathbf{q}, \Delta_X \rightarrow -\Delta_M), \end{aligned} \quad (5.44)$$

with $\Delta_\Gamma = \Delta + 3$, $\Delta_R = \Delta - 3$, $\Delta_X = \Delta + 1$ and $\Delta_M = \Delta - 1$. Note that there are three different continuum models for the three points X_i and M_i , where $i = 1, 2, 3$. The continuum models (5.43) have an energy spectrum

$$\epsilon_\pm(\mathbf{q}) = \pm(|\mathbf{q}|^2 + \Delta_\nu^2), \quad (5.45)$$

such that there is an isotropic quadratic touching point whenever $\Delta_\nu = 0$. Next, let us consider the Berry curvature, the key quantity of interest for our purposes. For the continuum model $H_\Gamma(\mathbf{q})$ we find

$$\boldsymbol{\Omega}_\alpha(\mathbf{q}) = \frac{\kappa_\alpha}{(|\mathbf{q}|^2 + \Delta_\Gamma^2)^2} [(\mathbf{q} \cdot \mathbf{d})\mathbf{q} + \Delta_\Gamma(\mathbf{q} \times \mathbf{d}) + \Delta_\Gamma^2 \mathbf{d}] \quad (5.46)$$

with $\mathbf{d} = (0, 0, 1)$, and very similar expressions are obtained for all other continuum models $H_\nu(\mathbf{q})$. In other words, at any topological phase transition of the Moore-Ran-Wen model, there exists a *twofold Hopf semimetal* characterized by a quadratic two-band touching (5.45) and a *Berry dipole*. This fact was recently studied in considerable detail by Alexandradinata et al. (2021) and Nelson et al. (2022).

We have to emphasize, however, that the nature of the Berry dipole of such a two-band Hopf semimetal is fundamentally different from that of the linear multiband Hopf semimetals (5.4). In particular, the dipole charge κ_α in Eq. (5.46), which takes the explicit values $\kappa_\pm = \mp 2$ for the two bands, clearly has the property $\kappa_\alpha = -\kappa_{-\alpha}$, which is enforced by the Berry curvature sum rule $\sum_\alpha \mathbf{\Omega}_\alpha = 0$. In stark contrast, as we have stated repeatedly, the multifold Hopf semimetals (5.4) have a Berry dipole with $\kappa_\alpha = \kappa_{-\alpha}$, something that is impossible to achieve in a two-band system (see also Fig. 5.10).

One may also attempt to employ the continuum models (5.43) to determine the Hopf number without the need to carry out numerical integration. In particular, using the eigenstates of the continuum models $H_\nu(\mathbf{q})$, (Nelson et al. 2022) define a *continuum Hopf number* as

$$\mathcal{N}_\nu^{\text{Hopf}}(\Delta_\nu) = \frac{1}{4\pi^2} \int_{\mathbb{R}^3} d^3q \mathcal{A}_\alpha(\mathbf{q}) \cdot \mathbf{\Omega}_\alpha(\mathbf{q}). \quad (5.47)$$

The goal is then to compute the jump $\delta\mathcal{N}_{\text{Hopf}}$ of the Hopf number at a topological phase transition as the difference between the continuum Hopf numbers on both sides of the transition, summed over all points where the gap closes:

$$\delta\mathcal{N}_{\text{Hopf}} = \sum_\nu \left[\mathcal{N}_\nu^{\text{Hopf}}(\Delta_\nu > 0) - \mathcal{N}_\nu^{\text{Hopf}}(\Delta_\nu < 0) \right]. \quad (5.48)$$

This sum consists of one term for the transitions at Γ and R, and of three terms for the transitions at X and M. For a convenient gauge choice, this indeed seems to confirm the lattice results shown in Fig. 5.11(a); for example for the model $H_\Gamma(\mathbf{q})$ one finds $\mathcal{N}_\Gamma^{\text{Hopf}}(\Delta_\Gamma) = -\frac{1}{2}\text{sgn}(\Delta_\Gamma)$ and thus $\delta\mathcal{N}_{\text{Hopf}} = -1$. However the formula (5.47) is explicitly gauge-dependent, such that it should not be trusted for predicting the true Hopf number of the lattice model without a confirmation via Eq. (1.25).

Multifold Hopf semimetals from linear multiband Hopf insulators

Next, let us consider the topological phase transitions of the linear multiband Hopf insulators (5.34). They also happen at parameter values $\Delta = \pm 1, \pm 3$, and it is evident that at these transitions the topological Hopf semimetals (5.26) introduced earlier are exactly recovered. These semimetals are characterized by a linear multifold crossing (5.4) and a Berry dipole (5.1) with the property $\kappa_\alpha = \kappa_{-\alpha}$, see Fig. 5.10. The fact that the continuum models (5.4) are representative Hamiltonians for topological phase transitions of (linear) multiband Hopf insulators justifies the use of the word ‘‘Hopf’’ in the name for those semimetals.

One may again study the jump $\delta\mathcal{N}_{\text{Hopf}}$ at the topological phase transitions shown in Fig. 5.12 in terms of the continuum limit $H_\nu(\mathbf{q})$ of $h_N^{\text{Hopf}}(\mathbf{k})$ around a gap-closing

momentum \mathbf{k}_ν , where $\nu \in \{\Gamma, X, M, R\}$. In particular, one may be tempted to define a continuum Hopf number for the N -band system via the two equivalent expressions

$$\begin{aligned}\mathcal{N}_\nu^{\text{Hopf}}(\Delta_\nu) &= \frac{1}{24\pi^2} \int_{\mathbb{R}^3} d^3q \chi(\mathbf{q}), \quad \chi(\mathbf{q}) \equiv \epsilon_{ijk} \text{Tr}[u_i(\mathbf{q})u_j(\mathbf{q})u_k(\mathbf{q})], \\ \mathcal{N}_\nu^{\text{Hopf}}(\Delta_\nu) &= \frac{1}{8\pi^2} \int_{\mathbb{R}^3} d^3q \text{Tr} \left[\mathcal{A} \cdot (\nabla \times \mathcal{A}) - \frac{2i}{3} \mathcal{A} \cdot (\mathcal{A} \times \mathcal{A}) \right],\end{aligned}\tag{5.49}$$

which can be viewed as a multiband generalization of Eq. (5.47). Here, $\mathcal{A} = \mathcal{A}(\mathbf{q}) = (\mathcal{A}_x(\mathbf{q}), \mathcal{A}_y(\mathbf{q}), \mathcal{A}_z(\mathbf{q}))$ is a vector formed from $N \times N$ non-Abelian Berry connection matrices with matrix elements $\mathcal{A}_{i,\alpha\beta}(\mathbf{q}) = i\langle \psi_\alpha(\mathbf{q}) | \partial_i \psi_\beta(\mathbf{q}) \rangle$. Using the continuum Hopf numbers of all gap-closing momenta (see Appendix V.F) along with Eq. (5.48), we find again that for a convenient gauge choice the jumps shown in Fig. 5.12(a) can be predicted from the continuum approach. However, the expressions (5.49) are again gauge-dependent and should be treated with care.

Multifold Hopf semimetals from quadratic multiband Hopf insulators

Finally, consider the topological phase transitions of the quadratic multiband Hopf insulator (5.40). By writing down continuum models $H_\nu(\mathbf{q})$ in analogy to the two-band models (5.43), one readily finds that the spectrum is given by

$$\epsilon_\alpha(\mathbf{q}) = c_\alpha(|\mathbf{q}|^2 + \Delta_\nu^2),\tag{5.50}$$

where the band velocities are as listed in Table 2.1. The transitions are thus characterized by quadratic multifold touchings as shown in Fig. 5.10(b). Further, the Berry curvature of these N -fold touchings ($N = 2s + 1$) is equivalent to Eq. (5.46) in that the Berry dipole charge always satisfies $\kappa_\alpha = -\kappa_{-\alpha}$ for any s . The Berry dipoles are thus fundamentally different from those of the linear multifold crossings (5.4).

5.5.4 | Berry dipoles from merging of monopoles

As we have stated repeatedly and as summarized in Fig. 5.10, the Berry dipoles carried by the quadratic touchings of a (generalized) Moore-Ran-Wen model and those carried by the multifold Hopf semimetals (5.4) are fundamentally different. While we have only justified this by a rather unphysical argument (the parity $\kappa_\alpha = \pm\kappa_{-\alpha}$ of the dipole charges), it can also be understood in more physical terms, as explained in the following.

When taking a look at Fig. 5.1(a), one might ask what happens when the two Berry monopoles merge at a single point, that is, when one takes $\mathbf{d}_0 \rightarrow 0$. In particular, one may expect to find some kind of band touching point with Berry dipole, and wonder if this scenario is equivalent to the one described by Eq. (5.4). Let us study this situation via a simple continuum model

$$H(\mathbf{q}) = q_x S_x + q_y S_y + (q_z^2 - \delta_0) S_z,\tag{5.51}$$

describing a pair of Berry monopoles merging along the \hat{z} direction, where $\delta_0 = |\mathbf{d}_0^2|/4$. It is straightforward to obtain the Berry curvature of this model as

$$\boldsymbol{\Omega}_\alpha(\mathbf{q}) = \frac{\mathcal{C}_\alpha}{[q_x^2 + q_y^2 + (q_z^2 - \delta_0)^2]^{3/2}} \begin{pmatrix} q_x q_z \\ q_y q_z \\ \frac{1}{2}(q_z^2 - \delta_0) \end{pmatrix}, \quad (5.52)$$

where \mathcal{C}_α is the Chern number as listed in Table 2.1. Clearly, this indeed corresponds to some kind of point-like Berry dipole for $\delta_0 = 0$. However, the situation is fundamentally different from the point-like dipole (5.1) of the Hopf semimetals (5.4). First, the Berry curvature (5.52) emerges from an anisotropic semi-Dirac touching point with an evident memory of the merging direction. More importantly, the CP symmetry and the property $\boldsymbol{\Omega}_\alpha = -\boldsymbol{\Omega}_{-\alpha}$ of the chiral multifold semimetal phase ($\delta_0 > 0$) are also retained after the two Berry monopoles annihilate. The same behavior can be confirmed when studying the merging of two Berry monopoles in a lattice model. In fact, we have already computed the Berry curvature of such a model in Eq. (2.14), and to obtain two merged monopoles we just need to insert $k_0 = 0$ or $k_0 = \pi$. Clearly, one arrives at the same conclusions as for the continuum model (5.51).

The situation described by the merging model (5.51) is at first glance also different from the twofold Hopf semimetal (5.43) existing at topological phase transitions of the Moore-Ran-Wen model, since the latter has a fully isotropic quadratic band touching. However, this difference is not fundamental. Indeed, Nelson et al. (2022) recently introduced a minimal model

$$H(\mathbf{q}) = 2q_x q_z \sigma_1 - 2q_y q_z \sigma_2 + (q_x^2 + q_y^2 - q_z^2 - \delta_0) \sigma_3 \quad (5.53)$$

which shows that the twofold Hopf semimetal (5.43) *can* be obtained from merging a pair of Weyl nodes. Indeed, the model (5.53) represents a Weyl semimetal for $\delta_0 < 0$ and a nodal-line semimetal for $\delta_0 > 0$. The twofold Hopf semimetal (5.43) with isotropic spectrum $\epsilon_\pm(\mathbf{q}) = \pm|\mathbf{q}|^2$ and Berry dipole $\boldsymbol{\Omega}_\pm = \mp 2q_z \mathbf{q}/|\mathbf{q}|^4$ appears for $\delta_0 = 0$. By extending the model (5.53) to the multiband case (again replacing $\boldsymbol{\sigma} \rightarrow \mathbf{S}$), it is clear that the multifold quadratic touchings at topological phase transitions of the models (5.40) can be obtained from merging a pair of pseudospin- s monopoles.

In summary, the quadratic touching points appearing at topological phase transitions between quadratic Hopf insulators [Fig. 5.10(b)] are not fundamentally different from touching points that exist at the critical point between a chiral multifold semimetal and a nodal-line semimetal. In contrast, the linear crossing points appearing at topological phase transitions between linear Hopf insulators [Fig. 5.10(a)] cannot be obtained by such a process. This provides a physical argument for the fundamental difference between these two types of Berry dipole touchings, in addition to the different parity of the dipole charges κ_α .

Note also that the physical properties of the quadratic semimetals at phase transitions of the generalized Moore-Ran-Wen model (5.40) are thus somewhere in between those of chiral multifold semimetals and linear multifold Hopf semimetals: On the one hand, just like for the multifold Hopf semimetals (5.4), there is a quantum geometric

anisotropy already for a single touching point, which will create non-trivial Landau levels, as well as an anomalous Hall effect and linear magnetocurrents. On the other hand, the parity as a function of E_F will be as for a chiral multifold semimetal.

5.6 | Perspectives of Hopf semimetals and insulators

To conclude this chapter, we discuss several extensions and perspectives.

5.6.1 | Linear band crossings with Berry multipole structure

As argued in Section 5.2, linear band crossings of $N > 2$ bands can be obtained from several different Hamiltonians. So far, we have mainly compared pseudospin-like crossings and Hopf-like crossings, characterized by a Berry monopole and Berry dipole, respectively. However, there is no fundamental reason why other, yet more exotic geometric structures should not be possible. To illustrate this, we here propose models for fivefold crossings that give rise to a *Berry quadrupole* or *Berry octupole*.

Consider the five-band model

$$H_{5a}^{\xi}(\mathbf{q}) = \begin{pmatrix} 0 & q_+^{\xi} & 0 & iq_z & 0 \\ q_-^{\xi} & 0 & -iq_z & 0 & iq_z \\ 0 & iq_z & 0 & q_-^{\xi} & 0 \\ -iq_z & 0 & q_+^{\xi} & 0 & q_+^{\xi} \\ 0 & -iq_z & 0 & q_-^{\xi} & 0 \end{pmatrix}, \quad (5.54)$$

where again $q_{\pm}^{\xi} = \xi q_x \pm iq_y$. The spectrum is exactly the same as for the five-band model (5.4c), namely $\epsilon_{\alpha}(\mathbf{q}) = c_{\alpha}|\mathbf{q}|$ with $c_{\alpha} = 0, \pm 1, \pm\sqrt{2}$. However, the Berry curvature takes a different form,

$$\Omega_{\alpha}(\mathbf{q}) = \kappa_{\alpha}(\mathbf{q} \cdot \mathbf{d}) \frac{\mathbf{q}}{|\mathbf{q}|^4} + \tilde{\kappa}_{\alpha}(\mathbf{q} \cdot \mathbf{d})^3 \frac{\mathbf{q}}{|\mathbf{q}|^6}, \quad (5.55)$$

where $\mathbf{d} = (0, 0, \xi)$, which corresponds to a dipolar together with an octupolar term. The dipole and octupole charges are $\kappa_{\alpha} = 1, -3, 4, -3, 1$ and $\tilde{\kappa}_{\alpha} = -4, 8, -8, 8, -4$ from the lowest to the highest band. The fivefold crossing with Berry octupole is visualized in Fig. 5.14(b).

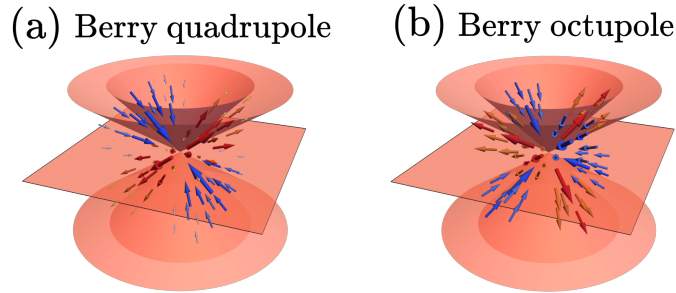


Fig. 5.14 – A fivefold linear crossing acting as (a) a Berry quadrupole. (b) a Berry octupole.

As a second example, consider the Hamiltonian

$$H_{5b}^{\xi}(\mathbf{q}) = \begin{pmatrix} 0 & q_-^{\xi} & iq_z & iq_z & 0 \\ q_+^{\xi} & 0 & q_+^{\xi} & 0 & -iq_z \\ -iq_z & q_-^{\xi} & 0 & -q_+^{\xi} & -iq_z \\ -iq_z & 0 & -q_-^{\xi} & 0 & q_-^{\xi} \\ 0 & iq_z & iq_z & q_+^{\xi} & 0 \end{pmatrix}. \quad (5.56)$$

The spectrum is again of the form $\epsilon_{\alpha}(\mathbf{q}) = c_{\alpha}|\mathbf{q}|$ where now $c_{\alpha} = 0, \pm 1, \pm\sqrt{3}$. The Berry curvature takes the exotic form

$$\Omega_{\alpha}(\mathbf{q}) = \tilde{\kappa}_{\alpha} q_x q_z \frac{\mathbf{q}}{|\mathbf{q}|^5} + \xi \tilde{\tilde{\kappa}}_{\alpha} q_y q_z^2 \frac{\mathbf{q}}{|\mathbf{q}|^6}, \quad (5.57)$$

with $\tilde{\kappa}_{\alpha} = -\sqrt{3}, 3, 0, -3, \sqrt{3}$ and $\tilde{\tilde{\kappa}}_{\alpha} = -4/3, 4, -16/3, 4, -4/3$. This corresponds to a quadrupolar and an octupolar term, as visualized in Fig. 5.14.

Considering these examples, it appears very interesting to speculate that the Berry curvature of any linear crossing in 3D takes the form of a multipole expansion

$$\Omega_{\alpha}(\mathbf{q}) = \sum_{n=0}^{\infty} \kappa_{\alpha}^{(n)} \prod_{i=1}^n (\mathbf{q} \cdot \mathbf{d}_i) \frac{\mathbf{q}}{|\mathbf{q}|^{n+3}}, \quad (5.58)$$

where $\kappa_{\alpha}^{(n)}$ are geometric charges and \mathbf{d}_i are 3D unit vectors. The allowed terms in Eq. (5.58) should be selected depending on the symmetries of the model and the number N of bands involved in the crossing. Indeed, we know that for $N = 2$ only the $n = 0$ term in Eq. (5.58) is allowed. For $N = 3$ and $N = 4$ we have seen that the $n = 0$ term is allowed in the presence of CP symmetry, whereas the $n = 1$ term is allowed in the presence of chiral symmetry. The examples (5.54) and (5.56) show that for $N = 5$ all terms $n = 0, 1, 2, 3$ are in principle possible, depending on the symmetries. For example the model (5.54) has a chiral symmetry $\mathcal{S} = \text{diag}(1, -1, 1, -1, 1)$, which appears to select the terms with odd n .

There are many open questions, such as whether Berry quadrupoles and octupoles are possible for $N < 5$, whether hexadecapoles are possible for $N = 5$, and so on. Moreover, very rich physical properties can be expected for such exotic crossings, for example in the Landau level spectrum, anomalous Hall conductivity, et cetera. The possibility to establish a full hierarchy of Berry multipole crossings thus appears very intriguing.

5.6.2 | Hopf-Haldane analogy

We here observe that the (linear) multiband Hopf semimetals and insulators presented in this chapter can be viewed as a family of 3D systems that is quite analogous to the family of 2D Dirac semimetals and Chern insulators that we described in Section 1.4.

Valley-Dirac semimetal versus valley-Hopf semimetal. Consider a 2D Dirac semimetal such as graphene, with a Hamiltonian (1.26). In fact, to be precise, graphene is an example for a *valley-Dirac semimetal*, because it has an even

number of linear nodal points in the Brillouin zone, with “opposite” quantum geometric properties in the two valleys. More precisely, the Berry curvature vanishes everywhere in the Brillouin zone except for singularities at the two nodal points,

$$\Omega_{\alpha,xy}(\mathbf{k}) \sim \xi\delta(\mathbf{k} - \mathbf{K}_\xi). \quad (5.59)$$

Accordingly, the Berry phase computed as a line integral around these points is given by $\phi_\alpha \sim \xi\pi$. In a very similar way, the 3D valley-Hopf semimetals (5.22) and (5.24) have two linear nodal points with opposite quantum geometry. To be more precise, the Hopf density vanishes everywhere in the Brillouin zone, except for singularities at these nodal points:

$$\chi(\mathbf{k}) \sim \xi\delta(\mathbf{k} - \mathbf{k}_\nu), \quad (5.60)$$

where $\mathbf{k}_\nu \in \{\mathbf{K}_+, \mathbf{K}_-\}$ for the model (5.22) based on hexagonal layers and $\mathbf{k}_\nu \in \{\mathbf{k}_\Gamma, \mathbf{k}_M\}$ for the model (5.24) based on square layers. Additionally, the Berry dipoles have opposite orientation in the two valleys, $\mathbf{d} = (0, 0, \xi)$. The analogy between these two kinds of semimetals is visualized in Fig. 5.15.

Topological Dirac semimetal versus topological Hopf semimetal. Second, consider the topological phase transition lines $\Delta = \pm 3\sqrt{3}t' \sin \phi$ in Haldane’s model (1.33), as visualized in Fig. 1.5(a). We may call the semimetallic phase along these lines a *Haldane semimetal*. The Haldane semimetal is an example for a 2D *topological Dirac semimetal*, as it exists at the transition between two insulators with different Chern number. The Haldane semimetal has only a single nodal point in the Brillouin zone (Thonhauser and Vanderbilt 2006). The Berry curvature

$$\Omega_{\alpha,xy}(\mathbf{k}) = -\frac{\sqrt{3}}{\epsilon_\alpha^3(\mathbf{k})} [\pm 3\sqrt{3}w_\Delta(\mathbf{k}) - w_\phi(\mathbf{k})]t' \sin \phi, \quad (5.61)$$

as obtained from Eq. (1.35), is peaked at this nodal point, but also non-zero in other regions of the Brillouin zone. In a very similar way, the 3D topological Hopf semimetals (5.26) exist at the transition between two insulators with different Hopf number. They have an odd number of nodal points in the Brillouin zone. The corresponding Hopf density (for $N = 3, 4$) is given by

$$\chi(\mathbf{k}) = \frac{12}{\epsilon^4} (c_x c_y + c_y c_z + c_z c_x + \Delta_0 c_x c_y c_z), \quad (5.62)$$

as obtained from Eq. (5.36), where $\Delta_0 \in \{\pm 1, \pm 3\}$. It is peaked at the nodal points but also non-zero away from them. The analogy is again visualized in Fig. 5.15.

Valley-Chern insulator versus valley-Hopf insulator. Third, consider Semenoff’s model (1.31), which we may view as an example for a 2D *valley-Chern insulator*. It has a Berry curvature (1.32) which is non-zero in each valley [Fig. 1.4(b)], but distributed such that the Chern number vanishes. By analogy, we may write down a model for a 3D *valley-Hopf insulator* as

$$h_N^{\text{v-Hopf}}(\mathbf{k}) = \begin{pmatrix} 0 & Q_N^{\text{v-Hopf}} \\ (Q_N^{\text{v-Hopf}})^\dagger & 0 \end{pmatrix}, \quad (5.63)$$

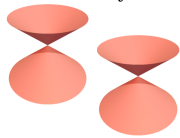
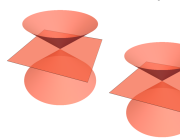
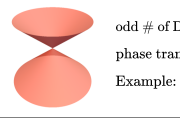

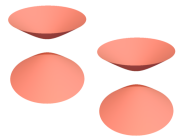
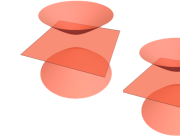
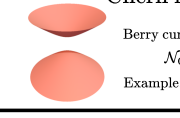
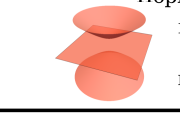
2D	3D
valley-Dirac semimetal  even # of Dirac points Berry curvature singular Example: graphene	valley-Hopf semimetal  even # of Berry dipoles Hopf density singular Example: $h_N(\mathbf{k})$
topological Dirac semimetal  odd # of Dirac points phase transition between Chern insulators Example: Haldane semimetal	topological Hopf semimetal  odd # of Berry dipoles phase transition between Hopf insulators Example: $h_N(\mathbf{k})$
valley-Chern insulator  Berry curvature finite but trivial $\mathcal{N}_{\text{Chern}} = 0$ Example: Semenoff insulator	valley-Hopf insulator  Hopf density finite but trivial $\mathcal{N}_{\text{Hopf}} = 0$ Example: $h_N^{\text{v-Hopf}}(\mathbf{k})$
Chern insulator  Berry curvature nontrivial $\mathcal{N}_{\text{Chern}} \neq 0$ Example: Haldane insulator	Hopf insulator  Hopf density nontrivial $\mathcal{N}_{\text{Hopf}} \neq 0$ Example: $h_N^{\text{Hopf}}(\mathbf{k})$

Fig. 5.15 – Analogy between 2D Dirac semimetals (Chern insulators) and 3D Hopf semimetals (Hopf insulators), based on the number of linear nodal points and the properties of the relevant topological densities (Berry curvature versus Hopf density).

where the matrices $Q_N^{\text{v-Hopf}}$ are obtained from Eq. (5.34) upon deleting the cosine terms, for example $Q_3^{\text{v-Hopf}} = (s_- \Delta - i s_z)$. We then find a Hopf density

$$\chi_{N=3,4}(\mathbf{k}) = \frac{12}{\epsilon^4} \Delta c_x c_y c_z, \quad \chi_{N=5}(\mathbf{k}) = \frac{60}{\epsilon^4} \Delta c_x c_y c_z, \quad (5.64)$$

where $\epsilon^2 = s_x^2 + s_y^2 + s_z^2 + \Delta^2$. It is non-zero throughout the Brillouin zone but topologically trivial in the sense that the Hopf number vanishes. This analogy is also visualized in Fig. 5.15.

Chern insulator versus Hopf insulator. Finally, a 2D Chern insulator such as Haldane’s insulator (1.33) has a non-trivial Berry curvature (1.35) that produces a non-zero Chern number. In the same way, the 3D Hopf insulators (5.34) have a non-trivial Hopf density, cf. Eqs. (5.36) and (5.38), which produces a non-zero Hopf number; this is also visualized in Fig. 5.15.

In summary, all 3D multiband Hopf semimetals and Hopf insulators introduced in this chapter have a 2D counterpart in Haldane’s model, in the sense that the relevant topological density (the Berry curvature in 2D and the Hopf density in 3D) has very similar properties. In order to make this *Hopf-Haldane analogy* more precise, one should systematically analyze all possible ways to gap out multifold Hopf semimetals, and establish the corresponding phase diagrams. Such an approach is quite similar in spirit to recent work on two-band systems, concerning the conversion between Weyl points, nodal lines, quadratic Berry dipole touchings and two-band Hopf insulators (Liu et al. 2017; Sun et al. 2018; Bouhon et al. 2020; Nelson et al. 2022).

5.6.3 | Dimensional reduction and tensor monopoles

Finally, here we describe that the Hopf semimetals and insulators presented above are related to 4D semimetals with so-called tensor monopoles by dimensional reduction.

Consider the 4D continuum model

$$H(\mathbf{q}) = \begin{pmatrix} 0 & q_x - iq_y & 0 \\ q_x + iq_y & 0 & q_z + iq_w \\ 0 & q_z - iq_w & 0 \end{pmatrix}, \quad (5.65)$$

as proposed by Palumbo and Goldman (2018). It has a chiral symmetry with $\mathcal{S} = \text{diag}(1, -1, 1)$ and an energy spectrum $\epsilon_\alpha(\mathbf{q}) = c_\alpha |\mathbf{q}|$, with band index $\alpha = 0, \pm 1$ and band velocity $c_\alpha = \alpha$. Its quantum geometric structure is that of a *Kalb-Ramond monopole* or *tensor monopole*. Namely, one can associate to each band a gauge-invariant anti-symmetric tensor field

$$\mathcal{H}_{\alpha,ijk}(\mathbf{q}) = -\alpha \epsilon_{ijkl} \frac{q_l}{|\mathbf{q}|^4}. \quad (5.66)$$

The corresponding topological number is the *Dixmier-Douady invariant*. It is defined from the monopole flux in a way completely analogous to the Chern number of a Weyl point. Namely, for a Weyl point (1.36) with helicity $\gamma = +$ the integral of the Berry flux through an enclosing sphere \mathbb{S}^2 , which we already considered in Eq. (1.24), can alternatively be written as

$$\mathcal{C}_\alpha = \frac{1}{2\pi} \int_{\mathbb{S}^2} dq_i \wedge dq_j \Omega_{\alpha,ij}(\mathbf{q}) = \frac{1}{4\pi} \int_0^\pi d\theta \int_0^{2\pi} d\phi \sin \theta = -\alpha. \quad (5.67)$$

Here we used $\Omega_{ij} = -\alpha \epsilon_{ijk} q_k / (2q^3)$, where $q = |\mathbf{q}|$, and spherical coordinates (q, θ, ϕ) with surface element $dS = q^2 \sin \theta d\theta d\phi$. Analogously, for the 4D model (5.65), the monopole flux of the Kalb-Ramond curvature \mathcal{H}_{ijk} through a sphere \mathbb{S}^3 enclosing the nodal point is given by (Palumbo and Goldman 2018)

$$\begin{aligned} \mathcal{N}_\alpha^{\text{DD}} &= \frac{1}{2\pi^2} \int_{\mathbb{S}^3} dq_i \wedge dq_j \wedge dq_k \mathcal{H}_{\alpha,ijk}(\mathbf{q}) \\ &= \frac{1}{2\pi^2} \int_0^\pi d\theta_1 \int_0^\pi d\theta_2 \int_0^{2\pi} d\phi \sin^2 \theta_1 \sin \theta_2 = -\alpha, \end{aligned} \quad (5.68)$$

where we used Eq. (5.66) and hyperspherical coordinates $(q, \theta_1, \theta_2, \phi)$ with surface element $dS = q^3 \sin^2 \theta_1 \sin \theta_2 d\theta_1 d\theta_2 d\phi$.

To make a link with our 3D Hopf systems, it suffices to take a 3D slice $q_z = 0$ out of the 4D model (5.65), which exactly recovers the threefold Hopf semimetal (5.4a). Similarly, if we take a 3D slice at finite $q_z = \Delta$, we obtain a continuum model which exactly describes the Hopf insulator (5.34) (with $N = 3$) in the vicinity of a topological phase transition; compare in particular Eq. (V.49).

We can push the dimensional reduction correspondence even further, by considering a lattice model for a 4D semimetal with tensor monopoles, as introduced by Zhu

et al. (2020). This model is given by

$$H(\mathbf{k}) = \begin{pmatrix} 0 & Q(\mathbf{k}) \\ Q^\dagger(\mathbf{k}) & \end{pmatrix}, \quad Q(\mathbf{k}) = \begin{pmatrix} ag_{\mathbf{k}} + h_{\mathbf{k}} & g_{\mathbf{k}} + ah_{\mathbf{k}} \\ g_{\mathbf{k}}^* - ah_{\mathbf{k}}^* & ag_{\mathbf{k}}^* - h_{\mathbf{k}}^* \end{pmatrix}, \quad (5.69)$$

where $g_{\mathbf{k}} = s_x - is_z$ and $h_{\mathbf{k}} = \Delta - c_x - c_z - c_w - e^{iy}$, and with $a \geq 0$ a real parameter. It has a chiral symmetry¹¹ and an energy spectrum

$$\epsilon_\alpha(\mathbf{k}) = c_\alpha \sqrt{s_x^2 + s_y^2 + s_z^2 + (\Delta - c_x - c_y - c_z - c_w)^2}, \quad (5.70)$$

where the band velocity $c_\alpha = \pm(1 \pm a)$. For $2 < \Delta < 4$ there is a pair of fourfold crossings in the Brillouin zone; taking $\Delta = 3$ without loss of generality, the crossings are located at $\mathbf{k}_\xi = (0, 0, 0, \xi\pi/2)$, where $\xi = \pm$. The corresponding 4D continuum Hamiltonian $H^\xi(\mathbf{q})$ is given by Eq. (5.69) with $g_{\mathbf{k}} \rightarrow q_x - iq_z$ and $h_{\mathbf{k}} \rightarrow \xi q_w - iq_y$. It has a linear spectrum of four crossing bands, $\epsilon_\alpha(\mathbf{q}) = c_\alpha |\mathbf{q}|$. For $a = 0$, it reduces to a 4D Dirac Hamiltonian $H_D = \mathbf{q} \cdot \mathbf{\Gamma}$ with four matrices Γ_i that satisfy a Clifford algebra. Accordingly, the spectrum is twofold degenerate. For $a > 0$, however, the two cones have different band velocities, and the crossings carry tensor monopoles with topological charges $\mathcal{N}_\alpha^{\text{DD}} = \xi, \xi, -\xi, -\xi$ from lowest to highest band. At half filling, the nodal points thus carry Dixmier-Douady numbers $\mathcal{N}_{\text{DD}} = 2\xi$. We note that certain physical phenomena such as Fermi arcs on the 3D surface can be associated to these topological charges.

It is again easy to make a link with our Hopf models. Taking a 3D slice at $k_w = \pi/2$, the model (5.69) becomes similar to the Hopf insulator (5.34) with $N = 4$. For example, the corresponding continuum model for $\Delta = 3$ is given by

$$Q(\mathbf{q}) = \begin{pmatrix} a(q_x - iq_z) - iq_y & q_x - iq_z - iaq_y \\ q_x + iq_z - iaq_y & a(q_x + iq_z) - iq_y \end{pmatrix}, \quad (5.71)$$

and it exhibits a Berry dipole (5.1) with $\mathbf{d} = (0, 0, 1)$ and $\kappa_\alpha = 4, -4, -4, 4$ from the lowest to the highest band. Clearly, the dipole charges are as expected for a system with chiral symmetry, but have numerical values different from the model (5.4b). It would thus be interesting to verify that Eq. (5.69) really represents a four-band Hopf insulator, and to compute the corresponding Hopf number as a function of Δ .

5.7 | Conclusions

In this chapter we have demonstrated that linear band crossings in 3D exhibit rich physical properties if more than two bands cross simultaneously. In particular, beyond the well-known Berry monopoles of Weyl semimetals (Armitage et al. 2018) and chiral multifold semimetals (Lv et al. 2021), other types of band crossings with more exotic quantum geometric structure are possible. We have focused on the case where each

¹¹In the work of Zhu et al. (2020) the basis is chosen such that $\mathcal{S} = \text{diag}(1, -1, -1, 1)$. We have transformed the model to the chiral basis where $\mathcal{S} = \text{diag}(1, 1, -1, -1)$.

crossing point acts as a Berry dipole, but also more general Berry multipoles are in principle possible.

To study linear N -fold crossings with Berry dipole in detail, we have introduced several lattice models whose low-energy theory is of the form (5.4), which we call multifold Hopf semimetals. The lattice models can be distinguished according to whether they exhibit an even (valley-Hopf semimetal) or odd (topological Hopf semimetal) number of Berry dipoles in the Brillouin zone. For the topological Hopf semimetals there are clear signatures of the Berry dipole in the anomalous Hall effect and magnetoconductivities. It is expected that this extends to a host of other physical quantities. For the valley-Hopf semimetals the anomalous Hall and magnetoconductivities cancel, but the effect of the Berry dipole is still clearly visible in the Landau level spectrum. It would be interesting to study responses for which the contributions from the different valleys do not cancel, and a first step in this direction was made very recently by Habe (2022). This is promising in particular because the lattice models for valley-Hopf semimetals are very simple and quite close to the graphene tight-binding model.

We further introduced two different classes of lattice models for multiband Hopf insulators (Lapierre et al. 2021). The first class is a simple multiband generalization of the Moore-Ran-Wen model (Moore et al. 2008), see Eq. (5.40). More importantly, we introduced a second class of multiband Hopf insulators (5.34), which becomes exactly equivalent to the Hopf semimetals (5.26) at topological phase transitions. One considerable advantage of these models is that they require only nearest-neighbor hoppings, thus avoiding the complicated second-neighbor hoppings of two-band Hopf insulators (Moore et al. 2008; Nelson et al. 2022). These models might provide a fertile platform to test theoretical predictions for the bulk-boundary correspondence of delicate topological insulators (Alexandradinata et al. 2021; Lapierre et al. 2021).

Many fundamental questions remain as to the conversion processes between the different systems discussed here. To be more precise, a systematic investigation of the phase diagrams that can be obtained by gapping out or merging one or several Berry dipoles and/or monopoles is called for. Additionally, there appear to be interesting connections to systems of different spatial dimensions. We have pointed out analogies to the 2D Haldane model as well as to 4D semimetals with tensor monopoles. It appears very intriguing to develop the corresponding dimensional hierarchies in more detail, as has been done years ago for stable topological insulators and superconductors (Ryu et al. 2010).

From an experimental point of view, the existence of the valley-Hopf semimetals, in particular the graphene-like models (5.22), appears possible. To make progress in this regard, one should determine the space groups of the models and check in which materials they might occur. If realized in a crystal, the Berry dipole crossings could potentially be probed via the peculiar, strongly valley-dependent dependence of the Landau levels on the magnetic field orientation (Fig. 5.3). Anomalous Hall currents and linear magnetocurrents induced by the Berry dipoles have symmetries opposite to those of a pair of Weyl nodes (Fig. 5.5), which could be probed by varying the electron density close to half filling. A different route involves artificial systems such as ultracold atoms, photonic crystals, or superconducting circuits. Those have been

suggested and used many times to realize semimetallic phases with two- and multifold crossings (Lu et al. 2015; Chen et al. 2016; Riwar et al. 2016; Wang et al. 2017; Zhu et al. 2017; Zhang et al. 2018; Tan et al. 2018; Fulga et al. 2018; Hu et al. 2018). Moreover, the tensor monopole crossing (5.65), which is very similar to Eq. (5.4a) as we have discussed, was recently observed experimentally using a transmon in a cavity (Tan et al. 2021).

Finally, we mention that there is considerable activity regarding the observation of Hopf numbers in two-band insulators (Deng et al. 2017; Ünal et al. 2019; Schuster et al. 2021a; Schuster et al. 2021b). Such proposals could potentially be extended to the multiband Hopf insulators (5.34) and (5.40). Most notably, for the three-band Hopf insulator $h_3^{\text{Hopf}}(\mathbf{k})$ (viewed as a chiral topological insulator) there already exists not only a proposal based on ultracold atoms (Wang et al. 2014), but also a claimed experimental realization based on machine learning analysis of a nitrogen-vacancy center in diamond (Lian et al. 2019). In such experiments, the topological Hopf semimetal (5.26) is reached at critical parameter values corresponding to topological phase transitions.

Conclusions

The present work is concerned with three closely related aspects of multiband problems in solid-state physics and, more generally, of arbitrary parametric quantum systems: (i) The quantum geometry of wave functions. (ii) The properties of flat bands, that is, bands with vanishing group velocity. (iii) The properties of linear band crossings, that is, bands with constant group velocity meeting at a single point in momentum space.

In general, the study of such situations is inspired by numerous recent breakthroughs in materials physics, as we described in Chapter 2. In particular, quasi-two-dimensional crystals such as twisted bilayer graphene or transition metal dichalcogenides exhibit nearly flat bands with non-trivial quantum geometry. Similarly, three-dimensional topological semimetals (e.g., Mn_3Sn , CoSi , or RhSi) are characterized by linear (two- or multifold) crossings that may also include flat bands, and where quantum geometry and topology play a fundamental role.

While the existence of such materials provides an important context, it is not the primary motivation for the work presented here. In fact, the main motivation underlying all chapters of this thesis is to develop a better analytical understanding of multiband systems. While two-band systems are easy to master, one quickly reaches the limits of what is analytically feasible when the number of bands is increased, as described in Chapter 2. The interest in developing an improved analytical understanding, beyond just calculating things for a given system, is to be able to construct insightful models with some desired physical properties in a controlled way, and eventually make new physical predictions. The results presented in Chapters 3–5 have in common that they are all consistent with this basic idea, as we would like to illustrate in the following. For a more detailed summary of the technical results of each chapter, we refer the reader to the individual conclusions in Sections 3.6, 4.8, and 5.7.

The development of the formalism in Chapter 3, which uses $\text{SU}(N)$ -Gell-Mann matrices and the associated vector algebra, is based on the simple desire to generalize the well-known formula (2.41) for the Berry curvature [which makes the unwieldy eigenstates (2.37) superfluous] to systems with arbitrarily many bands. This generalization, given in Eq. (3.10) or more explicitly in Eqs. (3.34)–(3.36), can now, on the one hand, be used for explicit calculations. This has proved very convenient countless times in the preparation of this work. On the other hand, the improved analytical understanding afforded by these expressions can also be used for new qualitative predictions. For example, the structure of Eqs. (3.34)–(3.36) already suggests what we found later in Chapter 5, namely that a multipole form (5.58) of the Berry curvature should be possible.

Certainly, it would be desirable to establish Bloch vector-based expressions for quantities beyond the quantum geometric tensor and the orbital magnetization. They can be used both for practical purposes, since they obviate the need to choose a gauge and explicitly parametrize the energy eigenstates, and at the same time be useful for gaining insight into the generic structure (in particular regarding intra- and interband

contributions) of the quantity of interest.

The flat-band design scheme presented in Chapter 4 arose from a persistent dissatisfaction with existing strategies for generating flat bands. Such strategies typically involve either fine-tuning of the hopping processes on a given lattice or developing numerical algorithms to obtain a flat-band Hamiltonian. In both cases, it is difficult to predict which topology of the lattice will work or what modifications of a given flat-band model are allowed without destroying the flat band; more generally, it is difficult to gain any unified understanding beyond the specific model in question.

Our motivation was therefore to develop a general, simple analytical approach to flat-band systems. Chapter 4 shows that such a method does indeed exist and can be based on the important concept of a compact localized state. Our method clearly shows that the specific lattice does not play a crucial role. In fact, any lattice geometry with an arbitrary number of orbitals per unit cell and in any spatial dimension can accommodate an arbitrarily large number of different flat-band models. We are convinced that the presented method is not only the simplest, but also the most natural and general framework for describing flat bands. Incidentally, it captures almost all flat-band models known in the literature.

We further emphasize that simple modifications of the method are suitable for the study of more general systems beyond the approximation of spinless, non-interacting electrons. In particular, this concerns magnetic flat-band systems in the presence of spin-orbit coupling. Compact localized states also appear to be an ideal starting point for the study of electronic correlations in flat bands and, more generally, for the study of any physical process for which visualization in real space is useful.

The results obtained in Chapter 5 again emerged from a simple question: Is it possible to change the quantum geometry of a linear band crossing in 3D without changing the energy spectrum? The answer is positive, and in this way we have found a new class of semimetals, which we call multifold Hopf semimetals. They have a “Weyl-like” energy dispersion just like the known (multifold) topological semimetals, but are topologically trivial in the Berry-Chern sense, that is, they do not carry a Berry monopole. Instead, they are characterized by a Berry dipole or, more generally, a Berry multipole. We emphasize that any differences between the physical properties of these hypothetical semimetals – we have described, in particular, the Landau levels, the anomalous Hall effect, and magnetotransport – and those of known topological semimetals are due exclusively to the anisotropy of the quantum geometric structure. It would be interesting to see if the existence of such multifold Berry dipole crossings, predicted from minimal models, can actually be confirmed in the band structure of a crystalline material.

In the course of studying Hopf semimetals, we have confirmed the recent claim of Lapierre et al. (2021), namely that the family of topological Hopf insulators is not restricted to two-band systems, via the introduction of concrete lattice models. As mentioned earlier, there are several proposals for the experimental realization of two-band Hopf insulators (Deng et al. 2017; Ünal et al. 2019; Schuster et al. 2021a; Schuster et al. 2021b), which can certainly be adapted to our proposed models. Indeed, the linear multiband Hopf insulators in Eq. (5.34), which involve only nearest-neighbor couplings, seem easier to realize than the paradigmatic Moore-Ran-Wen model (5.29),

which has unrealistically large second-neighbor hoppings. As also mentioned earlier, the linear three-band Hopf insulator is nothing but the chiral topological insulator introduced by Neupert et al. (2012), which is close to experimental realization (Wang et al. 2014; Lian et al. 2019).

To conclude this thesis, we would like to return to some of the perspectives already described in the individual chapters. First, it appears interesting to apply the Bloch vector formalism developed in Chapter 3 to non-Hermitian systems. In such systems, which can be described by so-called biorthogonal quantum mechanics (Brody 2013), each eigenprojector is a mixture of left and right eigenstates. Such a projector appears as the natural object for the correct definition of quantum geometry. It can again be related to the Hamiltonian by the Cayley-Hamilton theorem, and it can furthermore be used to define a complex Bloch vector via Eq. (2.50). The study of such Bloch vectors should provide valuable insights into the properties of non-Hermitian parametric Hamiltonians.

Further, it seems promising to investigate more systematically the quantum geometric properties of flat-band systems with multiband crossings, which we considered only superficially in Chapter 4. In fact, we found two fundamentally different types of band crossings in the superficial consideration (three-band crossings with Berry monopole and dipole, respectively), and it is expected that other interesting situations will arise if the number of bands is increased or the spatial dimension is changed.

Finally, it is a necessary task to study the transformation processes and stability of the topological semimetals and insulators we presented in Chapter 5. This should lead to rich phase diagrams containing fundamentally different multiband systems (trivial insulators, Hopf insulators, topological semimetals, Hopf semimetals, nodal line semimetals, et cetera). Moreover, from a fundamental point of view, it seems very interesting to properly establish and generalize the dimensional hierarchies that we have observed when connecting Berry dipoles in 3D with tensor monopoles in 4D.

Appendix I

I.A | Recap on tight-binding theory and Bloch basis

Within a tight-binding approximation (Simon 2013), one constructs the wave function of electrons moving through the crystal (single-particle excitations) from valence orbitals located at the atomic lattice sites. At the same time, this approach has to respect Bloch's theorem, which can be done in the following way.

Assume one has atomic orbitals $|a, i\rangle$, where $a = A, B, C, \dots$ denotes the N inequivalent orbitals per unit cell and i is the index of the unit cell. The wave function of an atomic orbital is $\langle \mathbf{r} | a, i \rangle \equiv \phi_a(\mathbf{r} - \mathbf{R}_i - \mathbf{r}_a)$, assumed to be centered at and "tightly bound" to an atom at position $\mathbf{R}_i + \mathbf{r}_a$, where \mathbf{R}_i is the origin of the unit cell and \mathbf{r}_a the position of the atom relative to this origin. Then the total wave function entering the time-independent Schrödinger equation (1.1) can be chosen as

$$\begin{aligned} |\Psi_\alpha(\mathbf{k})\rangle &= \sum_a c_{\alpha,a}(\mathbf{k}) |a, \mathbf{k}\rangle, \\ |a, \mathbf{k}\rangle &= \frac{1}{\sqrt{\mathcal{N}}} \sum_i e^{-i\mathbf{k}\cdot(\mathbf{R}_i + \mathbf{r}_a)} |a, i\rangle, \end{aligned} \quad (\text{I.1})$$

where i is summed over all lattice sites and \mathcal{N} is the total number of unit cells. It is easy to see that this works: the wave function

$$\Psi_{\alpha,\mathbf{k}}(\mathbf{r}) = \langle \mathbf{r} | \Psi_\alpha(\mathbf{k}) \rangle = \frac{1}{\sqrt{\mathcal{N}}} \sum_a c_{\alpha,a}(\mathbf{k}) \sum_i e^{-i\mathbf{k}\cdot(\mathbf{R}_i + \mathbf{r}_a)} \phi_a(\mathbf{r} - \mathbf{R}_i - \mathbf{r}_a) \quad (\text{I.2})$$

is clearly an eigenfunction of the translation operator $\mathcal{T}_{\mathbf{R}_j}$, with eigenvalue $\exp(-i\mathbf{k}\cdot\mathbf{R}_j)$. Since $\mathcal{T}_{\mathbf{R}_j}$ and H commute, $\Psi_{\alpha,\mathbf{k}}(\mathbf{r})$ is also an eigenfunction of H , as required.

To work with Eq. (I.1) in practice, it is convenient to switch to the *Bloch basis*, with basis states $|a, \mathbf{k}\rangle$. Namely, combining Eqs. (1.1) and (I.1) we have

$$\sum_b c_{\alpha,b}(\mathbf{k}) \langle a, \mathbf{k} | H | b, \mathbf{k} \rangle = \epsilon_\alpha(\mathbf{k}) \sum_b c_{\alpha,b}(\mathbf{k}) \langle a, \mathbf{k} | b, \mathbf{k} \rangle. \quad (\text{I.3})$$

Assuming orthonormality of the Bloch basis states, $\langle a, \mathbf{k} | b, \mathbf{k} \rangle = \delta_{ab}$, that is, neglecting overlap corrections by assuming $\langle a, i | b, j \rangle = \delta_{ab} \delta_{ij}$,¹ this can be rewritten in matrix form as

$$\begin{pmatrix} H_{AA}(\mathbf{k}) & H_{AB}(\mathbf{k}) & \dots \\ H_{BA}(\mathbf{k}) & H_{BB}(\mathbf{k}) & \dots \\ \dots & \dots & \dots \end{pmatrix} \begin{pmatrix} c_{\alpha,A}(\mathbf{k}) \\ c_{\alpha,B}(\mathbf{k}) \\ \dots \end{pmatrix} = \epsilon_\alpha(\mathbf{k}) \begin{pmatrix} c_{\alpha,A}(\mathbf{k}) \\ c_{\alpha,B}(\mathbf{k}) \\ \dots \end{pmatrix}. \quad (\text{I.4})$$

¹This is not always well-justified, but it is common practice in order to simplify the tight-binding approach. We will adopt this approximation throughout the thesis.

Comparing with Eq. (1.3), we see that, for a tight-binding model in the Bloch basis, the state $|\psi_\alpha(\mathbf{k})\rangle$ takes the form of a complex column vector, $|\psi_\alpha(\mathbf{k})\rangle = (c_{\alpha,A}(\mathbf{k}), c_{\alpha,B}(\mathbf{k}), \dots)^T$, and the Hamiltonian H takes the form of an $N \times N$ matrix, with matrix elements $H_{ab}(\mathbf{k}) \equiv \langle a, \mathbf{k} | H | b, \mathbf{k} \rangle$.

I.B | Quantum geometry in early band theory formalisms

The ideas exposed here have emerged from a set of papers on the problem of electrons moving in a perturbed periodic potential (Wannier 1937; Slater 1949; Adams 1952; Adams 1953b), that is, an extended version of the basic Bloch problem (1.1):

$$H = \frac{p^2}{2m} + V(\mathbf{r}) + U(\mathbf{r}, \mathbf{p}). \quad (\text{I.5})$$

Due to the perturbing potential U , the full Hamiltonian H is no longer diagonal in the eigenbasis of the unperturbed Hamiltonian. Interband effects are then expected to arise much in the same way as discussed below Eq. (1.14). Indeed, the situation (I.5) has been investigated in several different physical contexts ranging from impurities in semiconductors (Luttinger and Kohn 1955) to electronic transport and Hall currents (Karpus and Luttinger 1954; Adams and Blount 1959), magnetic susceptibility (Adams 1953a; Blount 1962a; Roth 1962), and more, all of which exhibit interband effects.

Let us see more quantitatively how interband effects arise. Any wave function of the unperturbed system can be written as a general superposition

$$|\Phi\rangle = \sum_{\alpha} \int d^3k \Phi_{\alpha}(\mathbf{k}) |\Psi_{\alpha}(\mathbf{k})\rangle \quad (\text{I.6})$$

of Bloch states (1.2). Blount calls $\Phi_{\alpha}(\mathbf{k})$ the wave function in the *crystal momentum representation*. When treating U as a perturbation to the Bloch states, it is natural to be interested in the matrix elements of basic quantum mechanical operators in this representation. The matrix elements of the crystal momentum operator \mathbf{k}_c and true momentum operator \mathbf{p} are readily obtained,

$$\begin{aligned} \langle \Psi_{\alpha}(\mathbf{k}) | \mathbf{k}_c | \Psi_{\beta}(\mathbf{k}') \rangle &= \mathbf{k} \delta_{\alpha\beta} \delta_{\mathbf{k}\mathbf{k}'}, \\ \langle \Psi_{\alpha}(\mathbf{k}) | \mathbf{p} | \Psi_{\beta}(\mathbf{k}') \rangle &= (\mathbf{k} \delta_{\alpha\beta} + \mathbf{Y}_{\alpha\beta}(\mathbf{k})) \delta_{\mathbf{k}\mathbf{k}'}, \end{aligned} \quad (\text{I.7})$$

where $\mathbf{Y}_{\alpha\beta}(\mathbf{k}) \equiv -i \int_{\text{UC}} d^3r \psi_{\alpha,\mathbf{k}}^*(\mathbf{r}) \nabla_{\mathbf{r}} \psi_{\beta,\mathbf{k}}(\mathbf{r})$ and UC designates integration over a single real-space unit cell. It follows that the operators act on $|\Phi\rangle$ as

$$\begin{aligned} \langle \Psi_{\alpha}(\mathbf{k}) | \mathbf{k}_c | \Phi \rangle &= \mathbf{k} \Phi_{\alpha}(\mathbf{k}), \\ \langle \Psi_{\alpha}(\mathbf{k}) | \mathbf{p} | \Phi \rangle &= \mathbf{k} \Phi_{\alpha}(\mathbf{k}) + \sum_{\beta} \mathbf{Y}_{\alpha\beta}(\mathbf{k}) \Phi_{\beta}(\mathbf{k}). \end{aligned} \quad (\text{I.8})$$

The matrix elements of the position operator \mathbf{r} pose a bigger problem, since the integral $\langle \Psi_{\alpha}(\mathbf{k}) | \mathbf{r} | \Psi_{\beta}(\mathbf{k}') \rangle = \int d^3r \Psi_{\alpha,\mathbf{k}}^*(\mathbf{r}) \mathbf{r} \Psi_{\beta,\mathbf{k}'}(\mathbf{r})$ is not well defined. However, through a careful derivation, one can show that the action of \mathbf{r} on $|\Phi\rangle$ is given by

$$\langle \Psi_{\alpha}(\mathbf{k}) | \mathbf{r} | \Phi \rangle = i \nabla_{\mathbf{k}} \Phi_{\alpha}(\mathbf{k}) + \sum_{\beta} \mathbf{X}_{\alpha\beta}(\mathbf{k}) \Phi_{\beta}(\mathbf{k}), \quad (\text{I.9})$$

where

$$\mathbf{X}_{\alpha\beta}(\mathbf{k}) \equiv i \int_{\text{UC}} d^3r \psi_{\alpha,\mathbf{k}}^*(\mathbf{r}) \nabla_{\mathbf{k}} \psi_{\beta,\mathbf{k}}(\mathbf{r}) = i \langle \psi_{\alpha}(\mathbf{k}) | \nabla_{\mathbf{k}} \psi_{\beta}(\mathbf{k}) \rangle_{\text{UC}}. \quad (\text{I.10})$$

Crucially, the momentum operator (I.8) and position operator (I.9) are not diagonal in the band index, and thus interband effects are, a priori, always expected in the presence of a perturbing potential U .

The object $\mathbf{X}_{\alpha\beta}$ determining the crystal momentum representation of the position operator is of particular importance. It is nothing else than what is now known as the non-Abelian Berry connection (Wilczek and Zee 1984), and its diagonal (intra-band) part $\mathbf{X}_{\alpha\alpha}$ is just the (Abelian) Berry connection (1.7). Blount understood all key aspects of this connection, such as its gauge arbitrariness, its role dual to the electromagnetic vector potential, and the fact that *“its curl is a well-defined quantity invariant under the phase transformations and is thus a characteristic of the band structure”* (Blount 1962b); this characteristic is just the Berry curvature (1.8).

I.C | Magnetotransport in multiband systems to linear order in \mathbf{B}

The equations of motion (1.56) can be fully decoupled as

$$\begin{aligned} (1 + e\boldsymbol{\Omega}_{\alpha} \cdot \mathbf{B})\dot{\mathbf{r}} &= \mathbf{w}_{\alpha} - e\boldsymbol{\Omega}_{\alpha} \times \mathbf{E} + e(\mathbf{w}_{\alpha} \cdot \boldsymbol{\Omega}_{\alpha})\mathbf{B}, \\ (1 + e\boldsymbol{\Omega}_{\alpha} \cdot \mathbf{B})\dot{\mathbf{k}} &= -e\mathbf{E} - e\mathbf{w}_{\alpha} \times \mathbf{B} - e^2(\mathbf{E} \cdot \mathbf{B})\boldsymbol{\Omega}_{\alpha}. \end{aligned}$$

Now, for a homogeneous system in the steady state, and to first order in the electric field (linear response regime), the Boltzmann equation (1.55) becomes

$$e[\mathbf{E} + \mathbf{w}_{\alpha} \times \mathbf{B} + e(\mathbf{E} \cdot \mathbf{B})\boldsymbol{\Omega}_{\alpha}] \cdot \nabla_{\mathbf{k}} f_{\alpha}(\mathbf{k}) = (1 + e\boldsymbol{\Omega}_{\alpha} \cdot \mathbf{B}) \frac{f_{\alpha}(\mathbf{k}) - f_{\alpha}^{\text{eq}}(\mathbf{k})}{\tau}. \quad (\text{I.11})$$

This equation has to be solved for the distribution function $f_{\alpha}(\mathbf{k})$. To proceed, it is convenient to rewrite the Boltzmann equation (I.11) as

$$[1 + e\boldsymbol{\Omega}_{\alpha} \cdot \mathbf{B} + e\tau\mathbf{B} \cdot (\mathbf{v}_{\alpha} \times \nabla_{\mathbf{k}})] f_{\alpha}^{\text{neq}}(\mathbf{k}) = [e\tau\mathbf{E} + e^2\tau(\mathbf{E} \cdot \mathbf{B})\boldsymbol{\Omega}_{\alpha}] \cdot \nabla_{\mathbf{k}} f_{\alpha}^{\text{eq}}(\mathbf{k}),$$

where $f_{\alpha}^{\text{neq}}(\mathbf{k}) = f_{\alpha}(\mathbf{k}) - f_{\alpha}^{\text{eq}}(\mathbf{k})$ is the nonequilibrium part of the distribution function, and $f_{\alpha}^{\text{eq}}(\mathbf{k}) \equiv f(\tilde{\epsilon}_{\alpha})$ is the equilibrium part with $f(x) \equiv 1/(1 + \exp[\beta(x - \mu)])$ the Fermi-Dirac distribution function with inverse temperature $\beta = 1/(k_B T)$ and chemical potential μ . To first order in B , the nonequilibrium part can be obtained as

$$\begin{aligned} f_{\alpha}^{\text{neq}}(\mathbf{k}) &= e\tau[1 - e\boldsymbol{\Omega}_{\alpha} \cdot \mathbf{B} - e\tau\mathbf{B} \cdot (\mathbf{v}_{\alpha} \times \nabla_{\mathbf{k}})][\mathbf{E} + e(\mathbf{E} \cdot \mathbf{B})\boldsymbol{\Omega}_{\alpha}] \cdot \mathbf{w}_{\alpha} f'(\tilde{\epsilon}_{\alpha}) \\ &= e\tau(\mathbf{E} \cdot \mathbf{v}_{\alpha})f'(\epsilon_{\alpha}) + e^2\tau[(\mathbf{E} \cdot \mathbf{B})(\boldsymbol{\Omega}_{\alpha} \cdot \mathbf{v}_{\alpha}) - (\boldsymbol{\Omega}_{\alpha} \cdot \mathbf{B})(\mathbf{E} \cdot \mathbf{v}_{\alpha})]f'(\epsilon_{\alpha}) \\ &\quad - e\tau \{ \mathbf{E} \cdot [\nabla_{\mathbf{k}}(\mathbf{m}_{\alpha} \cdot \mathbf{B})]f'(\epsilon_{\alpha}) + (\mathbf{E} \cdot \mathbf{v}_{\alpha})(\mathbf{m}_{\alpha} \cdot \mathbf{B})f''(\epsilon_{\alpha}) \} \\ &\quad - e^2\tau^2[\mathbf{B} \cdot (\mathbf{v}_{\alpha} \times \nabla_{\mathbf{k}})](\mathbf{E} \cdot \mathbf{v}_{\alpha})f'(\epsilon_{\alpha}). \end{aligned}$$

The full electrical current is then obtained by integrating over the full phase space using the full distribution function (Xiao et al. 2010),

$$\begin{aligned}\mathbf{j} &= -e \sum_{\alpha} \int \frac{d^3k}{(2\pi)^3} (1 + e\boldsymbol{\Omega}_{\alpha} \cdot \mathbf{B}) \mathbf{r} [f(\tilde{\epsilon}_{\alpha}) + f_{\alpha}^{\text{neq}}(\mathbf{k})] \\ &= -e \sum_{\alpha} \int \frac{d^3k}{(2\pi)^3} [\mathbf{w}_{\alpha} - e\boldsymbol{\Omega}_{\alpha} \times \mathbf{E} + e(\mathbf{v}_{\alpha} \cdot \boldsymbol{\Omega}_{\alpha})\mathbf{B}] [f(\tilde{\epsilon}_{\alpha}) + f_{\alpha}^{\text{neq}}(\mathbf{k})],\end{aligned}\tag{I.12}$$

and consists of three parts, $\mathbf{j} = \mathbf{j}_0 + \mathbf{j}_{\text{AH}} + \mathbf{j}_{\text{out}}$. The first term \mathbf{j}_0 is an equilibrium current (typically vanishing) independent of \mathbf{E} , which we will not consider here. The second term \mathbf{j}_{AH} describes the (non-dissipative) anomalous Hall current, which requires the presence of an electric field but is determined by the equilibrium distribution function; the third term \mathbf{j}_{out} is the true out-of-equilibrium current with both dissipative and non-dissipative contributions, determined by the nonequilibrium part of the distribution function:

$$\begin{aligned}\mathbf{j}_{\text{AH}} &= e^2 \sum_{\alpha} \int \frac{d^3k}{(2\pi)^3} (\boldsymbol{\Omega}_{\alpha} \times \mathbf{E}) f(\tilde{\epsilon}_{\alpha}), \\ \mathbf{j}_{\text{out}} &= -e \sum_{\alpha} \int \frac{d^3k}{(2\pi)^3} [\mathbf{w}_{\alpha} + e(\mathbf{v}_{\alpha} \cdot \boldsymbol{\Omega}_{\alpha})\mathbf{B}] f_{\alpha}^{\text{neq}}(\mathbf{k}).\end{aligned}\tag{I.13}$$

Expanding to linear order in B and introducing an anomalous Hall conductivity tensor as $j_i^{\text{AH}} = \sum_j \sigma_{ij}^{\text{AH}}(\mathbf{B}) E_j$, where $\sigma_{ij}^{\text{AH}}(\mathbf{B}) = \sigma_{ij}^{\text{AH0}} + \sigma_{ij}^{\text{AH1}}(\mathbf{B})$, we have

$$\begin{aligned}\sigma_{ij}^{\text{AH0}} &= -e^2 \sum_{\alpha} \int \frac{d^3k}{(2\pi)^3} f(\epsilon_{\alpha}) \epsilon_{ijk} (\Omega_{\alpha})_k, \\ \sigma_{ij}^{\text{AH1}}(\mathbf{B}) &= e^2 \sum_{\alpha} \int \frac{d^3k}{(2\pi)^3} f'(\epsilon_{\alpha}) (\mathbf{m}_{\alpha} \cdot \mathbf{B}) \epsilon_{ijk} (\Omega_{\alpha})_k,\end{aligned}\tag{I.14}$$

where σ_{ij}^{AH0} is the true anomalous Hall effect and $\sigma_{ij}^{\text{AH1}}(\mathbf{B})$ is a magnetic field dependent quantum geometric correction caused by the orbital magnetic moment. Similarly, the out-of-equilibrium conductivity tensor can be defined as $j_i^{\text{out}} = \sum_j \sigma_{ij}^{\text{out}}(\mathbf{B}) E_j$, with

$$\sigma_{ij}(\mathbf{B}) = \sigma_{ij}^{\text{Drude}} + \sigma_{ij}^{\text{Lorentz}}(\mathbf{B}) + \sigma_{ij}^{\text{Berry}}(\mathbf{B}) + \sigma_{ij}^{\text{OMM}}(\mathbf{B}),\tag{I.15}$$

where $\sigma_{ij}^{\text{Drude}}$ is the Drude conductivity, $\sigma_{ij}^{\text{Lorentz}}(\mathbf{B})$ the classical Hall conductivity induced by the Lorentz force, and $\sigma_{ij}^{\text{Berry}}(\mathbf{B})$ and $\sigma_{ij}^{\text{OMM}}(\mathbf{B})$ are interband contributions induced by Berry curvature and orbital magnetic moment. The classical conductivity tensors read explicitly as

$$\begin{aligned}\sigma_{ij}^{\text{Drude}} &= -e^2 \tau \sum_{\alpha} \int \frac{d^3k}{(2\pi)^3} f'(\epsilon_{\alpha}) (v_{\alpha})_i (v_{\alpha})_j, \\ \sigma_{ij}^{\text{Lorentz}}(\mathbf{B}) &= e^3 \tau^2 \sum_{\alpha} \int \frac{d^3k}{(2\pi)^3} f'(\epsilon_{\alpha}) (v_{\alpha})_i [\mathbf{B} \cdot (\mathbf{v}_{\alpha} \times \boldsymbol{\nabla}_{\mathbf{k}})] (v_{\alpha})_j,\end{aligned}\tag{I.16}$$

while the quantum geometric contributions take the form

$$\begin{aligned}
\sigma_{ij}^{\text{Berry}}(\mathbf{B}) &= -e^3\tau \sum_{\alpha} \int \frac{d^3k}{(2\pi)^3} f'(\epsilon_{\alpha}) \\
&\quad \times \{(\boldsymbol{\Omega}_{\alpha} \cdot \mathbf{v}_{\alpha}) [(v_{\alpha})_i B_j + (v_{\alpha})_j B_i] - (\boldsymbol{\Omega}_{\alpha} \cdot \mathbf{B})(v_{\alpha})_i (v_{\alpha})_j\}, \\
\sigma_{ij}^{\text{OMM}}(\mathbf{B}) &= e^2\tau \sum_{\alpha} \int \frac{d^3k}{(2\pi)^3} \{f''(\epsilon_{\alpha})(\mathbf{m}_{\alpha} \cdot \mathbf{B})(v_{\alpha})_i (v_{\alpha})_j \\
&\quad + f'(\epsilon_{\alpha}) [(v_{\alpha})_i \partial_j (\mathbf{m}_{\alpha} \cdot \mathbf{B}) + (v_{\alpha})_j \partial_i (\mathbf{m}_{\alpha} \cdot \mathbf{B})]\} \\
&= e^2\tau \sum_{\alpha} \int \frac{d^3k}{(2\pi)^3} f'(\epsilon_{\alpha}) \{- (\mathbf{m}_{\alpha} \cdot \mathbf{B}) \partial_j (v_{\alpha})_i \\
&\quad + [(v_{\alpha})_i \partial_j (\mathbf{m}_{\alpha} \cdot \mathbf{B}) + (v_{\alpha})_j \partial_i (\mathbf{m}_{\alpha} \cdot \mathbf{B})] / 2\}.
\end{aligned} \tag{I.17}$$

Note that these results appear to agree exactly with a microscopic (fully quantum mechanical) approach, see Eqs. (8) and (12) of in the work of Könye and Ogata (2021).

Appendix II

II.A | Gell-Mann and spin matrices

Here we list the $N = 3$ ($N = 4$) Gell-Mann matrices and relate them to spin-1 (spin-3/2) matrices. Note that the generalization to $N \geq 5$ Gell-Mann matrices (not listed here explicitly) is straightforward, see for example the book by Pfeifer (2003) or the article by Bertlmann and Krammer (2008): There are $N(N - 1)/2$ symmetric matrices (purely real), $N(N - 1)/2$ antisymmetric matrices (purely imaginary), and $N - 1$ diagonal matrices.

$N = 3$ Gell-Mann matrices

The $N = 3$ Gell-Mann matrices (Gell-Mann 1962) are given by

$$\begin{aligned} \lambda_1 &= \begin{pmatrix} 0 & 1 & 0 \\ 1 & 0 & 0 \\ 0 & 0 & 0 \end{pmatrix}, & \lambda_2 &= \begin{pmatrix} 0 & -i & 0 \\ i & 0 & 0 \\ 0 & 0 & 0 \end{pmatrix}, & \lambda_3 &= \begin{pmatrix} 1 & 0 & 0 \\ 0 & -1 & 0 \\ 0 & 0 & 0 \end{pmatrix}, \\ \lambda_4 &= \begin{pmatrix} 0 & 0 & 1 \\ 0 & 0 & 0 \\ 1 & 0 & 0 \end{pmatrix}, & \lambda_5 &= \begin{pmatrix} 0 & 0 & -i \\ 0 & 0 & 0 \\ i & 0 & 0 \end{pmatrix}, & \lambda_6 &= \begin{pmatrix} 0 & 0 & 0 \\ 0 & 0 & 1 \\ 0 & 1 & 0 \end{pmatrix}, \\ \lambda_7 &= \begin{pmatrix} 0 & 0 & 0 \\ 0 & 0 & -i \\ 0 & i & 0 \end{pmatrix}, & \lambda_8 &= \frac{1}{\sqrt{3}} \begin{pmatrix} 1 & 0 & 0 \\ 0 & 1 & 0 \\ 0 & 0 & -2 \end{pmatrix}. \end{aligned}$$

They can easily be related to spin-1 matrices, which in the standard representation read

$$\begin{aligned} S_x &= \frac{1}{\sqrt{2}}(\lambda_1 + \lambda_6), \\ S_y &= \frac{1}{\sqrt{2}}(\lambda_2 + \lambda_7), \\ S_z &= \frac{1}{2}(\lambda_3 + \sqrt{3}\lambda_8). \end{aligned} \tag{II.1}$$

$N = 4$ Gell-Mann matrices

The $N = 4$ Gell-Mann matrices are given by extended $SU(3)$ Gell-Mann matrices as (Pfeifer 2003; Bertlmann and Kramer 2008)

$$\begin{aligned}
 \lambda_1 &= \begin{pmatrix} 0 & 1 & 0 & 0 \\ 1 & 0 & 0 & 0 \\ 0 & 0 & 0 & 0 \\ 0 & 0 & 0 & 0 \end{pmatrix}, & \lambda_2 &= \begin{pmatrix} 0 & -i & 0 & 0 \\ i & 0 & 0 & 0 \\ 0 & 0 & 0 & 0 \\ 0 & 0 & 0 & 0 \end{pmatrix}, & \lambda_3 &= \begin{pmatrix} 1 & 0 & 0 & 0 \\ 0 & -1 & 0 & 0 \\ 0 & 0 & 0 & 0 \\ 0 & 0 & 0 & 0 \end{pmatrix}, \\
 \lambda_4 &= \begin{pmatrix} 0 & 0 & 1 & 0 \\ 0 & 0 & 0 & 0 \\ 1 & 0 & 0 & 0 \\ 0 & 0 & 0 & 0 \end{pmatrix}, & \lambda_5 &= \begin{pmatrix} 0 & 0 & -i & 0 \\ 0 & 0 & 0 & 0 \\ i & 0 & 0 & 0 \\ 0 & 0 & 0 & 0 \end{pmatrix}, & \lambda_6 &= \begin{pmatrix} 0 & 0 & 0 & 0 \\ 0 & 0 & 1 & 0 \\ 0 & 1 & 0 & 0 \\ 0 & 0 & 0 & 0 \end{pmatrix}, \\
 \lambda_7 &= \begin{pmatrix} 0 & 0 & 0 & 0 \\ 0 & 0 & -i & 0 \\ 0 & i & 0 & 0 \\ 0 & 0 & 0 & 0 \end{pmatrix}, & \lambda_8 &= \frac{1}{\sqrt{3}} \begin{pmatrix} 1 & 0 & 0 & 0 \\ 0 & 1 & 0 & 0 \\ 0 & 0 & -2 & 0 \\ 0 & 0 & 0 & 0 \end{pmatrix},
 \end{aligned}$$

plus an additional seven matrices

$$\begin{aligned}
 \lambda_9 &= \begin{pmatrix} 0 & 0 & 0 & 1 \\ 0 & 0 & 0 & 0 \\ 0 & 0 & 0 & 0 \\ 1 & 0 & 0 & 0 \end{pmatrix}, & \lambda_{10} &= \begin{pmatrix} 0 & 0 & 0 & -i \\ 0 & 0 & 0 & 0 \\ 0 & 0 & 0 & 0 \\ i & 0 & 0 & 0 \end{pmatrix}, & \lambda_{11} &= \begin{pmatrix} 0 & 0 & 0 & 0 \\ 0 & 0 & 0 & 1 \\ 0 & 0 & 0 & 0 \\ 0 & 1 & 0 & 0 \end{pmatrix}, \\
 \lambda_{12} &= \begin{pmatrix} 0 & 0 & 0 & 0 \\ 0 & 0 & 0 & -i \\ 0 & 0 & 0 & 0 \\ 0 & i & 0 & 0 \end{pmatrix}, & \lambda_{13} &= \begin{pmatrix} 0 & 0 & 0 & 0 \\ 0 & 0 & 0 & 0 \\ 0 & 0 & 0 & 1 \\ 0 & 0 & 1 & 0 \end{pmatrix}, & \lambda_{14} &= \begin{pmatrix} 0 & 0 & 0 & 0 \\ 0 & 0 & 0 & 0 \\ 0 & 0 & 0 & -i \\ 0 & 0 & i & 0 \end{pmatrix}, \\
 \lambda_{15} &= \frac{1}{\sqrt{6}} \begin{pmatrix} 1 & 0 & 0 & 0 \\ 0 & 1 & 0 & 0 \\ 0 & 0 & 1 & 0 \\ 0 & 0 & 0 & -3 \end{pmatrix}.
 \end{aligned}$$

This can easily be used to express the standard representation of spin-3/2 matrices:

$$\begin{aligned} S_x &= \frac{1}{2}(\sqrt{3}\lambda_1 + 2\lambda_6 + \sqrt{3}\lambda_{13}), \\ S_y &= \frac{1}{2}(\sqrt{3}\lambda_2 + 2\lambda_7 + \sqrt{3}\lambda_{14}), \\ S_z &= \frac{1}{2}(\lambda_3 + \sqrt{3}\lambda_8 + \sqrt{6}\lambda_{15}). \end{aligned} \tag{II.2}$$

II.B | The generalized Bloch sphere

We give here a short summary of the concept of a *generalized Bloch sphere* [that is, the eigenprojector's Bloch sphere $\mathcal{B}_{P_\alpha}^{(N)}$ introduced in Section 2.4.2], drawing largely on the work of Harriman (1978), Jakóbczyk and Siennicki (2001), Kimura (2003), Zyczkowski and Sommers (2003), Byrd and Khaneja (2003), Kimura and Kossakowski (2005), Mendaš (2006) and Goyal et al. (2016).

For an N -dimensional Hilbert space, the three defining properties of a (mixed state) density matrix ρ_α representing an N -component (mixed) quantum state $|\psi_\alpha\rangle$, where $\alpha = 1, \dots, N$, are hermiticity $\rho_\alpha^\dagger = \rho_\alpha$, probability conservation $\text{Tr } \rho_\alpha = 1$ and positive semi-definiteness, $\rho_\alpha \geq 0$. Pure states have, in addition, $\rho_\alpha^2 = \rho_\alpha$, in which case $\rho_\alpha = P_\alpha$ is an eigenprojector. An expansion in the basis of $\text{SU}(N)$ generator matrices analogous to Eq. (2.50) can be made for a general (mixed state) density matrix:

$$\rho_\alpha = \frac{1}{N}1_N + \frac{1}{2}\mathbf{b}_\alpha \cdot \boldsymbol{\lambda}, \tag{II.3}$$

where now $|\mathbf{b}_\alpha|$ can take various values depending on the pureness of the state. In the pure state case, we have $|\mathbf{b}_\alpha| = \sqrt{2(N-1)/N}$. Considering the vector space \mathbb{R}^{N^2-1} , and denoting the (N^2-1) -dimensional subspace accessible to the (mixed state) Bloch vector \mathbf{b}_α as $\Sigma_{\rho_\alpha}^{(N)}$, one needs to distinguish between two kinds of boundaries, namely its (N^2-2) -dimensional *topological boundary* $\partial\Sigma_{\rho_\alpha}^{(N)}$ and its *extremal boundary* $\mathcal{B}_{P_\alpha}^{(N)}$. The latter is of dimension $2(N-1)$, and it comprises the vectors of maximal $|\mathbf{b}_\alpha|$, that is, it is the space of pure state Bloch vectors, or in other words the generalized Bloch sphere. This is sketched in Fig. II.1.

Another set of immediate interest in this discussion is the sphere

$$\mathcal{W}^{N^2-2} \equiv \left\{ \mathbf{r} \in \mathbb{R}^{N^2-1} \mid |\mathbf{r}| = \sqrt{\frac{2(N-1)}{N}} \right\} \tag{II.4}$$

that contains all pure state Bloch vectors; in other words, it is the surface of the ball \mathbb{B}^{N^2-1} , the smallest ball that contains $\Sigma_{\rho_\alpha}^{(N)}$. For $N = 2$, one trivially has $\partial\Sigma_{\rho_\alpha}^{(2)} = \mathcal{B}_{P_\alpha}^{(2)} = \mathcal{W}^2$ (and $\mathcal{W}^2 = \mathcal{S}^2$, with the unit two-sphere \mathcal{S}^2), as illustrated in Fig. II.1; but for higher N the three spaces are different. One has $\mathcal{B}_{P_\alpha}^{(N)} \subset \partial\Sigma_{\rho_\alpha}^{(N)}$ and $\mathcal{B}_{P_\alpha}^{(N)} \subset \mathcal{W}^{N^2-2}$, meaning that the generalized Bloch sphere is a proper subset of (i) the boundary of the space of mixed states and (ii) the sphere \mathcal{W}^{N^2-2} ; in fact, it is their intersection: $\partial\Sigma_{\rho_\alpha}^{(N)} \cap \mathcal{W}^{N^2-2} = \mathcal{B}_{P_\alpha}^{(N)}$. In other words, if \mathbf{b}_α corresponds to a pure state, it lies on \mathcal{W}^{N^2-2} , but not necessarily the other way around: not all points on \mathcal{W}^{N^2-2} represent physically valid pure states.

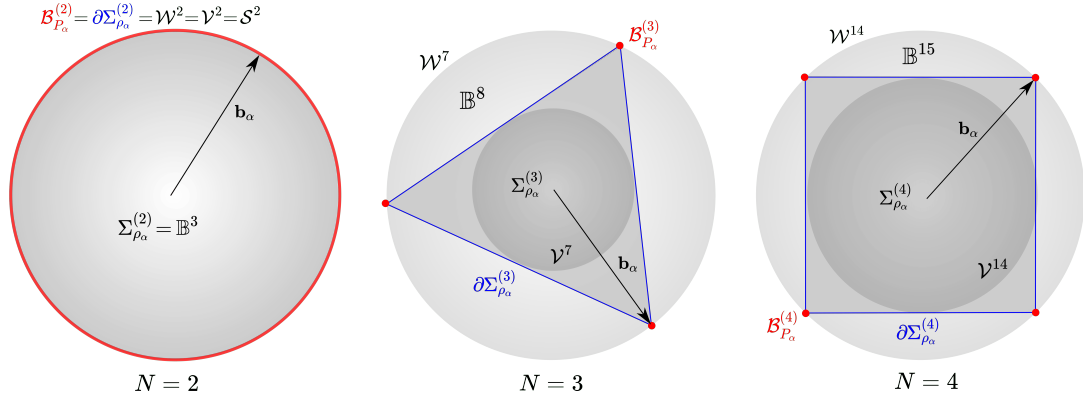


Fig. II.1 – Schematic illustration of the generalized Bloch sphere and other relevant sets, for $N = 2, 3, 4$. The large $(N^2 - 2)$ -sphere \mathcal{W}^{N^2-2} , of radius $\sqrt{2(N-1)/N}$, corresponds to the highest permissible length of a Bloch vector. In its interior, the Ball \mathbb{B}^{N^2-1} , there is the space $\Sigma_{\rho_\alpha}^{(N)}$ accessible to a mixed state (II.3), with topological boundary $\partial\Sigma_{\rho_\alpha}^{(N)}$, and in the interior of $\Sigma_{\rho_\alpha}^{(N)}$ there is the small $(N^2 - 2)$ -sphere \mathcal{V}^{N^2-2} , of radius $\sqrt{2/[N(N-1)]}$. The extremal boundary $\mathcal{B}_{P_\alpha}^{(N)}$ of $\Sigma_{\rho_\alpha}^{(N)}$, which is the intersection of $\Sigma_{\rho_\alpha}^{(N)}$ with the large sphere, is the generalized (eigenprojector's) Bloch sphere. For the familiar $N = 2$ case, these complications are hidden, since all the relevant sets coincide.

Analogously, the interior of \mathcal{W}^{N^2-2} , that is, the ball \mathbb{B}^{N^2-1} , is not composed of only physically valid mixed states. In fact, calculations (Zyczkowski and Sommers 2003) of the volume of $\Sigma_{\rho_\alpha}^{(N)}$ show that $\text{vol}(\Sigma_{\rho_\alpha}^{(3)})/\text{vol}(\mathbb{B}^8) \approx 0.26$ as well as $\text{vol}(\Sigma_{\rho_\alpha}^{(4)})/\text{vol}(\mathbb{B}^{15}) \approx 0.12$, meaning that most points in \mathbb{B}^{N^2-1} do actually not represent physically valid states as soon as $N > 2$.

At the origin of all of these complications is the constraint of positive semi-definiteness, $\rho_\alpha \geq 0$: for $N = 1$, this condition is trivially fulfilled. For $N = 2$, it is equivalent to $\text{Tr}(\rho_\alpha^2) \leq 1$, so for a given density matrix there is *one additional constraint* as compared to $N = 1$. In the same way, whenever N increases by one, one additional constraint involving traces $D_{\alpha,n} \equiv \text{Tr}(\rho_\alpha^n)$ needs to be fulfilled in order to have positive semi-definiteness. For example, for $N = 3$, there are the three constraints (Kimura 2003) $D_{\alpha,1} = 1$, $D_{\alpha,2} \leq 1$, and $-2D_{\alpha,3} + 3D_{\alpha,2} \leq 1$, which can be translated to constraints on the Bloch vectors via Eq. (II.3). This restricts the elements of \mathbb{B}^8 that represent physically valid states. As a consequence, the relevant sets (including the generalized Bloch sphere) acquire a very non-trivial shape already for $N = 3$ (Goyal et al. 2016):

$$\begin{aligned}
\mathcal{B}_{P_\alpha}^{(3)} &= \left\{ \mathbf{b}_\alpha \in \mathbb{R}^8 \left| |\mathbf{b}_\alpha|^2 = \frac{4}{3}, |\mathbf{b}_\alpha|^2 - \mathbf{b}_\alpha \cdot (\mathbf{b}_\alpha \star \mathbf{b}_\alpha) = \frac{4}{9} \right. \right\}, \\
\partial\Sigma_{\rho_\alpha}^{(3)} &= \left\{ \mathbf{b}_\alpha \in \mathbb{R}^8 \left| |\mathbf{b}_\alpha|^2 \leq \frac{4}{3}, |\mathbf{b}_\alpha|^2 - \mathbf{b}_\alpha \cdot (\mathbf{b}_\alpha \star \mathbf{b}_\alpha) = \frac{4}{9} \right. \right\}, \\
\Sigma_{\rho_\alpha}^{(3)} &= \left\{ \mathbf{b}_\alpha \in \mathbb{R}^8 \left| |\mathbf{b}_\alpha|^2 \leq \frac{4}{3}, |\mathbf{b}_\alpha|^2 - \mathbf{b}_\alpha \cdot (\mathbf{b}_\alpha \star \mathbf{b}_\alpha) \leq \frac{4}{9} \right. \right\},
\end{aligned} \tag{II.5}$$

where the agreement of the first line with Eq. (2.51) is to be noted. Similarly, more complicated constraints can be obtained for higher N , see Kimura (2003).

Yet another way to understand the complexity of the generalized Bloch sphere is to realize that $\mathbf{b}_\gamma = \langle \psi_\gamma | \boldsymbol{\lambda} | \psi_\gamma \rangle$ is a vector of expectation values of the operators λ_i

(Kimura and Kossakowski 2005). The minimum and maximum values of the components $b_{\gamma,i}$ are thus fundamentally restricted by the eigenvalues of the generators λ_i . For example, for $N = 2$, the Pauli matrices have eigenvalues $\epsilon_{\sigma_i} = \pm 1$, which *a priori* restricts the Bloch vectors to a unit cube. Since the Pauli matrices do not commute, that is, $\langle \psi_\gamma | \sigma_i | \psi_\gamma \rangle$ cannot yield an eigenvalue for all i simultaneously, this cube gets restricted further, and this restriction results in the Bloch unit sphere \mathcal{S}^2 . In the same way, for $N = 3$, there is a polytope embedded in \mathbb{R}^8 and defined by the eigenvalues of the Gell-Mann matrices (cf. Appendix II.A): $\epsilon_{\Lambda_i} = 0, \pm 1$ for $i = 1, \dots, 7$, and $\epsilon_{\Lambda_8} = -\frac{2}{\sqrt{3}}, \frac{1}{\sqrt{3}}$. This polytope is asymmetric due to the eigenvalues of λ_8 , and it gets further restricted by the commutation relations (2.28), resulting in a quite complicated shape of Σ^3 .

Finally, note that there exists another sphere

$$\mathcal{V}^{N^2-2} \equiv \left\{ \mathbf{r} \in \mathbb{R}^{N^2-1} \mid |\mathbf{r}| = \sqrt{\frac{2}{N(N-1)}} \right\} \quad (\text{II.6})$$

inscribed inside $\Sigma_{\rho_\alpha}^{(N)}$, such that $\partial \Sigma_{\rho_\alpha}^{(N)}$ lies between \mathcal{V}^{N^2-2} and \mathcal{W}^{N^2-2} .

The essence of all these established facts is visualized schematically in Fig. II.1. Note that the figure is only a rough sketch supposed to highlight the different sets involved. A visual insight into the true (very complicated) shape of those sets can be gained by considering two- or three-sections, see for instance Jakóbczyk and Siennicki (2001), Kimura and Kossakowski (2005), Mendaš (2006), or Goyal et al. (2016).

Appendix III

III.A | General recipe to find a Bloch vector expression

Given a kernel such as (3.15), the general strategy to achieve a maximally compact expression in terms of Bloch vectors is the following.

- 1.) Write the Green's function and the Hamiltonian in terms of eigenprojectors as $G = \sum_{\alpha} D_{\alpha} P_{\alpha}$ [cf. Eq. (1.46)] and $H = \sum_{\alpha} H_{\alpha}$, respectively, where $D_{\alpha} = 1/(E - \varepsilon_{\alpha} + i\eta)$ and $H_{\alpha} \equiv \varepsilon_{\alpha} P_{\alpha}$.
- 2.) Use the chain rule $H_{\beta}^i = \varepsilon_{\beta}^i P_{\beta} + \varepsilon_{\beta} P_{\beta}^i$ and the eigenprojector identities

$$P_{\alpha} P_{\beta} = \delta_{\alpha\beta} P_{\alpha}, \quad P_{\alpha} P_{\beta}^i = \delta_{\alpha\beta} P_{\alpha}^i - P_{\alpha}^i P_{\beta} \quad (\text{III.1})$$

in order to maximally simplify the trace.

- 3.) In order to facilitate E -integration, it is useful to rewrite the expressions obtained from step 2.) in terms of powers of the Green's function's poles, as

$$K_{\text{indices}} = \sum_{n=1}^{N_G} \sum_{\alpha} D_{\alpha}^n F_{\alpha,n}^{(\text{indices})} \quad (\text{III.2})$$

where N_G is the total number of Green's functions in the kernel.

- 4.) Expand the eigenprojectors in the generators of $\text{SU}(N)$ using Eq. (2.50), such that the traces can be evaluated explicitly. In the final result for the kernel, conventional contributions depend only on the energies ε_{α} and their derivatives, while geometric contributions depend on the Bloch vectors \mathbf{b}_{α} and their derivatives.

Example: Simple kernels

Here we illustrate the above procedure using the simple kernels $K_i = \text{Tr}(GH^i)$ and $K_{ij} = \text{Tr}(GH^iGH^j)$. According to step 1.), we start by inserting G and H , such that

$$K_i = \sum_{\alpha\beta} D_{\alpha} \text{Tr}(P_{\alpha} H_{\beta}^i P_{\alpha}), \quad K_{ij} = \sum_{\alpha\beta\gamma\delta} D_{\alpha} D_{\gamma} \text{Tr}(P_{\alpha} H_{\beta}^i P_{\gamma} H_{\delta}^j P_{\alpha}). \quad (\text{III.3})$$

Note that we have symmetrized the kernels using the identity $P_{\alpha}^2 = P_{\alpha}$ and cyclicity of the trace. Using the chain rule and simplifying according to step 2.), one has

$$K_i = \sum_{\alpha} D_{\alpha} \varepsilon_{\alpha}^i, \quad K_{ij} = \sum_{\alpha} D_{\alpha}^2 \varepsilon_{\alpha}^i \varepsilon_{\alpha}^j + \sum_{\alpha\beta} D_{\alpha} D_{\beta} \Delta_{\alpha\beta}^2 \mathcal{T}_{\alpha\beta}^{(ij)}, \quad (\text{III.4})$$

with $\Delta_{\alpha\beta} \equiv \varepsilon_\alpha - \varepsilon_\beta$. Here we made use of the trace identities

$$\begin{aligned} \text{Tr}(P_\alpha P_\beta^i P_\alpha) &= 0, \\ \text{Tr}(P_\alpha P_\beta^i P_\gamma P_\delta^j P_\alpha) &= (\delta_{\alpha\beta} - \delta_{\beta\gamma})(\delta_{\gamma\delta} - \delta_{\delta\alpha}) \text{Tr}(P_\alpha P_\alpha^i P_\alpha^j) \\ &= (\delta_{\alpha\beta} - \delta_{\beta\gamma})(\delta_{\alpha\delta} - \delta_{\gamma\delta}) \mathcal{T}_{\alpha\gamma}^{(ij)}, \end{aligned} \quad (\text{III.5})$$

where we introduced the shorthand notation $\mathcal{T}_{\alpha\beta}^{(ij)} \equiv \text{Tr}(P_\alpha^i P_\beta P_\alpha^j)$. According to step 3.), the kernels can be expanded in powers of poles as

$$K_i = \sum_\alpha D_\alpha F_{\alpha,1}^{(i)}, \quad K_{ij} = \sum_\alpha \left(D_\alpha F_{\alpha,1}^{(ij)} + D_\alpha^2 F_{\alpha,2}^{(ij)} \right). \quad (\text{III.6})$$

It is trivial to see that $F_{\alpha,1}^{(i)} = \varepsilon_\alpha^i$ and $F_{\alpha,2}^{(ij)} = \varepsilon_\alpha^i \varepsilon_\alpha^j$. For determining the remaining coefficients of K_{ij} , one can make use of the partial fraction decomposition

$$D_\alpha D_\beta \Delta_{\alpha\beta}^2 = \Delta_{\alpha\beta} (D_\alpha - D_\beta), \quad (\text{III.7})$$

leading to

$$F_{\alpha,1}^{(ij)} = \sum_{\beta \neq \alpha} \Delta_{\alpha\beta} (\mathcal{T}_{\alpha\beta}^{(ij)} + \mathcal{T}_{\alpha\beta}^{(ji)}). \quad (\text{III.8})$$

Here we used the useful fact that

$$\mathcal{T}_{\alpha\beta}^{(ij)} = \mathcal{T}_{\beta\alpha}^{(ji)} \text{ for } \alpha \neq \beta, \quad (\text{III.9})$$

as can be deduced from Eq. (III.1).

We are now ready to apply step 4.) to achieve the final Bloch vector decomposition. The kernel K_i has no geometric contribution, as it depends only on the energies. The kernel K_{ij} , however, does have a geometric contribution determined by

$$F_{\alpha,1}^{(ij)} = -\frac{1}{4} \sum_{\beta \neq \alpha} \Delta_{\alpha\beta} \left(\mathbf{b}_\alpha^i \cdot \mathbf{b}_\beta^j + \mathbf{b}_\alpha^j \cdot \mathbf{b}_\beta^i \right), \quad (\text{III.10})$$

where we used the identity

$$\mathcal{T}_{\alpha\beta}^{(ij)} = \frac{1}{2} \left(\delta_{\alpha\beta} - \frac{1}{2} \right) \mathbf{b}_\alpha^i \cdot \mathbf{b}_\beta^j - \frac{i}{4} \mathbf{b}_\beta \cdot (\mathbf{b}_\alpha^i \times \mathbf{b}_\alpha^j). \quad (\text{III.11})$$

For $N = 2$, where the Bloch vector is given by Eq. (2.46), this reduces to a quantum metric contribution $F_{\alpha,1}^{(ij)} = \varepsilon_\alpha \mathbf{u}^i \cdot \mathbf{u}^j = 4\varepsilon_\alpha g_{\alpha,ij}$, but for general N a more complicated geometric object appears.

III.B | SU(N) Jacobi identities

The *first Jacobi identity* (Kaplan and Resnikoff 1967; Macfarlane et al. 1968) can be written alternatively for the generator matrices, the antisymmetric structure constants and the SU(N) vectors as

$$\begin{aligned} [[\lambda_i, \lambda_j], \lambda_k] + [[\lambda_j, \lambda_k], \lambda_i] + [[\lambda_k, \lambda_i], \lambda_j] &= 0, \\ f_{ijm} f_{klm} + f_{ikm} f_{ljm} + f_{ilm} f_{jkm} &= 0, \\ \mathbf{m} \times (\mathbf{n} \times \mathbf{o}) + \mathbf{n} \times (\mathbf{o} \times \mathbf{m}) + \mathbf{o} \times (\mathbf{m} \times \mathbf{n}) &= 0, \\ (\mathbf{m} \times \mathbf{n}) \cdot (\mathbf{o} \times \mathbf{p}) + (\mathbf{m} \times \mathbf{o}) \cdot (\mathbf{p} \times \mathbf{n}) + (\mathbf{m} \times \mathbf{p}) \cdot (\mathbf{n} \times \mathbf{o}) &= 0, \end{aligned} \quad (\text{III.12})$$

where the third and fourth lines are obtained from the second line depending on whether or not one keeps a free index. Similarly, the *second Jacobi identity* is given by

$$\begin{aligned}
& [\{\lambda_i, \lambda_j\}, \lambda_k] + [\{\lambda_j, \lambda_k\}, \lambda_i] + [\{\lambda_k, \lambda_i\}, \lambda_j] = 0, \\
& f_{ijm}d_{klm} + f_{ikm}d_{ljm} + f_{ilm}d_{jkm} = 0, \\
& \mathbf{m} \times (\mathbf{n} \star \mathbf{o}) + \mathbf{n} \times (\mathbf{o} \star \mathbf{m}) + \mathbf{o} \times (\mathbf{m} \star \mathbf{n}) = 0, \\
& (\mathbf{m} \times \mathbf{n}) \cdot (\mathbf{o} \star \mathbf{p}) + (\mathbf{m} \times \mathbf{o}) \cdot (\mathbf{p} \star \mathbf{n}) + (\mathbf{m} \times \mathbf{p}) \cdot (\mathbf{n} \star \mathbf{o}) = 0.
\end{aligned} \tag{III.13}$$

Furthermore, there is the identity

$$\begin{aligned}
& [\lambda_i, [\lambda_j, \lambda_k]] = \{\lambda_k, \{\lambda_i, \lambda_j\}\} - \{\lambda_j, \{\lambda_i, \lambda_k\}\}, \\
& f_{ijm}f_{klm} = \frac{2}{N}(\delta_{ik}\delta_{jl} - \delta_{il}\delta_{jk}) + d_{ikm}d_{jlm} - d_{ilm}d_{jkm}, \\
& \mathbf{m} \times (\mathbf{n} \times \mathbf{o}) = \frac{2}{N}[(\mathbf{m} \cdot \mathbf{o})\mathbf{n} - (\mathbf{m} \cdot \mathbf{n})\mathbf{o}] \\
& \quad + (\mathbf{m} \star \mathbf{o}) \star \mathbf{n} - (\mathbf{m} \star \mathbf{n}) \star \mathbf{o}, \\
& (\mathbf{m} \times \mathbf{n}) \cdot (\mathbf{o} \times \mathbf{p}) = \frac{2}{N}[(\mathbf{m} \cdot \mathbf{o})(\mathbf{n} \cdot \mathbf{p}) - (\mathbf{m} \cdot \mathbf{p})(\mathbf{n} \cdot \mathbf{o})] \\
& \quad + (\mathbf{m} \star \mathbf{o}) \cdot (\mathbf{n} \star \mathbf{p}) - (\mathbf{m} \star \mathbf{p}) \cdot (\mathbf{n} \star \mathbf{o}).
\end{aligned} \tag{III.14}$$

III.C | Alternative QGT formula in terms of Bloch vectors

From Eq. (3.7) together with Eq. (3.21) we have

$$g_{\alpha,ij} = \sum_{\beta \neq \alpha} \frac{S_{\alpha\beta}^{ij}}{(\varepsilon_\alpha - \varepsilon_\beta)^2}, \quad \Omega_{\alpha,ij} = - \sum_{\beta \neq \alpha} \frac{A_{\alpha\beta}^{ij}}{(\varepsilon_\alpha - \varepsilon_\beta)^2}, \tag{III.15}$$

where

$$\begin{aligned}
S_{\alpha\beta}^{ij} &= \frac{4}{N^2} \mathbf{h}^i \cdot \mathbf{h}^j + \frac{1}{N} [(\mathbf{b}_\alpha \cdot \mathbf{h}^i)(\mathbf{b}_\beta \cdot \mathbf{h}^j) + (\mathbf{b}_\alpha \cdot \mathbf{h}^j)(\mathbf{b}_\beta \cdot \mathbf{h}^i)] \\
& \quad + \frac{2}{N} (\mathbf{b}_\alpha + \mathbf{b}_\beta) \cdot (\mathbf{h}^i \star \mathbf{h}^j) + \frac{1}{2} [(\mathbf{b}_\alpha \star \mathbf{h}^i) \cdot (\mathbf{b}_\beta \star \mathbf{h}^j) + (\mathbf{b}_\alpha \star \mathbf{h}^j) \cdot (\mathbf{b}_\beta \star \mathbf{h}^i)], \\
A_{\alpha\beta}^{ij} &= \frac{2}{N} (\mathbf{b}_\alpha - \mathbf{b}_\beta) \cdot (\mathbf{h}^i \times \mathbf{h}^j) + (\mathbf{b}_\alpha \star \mathbf{h}^i) \cdot (\mathbf{b}_\beta \times \mathbf{h}^j) + (\mathbf{b}_\alpha \times \mathbf{h}^i) \cdot (\mathbf{b}_\beta \star \mathbf{h}^j).
\end{aligned}$$

It is straightforward to check that $S_{\alpha\beta}^{ij}$ is symmetric under an exchange of indices i, j (or of α, β), whereas $A_{\alpha\beta}^{ij}$ is antisymmetric under such an exchange, and as a consequence $\sum_\alpha \Omega_{\alpha,ij} = 0$. While much less compact than Eq. (3.10), the expressions (III.15) appear more convenient for numerical implementation. Conceptually, they mainly distinguish themselves from Eq. (3.10) in that, on the one hand, they involve solely the parametric derivatives of the Hamiltonian vector, while on the other hand they also illustrate the interband nature of the two geometric tensors, and lastly they also show explicitly the importance of the star product for both the N -band quantum metric and Berry curvature.

III.D | Derivation of Eq. (3.26)

To find the eigenprojector P_α as a polynomial in the Hamiltonian matrix, our starting point is the following textbook formula, involving the set $\{\varepsilon_\beta, \beta = 1, \dots, N\}$ of all energy eigenvalues (Halmos 2017):

$$P_\alpha = \prod_{\beta \neq \alpha} \frac{H - \varepsilon_\beta 1_N}{\varepsilon_\alpha - \varepsilon_\beta}. \quad (\text{III.16})$$

Note that in the language of matrix theory, Eq. (III.16) defines the *Frobenius covariants* of H . Note also that the denominator of Eq. (III.16) corresponds to the derivative $p'_N(\varepsilon_\alpha)$ of the Hamiltonian's characteristic polynomial, evaluated at the energy ε_α . Indeed, before proceeding, it proves useful to compile some more details on the characteristic polynomial $p_N(z)$.

Characteristic polynomial

The *characteristic polynomial* of an $N \times N$ matrix A is given by (Gantmacher 1980)

$$\tilde{p}_N(z) = \det(z1_N - A) = \sum_{k=0}^N \tilde{c}_k z^{N-k} = \prod_{\alpha=1}^N (z - a_\alpha), \quad (\text{III.17})$$

where a_α denotes an eigenvalue of A and $\tilde{c}_0 = 1$. According to the Faddeev-Le Verrier algorithm (Gantmacher 1980), the coefficients \tilde{c}_k may be computed from the traces $s_k \equiv \text{Tr } A^k$ of powers of A as

$$\begin{aligned} \tilde{c}_k &= -\frac{1}{k}(s_k + \tilde{c}_1 s_{k-1} + \dots + \tilde{c}_{k-1} s_1) \\ &= \frac{(-1)^k}{k!} Y_k(s_1, \dots, (-1)^{k-1} (k-1)! s_k). \end{aligned} \quad (\text{III.18})$$

The second equality involves (*exponential*) *complete Bell polynomials* $Y_k(z_1, \dots, z_k)$ (Bell 1934; Comtet 1974), the first few of which read explicitly

$$\begin{aligned} Y_0 &= 1, \\ Y_1(z_1) &= z_1, \\ Y_2(z_1, z_2) &= z_1^2 + z_2, \\ Y_3(z_1, z_2, z_3) &= z_1^3 + 3z_1 z_2 + z_3, \\ Y_4(z_1, z_2, z_3, z_4) &= z_1^4 + 6z_1^2 z_2 + 4z_1 z_3 + 3z_2^2 + z_4. \end{aligned} \quad (\text{III.19})$$

Focusing now on the case where $A = H$ represents a traceless $N \times N$ Hamiltonian matrix, we have the Hamiltonian's characteristic polynomial

$$p_N(z) = \det(z1_N - H) = \sum_{k=0}^N c_k z^{N-k} = \prod_{\alpha=1}^N (z - \varepsilon_\alpha). \quad (\text{III.20})$$

Using the Casimir invariants defined in Eq. (3.28), one may write the coefficients as

$$c_k = \frac{(-1)^k}{k!} Y_k(0, -C_2, \dots, (-1)^{k-1} (k-1)! C_k), \quad (\text{III.21})$$

and the first few of them read explicitly

$$\begin{aligned} c_0 &= 1, & c_1 &= 0, \\ c_2 &= -\frac{C_2}{2}, & c_3 &= -\frac{C_3}{3}, \\ c_4 &= \frac{C_2^2}{8} - \frac{C_4}{4}, & c_5 &= \frac{C_2 C_3}{6} - \frac{C_5}{5}, \\ c_6 &= -\frac{C_2^3}{48} + \frac{C_3^2}{18} + \frac{C_2 C_4}{8} - \frac{C_6}{6}. \end{aligned} \quad (\text{III.22})$$

Rewriting Eq. (III.16)

The goal is now to eliminate all $\varepsilon_{\beta \neq \alpha}$ from Eq. (III.16), such that P_α becomes a proper polynomial in H with coefficients that depend only on the single eigenvalue ε_α , that is, $P_\alpha = P_\alpha(\varepsilon_\alpha, H)$. Consider first the numerator of Eq. (III.16) and note that by explicit multiplication one may write

$$\prod_{\beta \neq \alpha} (H - \varepsilon_\beta 1_N) = \sum_{n=0}^{N-1} (-1)^n e_n(\varepsilon_1, \dots, \varepsilon_{\alpha-1}, \varepsilon_{\alpha+1}, \dots, \varepsilon_N) H^{N-1-n}, \quad (\text{III.23})$$

where $e_n = e_n(\varepsilon_1, \dots, \varepsilon_{\alpha-1}, \varepsilon_{\alpha+1}, \dots, \varepsilon_N)$ are known as *elementary symmetric polynomials* (Macdonald 1998). One has $e_0 = 1$ and all higher e_n are determined recursively by Newton's identities:

$$e_n = \frac{1}{n} \sum_{k=1}^n (-1)^{k-1} (C_k - \varepsilon_\alpha^k) e_{n-k}, \quad (\text{III.24})$$

where the C_k are the Casimir invariants of Eq. (3.28) and it was exploited that $\sum_{\beta \neq \alpha} \varepsilon_\beta^k = C_k - \varepsilon_\alpha^k$. This may further be rewritten as

$$e_n = (-1)^n \sum_{k=0}^n c_k \varepsilon_\alpha^{n-k}, \quad (\text{III.25})$$

where c_k are the coefficients (III.21) of the characteristic polynomial. If we now *define* polynomials $q_n(z)$ by Eq. (3.27), it is clear that $q_N(z) = p_N(z)$ is the characteristic polynomial (III.20), and $q_n(\varepsilon_\alpha) = (-1)^n e_n$. Moreover, inserting into Eq. (III.23), we have

$$\prod_{\beta \neq \alpha} (H - \varepsilon_\beta 1_N) = \sum_{n=0}^{N-1} q_{N-1-n}(\varepsilon_\alpha) H^n \quad (\text{III.26})$$

by relabeling the sum. This depends only on ε_α and H , as desired.

Similarly, for the denominator of Eq. (III.16), exactly the same procedure as above (where H gets replaced by ε_α) leads to

$$\prod_{\beta \neq \alpha} (\varepsilon_\alpha - \varepsilon_\beta) = \sum_{n=0}^{N-1} q_{N-1-n}(\varepsilon_\alpha) \varepsilon_\alpha^n. \quad (\text{III.27})$$

As mentioned above, $\prod_{\beta \neq \alpha} (\varepsilon_\alpha - \varepsilon_\beta)$ is equal to the derivative $p'_N(\varepsilon_\alpha)$ of the characteristic polynomial. From this one may also demonstrate the validity of the identity $\prod_{\beta \neq \alpha} (\varepsilon_\alpha - \varepsilon_\beta) = \sum_{n=0}^{N-1} q_{N-1-n}(\varepsilon_\alpha) C_n$. Combining all of these results, one finally arrives at Eq. (3.26) in the main text.

III.E | Closed-form solutions for energy eigenvalues

The solutions of the characteristic equation $p_N(z) = 0$, with $p_N(z)$ given by Eq. (III.20), are the eigenvalues of H . For $N = 2$, the solution of $p_2(\varepsilon_\alpha) = \varepsilon_\alpha^2 - C_2/2 = 0$ is simple, cf. Eq. (2.17). For $N > 2$, the complexity of the function $\varepsilon_\alpha(\{C_n\})$ grows very quickly. For $N = 3$, the solutions of $p_3(\varepsilon_\alpha) = \varepsilon_\alpha^3 - (C_2/2)\varepsilon_\alpha - C_3/3 = 0$ can be parametrized as (Abramowitz and Stegun 1965; Weisstein n.d.[a])

$$\varepsilon_\alpha = \frac{(-1)^\alpha}{1 + |\alpha|} (S_+ + S_-) + \alpha \frac{i\sqrt{3}}{2} (S_+ - S_-), \quad S_\pm \equiv \frac{1}{6^{1/3}} \left(C_3 \pm i\sqrt{\frac{C_2^3}{6} - C_3^2} \right)^{1/3},$$

where $\alpha = 0, \pm 1$. Note that since $C_2^3 \geq 6C_3^2$, all ε_α are of course real (Abramowitz and Stegun 1965; Rosen 1971). This allows to interpret the eigenvalues as lying on a circle, that is, one may parametrize the solutions using trigonometric functions, see for example Rosen (1971):

$$\varepsilon_\alpha = \sqrt{\frac{2C_2}{3}} \cos \left[\frac{1}{3} \arccos \left(\frac{\sqrt{6}C_3}{C_2^{3/2}} \right) + \frac{2(\alpha + 2)\pi}{3} \right] = \frac{2|\mathbf{h}|}{\sqrt{3}} \cos \gamma_\alpha, \quad (\text{III.28})$$

$$\gamma_\alpha \equiv \frac{1}{3} \left[\arccos \left(\sqrt{3} \mathbf{h} \cdot \mathbf{h}_\star / |\mathbf{h}|^3 \right) + 2(\alpha + 2)\pi \right].$$

For $N = 4$, there are again several ways to parametrize the solutions of $p_4(\varepsilon_\alpha) = \varepsilon_\alpha^4 - (C_2/2)\varepsilon_\alpha^2 - (C_3/3)\varepsilon_\alpha + C_2^2/8 - C_4/4 = 0$, for example (Abramowitz and Stegun 1965; Weisstein n.d.[b])

$$\varepsilon_\alpha = \frac{\text{sgn}(\alpha)}{2\sqrt{3}} \left[R + (-1)^\alpha \sqrt{2C_2 - D + \text{sgn}(\alpha) \frac{2\sqrt{3}C_3}{R}} \right],$$

$$R \equiv \sqrt{D + C_2},$$

$$D \equiv B \left(\frac{2}{A + \sqrt{A^2 - 4B^3}} \right)^{1/3} + \left(\frac{A + \sqrt{A^2 - 4B^3}}{2} \right)^{1/3}, \quad (\text{III.29})$$

$$A \equiv 3C_3^2 + C_2 \left(\frac{17}{4} C_2^2 - 9C_4 \right),$$

$$B \equiv \frac{7}{4} C_2^2 - 3C_4,$$

where $\alpha = \pm 1, \pm 2$. For $N \geq 5$, closed-form solutions $\varepsilon_\alpha(\{C_n\})$ of the characteristic equation are unknown (Van Kortryk 2016).

III.F | Eigenstates from eigenprojectors

The eigenprojector P_α permits to construct the eigenstate $|\psi_\alpha\rangle$ from a gauge freedom state $|\psi_g\rangle$. For example, in the two-band case, using the eigenprojector P_α given by Eq. (2.46), an eigenstate is easily constructed from Eq. (3.31) by projecting onto

$$|\psi_g\rangle = \begin{pmatrix} \cos \theta_g \\ \sin \theta_g e^{-i\phi_g} \end{pmatrix}, \quad (\text{III.30})$$

where the gauge freedom angles (θ_g, ϕ_g) can be chosen at will at any point in parameter space \mathbf{x} . For the particular gauge choice $\cos \theta_g = 1$ and $\sin \theta_g = 0$, one exactly recovers Eq. (2.35).

More generally, each N -band eigenstate $|\psi_\alpha\rangle$ in an arbitrary gauge may be obtained from Eq. (3.31), where $|\psi_g\rangle$ can be chosen arbitrarily. The only constraint is that the state $|\psi_g\rangle$ must not be orthogonal to the projector $P_\alpha(\mathbf{x})$, that is, one requires $P_\alpha(\mathbf{x})|\psi_g\rangle \neq 0$ for all \mathbf{x} . This constraint implies that it might be necessary to change $|\psi_g\rangle$ when the parameter \mathbf{x} is varying because it is never guaranteed that a single $|\psi_g\rangle$ (a fixed gauge) is sufficient to describe a given eigenstate $|\psi_\alpha\rangle$ over the entire parameter space.

III.G | Derivation of Eq. (3.32)

Here we detail the steps that allow to find $\mathbf{b}_\alpha(\mathbf{h}, \varepsilon_\alpha)$ from the eigenprojector formula (3.26). The only missing ingredient is $H^n = (\mathbf{h} \cdot \boldsymbol{\lambda})^n$ in terms of the generators of $SU(N)$. Defining vectors $\boldsymbol{\eta}_n \equiv \text{Tr}(H^n \boldsymbol{\lambda})/2$, we can write:

$$H^n = (\mathbf{h} \cdot \boldsymbol{\lambda})^n = \frac{C_n}{N} 1_N + \boldsymbol{\eta}_n \cdot \boldsymbol{\lambda}, \quad (\text{III.31})$$

where obviously $\boldsymbol{\eta}_0 = 0$ and $\boldsymbol{\eta}_1 = \mathbf{h}$. Here, the C_n are the Casimir invariants from Eq. (3.28), and we defined $\boldsymbol{\eta}_n \equiv \frac{1}{2} \text{Tr}(H^n \boldsymbol{\lambda})$. Inserting into Eq. (3.26) and using Eq. (2.50), we obtain the intermediate result:

$$\mathbf{b}_\alpha = 2 \frac{\sum_{n=0}^{N-1} q_{N-1-n}(\varepsilon_\alpha) \boldsymbol{\eta}_n}{\sum_{n=0}^{N-1} q_{N-1-n}(\varepsilon_\alpha) \varepsilon_\alpha^n}. \quad (\text{III.32})$$

At this point it remains the task to find the explicit form of the vectors $\boldsymbol{\eta}_n(\mathbf{h})$ for $n > 1$. To accomplish this task, we need to compute $H^n = (\mathbf{h} \cdot \boldsymbol{\lambda})^n$ by applying Eq. (2.32) repeatedly. In the course of this, it proves useful to employ the notation (2.33) for repeated star products of a vector with itself. The resulting vectors have the following properties (with $n_1, n_2 \in \mathbb{N}_0$):

$$\mathbf{m}_\star^{(n_1)} \cdot \mathbf{m}_\star^{(n_2)} = \left| \mathbf{m}_\star^{\binom{n_1+n_2}{2}} \right|^2, \quad n_1 + n_2 \text{ even}; \quad \mathbf{m}_\star^{(n_1)} \times \mathbf{m}_\star^{(n_2)} = 0 \quad \forall n_1, n_2. \quad (\text{III.33})$$

The former identity follows directly from the total symmetry of the structure constants (2.28), and the latter is a consequence of the second Jacobi identity (III.13), as can be proven by mathematical induction.

With all these prerequisites we may now calculate $(\mathbf{h} \cdot \boldsymbol{\lambda})^n$, that is, determine $C_n(\mathbf{h})$ and $\boldsymbol{\eta}(\mathbf{h})$. In particular, we obtain the following simple recursion relations:

$$C_{n+1} = 2 \mathbf{h} \cdot \boldsymbol{\eta}_n, \quad \boldsymbol{\eta}_{n+1} = \mathbf{h} \star \boldsymbol{\eta}_n + \frac{C_n}{N} \mathbf{h}, \quad (\text{III.34})$$

with initial conditions $C_0 = N$ and $\boldsymbol{\eta}_0 = 0$. Making use of the fact that $\boldsymbol{\eta}_n$ and the structure constants f_{ijk} are real by definition, we can also establish the identity

$$\boldsymbol{\eta}_{n_1} \times \boldsymbol{\eta}_{n_2} = 0, \quad \forall n_1, n_2. \quad (\text{III.35})$$

Applying the recursion (III.34), for a traceless Hamiltonian matrix, we obtain successively up to $n = 4$ the important identities

$$\begin{aligned} C_1 &= 0, & \boldsymbol{\eta}_1 &= \mathbf{h}, \\ C_2 &= 2|\mathbf{h}|^2, & \boldsymbol{\eta}_2 &= \mathbf{h}_\star, \\ C_3 &= 2 \mathbf{h} \cdot \mathbf{h}_\star, & \boldsymbol{\eta}_3 &= \frac{C_2}{N} \mathbf{h} + \mathbf{h}_{\star\star}, \\ C_4 &= \frac{4|\mathbf{h}|^4}{N} + 2|\mathbf{h}_\star|^2, & \boldsymbol{\eta}_4 &= \frac{C_3}{N} \mathbf{h} + \frac{C_2}{N} \mathbf{h}_\star + \mathbf{h}_{\star\star\star}, \\ C_5 &= \frac{8|\mathbf{h}|^2}{N} \mathbf{h} \cdot \mathbf{h}_\star + 2\mathbf{h}_\star \cdot \mathbf{h}_{\star\star}, & \boldsymbol{\eta}_5 &= \dots \end{aligned} \quad (\text{III.36})$$

More generally, for a generic $N > 1$, the form of the vector $\boldsymbol{\eta}_n(\mathbf{h})$ is compactly written as:

$$\boldsymbol{\eta}_n = \frac{1}{N} \sum_{p=0}^{n-1} C_p \mathbf{h}_\star^{(n-1-p)}. \quad (\text{III.37})$$

The final step required for completing our task of finding the explicit expressions of the Bloch vector $\mathbf{b}_\alpha(\mathbf{h}, \varepsilon_\alpha)$ consists in substituting Eqs. (III.36) and (III.37) into Eq. (III.32). One can then write down the explicit Bloch vectors for any N , as done explicitly in Eq. (3.32) for $N = 2$ to $N = 5$.

As a final remark, be aware that, for given N , only $C_{n \leq N}$ and $\boldsymbol{\eta}_{m < N}$ are relevant, and there are only $N - 1$ independent vectors $\mathbf{h}_\star^{(k)}$, $k = 0, \dots, N - 2$. For example, for $N = 3$, all information we need is encoded in C_2 , C_3 , \mathbf{h} and \mathbf{h}_\star . This again follows from the Cayley-Hamilton theorem, which states that $q_{n=N}(H) = p_N(H) = 0$. From this property it is easy to establish the following useful identities for $N = 3$:

$$\mathbf{h}_{\star\star} = \frac{C_2}{6} \mathbf{h}, \quad \mathbf{h}_\star \star \mathbf{h}_\star = \frac{C_3}{3} \mathbf{h} - \frac{C_2}{6} \mathbf{h}_\star, \quad (\text{III.38})$$

and for $N = 4$:

$$\mathbf{h}_{\star\star\star} = \frac{C_3}{12} \mathbf{h} + \frac{C_2}{4} \mathbf{h}_\star, \quad \mathbf{h}_\star \star \mathbf{h}_\star = \frac{C_3}{3} \mathbf{h}, \quad \mathbf{h}_\star \star \mathbf{h}_{\star\star} = \frac{|\mathbf{h}_\star|^2}{2} \mathbf{h} + \frac{C_3}{12} \mathbf{h}_\star. \quad (\text{III.39})$$

III.H | Berry curvature for N -band systems

A Berry curvature formula for arbitrary $SU(N)$ systems can be obtained from inserting Eq. (III.37) into Eq. (III.32), and further inserting the result into Eq. (3.10). To maximally simplify the formula, we require the total antisymmetry of the triple product $\mathbf{m} \cdot (\mathbf{n} \times \mathbf{o}) = f_{ijk} n_i o_j m_k$ and the orthogonality relations (III.33) or (III.35). The general formula then is

$$\Omega_{\alpha,ij} = -\frac{2\mathbf{b}_\alpha}{[q'_N(\varepsilon_\alpha)]^2} \cdot \left(\sum_{n,m=1}^{N-1} q_{N-1-n}(\varepsilon_\alpha) q_{N-1-m}(\varepsilon_\alpha) \boldsymbol{\tau}_n^{(i)} \times \boldsymbol{\tau}_m^{(j)} \right). \quad (\text{III.40})$$

Here we use the Bloch vectors (3.10), the polynomials $q_n(z)$ introduced in Eq. (3.27), and have defined vectors

$$\boldsymbol{\tau}_n^{(i)} \equiv \frac{1}{N} \sum_{p=0}^{n-1} C_p \partial_i \mathbf{h}_\star^{(n-1-p)}. \quad (\text{III.41})$$

With the notation $\mathbf{m}^i \equiv \partial_i \mathbf{m}$, the first few $\boldsymbol{\tau}_n^{(i)}$ read

$$\boldsymbol{\tau}_1^{(i)} = \mathbf{h}^i, \quad \boldsymbol{\tau}_2^{(i)} = \mathbf{h}_\star^i, \quad \boldsymbol{\tau}_3^{(i)} = \frac{C_2}{N} \mathbf{h}^i + \mathbf{h}_{\star\star}^i. \quad (\text{III.42})$$

From Eq. (III.40), one can obtain the Berry curvature for any given N , as we now illustrate.

For $N = 2$, Eq. (2.41) is immediately obtained. For $N = 3$, analogously, we have

$$\Omega_{\alpha,ij} = -\frac{4(\varepsilon_\alpha \mathbf{h} + \mathbf{h}_\star)}{(3\varepsilon_\alpha^2 - \frac{C_2}{2})^3} \cdot [\varepsilon_\alpha^2 \mathbf{h}^i \times \mathbf{h}^j + \varepsilon_\alpha (\mathbf{h}^i \times \mathbf{h}_\star^j + \mathbf{h}_\star^i \times \mathbf{h}^j) + \mathbf{h}_\star^i \times \mathbf{h}_\star^j], \quad (\text{III.43})$$

or equivalently Eq. (3.34) in the main text. This result can be simplified due to the following identities:

$$\begin{aligned} \mathbf{h} \cdot (\mathbf{h}^i \times \mathbf{h}_\star^j) &= \mathbf{h} \cdot (\mathbf{h}_\star^i \times \mathbf{h}^j) = \mathbf{h}_\star \cdot (\mathbf{h}^i \times \mathbf{h}^j), \\ \mathbf{h}_\star \cdot (\mathbf{h}^i \times \mathbf{h}_\star^j) &= \mathbf{h}_\star \cdot (\mathbf{h}_\star^i \times \mathbf{h}^j) = \mathbf{h} \cdot (\mathbf{h}_\star^i \times \mathbf{h}_\star^j), \\ \mathbf{h}_\star \cdot (\mathbf{h}_\star^i \times \mathbf{h}_\star^j) &= \left[-\frac{2}{3} (\mathbf{h} \cdot \mathbf{h}_\star) \mathbf{h} + |\mathbf{h}|^2 \mathbf{h}_\star \right] \cdot (\mathbf{h}^i \times \mathbf{h}^j). \end{aligned} \quad (\text{III.44})$$

The first two lines are valid for general N and can be proved using the second Jacobi identity (III.13). The proof of the third line requires the Jacobi identity as well, but additionally the $SU(3)$ -specific identities (III.38). Inserting all of these identities into Eq. (III.43), and exploiting the characteristic equation $\varepsilon_\alpha^3 = \frac{C_2}{2} \varepsilon_\alpha + \frac{C_3}{3}$, one obtains the generic $SU(3)$ Berry curvature formula

$$\begin{aligned} \Omega_{\alpha,ij} &= \frac{-4}{(3\varepsilon_\alpha^2 - |\mathbf{h}|^2)^3} \left\{ \varepsilon_\alpha [|\mathbf{h}|^2 \mathbf{h} \cdot (\mathbf{h}^i \times \mathbf{h}^j) + 3 \mathbf{h} \cdot (\mathbf{h}_\star^i \times \mathbf{h}_\star^j)] \right. \\ &\quad \left. + (3\varepsilon_\alpha^2 + |\mathbf{h}|^2) \mathbf{h}_\star \cdot (\mathbf{h}^i \times \mathbf{h}^j) \right\}. \end{aligned} \quad (\text{III.45})$$

The advantage of this formula, as compared to Eq. (3.34), consists in the fact that it contains only three terms, and that the Berry curvature sum rule $\sum_{\alpha} \Omega_{\alpha,ij} = 0$ is more evident.

In principle, one can continue in this way to obtain the Berry curvature for any N . As a shortcut, it is however useful to realize that, when the Bloch vectors (3.32) are substituted into Eq. (3.10), the derivatives effectively do not act on the prefactors but only on the vectors \mathbf{h} , \mathbf{h}_{\star} , etc. This is due to the orthogonality relations (III.33) and (III.35). For example, for the $N = 2$ case, it suffices to replace $\mathbf{b}_{\alpha}^i \rightarrow \frac{1}{\varepsilon_{\alpha}} \mathbf{h}^i$ in Eq. (3.10), which allows to directly read off the Berry curvature: $\Omega_{\alpha,ij} = -\frac{1}{2} \frac{\mathbf{h}}{\varepsilon_{\alpha}} \cdot \left(\frac{\mathbf{h}^i}{\varepsilon_{\alpha}} \times \frac{\mathbf{h}^j}{\varepsilon_{\alpha}} \right)$. Similarly, for $N = 3$, it suffices to replace $\mathbf{b}_{\alpha}^i \rightarrow \frac{2}{3\varepsilon_{\alpha}^2 - C_2/2} (\varepsilon_{\alpha} \mathbf{h}^i + \mathbf{h}_{\star}^i)$, and so on for higher N . In this way, one directly obtains Eqs. (3.34)–(3.36) in the main text.

Appendix IV

IV.A | Relation between CLSs and real-space tight-binding models

In order to determine the real-space tight-binding model corresponding to the Bloch Hamiltonian $H(\mathbf{k})$ built from some input CLS, we write the off-diagonal matrix elements ($a \neq b$) as

$$H_{ab}(\mathbf{k}) = \sum_n t_n^{ab} e^{i\mathbf{k} \cdot \mathbf{r}_n^{ab}}, \quad (\text{IV.1})$$

where \mathbf{r}_n^{ab} denotes the possible hopping directions (distinguished by the label n) from an orbital of type b towards orbitals of type a , and t_n^{ab} denotes the corresponding hopping parameters. Similarly, we write the diagonal matrix elements as

$$H_{aa}(\mathbf{k}) = V_a + \sum_n t_n^{aa} e^{i\mathbf{k} \cdot \mathbf{r}_n^{aa}}, \quad (\text{IV.2})$$

where V_a is the onsite energy, \mathbf{r}_n^{aa} denotes the possible hopping directions from an orbital of type a towards other orbitals of type a , and t_n^{aa} are the corresponding hopping parameters. Clearly, the expressions for the hopping directions, hopping parameters and onsite energies depend on whether the Bloch Hamiltonian is quadratic or linear, as described in the following.

For the quadratic flat-band models described by Eq. (4.43), the off-diagonal and diagonal matrix elements (4.44) read

$$\begin{aligned} H_{ab}(\mathbf{k}) &= -\lambda_{ab} \sum_{i,j \in \text{CLS}} w_{a_i} w_{b_j}^* e^{i\mathbf{k} \cdot (\delta_{a_i} - \delta_{b_j})}, \\ H_{aa}(\mathbf{k}) &= \sum_{b \neq a} \lambda_{ab} \sum_{i,j \in \text{CLS}} w_{b_i} w_{b_j}^* e^{i\mathbf{k} \cdot (\delta_{b_i} - \delta_{b_j})}, \end{aligned} \quad (\text{IV.3})$$

respectively, where Eq. (4.7) was used. Comparing this with Eqs. (IV.1) and (IV.2), we find that the possible hopping directions \mathbf{r}_n^{ab} are given by all vectors that connect orbitals b to orbitals a inside the CLS. Similarly, the hopping directions \mathbf{r}_n^{aa} are given by all vectors that connect orbitals $b \neq a$ to other orbitals b inside the CLS. This is well visible in Figs. 4.4 and 4.5. In other words, the position of the localization center is *irrelevant*, cf. Fig. IV.1(a). This is exactly why any CLS will give rise to a reasonable quadratic flat-band model. The relative distance between any two orbitals is automatically compatible with the underlying lattice. For the quadratic flat-band models, the hopping parameters as well as onsite energies are functions both of the CLS amplitudes and of the parameters λ_{ab} .

For the linear flat-band models described by Eq. (4.83), the exact form of the matrix elements depends on the input CLS. However, since all matrix elements are linear in $f_a(\mathbf{k})$, it is clear from Eq. (4.7) that they always contain phase factors of the

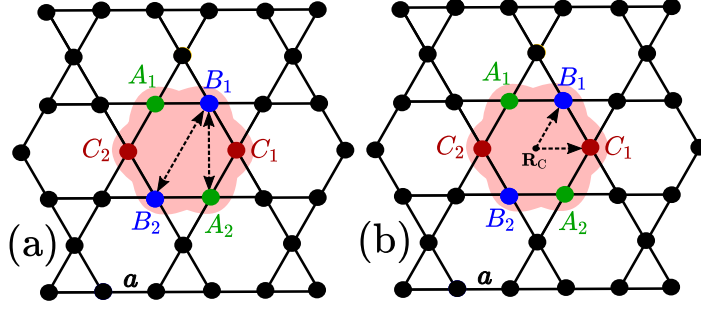


Fig. IV.1 – (a) For quadratic flat-band models, only the relative distance between each pair of orbitals within the CLS is relevant. (b) For linear flat-band models, only the position of each orbital with respect to the localization center is relevant.

form $\exp[i\mathbf{k} \cdot \boldsymbol{\delta}_{a_i}]$. Generically, the hopping directions \mathbf{r}_n^{ab} are given by the positions of some orbitals of a *third kind* $c \neq a, b$ with respect to the localization center. This is well visible in Figs. 4.8–4.11. Thus, for linear flat-band models, the position of the localization center is *very important*, cf. Fig. IV.1(b). This is why linear flat-band models can only be built from CLSs that fulfill certain compatibility relations with the underlying lattice. For the linear flat-band models, all onsite energies are zero. The hopping parameters are functions both of the CLS amplitudes and of the parameters λ_{abc} .

IV.B | Two-band Hamiltonian with a flat band

To find a 2×2 matrix $H(\mathbf{k})$ with a (unnormalized) flat-band eigenstate $|f(\mathbf{k})\rangle$, we may first assume that $|f(\mathbf{k})\rangle$ is such an eigenstate. Evidently, this uniquely determines the corresponding eigenprojector

$$P_0(\mathbf{k}) = \frac{|f(\mathbf{k})\rangle \langle f(\mathbf{k})|}{\langle f(\mathbf{k})|f(\mathbf{k})\rangle} = \frac{1}{|f_A|^2 + |f_B|^2} \begin{pmatrix} |f_A|^2 & f_A f_B^* \\ f_A^* f_B & |f_B|^2 \end{pmatrix}, \quad (\text{IV.4})$$

but, crucially, it also fixes the orthogonal eigenprojector

$$P_1(\mathbf{k}) = 1_2 - P_0(\mathbf{k}) = \frac{1}{|f_A|^2 + |f_B|^2} \begin{pmatrix} |f_B|^2 & -f_A f_B^* \\ -f_A^* f_B & |f_A|^2 \end{pmatrix}. \quad (\text{IV.5})$$

This latter property is unique to the two-band case. According to the spectral theorem, the desired flat-band Hamiltonian now necessarily takes the form

$$H(\mathbf{k}) = \epsilon_0 P_0(\mathbf{k}) + \epsilon_1(\mathbf{k}) P_1(\mathbf{k}) = \epsilon_0 1_2 + (\epsilon_1(\mathbf{k}) - \epsilon_0) P_1(\mathbf{k}), \quad (\text{IV.6})$$

with the flat-band energy ϵ_0 . Without loss of generality, we may now take $\epsilon_0 = 0$, such that Eq. (IV.6) turns into Eq. (4.25) of the main text. In summary, *all two-band models with a flat band* are of the form (4.25).

IV.C | Band touching scenarios for the quadratic three-band Hamiltonian

Consider the three-band Hamiltonian (4.35) with band structure (4.36). For any given point \mathbf{k}_0 in the Brillouin zone, one can distinguish four possibilities for the behavior of $|f(\mathbf{k}_0)\rangle$:

- (1) If $|f(\mathbf{k}_0)\rangle = 0$, there is a threefold (singular) band touching point.
- (2) If two out of the three components of $|f(\mathbf{k}_0)\rangle$ vanish (say $f_B(\mathbf{k}_0) = f_C(\mathbf{k}_0) = 0$ for concreteness), the local Bloch Hamiltonian becomes diagonal with eigenenergies $\epsilon_0(\mathbf{k}_0) = 0$, $\epsilon_1(\mathbf{k}_0) = \lambda_{AB}|f_A(\mathbf{k}_0)|^2$, $\epsilon_2(\mathbf{k}_0) = \lambda_{AC}|f_A(\mathbf{k}_0)|^2$. At the point \mathbf{k}_0 , the degeneracy of the band touching can now be controlled by the parameters λ_{ab} . If λ_{AB} and λ_{AC} are non-zero, the flat band is fully gapped. If $\lambda_{AB} = 0$ or $\lambda_{AC} = 0$, there is a twofold touching. If $\lambda_{AB} = \lambda_{AC} = 0$, there is a threefold touching, however this possibility should be ignored since the flat band would be trivially decoupled.
- (3) If one out of the three components of $|f(\mathbf{k}_0)\rangle$ vanishes (say $f_C(\mathbf{k}_0) = 0$ for concreteness), the degeneracy of the band touching point is again tunable by the λ_{ab} . For most values of the λ_{ab} , all bands will be gapped from each other at \mathbf{k}_0 , but choosing $\lambda_{AB} = 0$ leads to $\epsilon_0(\mathbf{k}_0) = \epsilon_2(\mathbf{k}_0) = 0$, $\epsilon_1(\mathbf{k}_0) = \lambda_{AC}|f_A(\mathbf{k}_0)|^2 + \lambda_{BC}|f_B(\mathbf{k}_0)|^2$, and choosing $\lambda_{AC}|f_A(\mathbf{k}_0)|^2 + \lambda_{BC}|f_B(\mathbf{k}_0)|^2 = 0$ similarly leads to $\epsilon_0(\mathbf{k}_0) = \epsilon_2(\mathbf{k}_0) = 0$, $\epsilon_1(\mathbf{k}_0) = \lambda_{AB}(|f_A(\mathbf{k}_0)|^2 + |f_B(\mathbf{k}_0)|^2)$. By a proper choice of the λ_{ab} , one can thus obtain a twofold touching and even a threefold touching *without* trivially decoupling the flat band.
- (4) If none of the components of $|f(\mathbf{k}_0)\rangle$ vanish, a threefold touching is impossible, but a twofold touching can be achieved by $\lambda_{AB}\lambda_{AC}|f_A(\mathbf{k}_0)|^2 + \lambda_{AB}\lambda_{BC}|f_B(\mathbf{k}_0)|^2 + \lambda_{AC}\lambda_{BC}|f_C(\mathbf{k}_0)|^2 = 0$.

In summary, the band structure of the Hamiltonian (4.35) can exhibit a gapped flat band, a twofold or a threefold band touching point, depending on the interplay between the BCLS $|f(\mathbf{k})\rangle$ and the parameters λ_{ab} .

IV.D | Examples for three-dimensional flat-band models

Quadratic case

Quadratic flat-band models can be built from any CLS on any d -dimensional lattice. For example, consider the CLS on the simple 3D cubic lattice shown in Fig. IV.2(a). The corresponding BCLS reads

$$|f(\mathbf{k})\rangle = \begin{pmatrix} w_{A_1} e^{-\frac{i}{2}(k_x+k_y+k_z)} + w_{A_2} e^{\frac{i}{2}(k_x+k_y+k_z)} \\ w_{B_1} e^{-\frac{i}{2}(k_x-k_y+k_z)} + w_{B_2} e^{\frac{i}{2}(k_x-k_y+k_z)} \\ w_{C_1} e^{\frac{i}{2}(k_x-k_y-k_z)} + w_{C_2} e^{-\frac{i}{2}(k_x-k_y-k_z)} \\ w_{D_1} e^{\frac{i}{2}(k_x+k_y-k_z)} + w_{D_2} e^{-\frac{i}{2}(k_x+k_y-k_z)} \end{pmatrix}. \quad (\text{IV.7})$$

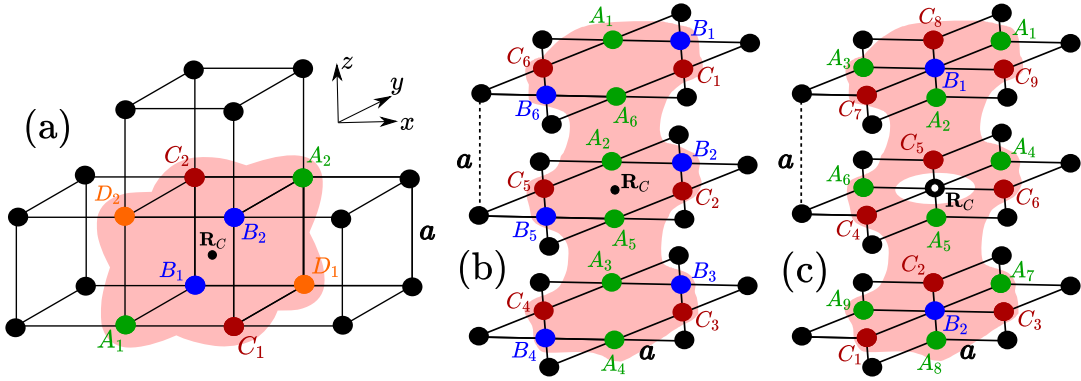


Fig. IV.2 – (a) A CLS on an $N = 4$ cubic lattice. (b) A CLS on the 3D-stacked Kagome lattice that is type \mathcal{B}_I if the amplitudes are properly correlated. (c) A CLS on the 3D-stacked dice lattice that is type \mathcal{B}_{II} if the amplitudes are properly correlated.

Inserting into Eq. (4.43), one obtains a flat-band tight-binding model tunable by the CLS amplitudes and six parameters λ_{ab} .

Linear case

The simplest linear flat-band models on a 3D lattice are three-band models. A type \mathcal{A}_I CLS can be easily found on any lattice. A type \mathcal{A}_{II} CLS can be easily constructed for example on a 3D cubic lattice. Finding CP-CLSs is more difficult, but a simple way consists in forming a 3D lattice by stacking up appropriate 2D lattices. Importantly, the localization center must be chosen within one of the 2D layers. For example, a \mathcal{B}_I -CLS can be found on the 3D-stacked Kagome lattice, see Fig. IV.2(b), where $w_{a_{i+3}} = -w_{a_i} \in \mathbb{R}$. The corresponding BCLS reads $|f(\mathbf{k})\rangle = |o^{ABC}\rangle = (f_A, f_B, f_C)$, where

$$\begin{aligned} f_A &= -2i[w_{A_1} \sin(k_- - k_z) + w_{A_2} \sin k_- + w_{A_3} \sin(k_- + k_z)], \\ f_B &= 2i[w_{B_1} \sin(k_+ + k_z) + w_{B_2} \sin k_+ + w_{B_3} \sin(k_+ - k_z)], \\ f_C &= 2i[w_{C_1} \sin(k_x + k_z) + w_{C_2} \sin k_x + w_{C_3} \sin(k_x - k_z)]. \end{aligned} \quad (\text{IV.8})$$

Inserting into Eq. (4.71), one obtains a linear 3D flat-band tight-binding model. Similarly, a \mathcal{B}_{II} -CLS can be found on the 3D dice lattice, see Fig. IV.2(c), where $w_{B_1} = w_{B_2} \in \mathbb{R}$ and $w_{C_i} = -w_{A_i}$. The corresponding BCLS reads $|f(\mathbf{k})\rangle = |q_B^{ABC}\rangle = (f_A, f_B, -f_A^*)$, where

$$\begin{aligned} f_A &= w_{A_1} e^{i(k_+ + k_z)} + w_{A_2} e^{i(k_- + k_z)} + w_{A_3} e^{-i(k_x - k_z)} + w_{A_4} e^{ik_+} + w_{A_5} e^{ik_-} \\ &\quad + w_{A_6} e^{-ik_x} + w_{A_7} e^{i(k_+ - k_z)} + w_{A_8} e^{i(k_- - k_z)} + w_{A_9} e^{-i(k_x + k_z)}, \\ f_B &= 2w_{B_1} \cos k_z. \end{aligned}$$

Inserting into Eq. (4.78), one obtains another linear 3D flat-band model.

Appendix V

V.A | Continuum model construction via pseudomolecule

Consider an $SU(N)$ Hamiltonian matrix (2.24) with matrix elements $H_{jk} \equiv z_{jk}e^{i\phi_{jk}}$. This representation in terms of magnitude $z_{jk} = z_{kj}$ and phase $\phi_{jk} = -\phi_{kj}$ allows for a convenient mapping to a pseudomolecule, see Fig. V.1. Each corner of the molecule represents a diagonal matrix element, and each directed link represents a complex off-diagonal matrix element. We can now make use of this to design Hamiltonians with a desired spectrum. Namely, the key idea is that any Casimir invariant $C_n = \text{Tr}(H^n)$ can be interpreted as *the sum of all possible closed paths of length n on the molecule*. Since the set $\{C_n, n \leq N\}$ uniquely determines the characteristic polynomial (see Appendix III.D), the spectrum can be understood from and controlled by these closed paths.

Specifically, we will be interested in zero-diagonal Hamiltonians with $H_{jj} = 0$, such that $C_1 = 0$ always. Accordingly, for $N = 2$, we have only one relevant Casimir invariant $C_2 = 2z_{AB}^2$, as is clear from Fig. V.1(a). For $N = 3$, one has two Casimir invariants of interest:

$$C_2 = 2(z_{AB}^2 + z_{BC}^2 + z_{CA}^2), \quad C_3 = 6z_{AB}z_{BC}z_{CA} \cos \Phi_{ABC}, \quad (\text{V.1})$$

where $\Phi_{ABC} \equiv \phi_{AB} + \phi_{BC} + \phi_{CA}$. Pictorially, C_2 corresponds to the three possible “back-and-forth” paths along the rim of the triangle in Fig. V.1(b), while C_3 captures the closed paths of length three, and thus Φ_{ABC} can be viewed as pseudoflux piercing

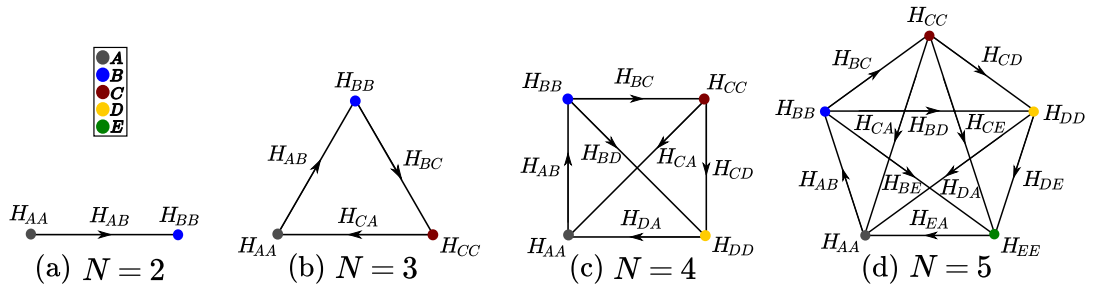


Fig. V.1 – An $N \times N$ Hamiltonian matrix mapped to a pseudomolecule. Links (dots) represent complex (real) off-diagonal (diagonal) matrix elements.

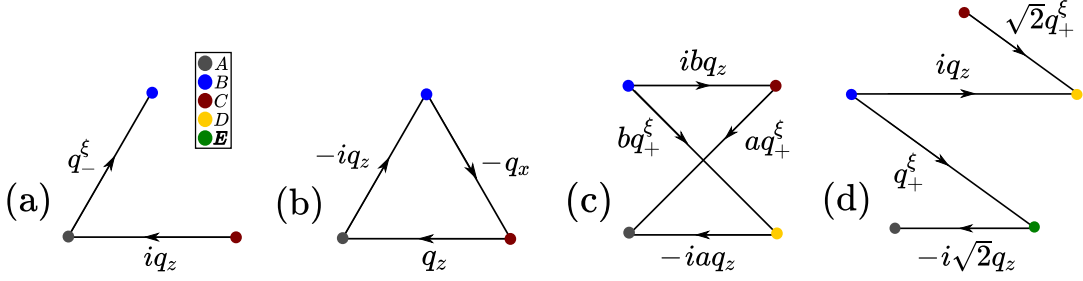


Fig. V.2 – Diagrammatic representation of (a) the threefold Hopf semimetal (5.4a). (b) a pseudospin-1 Hamiltonian. (c) the fourfold Hopf semimetal (5.4b). (d) the fivefold Hopf semimetal (5.4c)

the triangle. For $N = 4$, one has three relevant Casimir invariants

$$\begin{aligned}
C_2 &= 2(z_{AB}^2 + z_{AC}^2 + z_{AD}^2 + z_{BC}^2 + z_{BD}^2 + z_{CD}^2), \\
C_3 &= 6(z_{AB}z_{BC}z_{CA} \cos \Phi_{ABC} + z_{AB}z_{BD}z_{DA} \cos \Phi_{ABD} \\
&\quad + z_{AC}z_{CD}z_{DA} \cos \Phi_{ACD} + z_{BC}z_{CD}z_{DB} \cos \Phi_{BCD}), \\
C_4 &= C_2^2/2 - 4(z_{AB}^2z_{CD}^2 + z_{DA}^2z_{BC}^2 + z_{AC}^2z_{BD}^2) \\
&\quad + 8(z_{AB}z_{BC}z_{CD}z_{DA} \cos \Phi_{ABCD} + z_{DC}z_{CA}z_{AB}z_{BD} \cos \Phi_{DCAB} \\
&\quad + z_{CA}z_{AD}z_{DB}z_{BC} \cos \Phi_{CADB}),
\end{aligned} \tag{V.2}$$

where $\Phi_{jkl} \equiv \phi_{jk} + \phi_{kl} + \phi_{lj}$ is odd (even) under odd (even) index permutations, and where $\Phi_{jklm} \equiv \Phi_{jkm} + \Phi_{klm}$. Pictorially, the four interference terms in C_3 stem from the four triangles in Fig. V.1(c), and the three interference terms in C_4 from the three different four-link loops. Similarly, for $N = 5$, one has Casimir invariants C_2, C_3, C_4, C_5 determined by all single links, triangles, quadrangles, and pentagons of the diagram in Fig. V.1(d), respectively.

Now, multifold fermion models with a particle-hole symmetric spectrum can be easily designed by choosing matrix elements H_{jk} such that the C_n with n odd vanish. For $N = 3$ it suffices to choose the matrix elements H_{jk} such that $C_3 = 0$, which can be achieved, according to Eq. (V.1), either by eliminating one link of the triangle or by adjusting the pseudoflux Φ_{ABC} such that the cosine vanishes. The former case will give rise to a model with chiral symmetry, while the latter can give rise to a model with CP symmetry. For example, the threefold MHS model (5.4a) is visualized in Fig. V.2(a), while the pseudospin-1 Hamiltonian obtained from Eq. (4.92) with $\mathbf{v}_A = (1, 0, 0)$, $\mathbf{v}_B = (0, 1, 0)$, $\mathbf{v}_C = (0, 0, i)$ is shown in Fig. V.2(b). Similarly, to construct an $N = 4$ ($N = 5$) model with particle-hole symmetric spectrum, we have to make sure that we choose a Hamiltonian such that the corresponding pseudomolecule verifies $C_3 = 0$ ($C_3 = C_5 = 0$). In Fig. V.2(c) we show the fourfold Hopf semimetal (5.4b), where obviously $C_3 = 0$ since there are no triangles. In Fig. V.2(d) we show the fivefold Hopf semimetal (5.4c), where $C_3 = 0$ and $C_5 = 0$ since there are neither triangles nor pentagons.

Having ensured particle-hole symmetry of the spectrum, we can further use the pseudomolecule approach to design the isotropy of the spectrum. For $N = 3$ this is straightforward as it only requires C_2 to be isotropic. This is obviously the case for both models in Fig. V.2(a) and (b). For $N = 4$ and $N = 5$ we need to make sure

that both C_2 and C_4 are isotropic. This is non-trivial but one can verify that it is the case for both models in Fig. V.2(c) and (d).

V.B | Landau levels of multifold Hopf semimetals

Using the conventions introduced in Section 5.3.2, we here derive in detail the Landau levels (LLs) of the continuum models (5.4). The main tool to simplify the calculations is to make use of the chiral symmetry.

Threefold Hopf semimetal

The LL spectrum of the threefold Hopf semimetal (5.4a) is easily computed analytically. Replacing $q_i \rightarrow \Pi_i$, we have

$$\hat{H}_3^\xi = \begin{pmatrix} 0 & Q \\ Q^\dagger & 0_2 \end{pmatrix}, \quad Q = \begin{pmatrix} \Pi_-^\xi & -i\Pi_z \end{pmatrix}. \quad (\text{V.3})$$

Making an ansatz $\hat{H}_3^\xi \Psi_\alpha = \epsilon_\alpha \Psi_\alpha$, where $\epsilon_\alpha = \alpha\epsilon$, $\alpha = 0, \pm$ and $\Psi_\alpha = (\psi_1^\alpha, \Psi_2^\alpha)$ with Ψ_2^α a two-component spinor, it follows

$$\epsilon_\alpha \psi_1^\alpha = Q \Psi_2^\alpha, \quad \epsilon_\alpha \Psi_2^\alpha = Q^\dagger \psi_1^\alpha, \quad \epsilon_\alpha^2 \psi_1^\alpha = Q Q^\dagger \psi_1^\alpha. \quad (\text{V.4})$$

Using $\Pi_-^\xi \Pi_+^\xi = \Pi_x^2 + \Pi_y^2 + \xi \cos \theta / l_B^2$ and $\Pi^2 = (2\hat{d}^\dagger \hat{d} + 1) / l_B^2 + q_0^2$, one easily finds

$$Q Q^\dagger = [eB(2\hat{d}^\dagger \hat{d} + 1 + \xi \cos \theta) + q_0^2], \quad (\text{V.5})$$

implying that $\psi_1^\alpha \sim |n\rangle$. From the second identity of Eq. (V.4), one immediately obtains

$$\epsilon_\alpha \Psi_2^\alpha \sim \begin{pmatrix} \xi - \cos \theta & i \sin \theta q_0 & \xi + \cos \theta \\ \sin \theta & i \cos \theta q_0 & -\sin \theta \end{pmatrix} \begin{pmatrix} \beta_n |n-1\rangle \\ |n\rangle \\ \beta_{n+1} |n+1\rangle \end{pmatrix}, \quad (\text{V.6})$$

where $\beta_n = \sqrt{eBn/2}$, and finally the full solution for the LLs and their corresponding eigenstates reads as

$$\begin{aligned} \epsilon_\alpha^{n,\xi} &= \alpha \sqrt{2eB \left(n + \frac{1 + \xi \cos \theta}{2} \right) + q_0^2}, \quad n = 0, 1, 2, \dots \\ \Psi_\alpha^{n,\xi} &\sim \begin{pmatrix} 0 & \epsilon_\alpha^{n,\xi} & 0 \\ \xi - \cos \theta & i \sin \theta q_0 & \xi + \cos \theta \\ \sin \theta & i \cos \theta q_0 & -\sin \theta \end{pmatrix} \begin{pmatrix} \beta_n |n-1\rangle \\ |n\rangle \\ \beta_{n+1} |n+1\rangle \end{pmatrix}. \end{aligned} \quad (\text{V.7})$$

Fourfold Hopf semimetal

We proceed to compute the LL spectrum of the fourfold Hopf semimetal (5.4b). Replacing $q_i \rightarrow \Pi_i$, we have

$$\hat{H}_4^\xi = \begin{pmatrix} 0_2 & Q \\ Q^\dagger & 0_2 \end{pmatrix}, \quad Q = \begin{pmatrix} a\Pi_+^\xi & ia\Pi_z \\ ib\Pi_z & b\Pi_+^\xi \end{pmatrix}. \quad (\text{V.8})$$

We make an ansatz $\hat{H}_4^\xi \Psi_\alpha = \epsilon_\alpha \Psi_\alpha$, where $\epsilon_\alpha = \alpha_1 \epsilon_{\alpha_2}$ with $\alpha_1 = \pm$, $\alpha_2 = \pm$, and where $\Psi_\alpha = (\Psi_1^\alpha, \Psi_2^\alpha)$ with Ψ_1^α and Ψ_2^α being two-component spinors. It follows

$$\epsilon_\alpha \Psi_1^\alpha = Q \Psi_2^\alpha, \quad \epsilon_\alpha \Psi_2^\alpha = Q^\dagger \Psi_1^\alpha, \quad \epsilon_\alpha^2 \Psi_1^\alpha = Q Q^\dagger \Psi_1^\alpha. \quad (\text{V.9})$$

We first focus on the last identity. Straightforward computation yields

$$Q Q^\dagger = \begin{pmatrix} a^2[eB(2\hat{d}^\dagger \hat{d} + 1 + \xi \cos \theta) + q_0^2] & \xi abeB \sin \theta \\ \xi abeB \sin \theta & b^2[eB(2\hat{d}^\dagger \hat{d} + 1 - \xi \cos \theta) + q_0^2] \end{pmatrix},$$

and it is clear that $\Psi_1^\alpha \sim (u_{\alpha_2}, v_{\alpha_2}) |n\rangle$. Solving the eigenvalue problem

$$\begin{pmatrix} 2\eta_a & \nu \\ \nu & 2\eta_b \end{pmatrix} \begin{pmatrix} u_{\alpha_2} \\ v_{\alpha_2} \end{pmatrix} = \epsilon_\alpha^2 \begin{pmatrix} u_{\alpha_2} \\ v_{\alpha_2} \end{pmatrix}, \quad (\text{V.10})$$

where

$$\begin{aligned} \eta_a &= \frac{a^2}{2} \left[2eB \left(n + \frac{1 + \xi \cos \theta}{2} \right) + q_0^2 \right], \\ \eta_b &= \frac{b^2}{2} \left[2eB \left(n + \frac{1 - \xi \cos \theta}{2} \right) + q_0^2 \right], \\ \nu &= \xi abeB \sin \theta, \end{aligned} \quad (\text{V.11})$$

leads to

$$\begin{aligned} \epsilon_\alpha^2 &= \eta_a + \eta_b + \alpha_2 \sqrt{(\eta_a - \eta_b)^2 + \nu^2}, \\ u_{\alpha_2} &= \eta_a - \eta_b + \alpha_2 \sqrt{(\eta_a - \eta_b)^2 + \nu^2}, \\ v_{\alpha_2} &= \nu. \end{aligned} \quad (\text{V.12})$$

Turning now to the second identity of Eq. (V.9), we have

$$\epsilon_\alpha \Psi_2^\alpha \sim \begin{pmatrix} a\Pi_+^\xi & -ib\Pi_z \\ -ia\Pi_z & b\Pi_-^\xi \end{pmatrix} \begin{pmatrix} u_{\alpha_2} |n\rangle \\ v_{\alpha_2} |n\rangle \end{pmatrix} = M_1 \begin{pmatrix} u_{\alpha_2} \beta_n |n-1\rangle \\ v_{\alpha_2} \beta_n |n-1\rangle \\ u_{\alpha_2} |n\rangle \\ v_{\alpha_2} |n\rangle \\ u_{\alpha_2} \beta_{n+1} |n+1\rangle \\ v_{\alpha_2} \beta_{n+1} |n+1\rangle \end{pmatrix}$$

$$M_1 = \begin{pmatrix} a(\xi - \cos \theta) & -b \sin \theta & ia \sin \theta q_0 & -ib \cos \theta q_0 & a(\xi + \cos \theta) & b \sin \theta \\ -a \sin \theta & b(\xi + \cos \theta) & -ia \cos \theta q_0 & -ib \sin \theta q_0 & a \sin \theta & b(\xi - \cos \theta) \end{pmatrix}.$$

Finally, the complete solution for the LLs and their eigenstates is

$$\begin{aligned}
\epsilon_\alpha^{n,\xi} &= \alpha_1 \sqrt{\eta_a + \eta_b + \alpha_2 \sqrt{(\eta_a - \eta_b)^2 + \nu^2}}, \quad n = 0, 1, 2, \dots \\
\Psi_\alpha^{n,\xi} &\sim \begin{pmatrix} 0 & 0 & \epsilon_\alpha^{n,\xi} & 0 & 0 & 0 \\ 0 & 0 & 0 & \epsilon_\alpha^{n,\xi} & 0 & 0 \\ a(\xi - \cos \theta) & -b \sin \theta & ia \sin \theta q_0 & -ib \cos \theta q_0 & a(\xi + \cos \theta) & b \sin \theta \\ -a \sin \theta & b(\xi + \cos \theta) & -ia \cos \theta q_0 & -ib \sin \theta q_0 & a \sin \theta & b(\xi - \cos \theta) \end{pmatrix} \\
&\times \begin{pmatrix} u_{\alpha_2} \beta_n |n-1\rangle \\ v_{\alpha_2} \beta_n |n-1\rangle \\ u_{\alpha_2} |n\rangle \\ v_{\alpha_2} |n\rangle \\ u_{\alpha_2} \beta_{n+1} |n+1\rangle \\ v_{\alpha_2} \beta_{n+1} |n+1\rangle \end{pmatrix}.
\end{aligned} \tag{V.13}$$

Fivefold Hopf semimetal

The LL spectrum of the fivefold Hopf semimetal (5.4c) can be derived from the Hamiltonian

$$\hat{H}_5^\xi = \begin{pmatrix} 0_3 & Q \\ Q^\dagger & 0_2 \end{pmatrix}, \quad Q = \begin{pmatrix} 0 & i\sqrt{2}\Pi_z \\ i\Pi_z & \Pi_+^\xi \\ \sqrt{2}\Pi_+^\xi & 0 \end{pmatrix}. \tag{V.14}$$

We make an ansatz $\hat{H}_5^\xi \Psi_\alpha = \epsilon_\alpha \Psi_\alpha$, where $\epsilon_\alpha = \alpha_1 \epsilon_{\alpha_2}$, $\alpha_1 = 0, \pm$ and $\alpha_2 = \pm$. The wave function is of the form $\Psi_\alpha = (\Psi_1^\alpha, \Psi_2^\alpha)$ with Ψ_1^α a three-component and Ψ_2^α a two-component spinor, respectively. We again have to solve equations of the form

$$\epsilon_\alpha \Psi_1^\alpha = Q \Psi_2^\alpha, \quad \epsilon_\alpha \Psi_2^\alpha = Q^\dagger \Psi_1^\alpha, \quad \epsilon_\alpha^2 \Psi_2^\alpha = Q^\dagger Q \Psi_2^\alpha, \tag{V.15}$$

and thus consider

$$Q^\dagger Q = \begin{pmatrix} 2\Pi_-^\xi \Pi_+^\xi + \Pi_z^2 & -i\Pi_z \Pi_+ \\ (-i\Pi_z \Pi_+)^\dagger & \Pi_-^\xi \Pi_+^\xi + 2\Pi_z^2 \end{pmatrix}, \tag{V.16}$$

where

$$\begin{aligned}
2\Pi_-^\xi \Pi_+^\xi + \Pi_z^2 &= \frac{eB}{2} s_\theta^2 (\hat{d})^2 + \frac{eB}{2} s_\theta^2 (\hat{d}^\dagger)^2 + eB(3 + c_\theta^2) \hat{d}^\dagger \hat{d} \\
&\quad + \sqrt{\frac{eB}{2}} i q_0 s_{2\theta} \hat{d} - \sqrt{\frac{eB}{2}} i q_0 s_{2\theta} \hat{d}^\dagger \\
&\quad + \frac{eB}{2} (3 + c_\theta^2 + 4\xi c_\theta) + (1 + s_\theta^2) q_0^2, \\
-i\Pi_z \Pi_+ &= \frac{eB}{2} s_\theta (c_\theta - \xi) (\hat{d})^2 + \frac{eB}{2} s_\theta (\xi + c_\theta) (\hat{d}^\dagger)^2 - \frac{eB}{2} s_{2\theta} \hat{d}^\dagger \hat{d} \\
&\quad + \sqrt{\frac{eB}{2}} i q_0 (c_{2\theta} - \xi c_\theta) \hat{d} - \sqrt{\frac{eB}{2}} i q_0 (c_{2\theta} + \xi c_\theta) \hat{d}^\dagger \\
&\quad - \frac{eB}{2} s_\theta (\xi + c_\theta) + s_\theta c_\theta q_0^2, \\
\Pi_-^\xi \Pi_+^\xi + 2\Pi_z^2 &= -\frac{eB}{2} s_\theta^2 (\hat{d})^2 - \frac{eB}{2} s_\theta^2 (\hat{d}^\dagger)^2 + eB(2 + s_\theta^2) \hat{d}^\dagger \hat{d} \\
&\quad - \sqrt{\frac{eB}{2}} i q_0 s_{2\theta} \hat{d} + \sqrt{\frac{eB}{2}} i q_0 s_{2\theta} \hat{d}^\dagger \\
&\quad + \frac{eB}{2} (2 + s_\theta^2 + 2\xi c_\theta) + (1 + c_\theta^2) q_0^2.
\end{aligned}$$

Using an ansatz

$$\Psi_2^\alpha = \begin{pmatrix} U \\ V \end{pmatrix} = \begin{pmatrix} u_1 |n-1\rangle + u_2 |n\rangle + u_3 |n+1\rangle \\ v_1 |n-1\rangle + v_2 |n\rangle + v_3 |n+1\rangle \end{pmatrix},$$

a lengthy calculation yields

$$\begin{aligned}
(2\Pi_-^\xi \Pi_+^\xi + \Pi_z^2)U &= M_U^T N^T, \\
-i\Pi_z \Pi_+^\xi V &= M_V^T N^T,
\end{aligned}$$

where $N = (|n-3\rangle, |n-2\rangle, |n-1\rangle, |n\rangle, |n+1\rangle, |n+2\rangle, |n+3\rangle)$ and with

$$M_U = \begin{pmatrix} s_\theta^2 \beta_{n-1} \beta_{n-2} u_1 \\ \beta_{n-1} [s_{2\theta} i q_0 u_1 + s_\theta^2 \beta_n u_2] \\ \beta_n [s_{2\theta} i q_0 u_2 + s_\theta^2 \beta_{n+1} u_3] + eB [(3 + c_\theta^2)(n - \frac{1}{2}) + 2\xi c_\theta] u_1 + (1 + s_\theta^2) q_0^2 u_1 \\ s_{2\theta} i q_0 [\beta_{n+1} u_3 - \beta_n u_1] + eB [(3 + c_\theta^2)(n + \frac{1}{2}) + 2\xi c_\theta] u_2 + (1 + s_\theta^2) q_0^2 u_2 \\ \beta_{n+1} [-s_{2\theta} i q_0 u_2 + s_\theta^2 \beta_n u_1] + eB [(3 + c_\theta^2)(n + \frac{3}{2}) + 2\xi c_\theta] u_3 + (1 + s_\theta^2) q_0^2 u_3 \\ \beta_{n+2} [-s_{2\theta} i q_0 u_3 + s_\theta^2 \beta_{n+1} u_2] \\ s_\theta^2 \beta_{n+2} \beta_{n+3} u_3 \end{pmatrix}$$

and

$$M_V = \begin{pmatrix} s_\theta(c_\theta - \xi)\beta_{n-1}\beta_{n-2}v_1 \\ \beta_{n-1}[(c_{2\theta} - \xi c_\theta)iq_0v_1 + s_\theta(c_\theta - \xi)\beta_n v_2] \\ \beta_n[(c_{2\theta} - \xi c_\theta)iq_0v_2 + s_\theta(c_\theta - \xi)\beta_{n+1}v_3] - eBs_\theta \left[(n - \frac{1}{2})c_\theta + \frac{\xi}{2} \right] v_1 + s_\theta c_\theta q_0^2 v_1 \\ iq_0[(c_{2\theta} - \xi c_\theta)\beta_{n+1}v_3 - (c_{2\theta} + \xi c_\theta)\beta_n v_1] - eBs_\theta \left[(n + \frac{1}{2})c_\theta + \frac{\xi}{2} \right] v_2 + s_\theta c_\theta q_0^2 v_2 \\ \beta_{n+1}[-(c_{2\theta} + \xi c_\theta)iq_0v_2 + s_\theta(c_\theta + \xi)\beta_n v_1] - eBs_\theta \left[(n + \frac{3}{2})c_\theta + \frac{\xi}{2} \right] v_3 + s_\theta c_\theta q_0^2 v_3 \\ \beta_{n+2}[-(c_{2\theta} + \xi c_\theta)iq_0v_3 + s_\theta(c_\theta + \xi)\beta_{n+1}v_2] \\ s_\theta(c_\theta + \xi)\beta_{n+2}\beta_{n+3}v_3 \end{pmatrix}.$$

Solving the linear system $(M_U^T + M_V^T)N^T = \epsilon_\alpha^2 U$, one finds the LL spectrum

$$\begin{aligned} \epsilon_\alpha^{n,\xi} &= \alpha_1 \sqrt{\eta_+ + \eta_-} + \alpha_2 \sqrt{(\eta_+ - \eta_-)^2 + \tilde{v}^2}, \quad n = 1, 2, 3, \dots \\ \eta_\pm &= \frac{c_\pm^2}{2} \left[2eB \left(n + \frac{1 - \kappa_\pm \xi \cos \theta}{2} \right) + q_0^2 \right], \\ \tilde{v} &= 2\sqrt{3}\xi eB \sin \theta \end{aligned} \quad , \quad (\text{V.17})$$

where $c_\pm = \sqrt{2}, 1$ are the band velocities of the two cones and $\kappa_\pm = -3, 1$ are the corresponding Berry dipole charges. The corresponding eigenfunctions are very complicated and are not written here explicitly.

V.C | Landau levels of pseudospin- s fermions

The Landau levels (LLs) of pseudospin- s fermions were previously obtained for $s = 1/2$ by Nielsen and Ninomiya (1983), for $s = 1$ by Bradlyn et al. (2016), and for general s by Ezawa (2017). See also the review article by Delplace (2022) for a more general context. The LLs do not depend on the magnetic field direction due to the rotational invariance of the pseudospin continuum Hamiltonian (2.6). Moreover, since the magnetic field breaks parity symmetry, but not charge conjugation symmetry (Ryu et al. 2010), the spectrum is no longer particle-hole symmetric but satisfies $\epsilon_n(q_z) = -\epsilon_n(-q_z)$.

We here derive the LLs for $s = 1/2, 1, 3/2, 2$. To proceed, we replace $\mathbf{q} \rightarrow \Pi = \mathbf{q} + e\mathbf{A}$, with the gauge choice $\mathbf{A} = Bx(0, 1, 0)$ such that $\mathbf{B} = B\mathbf{e}_z$. In this situation, q_z is a conserved quantity. Using the canonical commutation relations, one finds $[\Pi_x, \Pi_y] = -i/l_B^2$, $[\Pi_y, \Pi_z] = [\Pi_z, \Pi_x] = 0$. One can define ladder operators as

$$\hat{d} = \frac{l_B}{\sqrt{2}}(\Pi_x - i\Pi_y), \quad \hat{d}^\dagger = \frac{l_B}{\sqrt{2}}(\Pi_x + i\Pi_y) \quad (\text{V.18})$$

such that $[\hat{d}, \hat{d}^\dagger] = 1$.

Consider first the Hamiltonian of a simple pseudospin-1/2 in the presence of a magnetic field, which reads as

$$\hat{H} = \frac{1}{2} \begin{pmatrix} q_z & \frac{\sqrt{2}}{l_B} \hat{d} \\ \frac{\sqrt{2}}{l_B} \hat{d}^\dagger & -q_z \end{pmatrix}. \quad (\text{V.19})$$

Its eigenstates consist of one chiral LL

$$|\psi^{\text{chir}}\rangle = (0, |0\rangle) \quad (\text{V.20})$$

with energy $\epsilon = -q_z/2$, and a series of nonchiral LLs

$$|\psi_n\rangle = (u_n |n\rangle, v_n |n+1\rangle), \quad (\text{V.21})$$

where $n = 0, 1, 2, \dots$ and with corresponding energies $\epsilon_n = \pm \frac{1}{2} \sqrt{2eB(n+1) + q_z^2}$. The full LL spectrum is shown in Fig. V.3(a). Similarly, the Hamiltonian of a pseudospin-1 is

$$\hat{H} = \begin{pmatrix} q_z & \frac{1}{l_B} \hat{d} & 0 \\ \frac{1}{l_B} \hat{d}^\dagger & 0 & \frac{1}{l_B} \hat{d} \\ 0 & \frac{1}{l_B} \hat{d}^\dagger & -q_z \end{pmatrix}. \quad (\text{V.22})$$

There are now two types of chiral Landau levels, namely

$$|\psi_a^{\text{chir}}\rangle = (0, 0, |0\rangle), \quad |\psi_b^{\text{chir}}\rangle = (0, v_b |0\rangle, w_b |1\rangle), \quad (\text{V.23})$$

with energies $\epsilon_a = -q_z$ and $\epsilon_b = -\frac{1}{2}q_z \pm \frac{1}{2}\sqrt{4eB + q_z^2}$. The nonchiral LLs are of the form

$$|\psi_n\rangle = (u_n |n\rangle, v_n |n+1\rangle, w_n |n+2\rangle) \quad (\text{V.24})$$

and have eigenvalues as obtained from the cubic equation $\epsilon_n^3 - [(2n+3)eB + q_z^2]\epsilon_n + eBq_z^2 = 0$. The LL spectrum of a pseudospin-1 thus takes the form shown in Fig. V.3(b).

For a pseudospin-3/2, the Hamiltonian reads as

$$\hat{H} = \frac{1}{2} \begin{pmatrix} 3q_z & \frac{\sqrt{6}}{l_B} \hat{d} & 0 & 0 \\ \frac{\sqrt{6}}{l_B} \hat{d}^\dagger & q_z & \frac{2\sqrt{2}}{l_B} \hat{d} & 0 \\ 0 & \frac{2\sqrt{2}}{l_B} \hat{d}^\dagger & -q_z & \frac{\sqrt{6}}{l_B} \hat{d} \\ 0 & 0 & \frac{\sqrt{6}}{l_B} \hat{d}^\dagger & -3q_z \end{pmatrix}. \quad (\text{V.25})$$

It admits three types of chiral solutions, namely

$$\begin{aligned} |\psi_a^{\text{chir}}\rangle &= (0, 0, 0, |0\rangle), \\ |\psi_b^{\text{chir}}\rangle &= (0, 0, w_b |0\rangle, x_b |0\rangle), \\ |\psi_c^{\text{chir}}\rangle &= (0, v_c |0\rangle, w_c |1\rangle, x_c |2\rangle), \end{aligned} \quad (\text{V.26})$$

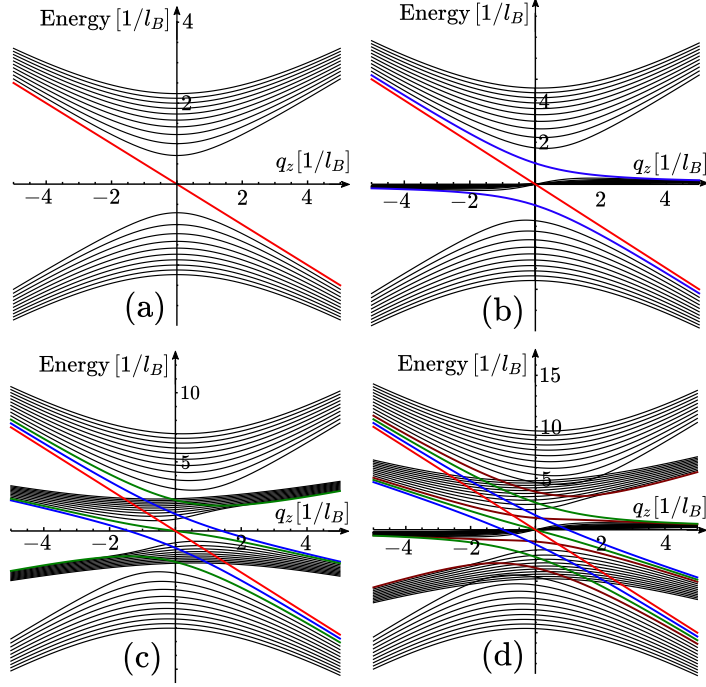


Fig. V.3 – Landau level spectrum of (a) pseudospin-1/2 (b) pseudospin-1 (c) pseudospin-3/2 and (d) pseudospin-2 fermions. Chiral LLs of different types are highlighted by colors.

with $\epsilon_a = -3q_z/2$, $\epsilon_b = -q_z \pm \frac{1}{2}\sqrt{6eB + q_z^2}$, and ϵ_c as determined by $\epsilon_c^3 + \frac{3}{2}q_z\epsilon_c^2 - (5eB + \frac{1}{4}q_z^2)\epsilon_c - \frac{3}{2}q_z(eB + \frac{1}{4}q_z^2) = 0$. The nonchiral LLs are of the form

$$|\psi_n\rangle = (u_n |n\rangle, v_n |n+1\rangle, w_n |n+2\rangle, x_n |n+3\rangle) \quad (\text{V.27})$$

and have energies as determined by the quartic equation $\epsilon_n^4 - 5[(n+2)eB + \frac{1}{2}q_z^2]\epsilon_n^2 + 6eBq_z\epsilon_n + \frac{9}{16}[2eB(n+1) + q_z^2][2eB(n+3) + q_z^2] = 0$. The full LL spectrum of a pseudospin-3/2 thus takes the form shown in Fig. V.3(c). Finally, for a pseudospin-2, the Hamiltonian reads as

$$\hat{H} = \begin{pmatrix} 2q_z & \frac{\sqrt{2}}{l_B}\hat{d} & 0 & 0 & 0 \\ \frac{\sqrt{2}}{l_B}\hat{d}^\dagger & q_z & \frac{\sqrt{3}}{l_B}\hat{d} & 0 & 0 \\ 0 & \frac{\sqrt{3}}{l_B}\hat{d}^\dagger & 0 & \frac{\sqrt{3}}{l_B}\hat{d} & 0 \\ 0 & 0 & \frac{\sqrt{3}}{l_B}\hat{d}^\dagger & -q_z & \frac{\sqrt{2}}{l_B}\hat{d} \\ 0 & 0 & 0 & \frac{\sqrt{2}}{l_B}\hat{d}^\dagger & -2q_z \end{pmatrix}. \quad (\text{V.28})$$

It admits four families of chiral solutions,

$$\begin{aligned} |\psi_a^{\text{chir}}\rangle &= (0, 0, 0, 0, |0\rangle), \\ |\psi_b^{\text{chir}}\rangle &= (0, 0, 0, x_b |0\rangle, y_b |1\rangle), \\ |\psi_c^{\text{chir}}\rangle &= (0, 0, w_c |0\rangle, x_c |1\rangle, y_c |2\rangle), \\ |\psi_d^{\text{chir}}\rangle &= (0, v_d |0\rangle, w_d |1\rangle, x_d |2\rangle, y_d |3\rangle), \end{aligned} \quad (\text{V.29})$$

with corresponding energies $\epsilon_a = -2q_z$ and $\epsilon_b = -\frac{3}{2}q_z \pm \frac{1}{2}\sqrt{8eB + q_z^2}$, as well as ϵ_c given by $\epsilon_c^3 + 3q_z\epsilon_c^2 + (2q_z^2 - 7eB)\epsilon_c - 6eBq_z = 0$ and ϵ_d obtained from $\epsilon_d^4 + 2q_z\epsilon_d^3 - (15eB + q_z^2)\epsilon_d^2 - (9eB + 2q_z^2)q_z\epsilon_d + 6eB(3eB + q_z^2) = 0$. The nonchiral LLs are of the form

$$|\psi_n\rangle = (u_n |n\rangle, v_n |n+1\rangle, w_n |n+2\rangle, x_n |n+3\rangle, y_n |n+4\rangle) \quad (\text{V.30})$$

and have energies as determined by a quintic equation. The full LL spectrum of a pseudospin-2 is shown in Fig. V.3(d).

V.D | Onsager quantization with intraband and interband coupling

Here we derive the Landau level spectrum of the MHS continuum models (5.4) using an alternative method, namely semiclassical quantization based on a generalized Onsager condition. We will find excellent agreement with the exact quantum mechanical results (5.13)–(5.15).

Cosider Eq. (5.4) in the presence of a strong magnetic field $\hat{\mathbf{B}} = (0, \sin \theta, \cos \theta)$. To proceed, we try to recover the exact Landau levels (LLs) by increasing the complexity of the semiclassical quantization condition in three steps: first, using the method of Onsager (1952) for a single closed orbit; second, using Onsager quantization for a single closed orbit, extended by intraband quantum geometric corrections important in a multiband system (Roth 1966; Mikitik and Sharlai 1999; Fuchs et al. 2010; Gao and Niu 2017; Fuchs et al. 2018); finally, we develop an approach to Landau quantization of degenerate orbits, taking into account also interband matrix elements of Berry curvature and orbital magnetic moment, similar in spirit to the work of Wang et al. (2019).

Onsager quantization of a single closed orbit

Consider a band dispersion relation $\epsilon_\alpha(\mathbf{q})$. Let's denote q_0 the component of \mathbf{q} parallel to the magnetic field and \mathbf{q}_\perp the momentum perpendicular to the magnetic field such that $\mathbf{q} \equiv (q_x, q_y, q_z) = q_0\hat{\mathbf{B}} + \mathbf{q}_\perp$, with $\mathbf{q}_\perp = q_\perp[\cos \phi_\perp \hat{\mathbf{x}} + \sin \phi_\perp (\hat{\mathbf{x}} \times \hat{\mathbf{B}})]$. We can then rewrite $q_x = q_\perp \cos \phi_\perp$, $q_y = q_0 \sin \theta - q_\perp \sin \phi_\perp \cos \theta$, $q_z = q_0 \cos \theta + q_\perp \sin \phi_\perp \sin \theta$. Let's assume that for a fixed q_0 , the constant energy curve $\epsilon_\alpha(\mathbf{q}_\perp, q_0) = E$ defines a closed orbit \mathcal{O}_α in the \mathbf{q}_\perp plane. Onsager quantization then corresponds to postulate that the Landau level energies ϵ_n (with LL index n) are obtained by quantizing the momentum space area $S_\alpha(\epsilon_n, q_0)$ of the orbit \mathcal{O}_α according to

$$S_\alpha(\epsilon_n, q_0)l_B^2 = 2\pi(n + \gamma), \quad (\text{V.31})$$

where γ is the Maslov index of the orbit, in particular for an orbit deformable to a circle $\gamma = 1/2$. Since $S_\alpha(E, q_0) = 4\pi^2 N_\alpha(E, q_0)$, where $N_\alpha(E, q_0) = \int \frac{d\mathbf{q}_\perp}{4\pi^2} \Theta(E - \epsilon_\alpha(\mathbf{q}_\perp, q_0))$ is equivalent to the effective 2D zero-field integrated density of states of the band $\epsilon_\alpha(\mathbf{q})$, the previous relation can be rewritten as

$$N_\alpha(\epsilon_n, q_0) = \left(n + \frac{1}{2}\right) \frac{eB}{2\pi}, \quad (\text{V.32})$$

where now $eB/(2\pi)$ is the degeneracy (per unit area) of each Landau level (note that $\hbar = 1$).

For a zero-field spectrum of the form $\epsilon_\alpha(\mathbf{q}) = c_\alpha|\mathbf{q}| = c_\alpha\sqrt{|\mathbf{q}_\perp|^2 + q_0^2}$ one immediately obtains

$$N_\alpha(E, q_0) = \frac{1}{4\pi} \left(\frac{E^2}{c_\alpha^2} - q_0^2 \right), \quad (\text{V.33})$$

from which we deduce

$$\epsilon_n = \pm |c_\alpha| \sqrt{2eB \left(n + \frac{1}{2} \right) + q_0^2}. \quad (\text{V.34})$$

For Weyl multifold topological semimetals (2.6), and also for Hopf semimetals (5.4), this last expression does not recover the correct results because it misses quantum geometric effects.

Quantization of a single closed orbit in a multiband system

To linear order in magnetic field, the modified Onsager quantization rule (which takes care of intraband effects but still ignores coupling between degenerate orbits) reads (Gao and Niu 2017; Fuchs et al. 2018)

$$N_\alpha(\epsilon_n, q_0) + \mathbf{M}'_\alpha(\epsilon_n, q_0) \cdot \mathbf{B} = \left(n + \frac{1}{2} \right) \frac{eB}{2\pi}, \quad (\text{V.35})$$

where $\mathbf{M}'_\alpha(E, q_0) = \partial/\partial E \mathbf{M}_\alpha(E, q_0)$ with $\mathbf{M}_\alpha(E, q_0)$ the orbital magnetization (for spinless particles) of the band α at fixed (E, q_0) . This orbital magnetization may be written as (at $T = 0$)

$$\mathbf{M}_\alpha(E, q_0) = \int \frac{d\mathbf{q}_\perp}{4\pi^2} [\mathbf{m}_\alpha(\mathbf{q}) + e(E - \epsilon_\alpha(\mathbf{q}))\boldsymbol{\Omega}_\alpha(\mathbf{q})]\Theta(E - \epsilon_\alpha(\mathbf{q})), \quad (\text{V.36})$$

Here the Berry curvature and orbital magnetic moment pseudovectors can be expressed in several ways, for example as in Eqs. (1.21) and (1.49) in terms of eigenstates, or as in Eqs. (3.10) and (3.12) in terms of Bloch vectors.

For our purposes, it is instructive to introduce an alternative notation that will ensure a seamless transition to the discussion of interband coupling below:

$$\begin{aligned} \mathbf{m}_\alpha(\mathbf{q}) &= -\frac{e}{2} \sum_{\gamma \neq \alpha} \mathcal{A}_{\alpha\gamma} \times \mathbf{v}_{\gamma\alpha}, \\ \boldsymbol{\Omega}_\alpha(\mathbf{q}) &= \nabla_{\mathbf{q}} \times \mathcal{A}_{\alpha\alpha} = i \sum_{\gamma} \mathcal{A}_{\alpha\gamma} \times \mathcal{A}_{\gamma\alpha}. \end{aligned} \quad (\text{V.37})$$

Here we have introduced the non-Abelian Berry connection $\mathcal{A}_{\alpha\gamma}(\mathbf{q}) = i\langle\psi_\alpha|\nabla_{\mathbf{q}}|\psi_\gamma\rangle$ and $\mathbf{v}_{\alpha\gamma} = \langle\psi_\alpha|\nabla_{\mathbf{q}}H(\mathbf{q})|\psi_\gamma\rangle$ is the velocity operator such that $\mathbf{v}_{\alpha\alpha}(\mathbf{q}) = \nabla_{\mathbf{q}}\epsilon_\alpha$. Note that, using the identity $\mathbf{v}_{\alpha\gamma} = i(\epsilon_\alpha - \epsilon_\gamma)\mathcal{A}_{\alpha\gamma}$, valid for $\alpha \neq \gamma$, one immediately recovers from Eq. (V.37) the textbook formulas (1.21) and (1.49).

For our MHS continuum models, these intraband contributions are given by Eqs. (5.1) and (5.7), with coefficients as listed in Table 5.1. From these expressions, using $\mathbf{q} = q_0 \hat{\mathbf{B}} + \mathbf{q}_\perp$, one first obtains

$$\mathbf{m}_\alpha(\mathbf{q}) \cdot \hat{\mathbf{B}} = \frac{e}{2} \omega_\alpha \frac{q_0^2 (\mathbf{d} \cdot \hat{\mathbf{B}}) + q_0 (\mathbf{d} \cdot \mathbf{q}_\perp)}{(|\mathbf{q}_\perp|^2 + q_0^2)^{3/2}}, \quad \Omega_\alpha(\mathbf{q}) \cdot \hat{\mathbf{B}} = \kappa_\alpha \frac{q_0^2 (\mathbf{d} \cdot \hat{\mathbf{B}}) + q_0 (\mathbf{d} \cdot \mathbf{q}_\perp)}{(|\mathbf{q}_\perp|^2 + q_0^2)^2}.$$

Performing the \mathbf{q}_\perp integration at fixed (E, q_0) , the contributions proportional to $(\mathbf{d} \cdot \mathbf{q}_\perp)$ average to zero and one finds

$$\mathbf{M}_\alpha(E, q_0) \cdot \mathbf{B} = \frac{eB}{2\pi} (\mathbf{d} \cdot \hat{\mathbf{B}}) \left[\frac{\kappa_\alpha}{2} E + \left(\frac{\omega_\alpha}{2c_\alpha} - \kappa_\alpha \right) c_\alpha q_0 - \left(\frac{\omega_\alpha}{c_\alpha} - \kappa_\alpha \right) \frac{(c_\alpha q_0)^2}{2E} \right].$$

By differentiating with respect to E one finally obtains

$$\mathbf{M}'_\alpha(E, q_0) \cdot \mathbf{B} = \frac{e}{2\pi} (\mathbf{d} \cdot \mathbf{B}) \left[\frac{\kappa_\alpha}{2} + \left(\frac{\omega_\alpha}{c_\alpha} - \kappa_\alpha \right) \frac{(c_\alpha q_0)^2}{2E^2} \right].$$

If we ignore the contribution $\sim 1/E^2$ then the semiclassical LL spectrum reads

$$\epsilon_n = \pm |c_\alpha| \sqrt{2eB \left(n + \frac{1}{2} - \frac{\kappa_\alpha}{2} \xi \cos \theta \right) + q_0^2}, \quad (\text{V.38})$$

where $\xi \cos \theta = (\mathbf{d} \cdot \hat{\mathbf{B}})$. For $N = 3$ since $\omega_\alpha/c_\alpha - \kappa_\alpha = 0$ this expression is identical to the exact LL spectrum (5.13). For $N = 4$, despite the fact that $\omega_\alpha/c_\alpha - \kappa_\alpha = 0$ this expression still fails to recover the exact LL spectrum (5.14) as it misses the coupling between degenerate orbits. For $N = 5$ since $\omega_\alpha/c_\alpha - \kappa_\alpha \neq 0$ it is strictly speaking no longer valid to ignore the contribution $\sim 1/E^2$. A more physical argument in favor of neglecting this contribution anyway consists in acknowledging that the semiclassical calculation should only be trustworthy in the large n or large E limit, where $1/E^2 \ll 1$. We adopt this approximation hereafter.

Quantization of two degenerate closed orbits in a multiband system

The previous calculation of the quantity $\mathbf{M}_\alpha(E, q_0)$ takes into account only the *intra-band* diagonal element of the orbital magnetization. As recently put forward by Wang et al. (2019), for systems with two (or more) bands exhibiting quasi-degenerate orbits (that is, orbits degenerate simultaneously in momentum space and energy space) it is necessary to also consider off-diagonal (interband) elements of the orbital magnetization. We here adopt a similar approach and define these interband contributions as

$$\begin{aligned} \mathbf{m}_{\alpha\beta}(\mathbf{q}) &= -\frac{e}{4} \left(\sum_{\gamma \neq \alpha} \mathcal{A}_{\alpha\gamma} \times \mathbf{v}_{\gamma\beta} - \sum_{\gamma \neq \beta} \mathbf{v}_{\alpha\gamma} \times \mathcal{A}_{\gamma\beta} \right), \\ \Omega_{\alpha\beta}(\mathbf{q}) &= \nabla_{\mathbf{q}} \times \mathcal{A}_{\alpha\beta} = i \sum_{\gamma} \mathcal{A}_{\alpha\gamma} \times \mathcal{A}_{\gamma\beta}, \end{aligned} \quad (\text{V.39})$$

which is a generalization of Eq. (V.37) that satisfies $\mathbf{m}_{\alpha\beta} = \mathbf{m}_{\beta\alpha}^*$ and $\Omega_{\alpha\beta} = \Omega_{\beta\alpha}^*$.

Considering the MHS models (5.4) with $N = 4, 5$ and $\xi = +$, and denoting $\epsilon_{\pm}(\mathbf{q}) > 0$ the two bands that are associated to degenerate electron orbits either in energy or momentum space, explicit calculation yields

$$\begin{aligned}\mathbf{m}_{+-}(\mathbf{q}) \cdot \hat{\mathbf{B}} &= \frac{e}{2}\omega_{+-} \frac{\sin \theta q_0^2 + q_0 q_{\perp} (i \cos \phi_{\perp} - \sin \phi_{\perp} \cos \theta)}{(|\mathbf{q}_{\perp}|^2 + q_0^2)^{3/2}}, \\ \mathbf{\Omega}_{+-}(\mathbf{q}) \cdot \hat{\mathbf{B}} &= \kappa_{+-} \frac{\sin \theta q_0^2 + q_0 q_{\perp} (i \cos \phi_{\perp} - \sin \phi_{\perp} \cos \theta)}{(|\mathbf{q}_{\perp}|^2 + q_0^2)^2},\end{aligned}\tag{V.40}$$

where $\omega_{+-} = \omega_{-+}$ and $\kappa_{+-} = \kappa_{-+}$ are effective parameters that play a similar role as their diagonal counterparts $\omega_{\alpha}, \kappa_{\alpha}$. More quantitatively, for $N = 4$ we obtain $\omega_{+-} = -(a+b)/4$ and $\kappa_{+-} = -1$ whereas for $N = 5$ we find $\omega_{+-} = -\sqrt{2}$ and $\kappa_{+-} = (1 + \sqrt{2})$. We now integrate these expressions over \mathbf{q}_{\perp} on a constant energy contour $E = (E_+ + E_-)/2 = c_{+-}|\mathbf{q}|$ with $c_{+-} = (c_+ + c_-)/2$ at fixed q_0 . Very similarly to the previous intraband calculation we obtain

$$\begin{aligned}\mathbf{M}_{+-}(E, q_0) \cdot \mathbf{B} &= \frac{eB}{2\pi} \sin \theta \left[\frac{\kappa_{+-}}{2} E + \left(\frac{\omega_{+-}}{2c_{+-}} - \kappa_{+-} \right) c_{+-} q_0 \right. \\ &\quad \left. - \left(\frac{\omega_{+-}}{c_{+-}} - \kappa_{+-} \right) \frac{(c_{+-} q_0)^2}{2E} \right], \\ \mathbf{M}'_{+-}(E, q_0) \cdot \mathbf{B} &= \frac{eB}{2\pi} \sin \theta \left[\frac{\kappa_{+-}}{2} + \left(\frac{\omega_{+-}}{c_{+-}} - \kappa_{+-} \right) \frac{(c_{+-} q_0)^2}{2E^2} \right].\end{aligned}\tag{V.41}$$

The most striking qualitative feature is that this off-diagonal contribution is proportional to $\sin \theta = |(\mathbf{d} \times \hat{\mathbf{B}})|$, whereas the diagonal contributions are proportional to $\cos \theta = \mathbf{d} \cdot \hat{\mathbf{B}}$. Taking this quantitative form of the off-diagonal term, the modified semiclassical LL quantization rule now takes a 2×2 matrix form for the two coupled orbits. More precisely, the LLs are found as the solutions of

$$\det \begin{pmatrix} \Xi_+ - \frac{eB}{2\pi} (n + \frac{1}{2}) & \mathbf{M}'_{+-}(\epsilon_n, q_0) \cdot \mathbf{B} \\ \mathbf{M}'_{-+}(\epsilon_n, q_0) \cdot \mathbf{B} & \Xi_- - \frac{eB}{2\pi} (n + \frac{1}{2}) \end{pmatrix} = 0,\tag{V.42}$$

where $\Xi_{\alpha} = N_{\alpha}(\epsilon_n, q_0) + \mathbf{M}'_{\alpha}(\epsilon_n, q_0) \cdot \mathbf{B}$. Within the approximation $1/E^2 \ll 1$ we only consider the simplified forms $\mathbf{M}'_{\pm}(\epsilon_n, q_0) \cdot \mathbf{B} = \frac{eB}{2\pi} \frac{\kappa_{\pm}}{2} \cos \theta$ and $\mathbf{M}'_{+-}(\epsilon_n, q_0) \cdot \mathbf{B} = \frac{eB}{2\pi} \frac{\kappa_{+-}}{2} \sin \theta$. Within that simplified scheme the semiclassical LLs are solutions of

$$\det \begin{pmatrix} \frac{\epsilon_n^2}{c_+^2} - [2eB(n + \frac{1-\kappa_+ \cos \theta}{2}) + q_0^2] & eB\kappa_{+-} \sin \theta \\ eB\kappa_{+-} \sin \theta & \frac{\epsilon_n^2}{c_-^2} - [2eB(n + \frac{1-\kappa_- \cos \theta}{2}) + q_0^2] \end{pmatrix} = 0,$$

from which we finally obtain

$$\begin{aligned}\epsilon_n &= \pm \sqrt{\eta_+ + \eta_- \pm \sqrt{(\eta_+ - \eta_-)^2 + \eta_{+-}^2}}, \\ \eta_{\pm} &= \frac{c_{\pm}^2}{2} \left[2eB \left(n + \frac{1}{2} - \frac{\kappa_{\pm}}{2} \cos \theta \right) + q_0^2 \right], \\ \eta_{+-} &= c_+ c_- eB \kappa_{+-} \sin \theta.\end{aligned}\tag{V.43}$$

Repeating the same calculation for $\xi = -$, we exactly recover the LLs (5.14) and (5.15) if we choose the effective interband parameters as $\kappa_{+-} = 1$ for $N = 4$ and $\kappa_{+-} = \sqrt{6}$ for $N = 5$.

V.E | Semiclassical transport theory for MHS models

Evaluating conductivities for MHS continuum models

For the MHS continuum models, we have an energy (5.5), Berry curvature (5.1) and orbital magnetic moment (5.7). Evaluating Eqs. (I.14)–(I.17) at zero temperature yields

$$\begin{aligned}\sigma_{ij}^{\text{Drude}} &= \frac{e^2\tau}{6\pi^2} E_F^2 \left(\sum_{c_\alpha > 0} \frac{1}{c_\alpha} \right) \delta_{ij}, \\ \sigma_{ij}^{\text{Lorentz}}(\mathbf{B}) &= -\frac{e^3\tau^2}{6\pi^2} E_F \left(\sum_{c_\alpha > 0} c_\alpha \right) \epsilon_{ijl} B_l\end{aligned}\tag{V.44}$$

for the classical Drude and Lorentz conductivities. Those are the same as for a pseudospin (2.6), since they only depend on the zero-field energy spectrum. Also, we have

$$\begin{aligned}\sigma_{ij}^{\text{AH}} &= -\xi \frac{e^2}{6\pi^2} \sum_{\alpha} \kappa_{\alpha} \int_0^{q_c} dq \Theta(E_F - c_{\alpha}q) \epsilon_{ijz}, \\ \sigma_{ij}^{\text{AH1}}(\mathbf{B}) &= -\frac{e^3}{60\pi^2 E_F} \left(\sum_{c_\alpha > 0} \kappa_{\alpha} \omega_{\alpha} \right) (1 + 2\delta_{ix}\delta_{jy} + 2\delta_{iy}\delta_{jx}) \epsilon_{ijl} B_l\end{aligned}\tag{V.45}$$

for the non-dissipative anomalous Hall conductivities, and

$$\begin{aligned}\sigma_{ij}^{\text{Berry}}(\mathbf{B}) &= \xi \frac{e^3\tau}{30\pi^2} \left(\sum_{c_\alpha > 0} \kappa_{\alpha} c_{\alpha} \right) \begin{pmatrix} -B_z & 0 & 4B_x \\ 0 & -B_z & 4B_y \\ 4B_x & 4B_y & 7B_z \end{pmatrix}, \\ \sigma_{ij}^{\text{OMM}}(\mathbf{B}) &= \xi \frac{e^3\tau}{60\pi^2} \left(\sum_{c_\alpha > 0} \omega_{\alpha} \right) \begin{pmatrix} 7B_z & 0 & -3B_x \\ 0 & 7B_z & -3B_y \\ -3B_x & -3B_y & B_z \end{pmatrix}\end{aligned}\tag{V.46}$$

for the dissipative currents at first order in \mathbf{B} . In this thesis, we restrict our attention to the three most interesting contributions: the true anomalous Hall contribution σ_{ij}^{AH} , as well as the quantum geometric contributions $\sigma_{ij}^{\text{Berry}}(\mathbf{B})$ and $\sigma_{ij}^{\text{OMM}}(\mathbf{B})$. To evaluate these contributions, recall the coefficients c_{α} , κ_{α} and ω_{α} listed in Table 5.1.

Proof of symmetry properties of anomalous Hall conductivities

Proof that AH conductivity is odd for multifold Hopf semimetals. Assume first that the number of bands N is even, such that there is no flat band. Due to chiral

symmetry, the bands are arranged in pairs $\pm\epsilon_\alpha$, where each pair contributes an AH conductivity $\sigma_{ij,\alpha}^{\text{AH}} \sim \epsilon_{ijl} \int d^3k [f(\epsilon_\alpha) + f(-\epsilon_\alpha)](\Omega_\alpha)_l$, cf. Eq. (1.57a), where we have used $\Omega_\alpha = \Omega_{-\alpha}$. Rewriting $f(\epsilon_\alpha) + f(-\epsilon_\alpha) = 1 + \rho_\alpha$, where ρ_α is an odd function of the Fermi energy, we have

$$\sigma_{ij}^{\text{AH}} \sim \epsilon_{ijl} \int d^3k \sum_{\alpha=1}^{N/2} \rho_\alpha(\Omega_\alpha)_l,$$

where we have used $\sum_{\alpha=1}^{N/2} (\Omega_\alpha)_l = 0$. Second, assume N odd, such that there is a flat band. Then we can conduct a similar procedure to find

$$\begin{aligned} \sigma_{ij}^{\text{AH}} &\sim \epsilon_{ijl} \int d^3k \left[\sum_{\alpha=1}^{(N-1)/2} (1 + \rho_\alpha)(\Omega_\alpha)_l + f(0)(\Omega_0)_l \right] \\ &= \epsilon_{ijl} \int d^3k \sum_{\alpha=1}^{(N-1)/2} [\rho_\alpha + 1 - 2f(0)](\Omega_\alpha)_l, \end{aligned}$$

where we have used the relation $\sum_{\alpha=1}^{(N-1)/2} (\Omega_\alpha)_l = -(1/2)(\Omega_0)_l$ between the Berry curvature of the flat band ϵ_0 and the dispersive bands. Both expressions for the AH conductivity derived above are odd in E_F .

Proof that AH conductivity is even for a Weyl semimetal. For a Weyl semimetal the Berry curvature has opposite signs in the two bands, $\Omega_\alpha = -\Omega_{-\alpha}$, such that the AH conductivity becomes

$$\sigma_{ij}^{\text{AH}} \sim \epsilon_{ijl} \int d^3k [f(\epsilon_+) - f(\epsilon_-)](\Omega_+)_l.$$

If the spectrum is particle-hole symmetric, $\epsilon_+ = -\epsilon_-$, the AH conductivity is necessarily even in E_F . Note that similar arguments can be used to show that the AH conductivity is even for a multifold topological semimetal.

Anomalous Hall conductivity for four- and fivefold Hopf semimetals

The AH conductivity σ_{ij}^{AH} in Eq. (V.45) requires a momentum cutoff as explained in the main text. For the three-band HS (5.4a) it is given by Eq. (5.17) in the main text. Similarly, for the four-band HS (5.4b) we find

$$\begin{aligned} \sigma_{xy}^{\text{AH}} &= -\xi \frac{e^2}{6\pi^2} \begin{cases} 0 \\ \kappa_{-a}(E_F/a + q_c) \\ E_F(\kappa_{-a}/a + \kappa_{-b}/b) \\ \kappa_a(E_F/a - q_c) \end{cases} \\ &= \xi \frac{e^2}{6\pi^2} \begin{cases} 0, & |E_F| > aq_c \\ E_F/a + q_c, & -aq_c < E_F < -bq_c \\ E_F(1/a - 1/b), & -bq_c < E_F < bq_c \\ E_F/a - q_c, & bq_c < E_F < aq_c \end{cases} \end{aligned} \quad (\text{V.47})$$

with Berry dipole charges $\kappa_{\pm a} = -1$, $\kappa_{\pm b} = 1$. Finally, for the five-band HS (5.4c), we obtain

$$\begin{aligned} \sigma_{xy}^{\text{AH}} &= -\xi \frac{e^2}{6\pi^2} \begin{cases} 0 \\ \kappa_{-\sqrt{2}}(E_F/\sqrt{2} + q_c) \\ E_F(\kappa_{-\sqrt{2}}/\sqrt{2} + \kappa_{-1}) + (\kappa_0/2)q_c \\ E_F(\kappa_{\sqrt{2}}/\sqrt{2} + \kappa_1) - (\kappa_0/2)q_c \\ \kappa_{\sqrt{2}}(E_F/\sqrt{2} - q_c) \end{cases} \\ &= \xi \frac{e^2}{6\pi^2} \begin{cases} 0, & |E_F| > \sqrt{2}q_c \\ 3(E_F/\sqrt{2} + q_c), & -\sqrt{2}q_c < E_F < -q_c \\ E_F(3/\sqrt{2} - 1) + 2q_c, & -q_c < E_F < 0 \\ E_F(3/\sqrt{2} - 1) - 2q_c, & 0 < E_F < q_c \\ 3(E_F/\sqrt{2} - q_c), & q_c < E_F < \sqrt{2}q_c \end{cases} \end{aligned} \quad (\text{V.48})$$

where $\kappa_{\pm\sqrt{2}} = -3$, $\kappa_{\pm 1} = 1$ and $\kappa_0 = 4$, cf. Table 5.1. These AH conductivities are plotted in Fig. 5.4(b).

Proof of symmetry properties of magnetoconductivities

Proof that magnetoconductivity is even for a multifold Hopf semimetal. For the MHS models (5.4), the Berry curvature (5.1) is symmetric with respect to zero energy, $\mathbf{\Omega}_\alpha = \mathbf{\Omega}_{-\alpha}$, while the orbital magnetic moment (5.7) is antisymmetric, $\mathbf{m}_\alpha = -\mathbf{m}_{-\alpha}$. It follows that both conductivities (1.57b) and (1.57c) are $\sim \sum_{\alpha=1}^{\lfloor N/2 \rfloor} (f'(\epsilon_\alpha) + f'(-\epsilon_\alpha))\mathcal{F}_\alpha$, that is, they are even in E_F . Here, \mathcal{F}_α is some function independent of E_F , and the flat band for N odd plays no role.

Proof that magnetoconductivity is odd for a Weyl semimetal. For a Weyl semimetal, or more generally for a multifold chiral topological semimetal, the Berry curvature (2.9) is antisymmetric with respect to zero energy, while the orbital magnetic moment (2.9) is symmetric. Thus, both conductivities (1.57b) and (1.57c) are $\sim (f'(\epsilon_\alpha) - f'(-\epsilon_\alpha))$, that is, they are odd in E_F .

V.F | Continuum limit of multiband Hopf insulators

Topological phase transitions at $\Delta = \pm 3$

The first type of topological phase transitions in the multiband Hopf insulator models (5.34) occurs for $\Delta = -3$, where gap closing happens at the Γ point. The continuum limit of the three-band Hamiltonian h_3^{Hopf} around this point takes the form of a threefold Hopf semimetal (5.4a) plus a gap term,

$$h_{3,\Gamma}^{\text{Hopf}}(\mathbf{q}) = H_3^+(\mathbf{q}) + \Delta_\Gamma \text{antidiag}(1, 0, 1), \quad (\text{V.49})$$

where $\Delta_\Gamma = \Delta + 3$. It has eigenvalues $\epsilon_\alpha = 0, \pm\epsilon$, where $\epsilon \equiv \sqrt{|\mathbf{q}|^2 + \Delta_\Gamma^2}$, and eigenvectors

$$\begin{aligned} |\psi_0\rangle &= \frac{1}{\epsilon} \left(0, \Delta_\Gamma^-, q_+^- \right), \\ |\psi_\pm\rangle &= \frac{1}{\sqrt{2}\epsilon} \left(\pm\epsilon, q_+^+, \Delta_\Gamma^+ \right), \end{aligned} \quad (\text{V.50})$$

where $q_\pm^\xi = \xi q_x \pm i q_y$ and $\Delta_\Gamma^\pm \equiv \Delta_\Gamma \pm i q_z$. Computing the continuum Hopf number (5.49) using these eigenstates, one finds

$$\chi_{\text{con}}(\mathbf{q}) \equiv \epsilon_{ijk} \text{Tr} \left(\mathcal{A}_i \partial_j \mathcal{A}_k - \frac{2i}{3} \mathcal{A}_i \mathcal{A}_j \mathcal{A}_k \right) = 4\Delta_\Gamma / \epsilon^4 \quad (\text{V.51})$$

and consequently $\mathcal{N}_\Gamma^{\text{Hopf}} = \frac{1}{2} \text{sgn}(\Delta_\Gamma)$. According to Eq. (5.48), the Hopf number thus changes by $\delta\mathcal{N}_{\text{Hopf}} = 1$ across the topological phase transition. Similarly, for the four-band Hopf insulator h_4^{Hopf} , we have

$$h_{4,\Gamma}^{\text{Hopf}}(\mathbf{q}) = H_4^+(\mathbf{q}) + \Delta_\Gamma \text{antidiag}(-a, b, b, -a), \quad (\text{V.52})$$

with eigenvalues $\epsilon_\alpha = c_\alpha \epsilon$, $c_\alpha = \frac{\alpha_1}{2} [a + b + \alpha_2(a - b)]$ with $\alpha = (\alpha_1, \alpha_2)$, $\alpha_i = \pm 1$, and eigenstates

$$\begin{aligned} |\psi_{\pm-}\rangle &= \frac{1}{\sqrt{2}\epsilon} \left(0, \pm\epsilon, \Delta_\Gamma^-, q_-^+ \right), \\ |\psi_{\pm+}\rangle &= \frac{1}{\sqrt{2}\epsilon} \left(\mp\epsilon, 0, q_-^-, \Delta_\Gamma^+ \right). \end{aligned} \quad (\text{V.53})$$

One again finds $\chi_{\text{con}}(\mathbf{q}) = 4\Delta_\Gamma / \epsilon^4$ and $\delta\mathcal{N}_{\text{Hopf}} = 1$. For the five-band insulator h_5^{Hopf} , we have

$$h_{5,\Gamma}^{\text{Hopf}}(\mathbf{q}) = H_5^+(\mathbf{q}) + \Delta_\Gamma \text{antidiag}(\sqrt{2}, 1, 0, 1, \sqrt{2}), \quad (\text{V.54})$$

with eigenvalues $\epsilon_\alpha = c_\alpha \epsilon$, $c_\alpha = \frac{\alpha_1}{2} [1 + \sqrt{2} - \alpha_2(1 - \sqrt{2})]$, with $\alpha = (\alpha_1, \alpha_2)$, $\alpha_1 = 0, \pm 1$, $\alpha_2 = \pm 1$, and eigenstates

$$\begin{aligned} |\psi_0\rangle &= \frac{1}{\epsilon^2} \left((q_-^+)^2, \sqrt{2} q_+^- \Delta_\Gamma^-, (\Delta_\Gamma^-)^2, 0, 0 \right), \\ |\psi_{\pm-}\rangle &= \frac{1}{\sqrt{2}\epsilon^2} \left(\pm\sqrt{2} q_-^+ \Delta_\Gamma^+, \pm(q_+^+ q_-^+ - \Delta_\Gamma^+ \Delta_\Gamma^-), \pm\sqrt{2} q_-^- \Delta_\Gamma^-, -\Delta_\Gamma^- \epsilon, q_-^+ \epsilon \right), \\ |\psi_{\pm+}\rangle &= \frac{1}{\sqrt{2}\epsilon^2} \left(\pm(\Delta_\Gamma^+)^2, \pm\sqrt{2} q_+^+ \Delta_\Gamma^+, \pm(q_+^+)^2, q_+^+ \epsilon, \Delta_\Gamma^+ \epsilon \right). \end{aligned} \quad (\text{V.55})$$

From this one obtains $\chi_{\text{con}}(\mathbf{q}) = 20\Delta_\Gamma / \epsilon^4$, $\mathcal{N}_\Gamma^{\text{Hopf}} = \frac{5}{2} \text{sgn}(\Delta_\Gamma)$ and hence $\delta\mathcal{N}_{\text{Hopf}} = 5$.

For the phase transition at $\Delta = 3$, which is characterized by a gap closing at the R point, one similarly has

$$\begin{aligned} h_{3,\text{R}}^{\text{Hopf}}(\mathbf{q}) &= -H_3^+(\mathbf{q}) + \Delta_\text{R} \text{antidiag}(1, 0, 1) = -h_{3,\Gamma}^{\text{Hopf}}(\mathbf{q}, -\Delta), \\ h_{4,\text{R}}^{\text{Hopf}}(\mathbf{q}) &= -H_4^+(\mathbf{q}) + \Delta_\text{R} \text{antidiag}(-a, b, b, -a) = -h_{4,\Gamma}^{\text{Hopf}}(\mathbf{q}, -\Delta), \\ h_{5,\text{R}}^{\text{Hopf}}(\mathbf{q}) &= -H_5^+(\mathbf{q}) + \Delta_\text{R} \text{antidiag}(\sqrt{2}, 1, 0, 1, \sqrt{2}) = -h_{5,\Gamma}^{\text{Hopf}}(\mathbf{q}, -\Delta), \end{aligned} \quad (\text{V.56})$$

where $\Delta_\text{R} = \Delta - 3$. The change in the Hopf number is thus $\delta\mathcal{N}_{\text{Hopf},\text{R}} = -\delta\mathcal{N}_{\text{Hopf},\Gamma}$.

Topological phase transitions at $\Delta = \pm 1$

The second type of topological phase transitions in the models (5.34) occurs for $\Delta = -1$, where gap closing happens at the three inequivalent X points. The continuum limit of the Hamiltonian h_3^{Hopf} around these points takes the forms

$$\begin{aligned} h_{3,X1}^{\text{Hopf}}(\mathbf{q}) &= H_3^+(-q_x, q_y, q_z) + \Delta_X \text{antidiag}(1, 0, 1), \\ h_{3,X2}^{\text{Hopf}}(\mathbf{q}) &= H_3^+(q_x, -q_y, q_z) + \Delta_X \text{antidiag}(1, 0, 1), \\ h_{3,X3}^{\text{Hopf}}(\mathbf{q}) &= H_3^+(q_x, q_y, -q_z) + \Delta_X \text{antidiag}(1, 0, 1), \end{aligned} \quad (\text{V.57})$$

where $\Delta_X = \Delta + 1$. All of these continuum Hamiltonians have eigenstates such that $\chi_{\text{con}}(\mathbf{q}) = -4\Delta_X/\epsilon^4$, where $\epsilon = \sqrt{|\mathbf{q}|^2 + \Delta_X^2}$, that is, $\mathcal{N}_{X_i}^{\text{Hopf}} = -\frac{1}{2}\text{sgn}(\Delta_X)$. It follows

$$\delta\mathcal{N}_{\text{Hopf}} = \sum_{i=1,2,3} \left(\mathcal{N}_{X_i}^{\text{Hopf}}(\Delta_X > 0) - \mathcal{N}_{X_i}^{\text{Hopf}}(\Delta_X < 0) \right) = -3. \quad (\text{V.58})$$

The same result is found for the four-band Hopf insulator h_4^{Hopf} . For the five-band model h_5^{Hopf} , the continuum limit around the X points takes the forms

$$\begin{aligned} h_{5,X1}^{\text{Hopf}}(\mathbf{q}) &= H_5^+(-q_x, q_y, q_z) + \Delta_X \text{antidiag}(\sqrt{2}, 1, 0, 1, \sqrt{2}), \\ h_{5,X2}^{\text{Hopf}}(\mathbf{q}) &= H_5^+(q_x, -q_y, q_z) + \Delta_X \text{antidiag}(\sqrt{2}, 1, 0, 1, \sqrt{2}), \\ h_{5,X3}^{\text{Hopf}}(\mathbf{q}) &= H_5^+(q_x, q_y, -q_z) + \Delta_X \text{antidiag}(\sqrt{2}, 1, 0, 1, \sqrt{2}), \end{aligned} \quad (\text{V.59})$$

such that each X point contributes $\chi_{\text{con}}(\mathbf{q}) = -20\Delta_X/\epsilon^4$. It follows $\delta\mathcal{N}_{\text{Hopf}} = -15$.

Finally, for the transition at $\Delta = 1$, which is characterized by a gap closing at the M points of the cubic Brillouin zone, one has

$$h_{N,Mi}^{\text{Hopf}}(\mathbf{q}) = -h_{N,Xi}^{\text{Hopf}}(\mathbf{q}, -\Delta), \quad (\text{V.60})$$

where $i = 1, 2, 3$. The change in the Hopf number is thus $\delta\mathcal{N}_{\text{Hopf},M} = -\delta\mathcal{N}_{\text{Hopf},X}$.

Synthèse en français

Contexte

Les solides cristallins ont joué un rôle majeur dans les révolutions scientifiques et industrielles du XIXe siècle, mais une compréhension microscopique approfondie de leur comportement n'est devenue possible qu'après l'émergence de la théorie de la mécanique quantique au début du XXe siècle, qui a donné naissance au domaine bien établi de la *physique de l'état solide* (Ashcroft and Mermin 1976). À première vue, décrire quantitativement la physique des solides est un problème à plusieurs corps très compliqué. Cependant, l'histoire nous a appris qu' "*il est possible de considérer une grande partie de la physique de l'état solide en termes de certaines excitations élémentaires qui n'interagissent que faiblement entre elles*" (Pines 1963). En fonction des circonstances physiques qui nous intéressent, la description théorique d'un solide se résume alors à se concentrer sur une certaine excitation élémentaire.

Cette thèse suit principalement l'approche standard qui approxime un solide comme étant un gaz de Fermi en présence d'un potentiel de réseau périodique. Dans ce cadre, on s'intéresse aux excitations de particules individuelles qui sont décrites par la célèbre *théorie des bandes des solides* (Singleton 2001). Au cours de la seconde moitié du XXe siècle, la théorie des bandes des solides a été utilisée avec succès pour construire les structures de bandes (et les surfaces de Fermi) des isolants, des semi-conducteurs et des métaux, une démarche essentielle qui a servi de base à l'industrie électronique moderne. Cependant, au-delà de la structure de bandes, il existe des informations importantes codées dans les états propres de la mécanique quantique de l'hamiltonien de Bloch. Cela donne lieu à des *effets interbande* sur les propriétés observables des cristaux, également appelés *effets géométriques quantiques*, ou simplement *effets géométriques*. Ces effets géométriques peuvent également donner lieu à une physique topologique dans des circonstances appropriées ; l'inclusion de concepts géométriques et topologiques a conduit à une théorie des bandes étendue, connue sous le nom de *théorie des bandes topologiques*. (Hasan and Kane 2010; Qi and Zhang 2011; Bansil et al. 2016; Cayssol and Fuchs 2021). Les matériaux décrits par la théorie des bandes topologiques sont actuellement au centre des préoccupations des laboratoires de recherche sur l'état solide du monde entier. En effet, ils abritent une variété de phénomènes non conventionnels lorsqu'il s'agit de conduire l'électricité, de réagir aux champs magnétiques, à la pression, aux faisceaux lumineux, et cetera, ce qui est prometteur pour les futures applications technologiques.

Du point de vue du physicien théorique, il faut noter qu'une grande partie des progrès réalisés dans la théorie des bandes topologiques peut être attribuée à des modèles effectifs basés sur l'approximation des liaisons fortes (Simon 2013) ou sur des théories du continu à basse énergie. Dans le cas le plus simple, les modèles de liaisons fortes utilisés dans la théorie des bandes topologiques sont des modèles à deux bandes, car on est souvent principalement intéressé par la physique des bords des bandes de conduction et de valence (dans le cas des isolants) ou par le croisement des deux

bandes près de l'énergie de Fermi (dans le cas des semi-métaux). Ces modèles à deux bandes ont des propriétés simples et bien connues. Parmi les exemples célèbres, citons les modèles qui ont été développés pour le graphène (Wallace 1947), les semi-métaux de Weyl (Nielsen and Ninomiya 1983), ou les isolants de Chern (Haldane 1988).

Cependant, ces dernières années, un nombre croissant de systèmes qui nécessitent d'aller au-delà d'une description à deux bandes ont été mis en évidence, tels que les réseaux avec des bandes d'énergie plates (Leykam et al. 2018) ou les semi-métaux topologiques avec de multiples bandes d'énergie qui se croisent simultanément en certains points de la zone de Brillouin (Bradlyn et al. 2016; Lv et al. 2021). Motivée par ces développements, cette thèse est consacrée à l'étude de la physique des *systèmes multibandes*, c'est-à-dire des systèmes qui impliquent $N > 2$ bandes d'énergie. En particulier, elle se concentre sur trois aspects : la géométrie quantique des systèmes multibandes, la physique des bandes plates dans les systèmes multibandes, et les propriétés des croisements de plusieurs bandes. Ces sujets sont a priori distincts, mais ils sont aussi intimement liés : la géométrie quantique est fortement renforcée au voisinage des croisements multibandes, les croisements multibandes sont souvent accompagnés de bandes plates, et les bandes plates ont des propriétés géométriques quantiques très particulières.

Organisation du manuscrit et principaux résultats

Principes fondamentaux

Les chapitres 1 et 2 fournissent une introduction aux sujets pertinents pour cette thèse qui sont pour la plupart connus dans la littérature, ainsi qu'une motivation pour le travail mené dans cette thèse.

Chapitre 1 – Pour commencer, nous rappelons les aspects fondamentaux de la théorie des bandes, tels que l'hamiltonien de Bloch et l'approche des liaisons fortes (Section 1.1). Nous introduisons ensuite le thème principal de cette thèse, c'est-à-dire le concept de géométrie quantique, ainsi que les principaux objets géométriques d'intérêt, à savoir la métrique quantique et la courbure de Berry (Section 1.2). Ensuite, nous traitons de la connexion entre la géométrie quantique et la topologie, et mentionnons un certain nombre d'invariants topologiques qui seront importants par la suite (Section 1.3). Ces concepts sont illustrés par une discussion des systèmes 2D allant du graphène aux isolants de Chern (Section 1.4). Pour clore le chapitre, nous voulons illustrer le fait que la géométrie et la topologie quantiques sont omniprésentes dans la réponse physique des systèmes cristallins, et nous présentons un certain nombre d'exemples pertinents allant des états de bord topologiques au rôle de la géométrie quantique dans le transport (Section 1.5).

Chapitre 2 – Ce chapitre est consacré à la motivation de l'étude des systèmes multibandes, c'est-à-dire des systèmes comportant plus de deux bandes. Nous donnons d'abord une motivation physique basée sur une sélection de systèmes multibandes qui ont été largement étudiés récemment, à savoir les réseaux de bandes plates en 2D (Section 2.1) et les croisements de bandes multiples en 3D (Section 2.2). Nous abordons ces deux types de systèmes au niveau des modèles simples et soulignons

leur importance pour les expériences. Nous présentons ensuite une motivation plus mathématique. Elle s’inspire de la riche structure mathématique de l’algèbre $\mathfrak{su}(N)$ qui est à la base des hamiltoniens multibandes (Section 2.3), et de la complexité correspondante de l’espace interne des paramètres (Section 2.4).

Résultats originaux

Après cette préparation, le matériel original qui constitue le cœur de cette thèse est présenté dans les chapitres 3–5, comme décrit ci-après.

Chapitre 3 – Dans ce court chapitre, nous développons un formalisme assez général qui exprime les observables dans les systèmes multibandes en termes de *vecteurs de Bloch* ; ceux-ci sont une représentation vectorielle des projecteurs propres de l’hamiltonien. Après une brève introduction (Section 3.1), nous soutenons que ces vecteurs de Bloch présentent plusieurs avantages par rapport à l’approche conventionnelle des observables basée sur les états propres (Section 3.2). Nous expliquons ensuite comment écrire n’importe quelle observable dans un système multibande en termes de vecteurs de Bloch, et illustrons ces idées par des exemples simples, notamment le tenseur géométrique quantique et l’aimantation orbitale (Section 3.3). Ensuite, nous discutons comment les projecteurs propres et les vecteurs de Bloch peuvent être reliés de manière unique à l’hamiltonien, ce qui permet (au moins en principe) de calculer n’importe quelle observable sans avoir besoin de construire des états propres d’énergie (Section 3.4). En particulier, nous arrivons ainsi à une généralisation multibande de la formule bien connue de la ”densité de skyrmion” pour la courbure de Berry d’un système à deux bandes. Pour clore le chapitre, nous appliquons le formalisme à un exemple pédagogique (Section 3.5) et fournissons un bref résumé (Section 3.6).

Principaux résultats du chapitre 3 – Pour un système quantique décrit par une matrice hamiltonienne paramétrique (2.24), les observables sont conventionnellement construites à partir d’éléments de matrice $O_{\alpha\beta}$ qui nécessitent la connaissance explicite des états propres d’énergie. Nous soutenons ici qu’il peut être intéressant de se débarrasser des états propres et de viser une reformulation (3.19) en termes de vecteurs de Bloch. Une telle approche des vecteurs de Bloch est motivée par le fait que les vecteurs de Bloch (comme les projecteurs propres correspondants) offrent plusieurs avantages par rapport aux états propres, à savoir qu’ils sont invariants de jauge, non-singuliers et possèdent une paramétrisation unique, voir Tableau 3.1. Une formulation en fonction des vecteurs de Bloch peut être effectuée pour n’importe quelle observable, comme le chapitre illustre à l’aide d’exemples simples tels que le tenseur géométrique quantique et l’aimantation orbitale, voir en particulier les équations (3.10) et (3.13).

Au niveau conceptuel, la forme du vecteur de Bloch (3.19) d’une quantité donnée rend explicite le caractère intrabande ou interbande des contributions individuelles, puisque les vecteurs de Bloch sont identiquement nuls dans un système à une bande (ou dans un système multibande avec des bandes trivialement découplées). De plus, on peut tirer la conclusion intéressante que toute observable peut (au moins en principe) être calculée en utilisant uniquement le vecteur hamiltonien et les valeurs propres de l’énergie, en accord avec les résultats récents de Pozo and Juan (2020). Cela devient évident lorsqu’on combine les équations (3.19) et (3.32). Les expressions résultantes $\chi = f(\varepsilon_\alpha, \mathbf{h})$ sont extrêmement pratiques pour le calcul explicite de la courbure de

Berry et du moment magnétique orbital. Nous soulignons également à nouveau que nous avons généralisé l'expression bien connue de la courbure de Berry (2.41) à un nombre de bandes N arbitraire, voir la section 3.4.3. Il est souhaitable d'étendre les idées exposées ici à des quantités plus compliquées que le tenseur géométrique et l'aimantation orbitale, et d'obtenir des expressions basées sur le vecteur de Bloch, par exemple pour les magnétoconductivités [au-delà du résultat de Boltzmann (1.57)] ou la susceptibilité magnétique orbitale.

Nous notons aussi que la validité du formalisme développé ici va au-delà du cas des matrices hamiltoniennes hermitiennes. En particulier, les expressions clés (3.29) pour le projecteur propre et (3.32) pour le vecteur de Bloch restent valides pour les systèmes où la condition d'herméticité est relâchée (Bender 2007; Brody 2013).

Chapitre 4 – Dans ce chapitre, nous abordons le domaine des bandes plates. Après une introduction donnant une vue d'ensemble des travaux antérieurs connexes (Section 4.1), nous résumons certaines bases de la physique des bandes plates, en particulier la notion importante d'un *état localisé compact* (Section 4.2). Sur la base de la connaissance de tels états, nous développons une méthode puissante pour construire des modèles de liaisons fortes à bande plate (Section 4.3). Cette méthode fournit (une infinité) de modèles à bande plate sur n'importe quel réseau périodique, dans n'importe quelle dimension spatiale et avec n'importe quel nombre de bandes. De plus, comme détaillé dans les sections 4.4 et 4.5, la méthode permet un contrôle considérable de l'existence et du caractère des croisements de bandes multiples à l'énergie de la bande plate, et peut être considérée comme un nouveau schéma de classification des bandes plates. Après quelques remarques supplémentaires sur les particularités des systèmes à bandes plates ainsi obtenus (Section 4.6), et après avoir mis en évidence certaines perspectives intéressantes telles que la géométrie quantique des croisements multiples ou la construction de bandes plates magnétiques (Section 4.7), le chapitre se termine par un résumé dans la Section 4.8.

Principaux résultats du chapitre 4 – On sait depuis longtemps que, pour tout hamiltonien à liaisons fortes H à bande plate sur un réseau périodique, il est possible de trouver un nombre macroscopique d'états localisés compacts (CLSs) comme états propres de H . Inversement, dans le chapitre 4, nous avons montré que *pour tout CLS donné* $|\Psi_{\text{CLS}}^{\text{RC}}\rangle$ sur n'importe quel réseau périodique, il est possible de concevoir une ou plusieurs familles de hamiltoniens à liaisons fortes H pour lesquels ce CLS et toutes ses copies sont des états propres. Nous avons fourni une procédure précise pour trouver de tels hamiltoniens, qui sont des *modèles à bande plate* par construction. Puisque l'on peut construire une infinité de CLSs différents sur n'importe quel réseau, ceci représente un schéma de construction de bande plate efficace : il produit une infinité de modèles à bande plate sur n'importe quel réseau périodique.

Cette procédure s'effectue le plus commodément dans l'espace réciproque et repose sur la correspondance biunivoque entre un CLS donné $|\Psi_{\text{CLS}}^{\text{RC}}\rangle$, voir Eq. (4.1), et sa transformée de Fourier, le BCLS $|f(\mathbf{k})\rangle$, voir Eq. (4.6). Les hamiltoniens de Bloch à bande plate $H(\mathbf{k})$ peuvent être commodément conçus comme une fonction du BCLS, à partir duquel le modèle H dans l'espace réel est naturellement déduit. Pour tout CLS de départ arbitrairement conçu, il est toujours possible de construire un modèle à bande plate $H(\mathbf{k})$ comme une fonction quadratique du BCLS. Cet hamiltonien

quadratique générique, qui fonctionne pour un nombre quelconque de bandes $N \geq 2$, est fourni dans l'équation (4.43) et donne lieu à des modèles avec des points de contact quadratiques à bandes multiples à l'énergie de la bande plate. En revanche, si le BCLS de départ possède certaines propriétés particulières, il peut être utilisé non seulement pour construire des modèles quadratiques, mais aussi pour construire un hamiltonien de Bloch $H(\mathbf{k})$ comme une fonction linéaire du BCLS. Un tel hamiltonien linéaire générique peut être construit à l'aide de l'équation (4.48) pour tout $N \geq 3$ donné, ou en utilisant une superposition (4.83) de blocs 3×3 . Il fournit des modèles à liaisons fortes avec des croisements linéaires de plusieurs bandes à l'énergie de la bande plate.

Bien que notre méthode permette de construire une infinité de modèles à bande plate, et qu'elle capture la plupart des modèles connus dans la littérature, elle peut être généralisée de plusieurs façons. Par exemple, une version plus générale de l'hamiltonien (4.43) se lit comme suit : $H_{\mathbf{k}} = \sum_{\alpha, \beta > \alpha} \sum_{\gamma, \delta > \gamma} \lambda_{\alpha\beta\gamma\delta} |f_{\mathbf{k}}^{\alpha\beta}\rangle \langle f_{\mathbf{k}}^{\gamma\delta}|$, où $\lambda_{\alpha\beta\gamma\delta}^* = \lambda_{\gamma\delta\alpha\beta}$. De plus, certains systèmes à bande plate importants, tels que le modèle standard sur le réseau de Kagome, ne font pas partie de notre schéma de classification.

Au-delà de la simple construction de bandes plates, nous avons présenté plusieurs perspectives intéressantes. Premièrement, nous avons montré que la géométrie quantique des croisements de bandes linéaires à trois bandes en 3D est essentiellement régie par un dipôle de Berry si la symétrie chirale est imposée. Cela contraste avec les croisements linéaires à trois bandes plus connus de type pseudospin-1, qui ont exactement le même spectre d'énergie mais une géométrie quantique régie par une symétrie CP et un monopole de Berry. Les propriétés physiques des croisements de dipôles de Berry sont le sujet principal du chapitre 5. Il serait certainement intéressant de mener une enquête plus détaillée sur les différents types de croisements multiples qui peuvent être obtenus par notre méthode, et d'établir une sorte de tableau de classification des propriétés géométriques quantiques en termes de dimension spatiale, de nombre de bandes impliquées dans le croisement, et de symétries. Deuxièmement, nous avons fait valoir qu'il est une voie prometteuse de créer des modèles magnétiques à bande plate à partir de CLSs avec texture de spin. Leurs propriétés géométriques magnétiques et quantiques sont un terrain assez inexploité.

D'autres perspectives peuvent être envisagées. Par exemple, nous n'avons utilisé que des états strictement localisés comme point de départ pour nos hamiltoniens, afin d'obtenir des modèles à liaisons fortes à courte portée avec une bande exactement plate. Ceci implique que toutes les bandes plates présentées dans ce travail ont un premier nombre de Chern $\mathcal{C}_0 = 0$. Il pourrait être intéressant d'utiliser notre schéma de construction en supposant que les états propres de la bande plate pourraient maintenant être représentés par des états localisés en loi de puissance au lieu de CLS - en particulier en ce qui concerne un éventuel caractère topologique des bandes plates.

Chapitre 5 – Ce dernier chapitre se concentre sur les semi-métaux en 3D avec des croisements de bandes multiples. Alors que les semi-métaux topologiques largement connus sont basés sur des singularités dans l'espace des moments avec une structure de monopole de Berry, les croisements multibandes en 3D peuvent également présenter des propriétés géométriques quantiques plus exotiques, comme expliqué dans les sections 5.1 et 5.2. Pour illustrer cela, nous présentons une classe de semi-métaux ayant

la propriété particulière que chaque point de croisement porte un *dipôle de Berry*. Nous les appelons *semi-métaux de Hopf multiples*, et nous étudions leurs propriétés physiques à la fois au niveau du continu (Section 5.3) et des Hamiltoniens à liaisons fortes (Section 5.4). En particulier, nous dévoilons des signatures claires du dipôle de Berry dans les niveaux de Landau ainsi que dans l'effet Hall anormal et dans la magnétoconductivité; ces effets sont similaires mais aussi fondamentalement différents de ce qui se passe dans les semi-métaux de Weyl. Nous établissons ensuite un lien entre les semi-métaux de Hopf multiples et une classe particulière d'isolants topologiques connus sous le nom d'isolants de Hopf (Section 5.5). Dans ce cadre, nous introduisons également les premiers modèles connus pour les isolants de Hopf multibandes. Après avoir mentionné quelques perspectives intrigantes dans la section 5.6 (telles que les liens étroits avec le modèle de Haldane et les monopoles tensoriels 4D), le chapitre se termine à nouveau par un bref résumé (Section 5.7).

Principaux résultats du chapitre 5 – Dans ce chapitre, nous avons démontré que les croisements de bandes linéaires en 3D présentent de riches propriétés physiques si plus de deux bandes se croisent en même temps. En particulier, au-delà des monopoles de Berry bien connus des semi-métaux de Weyl (Armitage et al. 2018) et des semi-métaux multiples chiraux (Lv et al. 2021), d'autres types de croisements de bandes avec une structure géométrique quantique plus exotique sont possibles. Nous nous sommes concentrés sur le cas où chaque point de croisement agit comme un dipôle de Berry, mais des multipôles de Berry plus généraux sont en principe possibles.

Pour étudier en détail les croisements linéaires de N bandes avec un dipôle de Berry, nous avons introduit plusieurs modèles sur réseau dont la théorie de basse énergie est de la forme (5.4), que nous appelons les semi-métaux de Hopf multiples. Les modèles de réseau peuvent être distingués selon qu'ils présentent un nombre pair (semi-métal de Hopf de vallée) ou impair (semi-métal de Hopf topologique) de dipôles de Berry dans la zone de Brillouin. Pour les semi-métaux de Hopf topologiques, il existe des signatures claires du dipôle de Berry dans l'effet Hall anormal et les magnétoconductivités. On s'attend à ce que cela s'étende à un grand nombre d'autres quantités physiques, par exemple la conductivité optique (Habe 2022). Pour les semi-métaux de Hopf de vallée, l'effet Hall anormal et les magnétoconductivités s'annulent, mais l'effet du dipôle de Berry est toujours clairement visible dans le spectre des niveaux de Landau. Il serait intéressant d'étudier des réponses pour lesquelles les contributions des différentes vallées ne s'annulent pas, en particulier si l'on considère le fait que les modèles de réseau pour les semi-métaux de Hopf de vallée sont très simples et assez proches du modèle du graphène.

Nous avons également introduit deux classes différentes de modèles sur réseau pour les isolants de Hopf multibandes (Lapierre et al. 2021). La première classe est une simple généralisation multibande du modèle de Moore-Ran-Wen (Moore et al. 2008), voir l'équation (5.40). Plus important encore, nous avons introduit une deuxième classe d'isolants de Hopf multibandes (5.34), qui devient exactement équivalente aux semi-métaux de Hopf (5.26) aux transitions de phase topologiques. L'un des avantages considérables de ces modèles est qu'ils ne nécessitent que des sauts entre les voisins les plus proches, évitant ainsi les sauts compliqués de seconds voisins des isolants de

Hopf à deux bandes (Moore et al. 2008; Nelson et al. 2022). Ces modèles pourraient constituer une plateforme fertile pour tester les prédictions théoriques concernant la correspondance bord-volume des isolants topologiques délicats.

De nombreuses questions fondamentales demeurent quant aux processus de conversion entre les différents systèmes abordés ici. Pour être plus précis, une étude systématique des diagrammes de phase qui peuvent être obtenus par le gapping ou la fusion d'un ou plusieurs dipôles et/ou monopôles de Berry s'impose. De plus, il semble y avoir des connexions intéressantes avec des systèmes de différentes dimensions spatiales. Nous avons souligné les analogies avec le modèle de Haldane en 2D ainsi qu'avec les semi-métaux en 4D avec des monopoles tensoriels. Il semble très intrigant de développer plus en détail les hiérarchies dimensionnelles correspondantes, comme cela a été fait il y a des années pour les isolants topologiques stables et les supraconducteurs (Ryu et al. 2010).

D'un point de vue expérimental, l'existence des semi-métaux de Hopf de vallée, en particulier les modèles de type graphène (5.22), semble possible. Pour progresser dans ce domaine, il faut déterminer les groupes d'espace de ces modèles et vérifier dans quels matériaux ils pourraient apparaître. S'ils sont réalisés dans un cristal, les croisements de dipôles de Berry pourraient potentiellement être sondés via la dépendance particulière et fortement dépendante de la vallée des niveaux de Landau sur l'orientation du champ magnétique (Fig. 5.3). Les courants de Hall anormaux et les magnétocourants linéaires induits par les dipôles de Berry ont des symétries opposées à celles d'une paire de nœuds de Weyl (Fig. 5.5), qui pourraient être sondés en faisant varier la densité d'électrons près de la moitié du remplissage. Une autre voie implique des systèmes artificiels tels que des atomes ultrafroids, des cristaux photoniques ou des circuits supraconducteurs. Ceux-ci ont été suggérés et utilisés à de nombreuses reprises pour réaliser des phases semi-métalliques avec des croisements à deux et plusieurs bandes (Lu et al. 2015; Chen et al. 2016; Riwar et al. 2016; Wang et al. 2017; Zhu et al. 2017; Zhang et al. 2018; Tan et al. 2018; Fulga et al. 2018; Hu et al. 2018). De plus, le croisement du monopole tensoriel (5.65), qui est très similaire à l'équation (5.4a), a récemment été observé expérimentalement en utilisant un transmon dans une cavité (Tan et al. 2021).

Enfin, nous notons qu'il existe une activité considérable concernant l'observation des nombres de Hopf dans les isolants à deux bandes (Deng et al. 2017; Ünal et al. 2019; Schuster et al. 2021a; Schuster et al. 2021b). Ces propositions pourraient potentiellement être étendues aux isolants de Hopf multibandes (5.34) et (5.40). Plus particulièrement, pour l'isolant de Hopf à trois bandes $h_3^{\text{Hopf}}(\mathbf{k})$ (considéré comme un isolant topologique chiral), il existe déjà non seulement une proposition basée sur des atomes ultrafroids (Wang et al. 2014), mais aussi une réalisation expérimentale revendiquée basée sur l'analyse par apprentissage automatique d'un centre de vacance d'azote dans le diamant (Lian et al. 2019). Dans ces expériences, le semi-métal de Hopf topologique (5.26) est atteint à des valeurs de paramètres critiques correspondant à des transitions de phase topologiques.

Bibliography

- Abilio, C. C., P. Butaud, et al. (1999). “Magnetic Field Induced Localization in a Two-Dimensional Superconducting Wire Network”. *Phys. Rev. Lett.* 83, 5102. DOI: [10.1103/PhysRevLett.83.5102](https://doi.org/10.1103/PhysRevLett.83.5102).
- Abramowitz, M. and I. A. Stegun (1965). *Handbook of Mathematical Functions: With Formulas, Graphs, and Mathematical Tables*. Applied Mathematics Series. Dover Publications. ISBN: 9780486612720.
- Adams, E. N. (1952). “Motion of an Electron in a Perturbed Periodic Potential”. *Phys. Rev.* 85, 41. DOI: [10.1103/PhysRev.85.41](https://doi.org/10.1103/PhysRev.85.41).
- (1953a). “Magnetic Susceptibility of a Diamagnetic Electron Gas – The Role of Small Effective Electron Mass”. *Phys. Rev.* 89, 633. DOI: [10.1103/PhysRev.89.633](https://doi.org/10.1103/PhysRev.89.633).
- (1953b). “The Crystal Momentum as a Quantum Mechanical Operator”. *The Journal of Chemical Physics* 21, 2013. DOI: [10.1063/1.1698734](https://doi.org/10.1063/1.1698734).
- Adams, E. N. and E. I. Blount (1959). “Energy bands in the presence of an external force field – II: Anomalous velocities”. *Journal of Physics and Chemistry of Solids* 10.4, 286. DOI: [10.1016/0022-3697\(59\)90004-6](https://doi.org/10.1016/0022-3697(59)90004-6).
- Alexandradinata, A., Aleksandra Nelson, and Alexey A. Soluyanov (2021). “Teleportation of Berry curvature on the surface of a Hopf insulator”. *Phys. Rev. B* 103, 045107. DOI: [10.1103/PhysRevB.103.045107](https://doi.org/10.1103/PhysRevB.103.045107).
- Ando, Yoichi and Liang Fu (2015). “Topological Crystalline Insulators and Topological Superconductors: From Concepts to Materials”. *Annual Review of Condensed Matter Physics* 6, 361. DOI: [10.1146/annurev-conmatphys-031214-014501](https://doi.org/10.1146/annurev-conmatphys-031214-014501).
- Andrei, Eva Y. and Allan H. MacDonald (2020). “Graphene bilayers with a twist”. *Nature Materials* 19, 1265. DOI: [10.1038/s41563-020-00840-0](https://doi.org/10.1038/s41563-020-00840-0).
- Aoki, Hideo, Masato Ando, and Hajime Matsumura (1996). “Hofstadter butterflies for flat bands”. *Phys. Rev. B* 54, R17296. DOI: [10.1103/PhysRevB.54.R17296](https://doi.org/10.1103/PhysRevB.54.R17296).
- Armitage, N. P., E. J. Mele, and Ashvin Vishwanath (2018). “Weyl and Dirac semimetals in three-dimensional solids”. *Rev. Mod. Phys.* 90, 015001. DOI: [10.1103/RevModPhys.90.015001](https://doi.org/10.1103/RevModPhys.90.015001).
- Ashcroft, Neil W. and N. David Mermin (1976). *Solid State Physics*. New York: Holt, Rinehart and Winston. ISBN: 9780030839931.
- Avron, J. E., R. Seiler, and B. Simon (1983). “Homotopy and Quantization in Condensed Matter Physics”. *Phys. Rev. Lett.* 51, 51. DOI: [10.1103/PhysRevLett.51.51](https://doi.org/10.1103/PhysRevLett.51.51).
- Bansil, A., Hsin Lin, and Tanmoy Das (2016). “Colloquium: Topological band theory”. *Rev. Mod. Phys.* 88, 021004. DOI: [10.1103/RevModPhys.88.021004](https://doi.org/10.1103/RevModPhys.88.021004).
- Barnett, Ryan, G. R. Boyd, and Victor Galitski (2012). “SU(3) Spin-Orbit Coupling in Systems of Ultracold Atoms”. *Phys. Rev. Lett.* 109, 235308. DOI: [10.1103/PhysRevLett.109.235308](https://doi.org/10.1103/PhysRevLett.109.235308).

- Bauer, David, T. S. Jackson, and Rahul Roy (2016). “Quantum geometry and stability of the fractional quantum Hall effect in the Hofstadter model”. *Phys. Rev. B* 93, 235133. DOI: [10.1103/PhysRevB.93.235133](https://doi.org/10.1103/PhysRevB.93.235133).
- Bell, E. T. (1934). “Exponential Polynomials”. *Annals of Mathematics* 35.2, 258. DOI: [10.2307/1968431](https://doi.org/10.2307/1968431).
- Bena, Cristina and Gilles Montambaux (2009). “Remarks on the tight-binding model of graphene”. *New Journal of Physics* 11, 095003. DOI: [10.1088/1367-2630/11/9/095003](https://doi.org/10.1088/1367-2630/11/9/095003).
- Bender, Carl M. (2007). “Making sense of non-Hermitian Hamiltonians”. *Reports on Progress in Physics* 70, 947. DOI: [10.1088/0034-4885/70/6/r03](https://doi.org/10.1088/0034-4885/70/6/r03).
- Bercioux, D., D. F. Urban, et al. (2009). “Massless Dirac-Weyl fermions in a \mathcal{T}_3 optical lattice”. *Phys. Rev. A* 80, 063603. DOI: [10.1103/PhysRevA.80.063603](https://doi.org/10.1103/PhysRevA.80.063603).
- Bergholtz, Emil J. and Zhao Liu (2013). “Topological flat-band models and fractional Chern insulators”. *International Journal of Modern Physics B* 27.24, 1330017. DOI: [10.1142/s021797921330017x](https://doi.org/10.1142/s021797921330017x).
- Bergman, Doron L., Congjun Wu, and Leon Balents (2008). “Band touching from real-space topology in frustrated hopping models”. *Phys. Rev. B* 78, 125104. DOI: [10.1103/PhysRevB.78.125104](https://doi.org/10.1103/PhysRevB.78.125104).
- Berry, M. V. (1984). “Quantal Phase Factors Accompanying Adiabatic Changes”. *Proceedings of the Royal Society of London A* 392, 45. DOI: [10.1098/rspa.1984.0023](https://doi.org/10.1098/rspa.1984.0023).
- (1985). “Aspects of Degeneracy”. *Chaotic Behavior in Quantum Systems: Theory and Applications*. Ed. by Giulio Casati. Boston, MA: Springer US, pp. 123–140. ISBN: 9781461324430. DOI: [10.1007/978-1-4613-2443-0_8](https://doi.org/10.1007/978-1-4613-2443-0_8).
- (1989). “The Quantum Phase, Five Years After”. *Geometric Phases in Physics*. Ed. by F. Wilczek and A. Shapere. Advanced Series in Mathematical Physics. World Scientific. ISBN: 9789971506216. DOI: [10.1142/9789812798381_0001](https://doi.org/10.1142/9789812798381_0001).
- Bertlmann, Reinhold A. and Philipp Krammer (2008). “Bloch vectors for qudits”. *Journal of Physics A: Mathematical and Theoretical* 41, 235303. DOI: [10.1088/1751-8113/41/23/235303](https://doi.org/10.1088/1751-8113/41/23/235303).
- Bloch, Felix (1929). “Über die Quantenmechanik der Elektronen in Kristallgittern”. *Zeitschrift für Physik* 52, 555. DOI: [10.1007/BF01339455](https://doi.org/10.1007/BF01339455).
- Blok, M. S., V. V. Ramasesh, et al. (2021). “Quantum Information Scrambling on a Superconducting Qutrit Processor”. *Phys. Rev. X* 11, 021010. DOI: [10.1103/PhysRevX.11.021010](https://doi.org/10.1103/PhysRevX.11.021010).
- Blount, E. I. (1962a). “Bloch Electrons in a Magnetic Field”. *Phys. Rev.* 126, 1636. DOI: [10.1103/PhysRev.126.1636](https://doi.org/10.1103/PhysRev.126.1636).
- (1962b). “Formalisms of Band Theory”. *Solid State Physics*. Ed. by Frederick Seitz and David Turnbull. Vol. 13. Academic Press, pp. 305–373. DOI: [10.1016/S0081-1947\(08\)60459-2](https://doi.org/10.1016/S0081-1947(08)60459-2).
- Bouhon, Adrien, QuanSheng Wu, et al. (2020). “Non-Abelian reciprocal braiding of Weyl points and its manifestation in ZrTe”. *Nature Physics* 16, 1137. DOI: [10.1038/s41567-020-0967-9](https://doi.org/10.1038/s41567-020-0967-9).

- Bradlyn, Barry, Jennifer Cano, et al. (2016). “Beyond Dirac and Weyl fermions: Unconventional quasiparticles in conventional crystals”. *Science* 353.6299. DOI: [10.1126/science.aaf5037](https://doi.org/10.1126/science.aaf5037).
- Brillouin, L. (1930). “Les électrons libres dans les métaux et le rôle des réflexions de Bragg”. *Journal de Physique Radium* 1, 377. DOI: [10.1051/jphysrad:01930001011037700](https://doi.org/10.1051/jphysrad:01930001011037700).
- Brody, Dorje C. (2013). “Biorthogonal quantum mechanics”. *Journal of Physics A: Mathematical and Theoretical* 47, 035305. DOI: [10.1088/1751-8113/47/3/035305](https://doi.org/10.1088/1751-8113/47/3/035305).
- Burkov, A. A. and Leon Balents (2011). “Weyl Semimetal in a Topological Insulator Multilayer”. *Phys. Rev. Lett.* 107, 127205. DOI: [10.1103/PhysRevLett.107.127205](https://doi.org/10.1103/PhysRevLett.107.127205).
- Büttiker, M. (1988). “Absence of backscattering in the quantum Hall effect in multi-probe conductors”. *Phys. Rev. B* 38, 9375. DOI: [10.1103/PhysRevB.38.9375](https://doi.org/10.1103/PhysRevB.38.9375).
- Byrd, Mark S. and Navin Khaneja (2003). “Characterization of the positivity of the density matrix in terms of the coherence vector representation”. *Phys. Rev. A* 68, 062322. DOI: [10.1103/PhysRevA.68.062322](https://doi.org/10.1103/PhysRevA.68.062322).
- Călugăru, Dumitru, Aaron Chew, et al. (2021). “General construction and topological classification of crystalline flat bands”. *Nature Physics* 18, 185. DOI: [10.1038/s41567-021-01445-3](https://doi.org/10.1038/s41567-021-01445-3).
- Cano, Jennifer, Barry Bradlyn, and M. G. Vergniory (2019). “Multifold nodal points in magnetic materials”. *APL Materials* 7, 101125. DOI: [10.1063/1.5124314](https://doi.org/10.1063/1.5124314).
- Carmo, M. P. do (2016). *Differential Geometry of Curves and Surfaces: Revised and Updated Second Edition*. Dover Books on Mathematics. Dover Publications. ISBN: 9780486806990.
- Castro Neto, A. H., F. Guinea, et al. (2009). “The electronic properties of graphene”. *Rev. Mod. Phys.* 81, 109. DOI: [10.1103/revmodphys.81.109](https://doi.org/10.1103/revmodphys.81.109).
- Cayley, Arthur (1858). “II. A memoir on the theory of matrices”. *Philosophical Transactions of the Royal Society of London* 148, 17. DOI: [10.1098/rstl.1858.0002](https://doi.org/10.1098/rstl.1858.0002).
- Cayssol, J. and J. N. Fuchs (2021). “Topological and geometrical aspects of band theory”. *Journal of Physics: Materials* 4, 034007. DOI: [10.1088/2515-7639/abf0b5](https://doi.org/10.1088/2515-7639/abf0b5).
- Chang, Cui-Zu, Jinsong Zhang, et al. (2013). “Experimental Observation of the Quantum Anomalous Hall Effect in a Magnetic Topological Insulator”. *Science* 340.6129, 167. DOI: [10.1126/science.1234414](https://doi.org/10.1126/science.1234414).
- Chang, Guoqing, Su-Yang Xu, et al. (2017a). “Nexus fermions in topological symmorphic crystalline metals”. *Scientific Reports* 7, 1688. DOI: [10.1038/s41598-017-01523-8](https://doi.org/10.1038/s41598-017-01523-8).
- Chang, Guoqing, Su-Yang Xu, et al. (2017b). “Unconventional Chiral Fermions and Large Topological Fermi Arcs in RhSi”. *Phys. Rev. Lett.* 119, 206401. DOI: [10.1103/PhysRevLett.119.206401](https://doi.org/10.1103/PhysRevLett.119.206401).
- Chen, Kuang-Ting and Patrick A. Lee (2011). “Unified formalism for calculating polarization, magnetization, and more in a periodic insulator”. *Phys. Rev. B* 84, 205137. DOI: [10.1103/PhysRevB.84.205137](https://doi.org/10.1103/PhysRevB.84.205137).
- Chen, Li, Tahereh Mazaheri, et al. (2014). “The impossibility of exactly flat non-trivial Chern bands in strictly local periodic tight binding models”. *Journal of*

- Physics A: Mathematical and Theoretical* 47, 152001. DOI: [10.1088/1751-8113/47/15/152001](https://doi.org/10.1088/1751-8113/47/15/152001).
- Chen, Wen-Jie, Meng Xiao, and C. T. Chan (2016). “Photonic crystals possessing multiple Weyl points and the experimental observation of robust surface states”. *Nature Communications* 7, 13038. DOI: [10.1038/ncomms13038](https://doi.org/10.1038/ncomms13038).
- Cheng, Yang, Chen Huang, et al. (2019). “Emerging properties of two-dimensional twisted bilayer materials”. *Chinese Physics B* 28, 107304. DOI: [10.1088/1674-1056/ab3e46](https://doi.org/10.1088/1674-1056/ab3e46).
- Chiu, Ching-Kai, Jeffrey C. Y. Teo, et al. (2016). “Classification of topological quantum matter with symmetries”. *Rev. Mod. Phys.* 88, 035005. DOI: [10.1103/RevModPhys.88.035005](https://doi.org/10.1103/RevModPhys.88.035005).
- Comtet, L. (1974). *Advanced Combinatorics: The Art of Finite and Infinite Expansions*. Springer Netherlands. ISBN: 9789027704412.
- Cooper, N. R., J. Dalibard, and I. B. Spielman (2019). “Topological bands for ultracold atoms”. *Rev. Mod. Phys.* 91, 015005. DOI: [10.1103/RevModPhys.91.015005](https://doi.org/10.1103/RevModPhys.91.015005).
- Cortijo, Alberto (2016). “Linear magnetochiral effect in Weyl semimetals”. *Phys. Rev. B* 94, 241105. DOI: [10.1103/PhysRevB.94.241105](https://doi.org/10.1103/PhysRevB.94.241105).
- Delplace, P., D. Ullmo, and G. Montambaux (2011). “Zak phase and the existence of edge states in graphene”. *Phys. Rev. B* 84, 195452. DOI: [10.1103/PhysRevB.84.195452](https://doi.org/10.1103/PhysRevB.84.195452).
- Delplace, Pierre (2022). “Berry-Chern monopoles and spectral flows”. *SciPost Phys. Lect. Notes*, 39. DOI: [10.21468/SciPostPhysLectNotes.39](https://doi.org/10.21468/SciPostPhysLectNotes.39).
- Deng, D.-L., S.-T. Wang, et al. (2013). “Hopf insulators and their topologically protected surface states”. *Phys. Rev. B* 88, 201105. DOI: [10.1103/PhysRevB.88.201105](https://doi.org/10.1103/PhysRevB.88.201105).
- Deng, Dong-Ling, Sheng-Tao Wang, et al. (2017). “Probe Knots and Hopf Insulators with Ultracold Atoms”. *Chinese Physics Letters* 35, 013701. DOI: [10.1088/0256-307x/35/1/013701](https://doi.org/10.1088/0256-307x/35/1/013701).
- Derzhko, Oleg, Johannes Richter, and Mykola Maksymenko (2015). “Strongly correlated flat-band systems: The route from Heisenberg spins to Hubbard electrons”. *International Journal of Modern Physics B* 29.12, 1530007. DOI: [10.1142/S0217979215300078](https://doi.org/10.1142/S0217979215300078).
- Dias, R. G. and J. D. Gouveia (2015). “Origami rules for the construction of localized eigenstates of the Hubbard model in decorated lattices”. *Scientific Reports* 5, 16852. DOI: [10.1038/srep16852](https://doi.org/10.1038/srep16852).
- Dirac, Paul Adrien Maurice (1926). “On the theory of quantum mechanics”. *Proceedings of the Royal Society of London A* 112, 661. DOI: [10.1098/rspa.1926.0133](https://doi.org/10.1098/rspa.1926.0133).
- (1928). “The quantum theory of the electron”. *Proceedings of the Royal Society of London A* 117, 610. DOI: [10.1098/rspa.1928.0023](https://doi.org/10.1098/rspa.1928.0023).
- Dóra, Balázs, Janik Kailasvuori, and R. Moessner (2011). “Lattice generalization of the Dirac equation to general spin and the role of the flat band”. *Phys. Rev. B* 84, 195422. DOI: [10.1103/PhysRevB.84.195422](https://doi.org/10.1103/PhysRevB.84.195422).
- Drude, P. (1900). “Zur Elektronentheorie der Metalle”. *Annalen der Physik* 306.3, 566. DOI: [10.1002/andp.19003060312](https://doi.org/10.1002/andp.19003060312).

- Essin, Andrew M. and Victor Gurarie (2011). “Bulk-boundary correspondence of topological insulators from their respective Green’s functions”. *Phys. Rev. B* 84, 125132. DOI: [10.1103/PhysRevB.84.125132](https://doi.org/10.1103/PhysRevB.84.125132).
- Ezawa, Motohiko (2017). “Chiral anomaly enhancement and photoirradiation effects in multiband touching fermion systems”. *Phys. Rev. B* 95, 205201. DOI: [10.1103/PhysRevB.95.205201](https://doi.org/10.1103/PhysRevB.95.205201).
- Fang, Zhong, Naoto Nagaosa, et al. (2003). “The Anomalous Hall Effect and Magnetic Monopoles in Momentum Space”. *Science* 302.5642, 92. DOI: [10.1126/science.1089408](https://doi.org/10.1126/science.1089408).
- Fermi, Enrico (1926). “Zur Quantelung des idealen einatomigen Gases”. *Zeitschrift für Physik* 36, 902. DOI: [10.1007/BF01400221](https://doi.org/10.1007/BF01400221).
- Ferro, Florent and Frédéric Piéchon (n.d.). to be published.
- Flach, Sergej, Daniel Leykam, et al. (2014). “Detangling flat bands into Fano lattices”. *Europhysics Letters* 105, 30001. DOI: [10.1209/0295-5075/105/30001](https://doi.org/10.1209/0295-5075/105/30001).
- Fuchs, J. N., F. Piéchon, et al. (2010). “Topological Berry phase and semiclassical quantization of cyclotron orbits for two dimensional electrons in coupled band models”. *The European Physical Journal B* 77, 351. DOI: [10.1140/epjb/e2010-00259-2](https://doi.org/10.1140/epjb/e2010-00259-2).
- Fuchs, J. N., F. Piéchon, and G. Montambaux (2018). “Landau levels, response functions and magnetic oscillations from a generalized Onsager relation”. *SciPost Physics* 4, 024. DOI: [10.21468/SciPostPhys.4.5.024](https://doi.org/10.21468/SciPostPhys.4.5.024).
- Fukushima, Kenji, Dmitri E. Kharzeev, and Harmen J. Warringa (2008). “Chiral magnetic effect”. *Phys. Rev. D* 78, 074033. DOI: [10.1103/PhysRevD.78.074033](https://doi.org/10.1103/PhysRevD.78.074033).
- Fulga, I. C., L. Fallani, and M. Burrello (2018). “Geometrically protected triple-point crossings in an optical lattice”. *Phys. Rev. B* 97, 121402. DOI: [10.1103/PhysRevB.97.121402](https://doi.org/10.1103/PhysRevB.97.121402).
- Gantmacher, F. R. (1980). *The Theory of Matrices*. Chelsea Publishing Company.
- Gao, Yang and Qian Niu (2017). “Zero-field magnetic response functions in Landau levels”. *Proceedings of the National Academy of Sciences* 114.28, 7295. DOI: [10.1073/pnas.1702595114](https://doi.org/10.1073/pnas.1702595114).
- Gell-Mann, Murray (1962). “Symmetries of Baryons and Mesons”. *Phys. Rev.* 125, 1067. DOI: [10.1103/PhysRev.125.1067](https://doi.org/10.1103/PhysRev.125.1067).
- Giovannetti, Gianluca, Massimo Capone, et al. (2015). “Kekulé textures, pseudospin-one Dirac cones, and quadratic band crossings in a graphene-hexagonal indium chalcogenide bilayer”. *Phys. Rev. B* 91, 121417. DOI: [10.1103/PhysRevB.91.121417](https://doi.org/10.1103/PhysRevB.91.121417).
- Giovannetti, Gianluca, Petr A. Khomyakov, et al. (2007). “Substrate-induced band gap in graphene on hexagonal boron nitride: Ab initio density functional calculations”. *Phys. Rev. B* 76, 073103. DOI: [10.1103/PhysRevB.76.073103](https://doi.org/10.1103/PhysRevB.76.073103).
- Girvin, Steven M. (2005). “Introduction to the Fractional Quantum Hall Effect”. *The Quantum Hall Effect: Poincaré Seminar 2004*. Ed. by Benoît Douçot, Vincent Pasquier, et al. Basel: Birkhäuser Basel, pp. 133–162. ISBN: 9783764373931. DOI: [10.1007/3-7643-7393-8_4](https://doi.org/10.1007/3-7643-7393-8_4).

- Gómez-Santos, G. and T. Stauber (2011). “Measurable Lattice Effects on the Charge and Magnetic Response in Graphene”. *Phys. Rev. Lett.* 106, 045504. DOI: [10.1103/PhysRevLett.106.045504](https://doi.org/10.1103/PhysRevLett.106.045504).
- Goyal, Sandeep K., B. Neethi Simon, et al. (2016). “Geometry of the generalized Bloch sphere for qutrits”. *Journal of Physics A: Mathematical and Theoretical* 49, 165203. DOI: [10.1088/1751-8113/49/16/165203](https://doi.org/10.1088/1751-8113/49/16/165203).
- Graf, Ansgar, Raphael Kozlovsky, et al. (2020). “Theory of magnetotransport in shaped topological insulator nanowires”. *Phys. Rev. B* 102, 165105. DOI: [10.1103/PhysRevB.102.165105](https://doi.org/10.1103/PhysRevB.102.165105).
- Graf, Ansgar and Frédéric Piéchon (2021a). “Berry curvature and quantum metric in N -band systems: An eigenprojector approach”. *Phys. Rev. B* 104, 085114. DOI: [10.1103/PhysRevB.104.085114](https://doi.org/10.1103/PhysRevB.104.085114).
- (2021b). “Designing flat-band tight-binding models with tunable multifold band touching points”. *Phys. Rev. B* 104, 195128. DOI: [10.1103/PhysRevB.104.195128](https://doi.org/10.1103/PhysRevB.104.195128).
- Graf, Ansgar and Frédéric Piéchon (2022). *Multifold Hopf semimetals*. DOI: [10.48550/arxiv.2203.09966](https://doi.org/10.48550/arxiv.2203.09966).
- Green, Dmitry, Luiz Santos, and Claudio Chamon (2010). “Isolated flat bands and spin-1 conical bands in two-dimensional lattices”. *Phys. Rev. B* 82, 075104. DOI: [10.1103/PhysRevB.82.075104](https://doi.org/10.1103/PhysRevB.82.075104).
- Guo, H.-M. and M. Franz (2009a). “Three-Dimensional Topological Insulators on the Pyrochlore Lattice”. *Phys. Rev. Lett.* 103, 206805. DOI: [10.1103/PhysRevLett.103.206805](https://doi.org/10.1103/PhysRevLett.103.206805).
- (2009b). “Topological insulator on the kagome lattice”. *Phys. Rev. B* 80, 113102. DOI: [10.1103/PhysRevB.80.113102](https://doi.org/10.1103/PhysRevB.80.113102).
- Guzmán-Silva, D., C. Mejía-Cortés, et al. (2014). “Experimental observation of bulk and edge transport in photonic Lieb lattices”. *New Journal of Physics* 16, 063061. DOI: [10.1088/1367-2630/16/6/063061](https://doi.org/10.1088/1367-2630/16/6/063061).
- Habe, Tetsuro (2022). “Optical conductivity of the threefold Hopf semimetal”. *Phys. Rev. B* 106, 205204. DOI: [10.1103/PhysRevB.106.205204](https://doi.org/10.1103/PhysRevB.106.205204).
- Haldane, F. D. M. (1988). “Model for a Quantum Hall Effect without Landau Levels: Condensed-Matter Realization of the ”Parity Anomaly””. *Phys. Rev. Lett.* 61, 2015. DOI: [10.1103/PhysRevLett.61.2015](https://doi.org/10.1103/PhysRevLett.61.2015).
- Haldane, F. Duncan M. (2017). “Nobel Lecture: Topological quantum matter”. *Rev. Mod. Phys.* 89, 040502. DOI: [10.1103/RevModPhys.89.040502](https://doi.org/10.1103/RevModPhys.89.040502).
- Halmos, P. R. (2017). *Finite-Dimensional Vector Spaces: Second Edition*. Dover Books on Mathematics. Dover Publications. ISBN: 9780486822266.
- Halperin, B. I. (1982). “Quantized Hall conductance, current-carrying edge states, and the existence of extended states in a two-dimensional disordered potential”. *Phys. Rev. B* 25, 2185. DOI: [10.1103/PhysRevB.25.2185](https://doi.org/10.1103/PhysRevB.25.2185).
- Hao, Ningning, Ping Zhang, et al. (2008). “Topological edge states and quantum Hall effect in the Haldane model”. *Phys. Rev. B* 78, 075438. DOI: [10.1103/PhysRevB.78.075438](https://doi.org/10.1103/PhysRevB.78.075438).
- Harriman, John E. (1978). “Geometry of density matrices. I. Definitions, N matrices and 1 matrices”. *Phys. Rev. A* 17, 1249. DOI: [10.1103/PhysRevA.17.1249](https://doi.org/10.1103/PhysRevA.17.1249).

- Hasan, M. Z. and C. L. Kane (2010). “Colloquium: Topological insulators”. *Rev. Mod. Phys.* 82, 3045. DOI: [10.1103/RevModPhys.82.3045](https://doi.org/10.1103/RevModPhys.82.3045).
- Hasan, M. Zahid and Joel E. Moore (2011). “Three-Dimensional Topological Insulators”. *Annual Review of Condensed Matter Physics* 2, 55. DOI: [10.1146/annurev-conmatphys-062910-140432](https://doi.org/10.1146/annurev-conmatphys-062910-140432).
- Hase, I., T. Yanagisawa, et al. (2018). “Possibility of Flat-Band Ferromagnetism in Hole-Doped Pyrochlore Oxides $\text{Sn}_2\text{Nb}_2\text{O}_7$ and $\text{Sn}_2\text{Ta}_2\text{O}_7$ ”. *Phys. Rev. Lett.* 120, 196401. DOI: [10.1103/PhysRevLett.120.196401](https://doi.org/10.1103/PhysRevLett.120.196401).
- Hase, Izumi, Takashi Yanagisawa, and Kenji Kawashima (2019). “Flat-band in pyrochlore oxides: a first-principles study”. *Nanomaterials* 9.6, 876. DOI: [10.3390/nano9060876](https://doi.org/10.3390/nano9060876).
- Hatsugai, Y. (1997). “Topological aspects of the quantum Hall effect”. *Journal of Physics: Condensed Matter* 9, 2507. DOI: [10.1088/0953-8984/9/12/003](https://doi.org/10.1088/0953-8984/9/12/003).
- He, Ke, Yayu Wang, and Qi-Kun Xue (2018). “Topological Materials: Quantum Anomalous Hall System”. *Annual Review of Condensed Matter Physics* 9, 329. DOI: [10.1146/annurev-conmatphys-033117-054144](https://doi.org/10.1146/annurev-conmatphys-033117-054144).
- He, Lixin and David Vanderbilt (2001). “Exponential Decay Properties of Wannier Functions and Related Quantities”. *Phys. Rev. Lett.* 86, 5341. DOI: [10.1103/PhysRevLett.86.5341](https://doi.org/10.1103/PhysRevLett.86.5341).
- Hioe, F. T. and J. H. Eberly (1981). “ N -Level Coherence Vector and Higher Conservation Laws in Quantum Optics and Quantum Mechanics”. *Phys. Rev. Lett.* 47, 838. DOI: [10.1103/PhysRevLett.47.838](https://doi.org/10.1103/PhysRevLett.47.838).
- Hopf, Heinz (1931). “Über die Abbildungen der dreidimensionalen Sphäre auf die Kugelfläche”. *Mathematische Annalen* 104, 637. DOI: [10.1007/BF01457962](https://doi.org/10.1007/BF01457962).
- Horiguchi, T. and C. C. Chen (1974). “Lattice Green’s function for the diced lattice”. *Journal of Mathematical Physics* 15, 659. DOI: [10.1063/1.1666703](https://doi.org/10.1063/1.1666703).
- Horn, R. A. and C. R. Johnson (2013). *Matrix Analysis*. Cambridge University Press. ISBN: 9780521839402.
- Hu, Haiping, Junpeng Hou, et al. (2018). “Topological Triply Degenerate Points Induced by Spin-Tensor-Momentum Couplings”. *Phys. Rev. Lett.* 120, 240401. DOI: [10.1103/PhysRevLett.120.240401](https://doi.org/10.1103/PhysRevLett.120.240401).
- Huhtinen, Kukka-Emilia, Jonah Herzog-Arbeitman, et al. (2022). “Revisiting flat band superconductivity: Dependence on minimal quantum metric and band touchings”. *Phys. Rev. B* 106, 014518. DOI: [10.1103/PhysRevB.106.014518](https://doi.org/10.1103/PhysRevB.106.014518).
- Hwang, Yoonseok, Junyeong Ahn, and Bohm-Jung Yang (2019). “Fragile topology protected by inversion symmetry: Diagnosis, bulk-boundary correspondence, and Wilson loop”. *Phys. Rev. B* 100, 205126. DOI: [10.1103/PhysRevB.100.205126](https://doi.org/10.1103/PhysRevB.100.205126).
- Hwang, Yoonseok, Jun-Won Rhim, and Bohm-Jung Yang (2021). “General construction of flat bands with and without band crossings based on wave function singularity”. *Phys. Rev. B* 104, 085144. DOI: [10.1103/PhysRevB.104.085144](https://doi.org/10.1103/PhysRevB.104.085144).
- Isaev, L., Y. H. Moon, and G. Ortiz (2011). “Bulk-boundary correspondence in three-dimensional topological insulators”. *Phys. Rev. B* 84, 075444. DOI: [10.1103/PhysRevB.84.075444](https://doi.org/10.1103/PhysRevB.84.075444).
- Jackson, J. D. (2012). *Classical Electrodynamics*. Wiley. ISBN: 9788126510948.

- Jakóbczyk, L. and M. Siennicki (2001). “Geometry of Bloch vectors in two-qubit system”. *Physics Letters A* 286.6, 383. DOI: [10.1016/S0375-9601\(01\)00455-8](https://doi.org/10.1016/S0375-9601(01)00455-8).
- Jotzu, Gregor, Michael Messer, et al. (2014). “Experimental realization of the topological Haldane model with ultracold fermions”. *Nature* 515, 237. DOI: [10.1038/nature13915](https://doi.org/10.1038/nature13915).
- Kane, C. L. (2013). “Topological Band Theory and the Z_2 Invariant”. *Topological Insulators*. Ed. by Marcel Franz and Laurens Molenkamp. Vol. 6. Contemporary Concepts of Condensed Matter Science. Elsevier, pp. 3–34. DOI: [10.1016/B978-0-444-63314-9.00001-9](https://doi.org/10.1016/B978-0-444-63314-9.00001-9).
- Kane, C. L. and E. J. Mele (2005). “Quantum Spin Hall Effect in Graphene”. *Phys. Rev. Lett.* 95, 226801. DOI: [10.1103/PhysRevLett.95.226801](https://doi.org/10.1103/PhysRevLett.95.226801).
- Kang, Mingu, Linda Ye, et al. (2020). “Dirac fermions and flat bands in the ideal kagome metal FeSn”. *Nature Materials* 19, 163. DOI: [10.1038/s41563-019-0531-0](https://doi.org/10.1038/s41563-019-0531-0).
- Kaplan, L. M. and M. Resnikoff (1967). “Matrix Products and the Explicit 3, 6, 9, and 12-j Coefficients of the Regular Representation of $SU(n)$ ”. *Journal of Mathematical Physics* 8, 2194. DOI: [10.1063/1.1705141](https://doi.org/10.1063/1.1705141).
- Karplus, Robert and J. M. Luttinger (1954). “Hall Effect in Ferromagnetics”. *Phys. Rev.* 95, 1154. DOI: [10.1103/PhysRev.95.1154](https://doi.org/10.1103/PhysRev.95.1154).
- Kennedy, Ricardo (2016). “Topological Hopf-Chern insulators and the Hopf superconductor”. *Phys. Rev. B* 94, 035137. DOI: [10.1103/PhysRevB.94.035137](https://doi.org/10.1103/PhysRevB.94.035137).
- Kimura, Gen (2003). “The Bloch vector for N -level systems”. *Physics Letters A* 314.5, 339. DOI: [10.1016/S0375-9601\(03\)00941-1](https://doi.org/10.1016/S0375-9601(03)00941-1).
- Kimura, Gen and Andrzej Kossakowski (2005). “The Bloch-Vector Space for N -Level Systems: the Spherical-Coordinate Point of View”. *Open Syst. Inf. Dyn.* 12.03, 207. DOI: [10.1007/s11080-005-0919-y](https://doi.org/10.1007/s11080-005-0919-y).
- Klinkhamer, F. R. and G. E. Volovik (2005). “Emergent CPT violation from the splitting of Fermi points”. *International Journal of Modern Physics A* 20.13, 2795. DOI: [10.1142/S0217751X05020902](https://doi.org/10.1142/S0217751X05020902).
- Klitzing, K. v., G. Dorda, and M. Pepper (1980). “New Method for High-Accuracy Determination of the Fine-Structure Constant Based on Quantized Hall Resistance”. *Phys. Rev. Lett.* 45, 494. DOI: [10.1103/PhysRevLett.45.494](https://doi.org/10.1103/PhysRevLett.45.494).
- Kohmoto, Mahito (1985). “Topological invariant and the quantization of the Hall conductance”. *Annals of Physics* 160.2, 343. DOI: [10.1016/0003-4916\(85\)90148-4](https://doi.org/10.1016/0003-4916(85)90148-4).
- Kolodrubetz, Michael, Dries Sels, et al. (2017). “Geometry and non-adiabatic response in quantum and classical systems”. *Physics Reports* 697, 1. DOI: [10.1016/j.physrep.2017.07.001](https://doi.org/10.1016/j.physrep.2017.07.001).
- Könye, Viktor and Masao Ogata (2021). “Microscopic theory of magnetoconductivity at low magnetic fields in terms of Berry curvature and orbital magnetic moment”. *Phys. Rev. Research* 3, 033076. DOI: [10.1103/PhysRevResearch.3.033076](https://doi.org/10.1103/PhysRevResearch.3.033076).
- Kozlovsky, Raphael, Ansgar Graf, et al. (2020). “Magnetoconductance, Quantum Hall Effect, and Coulomb Blockade in Topological Insulator Nanocones”. *Phys. Rev. Lett.* 124, 126804. DOI: [10.1103/PhysRevLett.124.126804](https://doi.org/10.1103/PhysRevLett.124.126804).

- Kundu, Anirban, Zhuo Bin Siu, et al. (2020). “Magnetotransport of Weyl semimetals with tilted Dirac cones”. *New Journal of Physics* 22, 083081. DOI: [10.1088/1367-2630/aba98d](https://doi.org/10.1088/1367-2630/aba98d).
- Kusnezov, Dimitri (1995). “Exact matrix expansions for group elements of $SU(N)$ ”. *Journal of Mathematical Physics* 36, 898. DOI: [10.1063/1.531165](https://doi.org/10.1063/1.531165).
- König, Markus, Steffen Wiedmann, et al. (2007). “Quantum Spin Hall Insulator State in HgTe Quantum Wells”. *Science* 318.5851, 766. DOI: [10.1126/science.1148047](https://doi.org/10.1126/science.1148047).
- Lan, Z., N. Goldman, et al. (2011). “Dirac-Weyl fermions with arbitrary spin in two-dimensional optical superlattices”. *Phys. Rev. B* 84, 165115. DOI: [10.1103/PhysRevB.84.165115](https://doi.org/10.1103/PhysRevB.84.165115).
- Landau, L. D. (1930). “Diamagnetismus der Metalle”. *Zeitschrift für Physik* 64, 629. DOI: [10.1007/BF01397213](https://doi.org/10.1007/BF01397213).
- Lapierre, Bastien, Titus Neupert, and Luka Trifunovic (2021). “ N -band Hopf insulator”. *Phys. Rev. Research* 3, 033045. DOI: [10.1103/PhysRevResearch.3.033045](https://doi.org/10.1103/PhysRevResearch.3.033045).
- Larson, Jonas, Erik Sjöqvist, and Patrik Öhberg (2020). *Conical Intersections in Physics*. Vol. 965. Lecture Notes in Physics. Springer. ISBN: 9783030348816. DOI: [10.1007/978-3-030-34882-3](https://doi.org/10.1007/978-3-030-34882-3).
- Lee, Chi-Cheng, Antoine Fleurence, et al. (2019). “Hidden mechanism for embedding the flat bands of Lieb, kagome, and checkerboard lattices in other structures”. *Phys. Rev. B* 100, 045150. DOI: [10.1103/PhysRevB.100.045150](https://doi.org/10.1103/PhysRevB.100.045150).
- Lee, Soo-Yong, Jin-Hong Park, et al. (2015). “Arbitrary Chern Number Generation in the Three-Band Model from Momentum Space”. *Journal of the Physical Society of Japan* 84, 064005. DOI: [10.7566/JPSJ.84.064005](https://doi.org/10.7566/JPSJ.84.064005).
- Leykam, Daniel, Alexei Andreanov, and Sergej Flach (2018). “Artificial flat band systems: from lattice models to experiments”. *Advances in Physics: X* 3.1, 1473052. DOI: [10.1080/23746149.2018.1473052](https://doi.org/10.1080/23746149.2018.1473052).
- Li, Weifeng, Meng Guo, et al. (2014). “Gapless MoS_2 allotrope possessing both massless Dirac and heavy fermions”. *Phys. Rev. B* 89, 205402. DOI: [10.1103/PhysRevB.89.205402](https://doi.org/10.1103/PhysRevB.89.205402).
- Li, Xiao, Bitan Roy, and S. Das Sarma (2016). “Weyl fermions with arbitrary monopoles in magnetic fields: Landau levels, longitudinal magnetotransport, and density-wave ordering”. *Phys. Rev. B* 94, 195144. DOI: [10.1103/PhysRevB.94.195144](https://doi.org/10.1103/PhysRevB.94.195144).
- Lian, Wenqian, Sheng-Tao Wang, et al. (2019). “Machine Learning Topological Phases with a Solid-State Quantum Simulator”. *Phys. Rev. Lett.* 122, 210503. DOI: [10.1103/PhysRevLett.122.210503](https://doi.org/10.1103/PhysRevLett.122.210503).
- Liang, Long, Tuomas I. Vanhala, et al. (2017). “Band geometry, Berry curvature, and superfluid weight”. *Phys. Rev. B* 95, 024515. DOI: [10.1103/PhysRevB.95.024515](https://doi.org/10.1103/PhysRevB.95.024515).
- Liang, Long and Yue Yu (2016). “Semimetal with both Rarita-Schwinger-Weyl and Weyl excitations”. *Phys. Rev. B* 93, 045113. DOI: [10.1103/PhysRevB.93.045113](https://doi.org/10.1103/PhysRevB.93.045113).
- Lieb, Elliott H. (1989). “Two theorems on the Hubbard model”. *Phys. Rev. Lett.* 62, 1201. DOI: [10.1103/PhysRevLett.62.1201](https://doi.org/10.1103/PhysRevLett.62.1201).
- Lin, Yu-Ping and Wei-Han Hsiao (2021). “Dual Haldane sphere and quantized band geometry in chiral multifold fermions”. *Phys. Rev. B* 103, L081103. DOI: [10.1103/PhysRevB.103.L081103](https://doi.org/10.1103/PhysRevB.103.L081103).

- Lin, Zhiyong, Jin-Ho Choi, et al. (2018). “Flatbands and Emergent Ferromagnetic Ordering in Fe_3Sn_2 Kagome Lattices”. *Phys. Rev. Lett.* 121, 096401. DOI: [10.1103/PhysRevLett.121.096401](https://doi.org/10.1103/PhysRevLett.121.096401).
- Liu, Chunxiao, Farzan Vafa, and Cenke Xu (2017). “Symmetry-protected topological Hopf insulator and its generalizations”. *Phys. Rev. B* 95, 161116. DOI: [10.1103/PhysRevB.95.161116](https://doi.org/10.1103/PhysRevB.95.161116).
- Liu, Enke, Yan Sun, et al. (2018). “Giant anomalous Hall effect in a ferromagnetic kagome-lattice semimetal”. *Nature physics* 14, 1125. DOI: [10.1038/s41567-018-0234-5](https://doi.org/10.1038/s41567-018-0234-5).
- Liu, Zheng, Feng Liu, and Yong-Shi Wu (2014). “Exotic electronic states in the world of flat bands: From theory to material”. *Chinese Physics B* 23, 077308. DOI: [10.1088/1674-1056/23/7/077308](https://doi.org/10.1088/1674-1056/23/7/077308).
- Liu, Zhonghao, Man Li, et al. (2020). “Orbital-selective Dirac fermions and extremely flat bands in frustrated kagome-lattice metal CoSn ”. *Nature Communications* 11, 4002. DOI: [10.1038/s41467-020-17462-4](https://doi.org/10.1038/s41467-020-17462-4).
- London, Fritz and Heinz London (1935). “The electromagnetic equations of the superconductor”. *Proceedings of the Royal Society of London A* 149, 71. DOI: [10.1098/rspa.1935.0048](https://doi.org/10.1098/rspa.1935.0048).
- Lu, Ling, Zhiyu Wang, et al. (2015). “Experimental observation of Weyl points”. *Science* 349.6248, 622. DOI: [10.1126/science.aaa9273](https://doi.org/10.1126/science.aaa9273).
- Luttinger, J. M. and W. Kohn (1955). “Motion of Electrons and Holes in Perturbed Periodic Fields”. *Phys. Rev.* 97, 869. DOI: [10.1103/PhysRev.97.869](https://doi.org/10.1103/PhysRev.97.869).
- Lv, B. Q., Z.-L. Feng, et al. (2017). “Observation of three-component fermions in the topological semimetal molybdenum phosphide”. *Nature* 546, 627. DOI: [10.1038/nature22390](https://doi.org/10.1038/nature22390).
- Lv, B. Q., Z.-L. Feng, et al. (2019). “Observation of multiple types of topological fermions in PdBiSe ”. *Phys. Rev. B* 99, 241104. DOI: [10.1103/PhysRevB.99.241104](https://doi.org/10.1103/PhysRevB.99.241104).
- Lv, B. Q., T. Qian, and H. Ding (2021). “Experimental perspective on three-dimensional topological semimetals”. *Rev. Mod. Phys.* 93, 025002. DOI: [10.1103/RevModPhys.93.025002](https://doi.org/10.1103/RevModPhys.93.025002).
- Ma, Da-Shuai, Yuanfeng Xu, et al. (2020a). “Spin-Orbit-Induced Topological Flat Bands in Line and Split Graphs of Bipartite Lattices”. *Phys. Rev. Lett.* 125, 266403. DOI: [10.1103/PhysRevLett.125.266403](https://doi.org/10.1103/PhysRevLett.125.266403).
- Ma, J.-Z., J.-B. He, et al. (2018). “Three-component fermions with surface Fermi arcs in tungsten carbide”. *Nature Physics* 14, 349. DOI: [10.1038/s41567-017-0021-8](https://doi.org/10.1038/s41567-017-0021-8).
- Ma, Jina, Jun-Won Rhim, et al. (2020b). “Direct Observation of Flatband Loop States Arising from Nontrivial Real-Space Topology”. *Phys. Rev. Lett.* 124, 183901. DOI: [10.1103/PhysRevLett.124.183901](https://doi.org/10.1103/PhysRevLett.124.183901).
- Mañes, J. L. (2012). “Existence of bulk chiral fermions and crystal symmetry”. *Phys. Rev. B* 85, 155118. DOI: [10.1103/PhysRevB.85.155118](https://doi.org/10.1103/PhysRevB.85.155118).
- Macdonald, I. G. (1998). *Symmetric Functions and Hall Polynomials*. Oxford Classic Texts in the Physical Sciences. Clarendon Press. ISBN: 9780198504504.

- Macfarlane, A. J., A. Sudbery, and P. H. Weisz (1968). “On Gell-Mann’s λ -matrices, d- and f-tensors, octets, and parametrizations of SU(3)”. *Communications in Mathematical Physics* 11, 77. DOI: [10.1007/BF01654302](https://doi.org/10.1007/BF01654302).
- Maciejko, Joseph, Taylor L. Hughes, and Shou-Cheng Zhang (2011). “The Quantum Spin Hall Effect”. *Annual Review of Condensed Matter Physics* 2, 31. DOI: [10.1146/annurev-conmatphys-062910-140538](https://doi.org/10.1146/annurev-conmatphys-062910-140538).
- Maimaiti, Wulayimu, Alexei Andreanov, and Sergej Flach (2021). “Flat-band generator in two dimensions”. *Phys. Rev. B* 103, 165116. DOI: [10.1103/PhysRevB.103.165116](https://doi.org/10.1103/PhysRevB.103.165116).
- Maimaiti, Wulayimu, Alexei Andreanov, et al. (2017). “Compact localized states and flat-band generators in one dimension”. *Phys. Rev. B* 95, 115135. DOI: [10.1103/PhysRevB.95.115135](https://doi.org/10.1103/PhysRevB.95.115135).
- Maimaiti, Wulayimu, Sergej Flach, and Alexei Andreanov (2019). “Universal $d = 1$ flat band generator from compact localized states”. *Phys. Rev. B* 99, 125129. DOI: [10.1103/PhysRevB.99.125129](https://doi.org/10.1103/PhysRevB.99.125129).
- Malcolm, J. D. and E. J. Nicol (2015). “Magneto-optics of massless Kane fermions: Role of the flat band and unusual Berry phase”. *Phys. Rev. B* 92, 035118. DOI: [10.1103/PhysRevB.92.035118](https://doi.org/10.1103/PhysRevB.92.035118).
- Matsuura, Shunji, Po-Yao Chang, et al. (2013). “Protected boundary states in gapless topological phases”. *New Journal of Physics* 15, 065001. DOI: [10.1088/1367-2630/15/6/065001](https://doi.org/10.1088/1367-2630/15/6/065001).
- Mendaš, Istok P. (2006). “The classification of three-parameter density matrices for a qutrit”. *Journal of Physics A: Mathematical and General* 39, 11313. DOI: [10.1088/0305-4470/39/36/012](https://doi.org/10.1088/0305-4470/39/36/012).
- Meyer, A. J. P. and G. Asch (1961). “Experimental g' and g Values of Fe, Co, Ni, and Their Alloys”. *Journal of Applied Physics* 32, S330. DOI: [10.1063/1.2000457](https://doi.org/10.1063/1.2000457).
- Mielke, A (1991a). “Ferromagnetic ground states for the Hubbard model on line graphs”. *Journal of Physics A: Mathematical and General* 24, L73. DOI: [10.1088/0305-4470/24/2/005](https://doi.org/10.1088/0305-4470/24/2/005).
- (1991b). “Ferromagnetism in the Hubbard model on line graphs and further considerations”. *Journal of Physics A: Mathematical and General* 24, 3311. DOI: [10.1088/0305-4470/24/14/018](https://doi.org/10.1088/0305-4470/24/14/018).
- Mikitik, G. P. and Yu. V. Sharlai (1999). “Manifestation of Berry’s Phase in Metal Physics”. *Phys. Rev. Lett.* 82, 2147. DOI: [10.1103/PhysRevLett.82.2147](https://doi.org/10.1103/PhysRevLett.82.2147).
- Mitscherling, Johannes and Tobias Holder (2022). “Bound on resistivity in flat-band materials due to the quantum metric”. *Phys. Rev. B* 105, 085154. DOI: [10.1103/PhysRevB.105.085154](https://doi.org/10.1103/PhysRevB.105.085154).
- Miyahara, Shin, Kenn Kubo, et al. (2005). “Flat-Bands on Partial Line Graphs – Systematic Method for Generating Flat-Band Lattice Structure”. *Journal of the Physical Society of Japan* 74, 1918. DOI: [10.1143/JPSJ.74.1918](https://doi.org/10.1143/JPSJ.74.1918).
- Mizoguchi, T. and Y. Hatsugai (2019). “Molecular-orbital representation of generic flat-band models”. *Europhysics Letters* 127, 47001. DOI: [10.1209/0295-5075/127/47001](https://doi.org/10.1209/0295-5075/127/47001).
- Mogera, Umesha and Giridhar U. Kulkarni (2020). “A new twist in graphene research: Twisted graphene”. *Carbon* 156, 470. DOI: [10.1016/j.carbon.2019.09.053](https://doi.org/10.1016/j.carbon.2019.09.053).

- Monarkha, Yu. P. and V. E. Syvokon (2012). “A two-dimensional Wigner crystal (Review Article)”. *Low Temperature Physics* 38, 1067. DOI: [10.1063/1.4770504](https://doi.org/10.1063/1.4770504).
- Mong, Roger S. K. and Vasudha Shivamoggi (2011). “Edge states and the bulk-boundary correspondence in Dirac Hamiltonians”. *Phys. Rev. B* 83, 125109. DOI: [10.1103/PhysRevB.83.125109](https://doi.org/10.1103/PhysRevB.83.125109).
- Moore, Joel E., Ying Ran, and Xiao-Gang Wen (2008). “Topological Surface States in Three-Dimensional Magnetic Insulators”. *Phys. Rev. Lett.* 101, 186805. DOI: [10.1103/PhysRevLett.101.186805](https://doi.org/10.1103/PhysRevLett.101.186805).
- Morales-Inostroza, Luis and Rodrigo A. Vicencio (2016). “Simple method to construct flat-band lattices”. *Phys. Rev. A* 94, 043831. DOI: [10.1103/PhysRevA.94.043831](https://doi.org/10.1103/PhysRevA.94.043831).
- Morfonios, C. V., M. Röntgen, et al. (2021). “Flat bands by latent symmetry”. *Phys. Rev. B* 104, 035105. DOI: [10.1103/PhysRevB.104.035105](https://doi.org/10.1103/PhysRevB.104.035105).
- Mukherjee, Seabratra, Alexander Spracklen, et al. (2015). “Observation of a Localized Flat-Band State in a Photonic Lieb Lattice”. *Phys. Rev. Lett.* 114, 245504. DOI: [10.1103/PhysRevLett.114.245504](https://doi.org/10.1103/PhysRevLett.114.245504).
- Nagaosa, Naoto, Jairo Sinova, et al. (2010). “Anomalous Hall effect”. *Rev. Mod. Phys.* 82, 1539. DOI: [10.1103/RevModPhys.82.1539](https://doi.org/10.1103/RevModPhys.82.1539).
- Naud, Cécile, Giancarlo Faini, and Dominique Mailly (2001). “Aharonov-Bohm Cages in 2D Normal Metal Networks”. *Phys. Rev. Lett.* 86, 5104. DOI: [10.1103/PhysRevLett.86.5104](https://doi.org/10.1103/PhysRevLett.86.5104).
- Nelson, Aleksandra, Titus Neupert, et al. (2021). “Multicellularity of Delicate Topological Insulators”. *Phys. Rev. Lett.* 126, 216404. DOI: [10.1103/PhysRevLett.126.216404](https://doi.org/10.1103/PhysRevLett.126.216404).
- Nelson, Aleksandra, Titus Neupert, et al. (2022). “Delicate topology protected by rotation symmetry: Crystalline Hopf insulators and beyond”. *Phys. Rev. B* 106, 075124. DOI: [10.1103/PhysRevB.106.075124](https://doi.org/10.1103/PhysRevB.106.075124).
- Neupert, Titus, M. Michael Denner, et al. (2022). “Charge order and superconductivity in kagome materials”. *Nature Physics* 18, 137. DOI: [10.1038/s41567-021-01404-y](https://doi.org/10.1038/s41567-021-01404-y).
- Neupert, Titus, Luiz Santos, et al. (2012). “Noncommutative geometry for three-dimensional topological insulators”. *Phys. Rev. B* 86, 035125. DOI: [10.1103/PhysRevB.86.035125](https://doi.org/10.1103/PhysRevB.86.035125).
- Nielsen, H. B. and M. Ninomiya (1981). “A no-go theorem for regularizing chiral fermions”. *Physics Letters B* 105.2, 219. DOI: [10.1016/0370-2693\(81\)91026-1](https://doi.org/10.1016/0370-2693(81)91026-1).
- Nielsen, H. B. and Masao Ninomiya (1983). “The Adler-Bell-Jackiw anomaly and Weyl fermions in a crystal”. *Physics Letters B* 130.6, 389. DOI: [10.1016/0370-2693\(83\)91529-0](https://doi.org/10.1016/0370-2693(83)91529-0).
- Nishino, Shinya and Masaki Goda (2005). “Three-dimensional Flat-Band Models”. *Journal of the Physical Society of Japan* 74, 393. DOI: [10.1143/JPSJ.74.393](https://doi.org/10.1143/JPSJ.74.393).
- Nishino, Shinya, Masaki Goda, and Koichi Kusakabe (2003). “Flat Bands of a Tight-Binding Electronic System with Hexagonal Structure”. *Journal of the Physical Society of Japan* 72, 2015. DOI: [10.1143/JPSJ.72.2015](https://doi.org/10.1143/JPSJ.72.2015).
- Niu, Qian and D. J. Thouless (1987). “Quantum Hall effect with realistic boundary conditions”. *Phys. Rev. B* 35, 2188. DOI: [10.1103/PhysRevB.35.2188](https://doi.org/10.1103/PhysRevB.35.2188).

- Norman, M. R. (2016). “Colloquium: Herbertsmithite and the search for the quantum spin liquid”. *Rev. Mod. Phys.* 88, 041002. DOI: [10.1103/RevModPhys.88.041002](https://doi.org/10.1103/RevModPhys.88.041002).
- Novoselov, K. S., A. K. Geim, et al. (2004). “Electric Field Effect in Atomically Thin Carbon Films”. *Science* 306.5696, 666. DOI: [10.1126/science.1102896](https://doi.org/10.1126/science.1102896).
- Ogata, Toshitaka, Mitsuaki Kawamura, and Taisuke Ozaki (2021). “Methods for constructing parameter-dependent flat-band lattices”. *Phys. Rev. B* 103, 205119. DOI: [10.1103/PhysRevB.103.205119](https://doi.org/10.1103/PhysRevB.103.205119).
- Onsager, L. (1952). “Interpretation of the de Haas-van Alphen effect”. *The London, Edinburgh, and Dublin Philosophical Magazine and Journal of Science* 43.344, 1006. DOI: [10.1080/14786440908521019](https://doi.org/10.1080/14786440908521019).
- Ortiz, Brenden R., Lídia C. Gomes, et al. (2019). “New kagome prototype materials: discovery of KV_3Sb_5 , RbV_3Sb_5 , and CsV_3Sb_5 ”. *Phys. Rev. Materials* 3, 094407. DOI: [10.1103/PhysRevMaterials.3.094407](https://doi.org/10.1103/PhysRevMaterials.3.094407).
- Ouyang, Fangping, Shenglin Peng, et al. (2011). “Bandgap opening in graphene antidot lattices: the missing half”. *ACS Nano* 5.5, 4023. DOI: [10.1021/nn200580w](https://doi.org/10.1021/nn200580w).
- Ozawa, Tomoki, Hannah M. Price, et al. (2019). “Topological photonics”. *Rev. Mod. Phys.* 91, 015006. DOI: [10.1103/RevModPhys.91.015006](https://doi.org/10.1103/RevModPhys.91.015006).
- Palumbo, Giandomenico and Nathan Goldman (2018). “Revealing Tensor Monopoles through Quantum-Metric Measurements”. *Phys. Rev. Lett.* 121, 170401. DOI: [10.1103/PhysRevLett.121.170401](https://doi.org/10.1103/PhysRevLett.121.170401).
- Parameswaran, Siddharth A., Rahul Roy, and Shivaji L. Sondhi (2013). “Fractional quantum Hall physics in topological flat bands”. *Comptes Rendus Physique* 14.9-10, 816. DOI: [10.1016/j.crhy.2013.04.003](https://doi.org/10.1016/j.crhy.2013.04.003).
- Pauli, W. (1925). “Über den Zusammenhang des Abschlusses der Elektronengruppen im Atom mit der Komplexstruktur der Spektren”. *Zeitschrift für Physik* 31, 765. DOI: [10.1007/BF02980631](https://doi.org/10.1007/BF02980631).
- Peierls, Rudolph (1933). “Zur Theorie des Diamagnetismus von Leitungselektronen”. *Zeitschrift für Physik* 80, 763. DOI: [10.1007/BF01342591](https://doi.org/10.1007/BF01342591).
- Peotta, Sebastiano and Päivi Törmä (2015). “Superfluidity in topologically nontrivial flat bands”. *Nature Communications* 6, 8944. DOI: [10.1038/ncomms9944](https://doi.org/10.1038/ncomms9944).
- Pfeifer, Walter (2003). “The Lie algebras $su(N)$ ”. *The Lie Algebras $su(N)$: An Introduction*. Basel: Birkhäuser Basel, pp. 15–21. ISBN: 9783034880978. DOI: [10.1007/978-3-0348-8097-8_2](https://doi.org/10.1007/978-3-0348-8097-8_2).
- Piéchon, Frédéric, Arnaud Raoux, et al. (2016). “Geometric orbital susceptibility: Quantum metric without Berry curvature”. *Phys. Rev. B* 94, 134423. DOI: [10.1103/PhysRevB.94.134423](https://doi.org/10.1103/PhysRevB.94.134423).
- Pines, D. (1963). *Elementary Excitations in Solids*. Lecture Notes and Supplements in Physics. Benjamin.
- Po, Hoi Chun, Haruki Watanabe, and Ashvin Vishwanath (2018). “Fragile Topology and Wannier Obstructions”. *Phys. Rev. Lett.* 121, 126402. DOI: [10.1103/PhysRevLett.121.126402](https://doi.org/10.1103/PhysRevLett.121.126402).
- Pontrjagin, Lev (1941). “A classification of mappings of the three-dimensional complex into the two-dimensional sphere”. *Matematicheskii Sbornik* 9.2, 331. DOI: [10.1201/9780367813758-17](https://doi.org/10.1201/9780367813758-17).

- Pozo, Oscar and Fernando de Juan (2020). “Computing observables without eigenstates: Applications to Bloch Hamiltonians”. *Phys. Rev. B* 102, 115138. DOI: [10.1103/PhysRevB.102.115138](https://doi.org/10.1103/PhysRevB.102.115138).
- Provost, J. P. and G. Vallee (1980). “Riemannian structure on manifolds of quantum states”. *Comm. Math. Phys.* 76, 289. DOI: [10.1007/BF02193559](https://doi.org/10.1007/BF02193559).
- Qi, Xiao-Liang and Shou-Cheng Zhang (2011). “Topological insulators and superconductors”. *Rev. Mod. Phys.* 83, 1057. DOI: [10.1103/RevModPhys.83.1057](https://doi.org/10.1103/RevModPhys.83.1057).
- Qiu, Wen-Xuan, Shuai Li, et al. (2016). “Designing an artificial Lieb lattice on a metal surface”. *Phys. Rev. B* 94, 241409. DOI: [10.1103/PhysRevB.94.241409](https://doi.org/10.1103/PhysRevB.94.241409).
- Rabi, I. I. (1928). “Das freie Elektron im homogenen Magnetfeld nach der Diracschen Theorie”. *Zeitschrift für Physik* 49, 507. DOI: [10.1007/BF01333634](https://doi.org/10.1007/BF01333634).
- Rachel, Stephan (2018). “Interacting topological insulators: a review”. *Reports on Progress in Physics* 81, 116501. DOI: [10.1088/1361-6633/aad6a6](https://doi.org/10.1088/1361-6633/aad6a6).
- Ramachandran, Ajith, Alexei Andreanov, and Sergej Flach (2017). “Chiral flat bands: Existence, engineering, and stability”. *Phys. Rev. B* 96, 161104. DOI: [10.1103/PhysRevB.96.161104](https://doi.org/10.1103/PhysRevB.96.161104).
- Rammal, R., G. Toulouse, et al. (1983). “Quantized Hall conductance and edge states: Two-dimensional strips with a periodic potential”. *Phys. Rev. B* 27, 5142. DOI: [10.1103/PhysRevB.27.5142](https://doi.org/10.1103/PhysRevB.27.5142).
- Rao, Zhicheng, Hang Li, et al. (2019). “Observation of unconventional chiral fermions with long Fermi arcs in CoSi”. *Nature* 567, 496. DOI: [10.1038/s41586-019-1031-8](https://doi.org/10.1038/s41586-019-1031-8).
- Raoux, A., M. Morigi, et al. (2014). “From Dia- to Paramagnetic Orbital Susceptibility of Massless Fermions”. *Phys. Rev. Lett.* 112, 026402. DOI: [10.1103/PhysRevLett.112.026402](https://doi.org/10.1103/PhysRevLett.112.026402).
- Raoux, Arnaud, Frédéric Piéchon, et al. (2015). “Orbital magnetism in coupled-bands models”. *Phys. Rev. B* 91, 085120. DOI: [10.1103/PhysRevB.91.085120](https://doi.org/10.1103/PhysRevB.91.085120).
- Reimers, J. N., A. J. Berlinsky, and A.-C. Shi (1991). “Mean-field approach to magnetic ordering in highly frustrated pyrochlores”. *Phys. Rev. B* 43, 865. DOI: [10.1103/PhysRevB.43.865](https://doi.org/10.1103/PhysRevB.43.865).
- Resta, R. (2011). “The insulating state of matter: a geometrical theory”. *The European Physical Journal B* 79, 121. DOI: [10.1140/epjb/e2010-10874-4](https://doi.org/10.1140/epjb/e2010-10874-4).
- Resta, Raffaele (2000). “Manifestations of Berry’s phase in molecules and condensed matter”. *Journal of Physics: Condensed Matter* 12, R107. DOI: [10.1088/0953-8984/12/9/201](https://doi.org/10.1088/0953-8984/12/9/201).
- Rhim, Jun-Won, Jens H. Bardarson, and Robert-Jan Slager (2018). “Unified bulk-boundary correspondence for band insulators”. *Phys. Rev. B* 97, 115143. DOI: [10.1103/PhysRevB.97.115143](https://doi.org/10.1103/PhysRevB.97.115143).
- Rhim, Jun-Won, Kyoo Kim, and Bohm-Jung Yang (2020). “Quantum distance and anomalous Landau levels of flat bands”. *Nature* 584, 59. DOI: [10.1038/s41586-020-2540-1](https://doi.org/10.1038/s41586-020-2540-1).
- Rhim, Jun-Won and Bohm-Jung Yang (2019). “Classification of flat bands according to the band-crossing singularity of Bloch wave functions”. *Phys. Rev. B* 99, 045107. DOI: [10.1103/PhysRevB.99.045107](https://doi.org/10.1103/PhysRevB.99.045107).

- Riwar, Roman-Pascal, Manuel Houzet, et al. (2016). “Multi-terminal Josephson junctions as topological matter”. *Nature Communications* 7, 11167. DOI: [10.1038/ncomms11167](https://doi.org/10.1038/ncomms11167).
- Röntgen, M., C. V. Morfonios, and P. Schmelcher (2018). “Compact localized states and flat bands from local symmetry partitioning”. *Phys. Rev. B* 97, 035161. DOI: [10.1103/PhysRevB.97.035161](https://doi.org/10.1103/PhysRevB.97.035161).
- Rosen, S. P. (1971). “Finite Transformations in Various Representations of SU(3)”. *Journal of Mathematical Physics* 12, 673. DOI: [10.1063/1.1665634](https://doi.org/10.1063/1.1665634).
- Roth, L. M. (1962). “Theory of Bloch electrons in a magnetic field”. *Journal of Physics and Chemistry of Solids* 23.5, 433. DOI: [10.1016/0022-3697\(62\)90083-5](https://doi.org/10.1016/0022-3697(62)90083-5).
- Roth, Laura M. (1966). “Semiclassical Theory of Magnetic Energy Levels and Magnetic Susceptibility of Bloch Electrons”. *Phys. Rev.* 145, 434. DOI: [10.1103/PhysRev.145.434](https://doi.org/10.1103/PhysRev.145.434).
- Ryu, Shinsei and Yasuhiro Hatsugai (2002). “Topological Origin of Zero-Energy Edge States in Particle-Hole Symmetric Systems”. *Phys. Rev. Lett.* 89, 077002. DOI: [10.1103/PhysRevLett.89.077002](https://doi.org/10.1103/PhysRevLett.89.077002).
- Ryu, Shinsei, Andreas P. Schnyder, et al. (2010). “Topological insulators and superconductors: tenfold way and dimensional hierarchy”. *New Journal of Physics* 12, 065010. DOI: [10.1088/1367-2630/12/6/065010](https://doi.org/10.1088/1367-2630/12/6/065010).
- Sanchez, Daniel S., Ilya Belopolski, et al. (2019). “Topological chiral crystals with helicoid-arc quantum states”. *Nature* 567, 500. DOI: [10.1038/s41586-019-1037-2](https://doi.org/10.1038/s41586-019-1037-2).
- Sathe, Pratik, Fenner Harper, and Rahul Roy (2021). “Compactly supported Wannier functions and strictly local projectors”. *Journal of Physics A: Mathematical and Theoretical* 54, 335302. DOI: [10.1088/1751-8121/ac1167](https://doi.org/10.1088/1751-8121/ac1167).
- Sato, Masatoshi and Yoichi Ando (2017). “Topological superconductors: a review”. *Reports on Progress in Physics* 80, 076501. DOI: [10.1088/1361-6633/aa6ac7](https://doi.org/10.1088/1361-6633/aa6ac7).
- Saykin, D. R., K. S. Tikhonov, and Ya. I. Rodionov (2018). “Landau levels with magnetic tunneling in a Weyl semimetal and magnetoconductance of a ballistic $p-n$ junction”. *Phys. Rev. B* 97, 041202. DOI: [10.1103/PhysRevB.97.041202](https://doi.org/10.1103/PhysRevB.97.041202).
- Schrödinger, E. (1926). “Quantisierung als Eigenwertproblem”. *Annalen der Physik* 384.6, 489. DOI: [10.1002/andp.19263840602](https://doi.org/10.1002/andp.19263840602).
- Schröter, Niels B. M., Ding Pei, et al. (2019). “Chiral topological semimetal with multifold band crossings and long Fermi arcs”. *Nature Physics* 15, 759. DOI: [10.1038/s41567-019-0511-y](https://doi.org/10.1038/s41567-019-0511-y).
- Schröter, Niels B. M., Samuel Stolz, et al. (2020). “Observation and control of maximal Chern numbers in a chiral topological semimetal”. *Science* 369.6500, 179. DOI: [10.1126/science.aaz3480](https://doi.org/10.1126/science.aaz3480).
- Schuster, Thomas, Felix Flicker, et al. (2021a). “Floquet engineering ultracold polar molecules to simulate topological insulators”. *Phys. Rev. A* 103, 063322. DOI: [10.1103/PhysRevA.103.063322](https://doi.org/10.1103/PhysRevA.103.063322).
- (2021b). “Realizing Hopf Insulators in Dipolar Spin Systems”. *Phys. Rev. Lett.* 127, 015301. DOI: [10.1103/PhysRevLett.127.015301](https://doi.org/10.1103/PhysRevLett.127.015301).
- Schuster, Thomas, Snir Gazit, et al. (2019). “Floquet Hopf Insulators”. *Phys. Rev. Lett.* 123, 266803. DOI: [10.1103/PhysRevLett.123.266803](https://doi.org/10.1103/PhysRevLett.123.266803).

- Semenoff, Gordon W. (1984). “Condensed-Matter Simulation of a Three-Dimensional Anomaly”. *Phys. Rev. Lett.* 53, 2449. DOI: [10.1103/PhysRevLett.53.2449](https://doi.org/10.1103/PhysRevLett.53.2449).
- Sharma, Girish, Pallab Goswami, and Sumanta Tewari (2017). “Chiral anomaly and longitudinal magnetotransport in type-II Weyl semimetals”. *Phys. Rev. B* 96, 045112. DOI: [10.1103/PhysRevB.96.045112](https://doi.org/10.1103/PhysRevB.96.045112).
- Shen, R., L. B. Shao, et al. (2010). “Single Dirac cone with a flat band touching on line-centered-square optical lattices”. *Phys. Rev. B* 81, 041410. DOI: [10.1103/PhysRevB.81.041410](https://doi.org/10.1103/PhysRevB.81.041410).
- Shiozaki, Ken and Masatoshi Sato (2014). “Topology of crystalline insulators and superconductors”. *Phys. Rev. B* 90, 165114. DOI: [10.1103/PhysRevB.90.165114](https://doi.org/10.1103/PhysRevB.90.165114).
- Simon, Barry (1983). “Holonomy, the Quantum Adiabatic Theorem, and Berry’s Phase”. *Phys. Rev. Lett.* 51, 2167. DOI: [10.1103/PhysRevLett.51.2167](https://doi.org/10.1103/PhysRevLett.51.2167).
- Simon, S. H. (2013). *The Oxford Solid State Basics*. OUP Oxford. ISBN: 9780199680764.
- Singleton, J. (2001). *Band Theory and Electronic Properties of Solids*. Oxford Master Series in Condensed Matter Physics. OUP Oxford. ISBN: 9780198506447.
- Slater, J. C. (1949). “Electrons in Perturbed Periodic Lattices”. *Phys. Rev.* 76, 1592. DOI: [10.1103/PhysRev.76.1592](https://doi.org/10.1103/PhysRev.76.1592).
- Slot, Marlou R, Thomas S Gardenier, et al. (2017). “Experimental realization and characterization of an electronic Lieb lattice”. *Nature Physics* 13, 672. DOI: [10.1038/nphys4105](https://doi.org/10.1038/nphys4105).
- Sommerfeld, A. (1928). “Zur Elektronentheorie der Metalle auf Grund der Fermischen Statistik”. *Zeitschrift für Physik* 47, 1. DOI: [10.1007/BF01391052](https://doi.org/10.1007/BF01391052).
- Song, Zhi-Da, Luis Elcoro, and B. Andrei Bernevig (2020). “Twisted bulk-boundary correspondence of fragile topology”. *Science* 367.6479, 794. DOI: [10.1126/science.aaz7650](https://doi.org/10.1126/science.aaz7650).
- Sun, Xiao-Qi, Shou-Cheng Zhang, and Tomáš Bzdušek (2018). “Conversion Rules for Weyl Points and Nodal Lines in Topological Media”. *Phys. Rev. Lett.* 121, 106402. DOI: [10.1103/PhysRevLett.121.106402](https://doi.org/10.1103/PhysRevLett.121.106402).
- Sutherland, Bill (1986). “Localization of electronic wave functions due to local topology”. *Phys. Rev. B* 34, 5208. DOI: [10.1103/PhysRevB.34.5208](https://doi.org/10.1103/PhysRevB.34.5208).
- Syôzi, Itiro (1951). “Statistics of Kagomé Lattice”. *Progress of Theoretical Physics* 6.3, 306. DOI: [10.1143/ptp/6.3.306](https://doi.org/10.1143/ptp/6.3.306).
- Takane, Daichi, Zhiwei Wang, et al. (2019). “Observation of Chiral Fermions with a Large Topological Charge and Associated Fermi-Arc Surface States in CoSi”. *Phys. Rev. Lett.* 122, 076402. DOI: [10.1103/PhysRevLett.122.076402](https://doi.org/10.1103/PhysRevLett.122.076402).
- Tan, Xinsheng, Dan-Wei Zhang, et al. (2018). “Topological Maxwell Metal Bands in a Superconducting Qutrit”. *Phys. Rev. Lett.* 120, 130503. DOI: [10.1103/PhysRevLett.120.130503](https://doi.org/10.1103/PhysRevLett.120.130503).
- Tan, Xinsheng, Dan-Wei Zhang, et al. (2021). “Experimental Observation of Tensor Monopoles with a Superconducting Qudit”. *Phys. Rev. Lett.* 126, 017702. DOI: [10.1103/PhysRevLett.126.017702](https://doi.org/10.1103/PhysRevLett.126.017702).
- Tang, Peizhe, Quan Zhou, and Shou-Cheng Zhang (2017). “Multiple Types of Topological Fermions in Transition Metal Silicides”. *Phys. Rev. Lett.* 119, 206402. DOI: [10.1103/PhysRevLett.119.206402](https://doi.org/10.1103/PhysRevLett.119.206402).

- Tasaki, Hal (1998). “From Nagaoka’s Ferromagnetism to Flat-Band Ferromagnetism and Beyond: An Introduction to Ferromagnetism in the Hubbard Model”. *Progress of Theoretical Physics* 99.4, 489. DOI: [10.1143/PTP.99.489](https://doi.org/10.1143/PTP.99.489).
- Thonhauser, T. (2011). “Theory of orbital magnetization in solids”. *International Journal of Modern Physics B* 25.11, 1429. DOI: [10.1142/S0217979211058912](https://doi.org/10.1142/S0217979211058912).
- Thonhauser, T., Davide Ceresoli, et al. (2005). “Orbital Magnetization in Periodic Insulators”. *Phys. Rev. Lett.* 95, 137205. DOI: [10.1103/PhysRevLett.95.137205](https://doi.org/10.1103/PhysRevLett.95.137205).
- Thonhauser, T. and David Vanderbilt (2006). “Insulator/Chern-insulator transition in the Haldane model”. *Phys. Rev. B* 74, 235111. DOI: [10.1103/PhysRevB.74.235111](https://doi.org/10.1103/PhysRevB.74.235111).
- Thouless, D. J., M. Kohmoto, et al. (1982). “Quantized Hall Conductance in a Two-Dimensional Periodic Potential”. *Phys. Rev. Lett.* 49, 405. DOI: [10.1103/PhysRevLett.49.405](https://doi.org/10.1103/PhysRevLett.49.405).
- Toikka, L. A. and A. Andreanov (2018). “Necessary and sufficient conditions for flat bands in M -dimensional N -band lattices with complex-valued nearest-neighbour hopping”. *Journal of Physics A: Mathematical and Theoretical* 52, 02LT04. DOI: [10.1088/1751-8121/aaf25c](https://doi.org/10.1088/1751-8121/aaf25c).
- Törmä, Päivi, Sebastiano Peotta, and Bogdan A. Bernevig (2022). “Superconductivity, superfluidity and quantum geometry in twisted multilayer systems”. *Nature Reviews Physics* 4, 528. DOI: [10.1038/s42254-022-00466-y](https://doi.org/10.1038/s42254-022-00466-y).
- Ünal, F. Nur, André Eckardt, and Robert-Jan Slager (2019). “Hopf characterization of two-dimensional Floquet topological insulators”. *Phys. Rev. Research* 1, 022003. DOI: [10.1103/PhysRevResearch.1.022003](https://doi.org/10.1103/PhysRevResearch.1.022003).
- Van Kortryk, T. S. (2016). “Matrix exponentials, $SU(N)$ group elements, and real polynomial roots”. *Journal of Mathematical Physics* 57, 021701. DOI: [10.1063/1.4938418](https://doi.org/10.1063/1.4938418).
- Vicencio, Rodrigo A., Camilo Cantillano, et al. (2015). “Observation of Localized States in Lieb Photonic Lattices”. *Phys. Rev. Lett.* 114, 245503. DOI: [10.1103/PhysRevLett.114.245503](https://doi.org/10.1103/PhysRevLett.114.245503).
- Vilenkin, Alexander (1980). “Equilibrium parity-violating current in a magnetic field”. *Phys. Rev. D* 22, 3080. DOI: [10.1103/PhysRevD.22.3080](https://doi.org/10.1103/PhysRevD.22.3080).
- Volovik, G. E. (1987). “Zeros in the fermion spectrum in superfluid systems as diabolical points”. *Journal of Experimental and Theoretical Physics Letters* 46.2, 98.
- Volovik, Grigory E. (2003). *The Universe in a Helium Droplet*. Vol. 117. International Series of Monographs on Physics. OUP Oxford. ISBN: 9780198507826.
- Wallace, P. R. (1947). “The Band Theory of Graphite”. *Phys. Rev.* 71, 622. DOI: [10.1103/PhysRev.71.622](https://doi.org/10.1103/PhysRev.71.622).
- Wan, Xiangang, Ari M. Turner, et al. (2011). “Topological semimetal and Fermi-arc surface states in the electronic structure of pyrochlore iridates”. *Phys. Rev. B* 83, 205101. DOI: [10.1103/PhysRevB.83.205101](https://doi.org/10.1103/PhysRevB.83.205101).
- Wang, Chong, Wenhui Duan, et al. (2019). “Landau quantization of nearly degenerate bands and full symmetry classification of Landau level crossings”. *Phys. Rev. B* 100, 014442. DOI: [10.1103/PhysRevB.100.014442](https://doi.org/10.1103/PhysRevB.100.014442).

- Wang, Fa and Ying Ran (2011). “Nearly flat band with Chern number $C = 2$ on the dice lattice”. *Phys. Rev. B* 84, 241103. DOI: [10.1103/PhysRevB.84.241103](https://doi.org/10.1103/PhysRevB.84.241103).
- Wang, Jinying, Huaqing Huang, et al. (2013). “Identifying Dirac cones in carbon allotropes with square symmetry”. *The Journal of Chemical Physics* 139, 184701. DOI: [10.1063/1.4828861](https://doi.org/10.1063/1.4828861).
- Wang, Qiang, Meng Xiao, et al. (2017). “Optical Interface States Protected by Synthetic Weyl Points”. *Phys. Rev. X* 7, 031032. DOI: [10.1103/PhysRevX.7.031032](https://doi.org/10.1103/PhysRevX.7.031032).
- Wang, S.-T., D.-L. Deng, and L.-M. Duan (2014). “Probe of Three-Dimensional Chiral Topological Insulators in an Optical Lattice”. *Phys. Rev. Lett.* 113, 033002. DOI: [10.1103/PhysRevLett.113.033002](https://doi.org/10.1103/PhysRevLett.113.033002).
- Wang, Yuchen, Zixuan Hu, et al. (2020). “Qudits and High-Dimensional Quantum Computing”. *Frontiers in Physics* 8, 589504. DOI: [10.3389/fphy.2020.589504](https://doi.org/10.3389/fphy.2020.589504).
- Wannier, Gregory H. (1937). “The Structure of Electronic Excitation Levels in Insulating Crystals”. *Phys. Rev.* 52, 191. DOI: [10.1103/PhysRev.52.191](https://doi.org/10.1103/PhysRev.52.191).
- Weeks, C. and M. Franz (2010). “Topological insulators on the Lieb and perovskite lattices”. *Phys. Rev. B* 82, 085310. DOI: [10.1103/PhysRevB.82.085310](https://doi.org/10.1103/PhysRevB.82.085310).
- Weisstein, Eric W. (n.d.[a]). *Cubic Formula*. From MathWorld—A Wolfram Web Resource. <https://mathworld.wolfram.com/CubicFormula.html>.
- (n.d.[b]). *Quartic Equation*. From MathWorld—A Wolfram Web Resource. <https://mathworld.wolfram.com/QuarticEquation.html>.
- Weng, Hongming, Chen Fang, et al. (2016a). “Coexistence of Weyl fermion and massless triply degenerate nodal points”. *Phys. Rev. B* 94, 165201. DOI: [10.1103/PhysRevB.94.165201](https://doi.org/10.1103/PhysRevB.94.165201).
- (2016b). “Topological semimetals with triply degenerate nodal points in θ -phase tantalum nitride”. *Phys. Rev. B* 93, 241202. DOI: [10.1103/PhysRevB.93.241202](https://doi.org/10.1103/PhysRevB.93.241202).
- Weng, Hongming, Rui Yu, et al. (2015). “Quantum anomalous Hall effect and related topological electronic states”. *Advances in Physics* 64.3, 227. DOI: [10.1080/00018732.2015.1068524](https://doi.org/10.1080/00018732.2015.1068524).
- Weyl, Hermann (1929). “Elektron und Gravitation. I”. *Zeitschrift für Physik* 56, 330. DOI: [10.1007/BF01339504](https://doi.org/10.1007/BF01339504).
- Wieder, Benjamin J., Youngkuk Kim, et al. (2016). “Double Dirac Semimetals in Three Dimensions”. *Phys. Rev. Lett.* 116, 186402. DOI: [10.1103/PhysRevLett.116.186402](https://doi.org/10.1103/PhysRevLett.116.186402).
- Wilczek, F. and A. Shapere (1989). *Geometric Phases in Physics*. Vol. 5. Advanced Series in Mathematical Physics. World Scientific. DOI: [10.1142/0613](https://doi.org/10.1142/0613).
- Wilczek, Frank and A. Zee (1984). “Appearance of Gauge Structure in Simple Dynamical Systems”. *Phys. Rev. Lett.* 52, 2111. DOI: [10.1103/PhysRevLett.52.2111](https://doi.org/10.1103/PhysRevLett.52.2111).
- Xia, Y., D. Qian, et al. (2009). “Observation of a large-gap topological-insulator class with a single Dirac cone on the surface”. *Nature Physics* 5, 398. DOI: [10.1038/nphys1274](https://doi.org/10.1038/nphys1274).
- Xiao, Di, Ming-Che Chang, and Qian Niu (2010). “Berry phase effects on electronic properties”. *Rev. Mod. Phys.* 82, 1959. DOI: [10.1103/RevModPhys.82.1959](https://doi.org/10.1103/RevModPhys.82.1959).
- Xiao, Di, Junren Shi, and Qian Niu (2005). “Berry Phase Correction to Electron Density of States in Solids”. *Phys. Rev. Lett.* 95, 137204. DOI: [10.1103/PhysRevLett.95.137204](https://doi.org/10.1103/PhysRevLett.95.137204).

- Xiao, Di, Wang Yao, and Qian Niu (2007). “Valley-Contrasting Physics in Graphene: Magnetic Moment and Topological Transport”. *Phys. Rev. Lett.* 99, 236809. DOI: [10.1103/PhysRevLett.99.236809](https://doi.org/10.1103/PhysRevLett.99.236809).
- Xin, Li, Yu Siyuan, et al. (2020). “Topological mechanical metamaterials: A brief review”. *Current Opinion in Solid State and Materials Science* 24.5, 100853. DOI: [10.1016/j.cossms.2020.100853](https://doi.org/10.1016/j.cossms.2020.100853).
- Yang, Hao, Yan Sun, et al. (2017). “Topological Weyl semimetals in the chiral antiferromagnetic materials Mn_3Ge and Mn_3Sn ”. *New Journal of Physics* 19, 015008. DOI: [10.1088/1367-2630/aa5487](https://doi.org/10.1088/1367-2630/aa5487).
- Yang, Kai-Yu, Yuan-Ming Lu, and Ying Ran (2011). “Quantum Hall effects in a Weyl semimetal: Possible application in pyrochlore iridates”. *Phys. Rev. B* 84, 075129. DOI: [10.1103/PhysRevB.84.075129](https://doi.org/10.1103/PhysRevB.84.075129).
- Yao, Mengyu, Kaustuv Manna, et al. (2020). “Observation of giant spin-split Fermi arc with maximal Chern number in the chiral topological semimetal PtGa”. *Nature Communications* 11, 2033. DOI: [10.1038/s41467-020-15865-x](https://doi.org/10.1038/s41467-020-15865-x).
- Yue, Di and Xiaofeng Jin (2017). “Towards a Better Understanding of the Anomalous Hall Effect”. *Journal of the Physical Society of Japan* 86, 011006. DOI: [10.7566/JPSJ.86.011006](https://doi.org/10.7566/JPSJ.86.011006).
- Zhang, Dan-Wei, Yan-Qing Zhu, et al. (2018). “Topological quantum matter with cold atoms”. *Advances in Physics* 67.4, 253. DOI: [10.1080/00018732.2019.1594094](https://doi.org/10.1080/00018732.2019.1594094).
- Zhou, Bin, Hai-Zhou Lu, et al. (2008). “Finite Size Effects on Helical Edge States in a Quantum Spin-Hall System”. *Phys. Rev. Lett.* 101, 246807. DOI: [10.1103/PhysRevLett.101.246807](https://doi.org/10.1103/PhysRevLett.101.246807).
- Zhou, Yi, Kazushi Kanoda, and Tai-Kai Ng (2017). “Quantum spin liquid states”. *Rev. Mod. Phys.* 89, 025003. DOI: [10.1103/RevModPhys.89.025003](https://doi.org/10.1103/RevModPhys.89.025003).
- Zhu, Yan-Qing, Nathan Goldman, and Giandomenico Palumbo (2020). “Four-dimensional semimetals with tensor monopoles: From surface states to topological responses”. *Phys. Rev. B* 102, 081109. DOI: [10.1103/PhysRevB.102.081109](https://doi.org/10.1103/PhysRevB.102.081109).
- Zhu, Yan-Qing, Dan-Wei Zhang, et al. (2017). “Emergent pseudospin-1 Maxwell fermions with a threefold degeneracy in optical lattices”. *Phys. Rev. A* 96, 033634. DOI: [10.1103/PhysRevA.96.033634](https://doi.org/10.1103/PhysRevA.96.033634).
- Zhu, Ziming, Georg W. Winkler, et al. (2016). “Triple Point Topological Metals”. *Phys. Rev. X* 6, 031003. DOI: [10.1103/PhysRevX.6.031003](https://doi.org/10.1103/PhysRevX.6.031003).
- Ziman, J.M. (1960). *Electrons and Phonons: The Theory of Transport Phenomena in Solids*. Clarendon Press.
- Zyczkowski, Karol and Hans-Jürgen Sommers (2003). “Hilbert-Schmidt volume of the set of mixed quantum states”. *Journal of Physics A: Mathematical and General* 36, 10115. DOI: [10.1088/0305-4470/36/39/310](https://doi.org/10.1088/0305-4470/36/39/310).
- Zyuzin, A. A., Si Wu, and A. A. Burkov (2012). “Weyl semimetal with broken time reversal and inversion symmetries”. *Phys. Rev. B* 85, 165110. DOI: [10.1103/PhysRevB.85.165110](https://doi.org/10.1103/PhysRevB.85.165110).
- Zyuzin, Vladimir A. (2017). “Magnetotransport of Weyl semimetals due to the chiral anomaly”. *Phys. Rev. B* 95, 245128. DOI: [10.1103/PhysRevB.95.245128](https://doi.org/10.1103/PhysRevB.95.245128).

